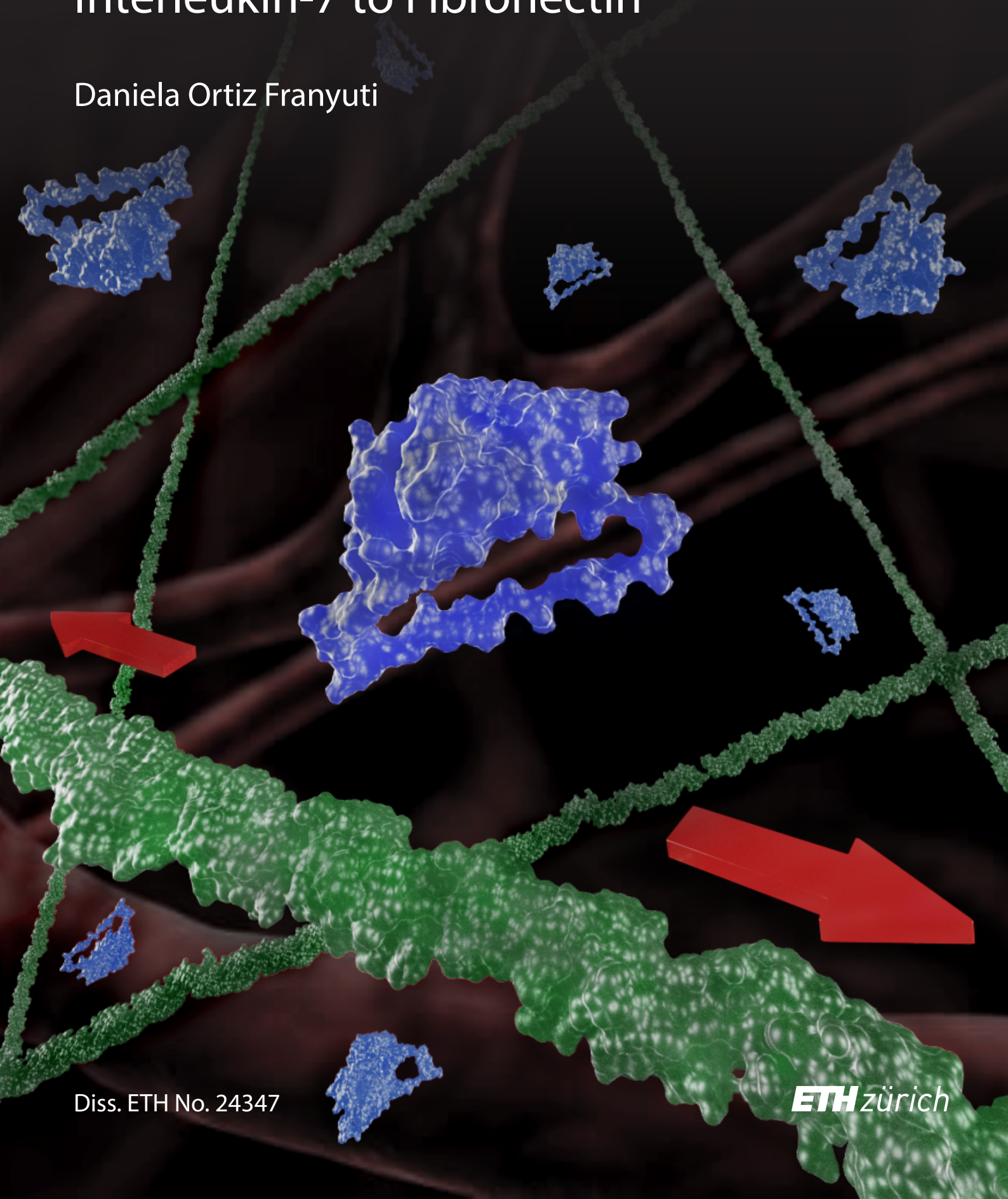


Mechanical force modulates binding of Interleukin-7 to Fibronectin

Daniela Ortiz Franyuti



Diss. ETH No. 24347

Mechanical force modulates binding of Interleukin-7 to Fibronectin

A thesis submitted to attain the degree of
DOCTOR OF SCIENCES of ETH ZURICH

(Dr. sc. ETH Zurich)

presented by

Daniela Ortiz Franyuti

M.Sc. in Biomedical Engineering, University of Bern, Switzerland

BEng (Hons) in Medical Engineering, Cardiff University, United Kingdom

born March 16th, 1984

Citizen of Mexico and Beromünster/Landiswil, Switzerland

accepted on the recommendation of

Prof. Dr. Viola Vogel

Prof. Dr. Michael Dustin

Prof. Dr. Cornelia Halin

2017

*Para mi Mamá,
Rosa María Franyuti Ordoñez
(1958-2016)*

*Todo tu esfuerzo, tu tiempo, tus detalles,
tu entrega completa, tu apoyo incondicional,
tu amor infinito...
me han puesto donde estoy.*

*Gracias por acompañarme,
Gracias por creer en mí.
Gracias por cuidar mis pasos.*

*Te amo con toda mi alma,
con todas mis fuerzas*

Tu Da

Abstract

The extracellular matrix (ECM) plays an important role in cell regulation, development, and homeostasis. Not only does it provide a structural scaffold for cell migration and interaction, but also acts as a deposit for cytokines and chemokines that regulate cellular function. Cells can modify the structure, composition, and biochemical characteristics of the ECM, and are able to apply mechanical forces that can alter the ECM and its components. One essential component of the ECM is fibronectin (FN). A protein that forms fibers in the ECM, and has various binding sites that allow intermolecular interactions among other FN molecules, with other ECM constituent proteins, carbohydrates, cell-ECM binding proteins such as integrins, and various cytokines and signaling molecules. FN has several mechanosensitive cryptic binding sites that open upon protein unfolding due to mechanical tension. During inflammation and other physiological processes, swelling of tissue and ECM remodeling can induce mechanical stretching or relaxing of the ECM, which can in turn induce a change in the conformation of FN.

This thesis contributes to the understanding of how force-induced conformational changes in FN can have an impact on cytokine binding, by focusing on how mechanically stretching FN fibers affect the binding of interleukin-7 (IL-7) to FN. IL-7 is a cytokine belonging to the γ -c interleukin family that plays an essential role in the survival, proliferation and differentiation of naive and memory T-cells in lymphatic tissues, and the development of B and T-cells in the thymus. It is produced by stromal cells in the lymph nodes and thymus, and has been previously shown to bind to fibronectin (FN).

In this thesis, a Förster Resonance Energy Transfer (FRET) based method to correlate ligand-binding to changes in FN conformation is presented. This method provides a quantitative tool to assess how changes in FN conformation result in modified cytokine binding. The developed method was used to assess whether FN's conformational changes due to mechanical force application result in changes in binding of IL-7. We found that stretching of FN fibers increased IL-7 binding, and localized the FN binding site on the CD-loop region of IL-7 using a synthetic CD-loop peptide which also showed increased binding to stretched fibrillar FN.

Upon structural analysis of IL-7 binding to its receptors IL7RA and IL2RG, we propose that the CD-loop is available for simultaneous interaction with FN while IL-7 is bound to its cognate cell receptors. We also propose a negative-feedback mechanism reciprocally regulating the tensional state of FN fibers and IL-7 signaling. Our data show then, for the first time, a mechano-regulated mechanism of IL-7 binding to the ECM, where stretching FN fibers might locally concentrate IL-7 in an extracellular matrix bound state.

Finally, first steps towards determining what impact these findings may have on cellular function are presented, to motivate the refinement and/or development of adequate assays to test the physiological implications of our findings. Since IL-7 is produced by lymph node stromal cells (LNSCs), and stromal cells from the thymus, and these cells in turn respond to IL-7, we aimed to characterize mechano-biological behaviour of these cells, their ECM, and make the first steps towards elucidating whether these cells can bring about changes in the ECM that could result in differential binding of IL-7 to fibronectin in the ECM, and in turn, whether changes in IL-7 binding levels can have an effect on their function.

The work presented here could be of relevance for the further understanding of how mechanically induced changes of the ECM affect chemokine and cytokine binding and the effects of this on cell function. These aspects should be considered in the future for the development of current and/or new IL-7 based immunotherapies that take into consideration possible changes in ECM due to disease, inflammation or ageing.

Zusammenfassung

Die Extrazelluläre Matrix (ECM) spielt eine wichtige Rolle bei der Zellregulation, der -entwicklung und der Homöostase. Sie schafft nicht nur ein strukturelles Gerüst für Zellmigration und -interaktion, sondern dient auch als Aufbewahrungsort für Zytokine und Chemokine, welche die Zellfunktion regulieren. Zellen können die Struktur, die Zusammensetzung und die Charakteristiken der ECM modifizieren und sind in der Lage, mechanische Kräfte anzuwenden, welche die ECM und ihre Komponenten beeinflussen. Eine essentielle Komponente der ECM ist Fibronectin (Fn), ein Protein, das die Fasern in der ECM gestaltet und zahlreiche Verbindungsstellen aufweist. Diese ermöglichen intermolekuläre Interaktionen zwischen Fn-Molekülen, anderen ECM-bildenden Molekülen, Kohlenhydraten, Verbindungsproteinen von Zell-ECM wie Integrinen, sowie zahlreichen Zytokinen und Signalmolekülen. Fn weist mehrere mechanosensitive, kryptische Verbindungsstellen auf, die sich bei Proteinfaltungen aufgrund mechanischer Kräfte öffnen. Während Entzündungsprozessen oder anderen physiologischen Prozessen, kann die Schwellung von Gewebe und ECM-Umgestaltungen zu mechanischem Strecken oder Entspannen führen, was wiederum eine Veränderung in der Anpassung von Fn resultieren kann.

Diese Thesis trägt zum Verständnis bei, wie kraftinduzierte Strukturveränderungen von Fn sich auf Zytokin-Verbindungen auswirken können, indem sie darauf fokussiert, wie das mechanische strecken von Fn-Fasern die Verbindung von Interleukin-7 (IL-7) zu Fn beeinflusst. IL-7 ist ein Zytokin, das zur Familie der 9-c-Interleukine gehört und eine essentielle Rolle im Überleben, in der Proliferation und in der Ausdifferenzierung von naiven T-Zellen und Memory-T-Zellen im Lymphgewebe spielt, sowie in der Entwicklung von B- und T-Zellen im Thymus. Es wird durch Stromazellen in den Lymphknoten und im Thymus gebildet und bindet - wie es sich erst kürzlich gezeigt hat - zu Fn.

In dieser Thesis wird eine auf dem Förster Resonance Energy Transfer (FRET) basierende Methode zur Korrelation zwischen einer Ligandenbindung und der Fn-Struktur präsentiert. Diese Methode dient als quantitatives Werkzeug, um festzustellen, wie eine Veränderung in der Fn-Anpassung in einer veränderten Zytokinbindung resultiert. Die entwickelte Methode wurde dazu verwendet, festzustellen, ob Fn- Strukturveränderungen aufgrund einer Anwendung mechanischer Kräfte in einer Veränderung der IL-7-Verbindungen resultiert. Wir haben festgestellt, dass die Dehnung von Fn-Fasern die IL-7-Bindungen erhöhen und lokalisierten die Fn-Bindungsstellen auf der CD-loop-Region von IL-7. Dazu verwendeten wir synthetische CD-loop-Peptide, welche auch eine erhöhte Bindung zu gestrecktem fibrillärem Fn gezeigt haben.

Aufgrund der strukturellen Analyse von IL-7-Verbindungen zu deren Rezeptoren IL7RA und IL2RG schlagen wir vor, dass der CD-loop für simultane Reaktionen mit Fn zur Verfügung steht, während IL-7 mit seinen verwandten Rezeptoren verbunden ist. Wir vermuten zudem einen negativen Feedbackmechanismus, der reziprok den Spannungszustand von Fn-Fasern und IL-7-Signalisierung reguliert. Unsere Daten zeigen zudem erstmalig einen mechanoregulierten Mechanismus von IL-7-Verbindungen mit der ECM.

Schliesslich präsentieren wir erste Schritte in der Beantwortung der Frage, welche Auswirkungen diese Erkenntnisse auf die Zellfunktion haben. Dies mit dem Ziel, die Verfeinerung und/oder die die Entwicklung von adäquaten Analysen anzuregen, um die physiologischen Implikationen unserer Ergebnisse zu testen. Da IL-7 durch Lymphknoten-Stromazellen (LNSCs) produziert wird, Stromazellen ihrerseits durch den Thymus und diese Zellen wiederum auf IL-7 reagieren, haben wir angestrebt, das mechanobiologische Verhalten dieser Zellen und ihrer ECM zu charakterisieren und haben erste Schritte unternommen in Richtung einer Erklärung, ob diese Zellen die ECM verändern können und ob diese Veränderungen in einer differenziellen Bindung von IL-7 in der ECM resultieren könnte, oder umgekehrt, ob Veränderungen in den IL-7 Bindungsniveaus Auswirkungen auf deren Funktion haben kann.

Die hier präsentierte Arbeit könnte dazu dienen, zu verstehen, wie mechanisch induzierte Veränderungen der ECM Chemokin- und Zytokinbindungen beeinflussen und wie sich dies auf die Zellfunktion auswirkt. Diesen Aspekten sollte in Zukunft Beachtung geschenkt werden, wenn IL-7-basierte Immuntherapien entwickelt werden, bei denen mögliche Veränderungen der ECM aufgrund von Krankheit, Entzündung oder Alter eine Rolle spielen.

Abbreviation List

α -SMA	Alpha-smooth muscle actin
A488	Alexa fluor 488
A546	Alexa fluor 546
A647	Alexa fluor 647
A647-IL-7	Alexa 647-labeled IL-7
APCs	Antigen Presenting Cells
Bcl-2	B-cell lymphoma 2 protein
BECs	Blood Endothelial Cells
CLEC2	C-type lectin domain family 1 member B
ECM	Extracellular Matrix
FGF	fibroblast growth factor
FN	Fibronectin
Fnl / FnII / FNIII	Fibronectin Module Type I / II or /III
FRCs	Fibroblastic Reticular Cells
FRET	Förster Resonance Energy Transfer
FN-FRET	FRET-labeled fibronectin
IFN- γ	Interferon Gamma
IL-2	Interleukin-2
IL-7	Interleukin-7
IL7RA	Interleukin-7 Receptor Alpha
IL2RG	Interleukin-2 Receptor Gamma (Common Gamma Receptor)
JAK3/5	Janus kinase 3/5
LECs	Lymphatic Endothelial Cells
LNSCs	Lymph Node Stromal Cells
MHC	Major Histocompatibility Complex
MMP	Matrix Metalloproteinase
NFAT	Nuclear factor of activated T-cells
NHDFs	Normal Human Dermal Fibroblasts
PDGF	Platelet-derived growth factor
PECAM-1	Platelet endothelial cell adhesion molecule
rhIL-7	Recombinant human Interleukin-7
rmIL-7	Recombinant murine Interleukin-7
STAT5	Signal transducer and activator of transcription 5
TCR	T-cell receptor
TGF- β 1	Transforming growth factor beta-1
TNF- α	Tumor necrosis factor alpha
VEGF	Vascular endothelial growth factor

Table of Contents

Abstract.....	iii
Zusammenfassung	iv
Abbreviation List.....	v
1. Scope of the thesis.....	1
1.1. Objectives	2
2. Introduction	3
2.1. Fibronectin	3
2.1.1. Structure	3
2.1.2. Protein-protein interactions and FN function.....	4
2.1.3. Functional consequences of ECM remodeling and fibronectin stretching.....	6
2.2. Interleukin-7	7
2.2.1. Structure and signaling pathways	7
2.2.2. IL-7 role in lymphocyte development	9
2.2.3. IL-7 has a role in T-cell activation and memory development.....	10
2.2.4. Stromal cells, IL-7 production and consumption.	11
2.3. IL-7/ FN interactions, ECM remodeling, and their reciprocal role in stromal and lymphocyte function.	12
2.4. IL-7 binding correlated to Fibronectin-FRET	15
2.5. Förster Resonance Energy Transfer (FRET)	15
2.6. Intramolecular FRET probe to assess fibronectin strain	18
2.6.1. Fibronectin purification	18
2.6.2. FRET Fibronectin labelling	19
2.6.3. FRET Fibronectin conformation sensitivity control	21
2.6.4. Mechano-sensitivity control.....	22

2.7.	Method to correlate ligand binding with FRET ratio	22
2.7.1.	Experimental context	23
2.7.2.	Data acquisition	24
2.7.3.	Post-acquisition processing	26
2.7.4.	Signal correction FRET ratio calculation	28
2.7.5.	Ligand Signal	34
2.7.6.	FN-FRET/Ligand correlation	34
2.8.	Matlab based Graphic User Interface software for FRET and Ligand Correlated FRET analysis.	35
2.8.1.	Features	35
2.8.2.	Workflow	35
2.8.3.	Generated Results	38

3. Mechanical stretching of fibronectin fibers upregulates binding of interleukin-7. 41

3.1.	Abstract	41
3.2.	Introduction	42
3.3.	Stretching of FN fibers increases IL-7 binding.	43
3.4.	The CD loop of IL-7 binds preferentially to more stretched FN fibers and is likely to mediate IL-7/FN binding.	48
3.5.	Sequence alignment between the CD-loop peptide and bacterial adhesins that also target the FN N-terminus.	50
3.6.	Model of how the tensional state of FN fibers might alter IL-7 signaling	52
3.7.	Conclusion	54
3.8.	Supporting Information: Materials and Methods	54
3.8.1.	FN purification	54
3.8.2.	Fluorescence resonance energy transfer (FRET) labeling of FN (FN-FRET)	54
3.8.3.	IL-7 labeling.	55
3.8.4.	Human IL-7 CD-loop peptide.	55
3.8.5.	IL-7 binding to fibrillar FN.	55
3.8.6.	Image processing.	56
3.8.7.	FRET intensity signal correction.	56
3.8.8.	Ratiometric FRET calculation.	58
3.8.9.	Ligand signal normalization.	58
3.9.	Supporting Information: Supplementary Figures	59
3.10.	Supportive Information: Additional files	74

4.	Preliminary studies contextualizing IL-7/FN binding and stromal cell behavior.	75
4.1.	Lymph Node Stromal Cell contractility characterization	75
4.1.1.	Method.....	75
4.1.2.	Results	77
4.1.3.	Conclusion	77
4.2.	FN conformation in Lymph Node Stromal Cell-assembled ECM in cell culture.	78
4.2.1.	Method.....	78
4.2.1.	Results	78
4.2.1.	Conclusion	79
4.3.	IL-7 internalization and FN conformation in LNSC cultures.	81
4.3.1.	Method.....	81
4.3.2.	Results	81
4.3.3.	Discussion and conclusions	83
4.4.	Time-frame of uptake and internalization of IL-7	85
4.4.1.	Method.....	85
4.4.2.	Results	85
4.4.3.	Conclusions	85
4.5.	Identification of LNSC subsets that internalize IL-7	87
4.5.1.	Method.....	87
4.5.2.	Results	88
4.5.3.	Conclusions	88
4.6.	Assay to assess cell function on de-cellularized ECM substrates subjected to perpendicular flow.	92
4.6.1.	Method.....	93
4.6.2.	Results	95
4.6.3.	Discussion and Conclusion	95
5.	Outlook	97

6. Conclusion 98

7. References 99

8. Acknowledgements 110

8.1. Funding Sources **110**

9. Curriculum Vitae 111

Appendix: 113

1. Scope of the thesis

Currently, a variety of immunotherapies are being investigated with the aim of harvesting the immune system's warfare to tackle diseases such as cancer or various infectious diseases, or to boost the immune response in patients that suffer from immunological deficiencies¹⁻³.

One cytokine that is currently under investigation as a potential immunotherapy is Interleukin-7 (IL-7)¹. IL-7 plays a crucial role in the development of B and T-cells in the thymus, but also in the survival, proliferation and differentiation of mature naive and memory T-cells⁴⁻⁸. For this reason, there are currently a number of clinical trials testing the use of recombinant human IL-7 (rhIL-7) to treat several diseases such as HIV, cancer, idiopathic CD4+ T-cell lymphocytopenia, chronic viral infections, hepatitis B and C viral infections, congenital immunodeficiency, for immunological restoration after hematopoietic stem cell transplantation or chemotherapy and even for immune insufficiencies related to ageing¹.

Alternatively, blocking of the IL-7 signaling pathway by means of antibodies against IL-7 or one of its receptors (IL7R α) is currently being investigated to treat diseases where the aim is suppression of an over-reactive immune response, for example multiple sclerosis, type 1 diabetes, rheumatoid arthritis, Sjögren's syndrome, inflammatory bowel disease and systemic lupus erythematosus⁹.

In clinical studies where rhIL-7 was administrated, it was shown that although the measured half-life was of several hours (from 6 to up to 23 hours), the biological effects persisted for days, and in some studies even several weeks, as reviewed by Mackall et al.¹. It has therefore been proposed that these long lasting effects could be the result of a combination of IL-7 binding to ECM components followed by slow release and the downstream changes in proliferation and survival that persist beyond the initial IL-7 stimulation¹.

Since circulating IL-7 is present at a rather low concentration (10 to 40 pg/ml in plasma, 15 to 35pg/ml in lymph)^{10,11}, and cells compete for the relatively small amount of IL-7 available¹², and because the composition, structure and binding availability of the extracellular matrix (ECM) are affected by inflammation and disease¹³⁻¹⁵, it is important to understand how changes in the ECM structure and composition, as well as IL-7/ECM interactions might affect the local and systemic availability of this cytokine.

The extracellular matrix (ECM) not only provides the scaffolding where cells interact and function, but also acts as a versatile extracellular signaling framework that affects cellular function¹⁶. Through biochemical and/or mechanical force induced structural modifications of ECM proteins, cells can alter the ECM and either reveal or close cryptic sites in ECM proteins for binding of cell receptors such as integrins, or other signaling molecules such as chemokines, and other cytokines^{13,17}. In a sense, the ECM can act as a storage location for signaling molecules that cells can deposit and sense to communicate with one other^{13,16,17}.

One of the ECM components to which IL-7 has been shown to bind is fibronectin (FN)^{18,19}. FN is a protein that is able to form fibrils that drive ECM assembly and has various binding sites that allow intermolecular interactions among other FN molecules, with other ECM constituent proteins and carbohydrates, cell-ECM binding proteins such as integrins, and other cytokines and signaling molecules²⁰⁻²⁴. More interestingly, FN has several mechanosensitive cryptic binding sites that open upon unfolding due to mechanical force^{16,17,20} and binding sites that are sensitive to mechanical stretching of FN fibers²⁵. During inflammation and other physiological processes, swelling of tissue and ECM remodeling can induce mechanical stretching or relaxing of the ECM^{13,26} which can induce a change in the conformation of FN²⁷.

The purpose of this work is to focus on the interaction between IL-7 and FN, and determine how force-induced conformational changes in FN can have an impact on IL-7 binding, and to lay the first steps in

determining what impact this may have on cellular function. This information could be of relevance for the further development of current and/or new IL-7 based immunotherapies that take into consideration possible changes in ECM due to disease, inflammation or ageing.

1.1. Objectives.

The main objective of this work is to understand the nature of the IL-7/ FN interactions and its effect on cellular function. We have divided the task in three main objectives as follows:

- To develop a FRET-correlated ligand-binding assay to quantitatively assess how changes in fibronectin fiber strain result in changes in IL-7 binding, that can also be applied in the future to other cytokines.
- To use this assay to assess whether stretching FN fibers result in changes of binding of IL-7, and define which structures and molecular interactions are involved.
- To develop relevant assays that can be used to assess how variations in IL-7 concentration due to binding to fibronectin could influence cellular responses, and that could also be applied in the future to other cytokines.

This thesis is built upon these three main objectives. Chapter 2 will cover the current relevant knowledge regarding fibronectin and interleukin-7, and IL-7/FN/ECM interactions with stromal and cells and lymphocytes. In Chapter 3, the basics of Förster Resonance Energy Transfer (FRET), and the method developed to correlate ligand-binding with mechanically-induced fibronectin's conformational changes as assessed by FRET will be described. Chapter 4 will cover how changes in Fibronectin conformation due to mechanical stretching affect binding of both human and murine Interleukin-7, a structural analysis that might explain this phenomenon, and the implications of such findings. Finally, Chapter 5 will outline several preliminary studies and assays that were developed to begin to assess the potential impact of variations in Interleukin-7 availability on cellular responses, as well as suggest further work could be performed along this line of research and to what possible ends. These preliminary studies include the characterization of lymph node stromal cell (LNSC) contractility, fibronectin conformation in LNSC-assembled ECM in cell culture, an assessment of IL-7 internalization and FN conformation in LNSC cultures, attempts at defining the time-frame of uptake and internalization of IL-7, as well as identification of LNSC subsets that internalize it, and the development of an assay to assess cell function on de-cellularized ECM substrates subjected to perpendicular flow.

2. Introduction

In this chapter I will introduce fibronectin's (FN) structure, main functions, its interactions with other proteins, and how unfolding of the molecule via mechanical forces can open cryptic sites for protein binding. I will also introduce interleukin-7 (IL-7) and describe its structure, function and signaling, its effect on stromal cells. Finally, I will introduce what is known regarding IL-7/FN interactions and ECM remodeling, and their reciprocal role in stromal and lymphocyte function, all in the context of inflammatory responses.

2.1. Fibronectin

Fibronectin is a high molecular weight (~240kDa) dimeric glycoprotein that forms part of the Extracellular Matrix (ECM) and is crucial for its function¹⁶. It can form fibrils that drive ECM assembly^{22,28,29} and has various binding sites that allow intermolecular interactions among other fibronectin molecules, with other ECM constituent proteins and carbohydrates, cell-ECM binding proteins such as integrins, and other cytokines and signaling molecules such as growth factors^{20,21,23,24,30}.

2.1.1. Structure

Fibronectin consists of a chain of fibronectin type I, II and III modules (FNI, FNII and FNIII respectively) and is found mainly as a homodimer with two chains covalently linked via disulphide bonds near their C-terminus^{28,30-32}. FNI modules consist of two stacked antiparallel β -sheets encompassing a hydrophobic core consisting of conserved aromatic residues as shown in Fig.2.1. The first β -sheet consists of two strands (A and B). The second one consists of three strands (C,D and E) with a disulphide bond linking strands D and E, and a second disulphide bond linking the two β -sheets between strands A and D. Both the hydrophobic core and the disulphide bonds stabilize the construct and make the FNI modules resistant to unfolding due to the application of mechanical forces^{28,31,33}. FNII modules consist of two antiparallel β -sheets perpendicular to each other, each one consisting of two strands, with two disulphide bonds connecting β -sheets 1 with 3 and 2 with 4, as shown in Fig.2.1^{28,31,34}. FNIII modules are very similar to Ig domains, except that they lack disulphide bonds. They consist of two antiparallel β -sheets, as shown in Fig.2.1, the first one formed by three strands (A,B and E) and the second one of four (G,F,C and D), stacked as a β -sandwich and enclosing a hydrophobic core)^{28,31,35,36}. Because they lack disulphide bonds, these modules are more vulnerable to unfolding due to the exertion of mechanical forces upon them¹⁷.

Fibronectin is encoded by the ~50kb human fibronectin gene and is subjected to alternative pre-mRNA splicing and diverse post-translational modifications that result in up to 20 different variants of the fibronectin protein^{37,38}. There are two alternative fibronectin segments that vary depending on exon usage, these are the extra-domain A (EDA) and extra-domain B (EDB), located between FNIII₁₁ and FNIII₁₂ and between FNIII₇ and FNIII₈ respectively^{37,38}. In addition, the variable region (V) is subject to exon subdivisions that result in five different variants named according to their amino acid residue length (V0, V64, V89, V95, and V120), and a special type of cartilage-specific fibronectin termed (V+C)-, which lacks the entire variable region through the FNI₁₀ module^{37,38}.

Fibronectin isolated from plasma tends to have a lower molecular weight than fibronectin isolated from cell culture and it generally lacks the EDA and EDB segments, and the variable region, therefore termed V0. Cellular fibronectin is a more heterogeneous group of splice variants and contains the EDA and EDB regions and various V isoforms^{37,38}.

FN Modules structure

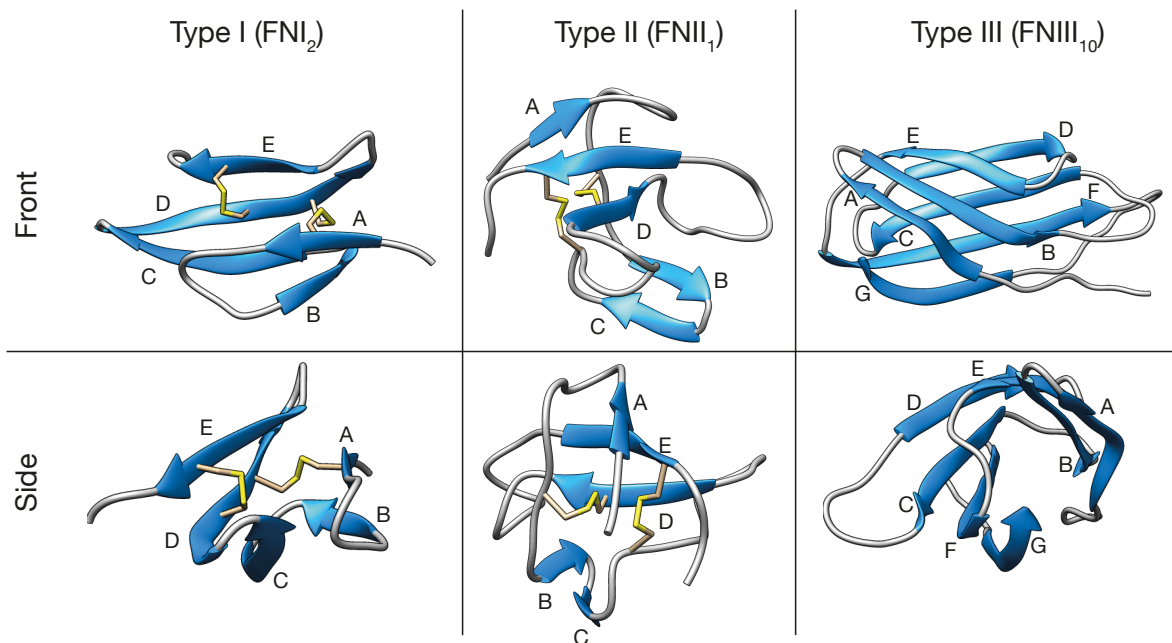


Figure 2.1. Fibronectin Modules exemplified by modules FNI_2 , $FNII_1$ and $FNIII_{10}$ molecular structure (PDB structures: 3CAL³⁹, 3MQL⁴⁰, and 1TTG⁴¹ respectively) rendered using Chimera Software⁴².

2.1.2. Protein-protein interactions and FN function

Fibronectin has numerous binding sites for other ECM constituent proteins such as Collagen, Fibrin, Gelatin, Tissue transglutaminase, and FN-FN binding sites which allow for cross-linking for proper formation of the ECM, as well as FN fibrillogenesis^{17,20-22,30}. It has also binding sites for carbohydrates such as Heparin, Heparan Sulphate and Syndecans, which allow for glycosylation of the molecule, and very importantly, numerous binding sites for integrins, which allow for cell-ECM binding^{17,20-24,30}.

It has also been shown that fibronectin has binding sites for several cytokines and growth factors, including tumor necrosis factor α (TNF- α), which was found to bind to the N-terminus of FN⁴³, and cytokines and growth factors that were found to interact with FN type III modules $FNIII_{12}$ – $FNIII_{14}$ ²³: insulin-like growth factor binding-protein-3, members of the platelet-derived growth factor PDGF family (PDGF-AA, PDGF-AB, PDGF-BB, PDGF-CC, PDGF-DD, vascular endothelial growth factors (VEGF) (VEGF-A165, VEGF-B, VEGF-C, EG-VEGF), placenta growth factors (PIGF-2, and PIGF-3), members of the fibroblast growth factor (FGF) family (FGF-2, FGF-4, FGF-5, FGF-7, FGF-8, FGF-9, FGF-10, FGF-17, FGF-18, FGF-21), transforming growth factor β (TGF) TGF- β 1, Bone morphogenetic proteins (BMP-2, and BMP-7), as well as NGF, NT-3, and BDNF from the neurotrophin growth factor family. In addition, it has been shown that FN has binding sites for bacterial peptides found in various bacterial species, including FnBPA (*S. aureus*), FnZ (*S. equisimilis*), BBK032 (*B. burgdorferi*), SfbI (*S. pyogenes*) and FnBB (*S. dysgalactiae*)^{25,39,44-47}. The availability of some of these binding sites have been shown to be sensitive to FN's conformation (Figure 2.2)^{20,25,47}.

Fibronectin not only has capacity of forming fibrils while providing an anchor for cell-ECM interactions, which other proteins or peptides can provide, such as Arg-Gly-Asp (RGD) motif peptides, which are often used in biomaterials applications because they bind to multiple integrin species, are amenable to

sterilization processes and have a lower risk of inducing immune reactivity or pathogen transfer⁴⁸. While these provide an integrin-mediated anchor for cell adhesion, FN provides a fibrillar framework with added functionality thanks to the multiple binding sites for additional proteins, carbohydrates, cytokines and growth factors. FN is therefore essential for proper cell adhesion, migration, growth and differentiation^{32,49}, and for many important functions such as embryonic development^{50,51}, wound healing and tissue repair⁵² and thrombosis⁵³, among other functions, but also involved in pathological processes such as bacterial adhesion^{25,45,47}, tumorigenesis^{54,55}, and ECM remodeling due to tumorigenesis⁵⁶ or inflammation¹⁴.

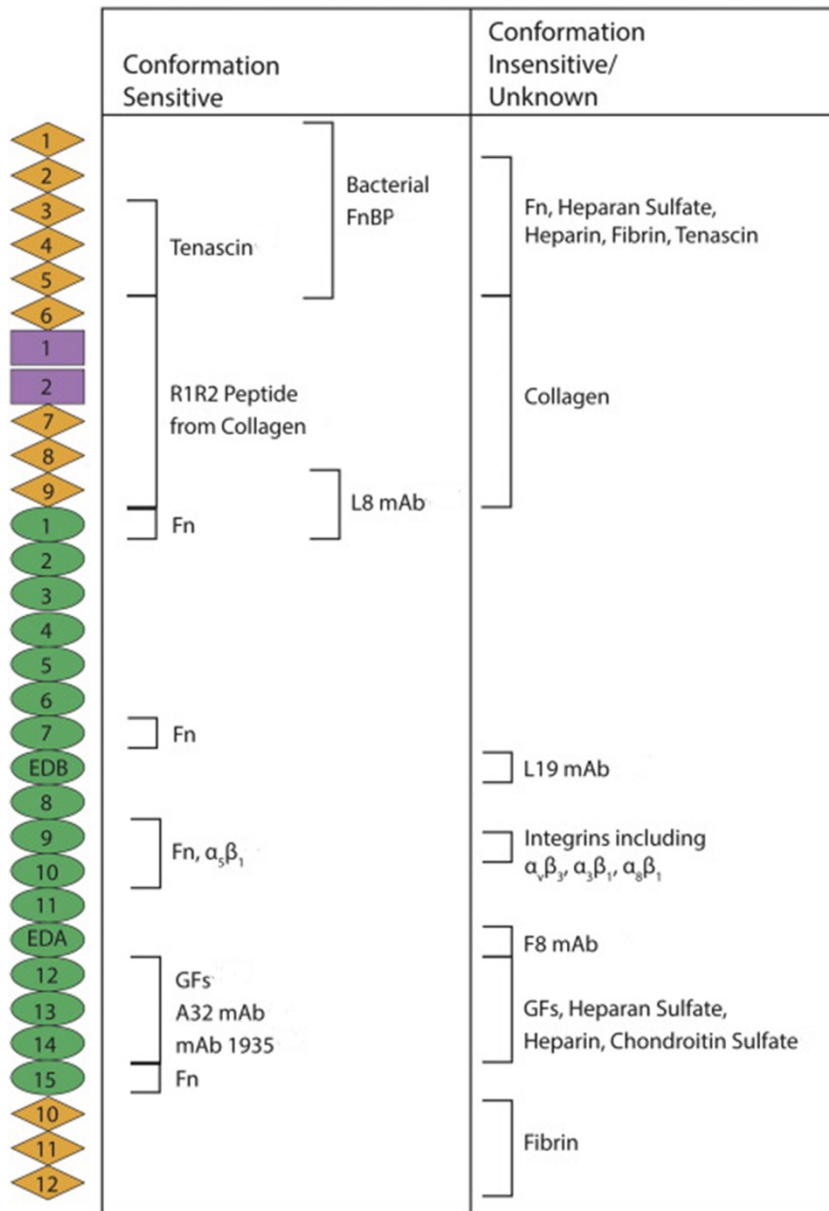


Figure 2.2. Structure of a FN monomer with constituent FN type I (diamonds), II (squares) and III (ovals) modules and conformation sensitive and insensitive (or unknown) binding sites. Reprinted from *Matrix Biology*, Vol. 60-61, Alicia J. Zollinger and Michael L. Smith, *Fibronectin, the extracellular glue*, Pages No. 27-37, Copyright (2016), with permission from Elsevier.²⁰

2.1.3. Functional consequences of ECM remodeling and fibronectin stretching

It has been shown that extensive ECM remodeling takes place during several processes such as organ development and morphogenesis, vasculogenesis and lymphogenesis¹³, but also in pathological processes such as inflammation, both in the local site of the lesion and in the associated lymph nodes where an immune response is mounted^{14,15}. ECM breakdown and remodeling needs to be finely tuned as imbalances can lead on the one hand to tissue destruction and conditions such as osteoarthritis, or on the other hand to fibrosis and tissue stiffening that can lead to organ failure or the development of cancer. This fine tuning is achieved by close feedback between the state of the ECM and the cells that modify it¹³⁻¹⁵.

ECM remodeling is mediated by the secretion of proteases^{13,57}, but also by the application of mechanical forces on the ECM,^{27,58,59} and is coupled with changes in ECM and tissue stiffness²⁶.

Reciprocal ECM-cell signaling

Cells are able to transmit the contractile forces that are produced intracellularly, to the underlying ECM via coupling of their actin-cytoskeleton to the ECM through transmembrane proteins (integrins) that bind FN^{26,61,62}. In a similar way, cells can sense the rigidity of the ECM through this same coupling and modify their function accordingly²⁶. Furthermore, mechanically-induced changes in FN conformation can regulate integrin attachment^{26,63}. This closes the feedback loop between cells and their surrounding ECM^{26,63}.

The cell-induced remodeling of the ECM seems to have further implications apart than those mediated by integrin signaling. It has been proposed that ECM remodeling might modulate cytokine and growth factor binding^{13,16,64} or can inhibit binding by modifying the spatial location of binding sites, such as is the case of several fibronectin-binding bacterial peptides^{17,25,47}.

FN fiber signaling as regulated by FN fiber strain

Cells are able to use FN in solution to form Fn fibrils. Binding of soluble FN dimers to integrin receptors is required to initiate fibrillogenesis, and FN-FN interactions are required to continue fibril formation. Clustering of integrins already bound to FN promotes an increase in local FN concentration and further fiber polymerization. As cells exert forces on fibers via linkage of their actin cytoskeleton to FN via integrin coupling, FN subunits change conformation from compact to an extended form.

Since cells can modify FN conformation through the application of mechanical forces^{27,58-60}, the opening or closing of cryptic binding sites during different stages of ECM remodeling might well be responsible for the regulation, activation, distribution and presentation of these cytokines and/or growth factors to cells, and various proteins could in this way be integrated into complex multivalent signals that are spatially and temporarily regulated by these processes¹⁶. In this sense, the ECM could be thought of as a reservoir of growth factors and other molecules that can be released by proteolysis of ECM constituents or, in the case of fibronectin, by mechanically-induced modifications that tune the binding or release of these molecules.

Indeed, it has been previously shown that mechanical forces can regulate the interactions between FN and other molecules. Stretching FN molecules that have been covalently bound to silicone substrates increases the binding of soluble FN^{65,66}, the N-terminus 70-kD fibronectin fragment and a FN-binding monoclonal antibody (L8)⁶⁶, as well as albumin⁶⁷. Increased binding of VEGF to increasingly unfolded states of adsorbed FN has also been observed⁶⁸, which can be associated with other previous observations that show that ECM stiffness controls VEGF signaling and processing as observed for endothelial cells⁶⁹.

Finally, binding of the previously mentioned bacterial peptides has been shown to be sensitive to disruption as a result of mechanical strains applied to FN^{25,47}: Binding of these bacterial peptides is mediated by the

formation of a multivalent binding via β -zippers with the β -strands of contiguous FNI modules located on the N-terminus of FN. Stretching FN fibers by the application of mechanical force on them, increases the distance between FNI modules, thereby introducing a structural mismatch that results in breakage of the hydrogen bonds that form the β -zipper bond, and effectively destroying the binding, as shown by steered molecular dynamic simulations. Stretching FN fibers in a manually pulled fibronectin assay confirmed the force-induced disruption of bacterial peptide binding. Bacterial peptide fragment B3 of FnBR-4 from *S. dysgalactiae*, peptide STAFF5 of the FN-binding protein A (FnBPA) of *S. aureus*, and peptide STATT1C of the FnBPA1 from *S. aureus* all showed decreased binding to FN upon FN fiber stretching^{25,47}.

These observations are of interest to this work, since we present evidence that IL-7 binding to FN is sensitive to changes in FN conformation due to the application of mechanical forces.

2.2. Interleukin-7

IL-7 is a 17.4kDa cytokine belonging to the γ -c interleukin family which plays a crucial role in the survival, proliferation and differentiation of naive and memory T-cells in lymphatic tissues, as well as the development of B and T-cells in the Thymus.⁸

2.2.1. Structure and signaling pathways

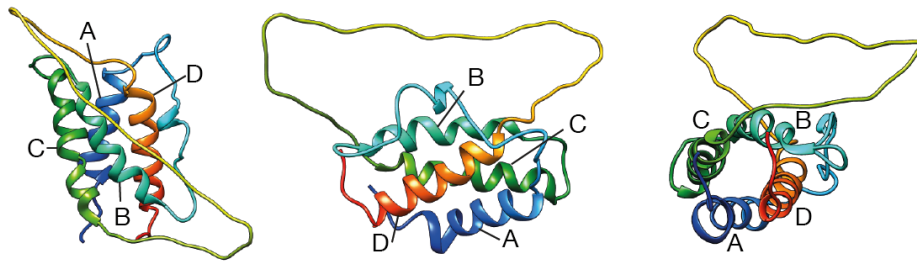
IL-7 consists of four α -helices (A to D) arranged in an Up-Up-Down-Down α -helix bundle with one short loop (BC) and two cross-over loops (AB and CD loop) (Fig. 2.3A) and it binds to a heterodimer of receptors IL-7 Receptor α (IL7R α) and the Common Gamma (IL2R γ) receptors (Fig.2.3B)⁸. These receptors form an inverted L-shaped structure with two fibronectin type III (FNIII) domains (D1 and D2) connected via a helical linker. IL-7 binds to the elbow region between these two domains through an interaction of residues on IL-7's α -helices A and C with the IL7R α receptor and residues on IL-7's α -helices A and D with the IL2R γ receptor.⁸

Structural studies of IL-7 have shown that the CD loop fails to crystalize (*residues 98 to 122 are not present in electron density maps used for the resolution of the molecule's structure*) and is therefore assumed to be highly flexible^{8,70}. Sequence alignment of human and murine IL-7 (presented in Chapter 4) show a high level of conservation among the residues in the α -helix bundle, as well as loops AB and BC, but showing some discrepancy in the CD loop, where human IL-7 has additional residues not present in murine IL7.

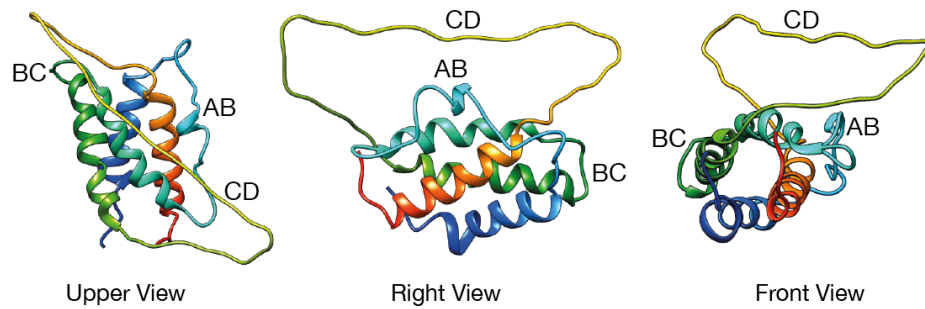
The function of the CD loop, as well as the implications of the differences in length and amino acid composition between human and murine IL-7 remain to be elucidated, though previous studies have suggested that the CD loop is not involved in binding of IL7 to its receptors^{8,70,71}. Current resolved structures of IL-7 binding to both glycosylated and non-glycosylated IL7R α do not include the CD-loop and show that is not needed for binding to this receptor⁷⁰, and while the full IL-7/IL7R α /IL2R γ complex has not yet been resolved, IL-7/models of IL-7 binding to both receptors, based on comparison to resolved structures of binding of other interleukins to the heterodimers formed by IL2R γ and their corresponding receptors, show that the CD loop is not needed for this interaction⁸. Furthermore, it has been shown that while recombinant human IL7 (rhIL7) was able to stimulate the proliferation of both human bone marrow cells and murine B-cells and recombinant murine IL-7 (rmIL-7) was only able to stimulate murine B-cells, deletion of the CD loop in rhIL-7 did not affect the proliferative response of either human or murine cell populations, thus suggesting that the failure of rmIL-7 to induce proliferation of human cells is not due to the discrepancies found in the CD loop, and that CD loop deletion does not affect the capability of IL-7 to stimulate immune cells, suggesting that is not involved in binding of IL7 to its receptors⁷¹.

A Interleukin-7 structure with inserted CD-loop

α -helices



Loops



B IL7Ra/IL2Ry/IL-7 model with inserted CD-loop

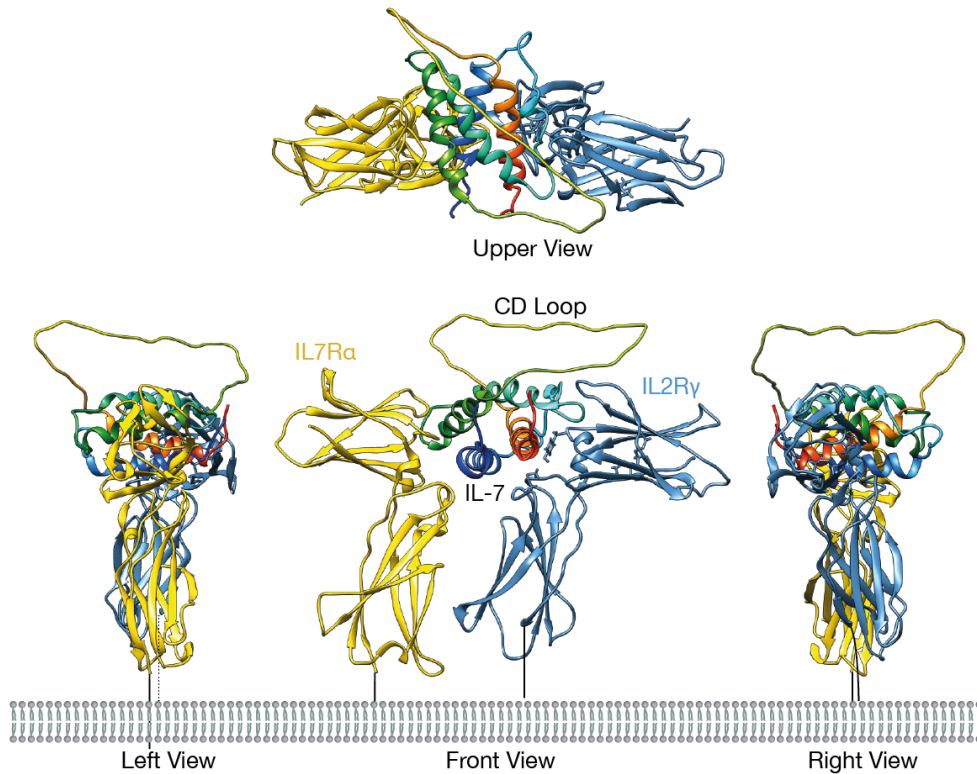


Figure 2.3. Interleukin-7, IL7RA and IL2RG receptors. A) IL-7 structure (from PDB: 3DI3⁷⁰) with inserted CD-loop using Modeler⁷² and Chimera⁴² software as described in Chapter 4, showing constituent α -helices and loops. B) Model of IL-7 binding to the IL7RA and IL2RG receptors (PDB: 3DI3 and 2B5I respectively) based on a published model^{8,70}, with the IL-7 CD loop modelled in the structure.

Binding of IL-7 to the transmembrane receptors IL7R α and the common receptor IL2R γ trigger various signaling cascades, the most thoroughly studied of them being the JAK-STAT pathway⁷³⁻⁷⁵. Structurally, it has been proposed that IL7R α and IL2R γ bind JAK1 and JAK3 respectively on their intracellular domain, but the JAK molecules remain separated in the resting state. The unbound receptors form homodimers or hetero-dimer that first need to dissociate to be able to bind IL-7, move away from the cell surface and form the IL7R α / IL2R γ /IL-7 complex⁷⁶. This interaction brings together the intracellular domains of the receptors and induces the formation of cholesterol-rich membrane micro domains that compartmentalize the activated receptors and allow the JAK-1/JAK3 cross-phosphorylation^{8,73,76,77}. Consequently, this results in phosphorylation of the IL7R α and IL2R γ receptors, which in turn bind and phosphorylate monomeric STAT5 to form homodimers. This initial IL-7 stimulation induces a transient cytoskeleton structuring which is essential for STAT phosphorylation and subsequent translocation into the nucleus about 2 min after IL-7 stimulation⁷³, where they initiate the transcription of several genes such as pro-survival genes Bcl2 and Bcl2l1 and Mcl1, but also other genes that control the expression of IL7RA and other molecules such as CD8, members of the suppressor of cytokine signalling (SOCS) family, and Growth Factor Independent 1 Transcriptional Repressor (Gfi1), among others^{8,73,77-79}.

IL-7 - JAK3 signals are also capable of activating the transcription factor NFATc1 in double negative (DN) thymocytes, which is critical for their survival and development, as NFATc1 deficiency results in blockage of thymocyte development at the DN1 stage and leads to T cell lymphopenia⁸⁰. Other pathways that have been shown to be activated by IL-7 stimulation in a dose and time dependent manner are STAT1 and p24 of MAPK⁷⁵, and Phosphatidylinositol 3 kinase, since the IL7R α cytoplasmic chain has a phosphotyrosine dependent recognition site for this pathway⁸¹. These signaling pathways are involved in the many downstream effects of IL-7 on both lymphocyte⁴⁻⁸ and stromal cell function^{10,11,15}.

2.2.2. IL-7 role in lymphocyte development

IL-7 has been implicated in numerous functions in T- and B-lymphocyte development and function. Lymphocyte development depends on various phases of T-cell receptor (TCR) or B-cell receptor (BCR) gene recombination and expression, with associated cellular selection that ensures variability of the cell-pool while selecting for proper rearrangement and function of the receptors in cells that proceed and successfully develop into mature T- or B-cells, respectively^{82,83}. IL-7 plays an essential role in the maintenance and selection of such cells. For example, during lymphocyte development in the thymus, IL-7 promotes the survival of TCR β (-) double negative (DN) thymocytes (precursors of T-lymphocytes) by inducing expression of the pro-survival molecule Bcl-2, and acts in cooperation with pre-T cell antigen receptor (pre-TCR) and the receptor Notch1 to coordinate cell proliferation, differentiation and Tcr α recombination during selection of cells that proceed to differentiate into CD4(+)CD8(+) double-positive (DP) thymocytes⁸⁴. IL-7 has also been shown to be involved in proliferation, differentiation and gene recombination during thymocyte B-selection. The expression of a functionally rearranged pre-B-cell receptor (pre-BCR) on the cell surface during development, allows these cells to proliferate in low concentrations of IL-7, giving them a survival advantage in a niche with limited IL-7 availability, thereby providing a mechanism to positively select for functionally rearranged cells⁸⁴⁻⁸⁶. Additionally, IL-7 has also been implicated in the development of dendritic cells, natural killer cells and lymphoid tissue inducer cells

1

After thymic development, mature Naïve T-cells have been shown to depend on IL-7 and TCR stimulation for their survival and maintenance of adequate cell numbers^{7,87}. Weak TCR signals from contact with antigen-free major histocompatibility complexes (MHCs) act in synergy with anti-apoptotic signals induced by IL-7 to promote the survival of naive T cells at rest⁸⁸.

Interestingly, the IL-7 signals required for the homeostatic maintenance of naïve CD8+ cells need to be intermittent, since prolonged, continuous stimulation induces cell proliferation together with interferon- γ (IFN- γ) production, which induces IFN- γ -triggered cell death⁸⁹. IL-7 stimulation can be interrupted by engagement of the TCR, and thus make IL-7 stimulation more intermittent⁸⁹, but failure to stimulate TCR abrogates proliferation induced by IL-7⁹⁰.

2.2.3. IL-7 has a role in T-cell activation and memory development.

T-cell activation (both of CD4+ and CD8+ cells) is mediated by the interaction between their T-cell receptor (TCR) and antigen bound to the Major Histocompatibility Complex (MHC) of Antigen Presenting Cells (APCs), as well as the interaction between several co-stimulatory and adhesive molecules between them, in what has been referred to as the immune synapse⁹¹.

These interactions take place in a complex three-dimensional environment in the para-cortex of the lymph node, where T-cells and APCs crawl along a complex three-dimensional reticular network which is built and maintained by Fibroblastic Reticular Cells (FRC) (Fig.2.4)⁹²⁻⁹⁵. FRCs produce ECM with a specific structure, forming a pipe-like network within which lymph and antigens flow through. These conduits hollow structures contain longitudinally arranged Collagen I fibers and the surrounding pipe-like ECM structure consists of a micro-fibrillar zone with components such as ERTR-7 and Fibrillin-1 and -2 covered by a basement membrane-like structure containing ECM components such as Fibronectin, Collagen IV, Perlecan, Nidogen I, and Laminins 8 and 10, and finally the FRCs themselves, which produce and surround the structure, as shown in Fig.2.4⁹²⁻⁹⁵. APCs are thought to be able to extend protrusions into these pipe-like structures, pick up and process antigens, and present them to the T-cells they interact with⁹⁵.

Lymph Node Conduit System Structure and components

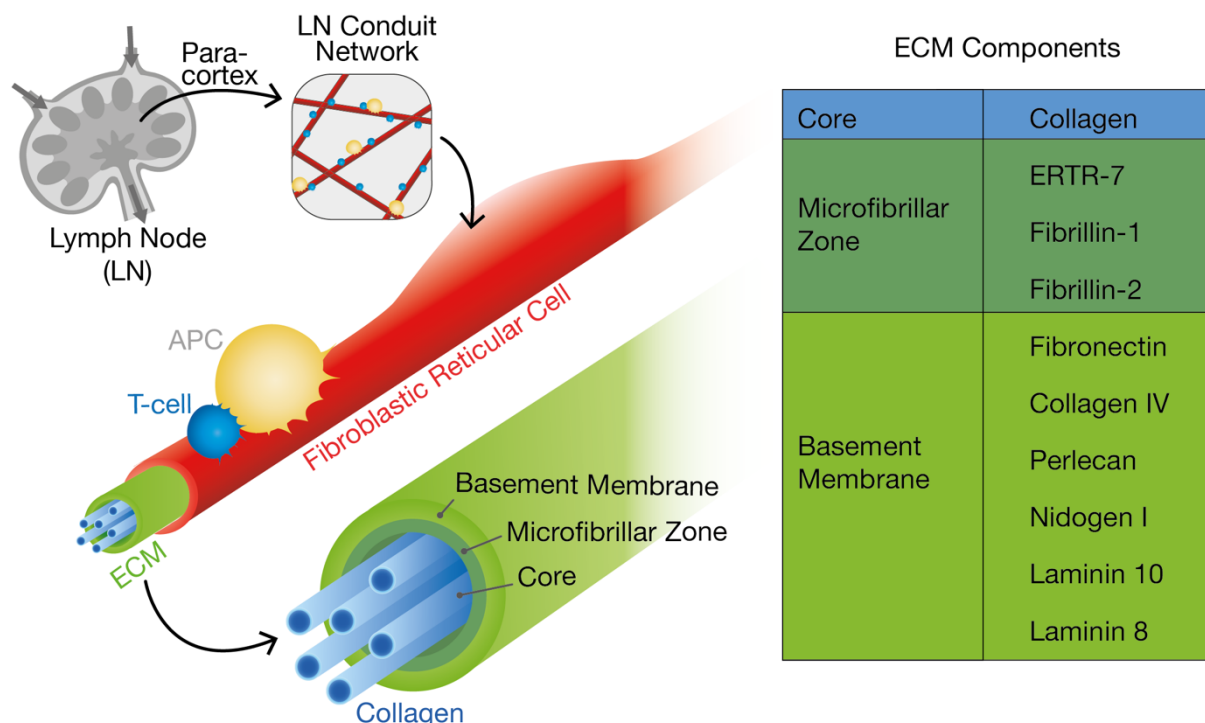


Figure 2.4. Structure of ECM/FRC conduits in the reticular network of the lymph nodes. FRCs produce a concentric ECM structure composed of a basement membrane, a microfibrillar zone, and a hollow core

containing collagen fibers. Each one of these concentric regions is composed of various specific ECM components as shown in the adjacent table. APCs and T-cells crawl and interact with one another as they migrate along the FRCs that form the network⁹²⁻⁹⁵.

Upon activation, T-cells increase IL-2 production and go through a process of expansion, where they downregulate the expression of the IL7R α receptor through a mechanism involving the PI-3K pathway. After the immune response subsides, a number of cells undergo a process to become either central (CD62L+,CCR7+) or effector (CD62L-,CCR7-) memory cells, and these cells upregulate once more the expression of IL7R α ^{7,96,97}.

These changes in IL7R α expression reflect the need of naïve and memory cells of IL-7 stimulation for their development and survival^{4,88,98}. Indeed, in the absence of IL-7, neither CD4 nor CD8 effectors generate persisting memory cell populations, and it has been shown, both in in vitro and in vivo studies of CD4 and CD8 cells, that IL-7-dependent differentiation of effector cells to memory cells can even occur in the absence of antigen, as reviewed by Bradley et al.⁴.

Just as with naïve cells, IL-7 is required to maintain T-cell memory cells. Indeed, TCR signals can only support homeostatic division when it is also present^{4,7}. Furthermore, it has been shown that IL-7 mediates the survival of resting memory CD4 cells by upregulating the expression of anti-apoptotic protein Bcl-2⁹⁹, and to be involved in the generation and persistence of CD8 memory T-cells, which is correlated with the level of IL7R α expression⁹⁸. These cells also showed an increased expression of anti-apoptotic molecules^{88,98}. Interestingly, the increased expression of IL7RA identifies the effector CD8 T cells that will differentiate into memory cells that could persist and confer protective immunity⁹⁸.

In addition to the survival-enhancing effects of TRC-IL7 stimulation, it has also been shown that IL-7 has the capacity of amplifying TCR-induced ERK phosphorylation by 2 to 3 fold, with increased proliferation and preferential differentiation of T-cells into T-helper Type I cells (Th1)¹⁰⁰.

There are some interesting implications regarding the use of IL-7 for therapeutic purposes, not only as an adjuvant for T-cell maintenance, but also as an aid for the development of T-cells for cancer immunotherapies. For example, it has been shown that activation of T-cells with bryostatin and ionomycin for 18 hours, followed by cell expansion in the presence of IL-7/IL-15 resulted in much faster and more prolonged proliferation (5-10 fold) than that observed when cell expansion was performed in the presence of IL-2 instead, and yielded higher proportions of CD8+ T-cells, a higher proportion of central memory phenotype, and lower secretion of IFN- γ . Furthermore, adoptive transfer of these cells resulted in more efficient targeting of 4T1 tumors in vivo¹⁰¹. Also, adoptive transfer of TCR transgenic OT-II CD4(+) T cells primed in vitro with OVA(323-339) peptide presented by syngeneic antigen-presenting cells (APCs), showed an elevated number of transferred CD4+ cells, both in the spleen and the lymph nodes, and an increased effector and central memory phenotypes when the cells were primed in the presence of IL-7 compared to controls in the absence of it¹⁰². These observations make it interesting to further investigate how IL-7 can be used for similar purposes, and what are additional interactions of IL-7 that could be exploited in the development of such therapies.

2.2.4. Stromal cells, IL-7 production and consumption.

One of the hallmarks of IL-7 stimulation, is that circulating soluble IL-7 is found in rather low concentrations (10 to 40 pg/ml in plasma, 15 to 35pg/ml in lymph)^{10,11}, and the production and consumption of IL-7 is tightly regulated, with cells competing for such small amounts of IL-7¹². Both, in the lymph nodes, as well as the thymus, and other lymphocyte niches, stromal cells have been shown to produce IL-7^{10,11,103,104}. While stromal production of IL-7 remains constant, it seems that competition for IL-7 availability is defined

by the number of IL7R α receptors a cell presents on their surface and the number of cells expressing these receptors^{12, 85}. Stimulation with IL-7 promotes T-cell survival and proliferation, and the presence of increasing numbers of daughter cells would consume the low concentrations of IL-7 and deplete the available IL-7 pool, but as previously mentioned, activated cells reduce IL7RA expression, and it is thought that by doing so, the small amount of IL-7 present is optimally used, allowing non-activated T-cells (with high IL7RA expression) to access the small amount of IL-7 present, and cells that have been activated (reduced IL7RA expression) reduce their IL-7 consumption, thereby maximizing the number of stimulated T-cells, and preventing depletion of the IL-7 pool^{12,85}.

Select populations of Lymph Node Stromal Cells (LNSCs) have been identified in lymph nodes, each of them with specific functions, and identified by their varied expression of podoplanin (also called glycoprotein gp38), and PECAM-1 (also called CD31)^{94,105-107}: FRCs, which express higher levels of podoplanin (+) and lower levels of PECAM-1 (-) form the lymph node conduits, and are also involved in the development of tolerance; Lymphatic Endothelial Cells (LECs) expressing higher levels of both podoplanin (+) and PECAM-1 (+), facilitate the entry of antigen-bearing dendritic cells (DCs) and soluble antigens into lymph nodes and control lymphocyte egress, and are also involved in the development of tolerance; Blood Endothelial Cells (BECs), which express low levels of podoplanin (-) and high levels of PECAM-1 (+), form vessels that allow naive lymphocytes to enter lymph nodes through high endothelial venules; Finally, a double negative subset (DN) expressing low levels of both podoplanin (-) and PECAM-1 (-) expression has been identified but has not yet been characterized.^{94,105-107}. From these four subsets, FRCs and LECs have been shown to be a source of IL-7^{11,103,104}, with LECs shown to produce IL-7 at concentrations similar to those found in blood and plasma (20pg/ml)¹⁰.

While production and consumption seem to be obvious mediators of levels of IL-7 stimulation, other mechanisms of modulation may also play a role, such as cell migration away from the IL-7 source, stromal cell autocrine consumption of IL-7, and importantly to this work and often overlooked, the role of the ECM in the storage and release of this and other cytokines that regulate cell function.

2.3. IL-7/ FN interactions, ECM remodeling, and their reciprocal role in stromal and lymphocyte function.

IL-7 has been previously shown to bind to ECM molecules such as fibronectin, collagen IV, Laminin, and to a lesser extent, to heparan sulphate^{18,19} and heparin¹⁰⁸. In this work, we are interested in the interactions between IL-7 and FN. Since IL-7 has been shown to bind to fibronectin's N-terminus fragment¹⁸, and bacterial adhesins binding to the N-terminus have been shown to be susceptible to disruption by the application of mechanical forces^{25,47}, and because FN has cryptic sites that open upon mechanical stretching of the molecule, as described in Section 2.1.3, we are interested in elucidating whether changes IL-7 binding to FN is affected by mechanically-induced changes in FN conformation, and the physiological role that these may have on lymphocyte, as well as stromal function.

The most comprehensive study of IL-7 binding to FN to date was performed by¹⁸. They showed, ¹²⁵I labelled IL-7 binding to immobilized FN, Laminin (LN) and collagen IV after various incubation times (binding at 4°C, up to 18 hrs) by removing unbound ¹²⁵I-IL-7, and eluting bound one with Tween-20 and counted in a gamma-counter. They also estimated binding affinities by incubating ¹²⁵I-IL-7 in the presence of increasing amounts of unlabelled IL-7 and found that the amount of unlabelled IL-7 required to effectively inhibit ¹²⁵I-IL-7 binding to was in the range of 1000-fold, with estimated IC₅₀ values for binding to LN, and FN in the range of 10-100 nM, but they found no reduction in binding of ¹²⁵I-IL-7 to ECM, even in the presence of higher amounts of unlabelled IL-7, and concluded that the residual binding of IL-7 to ECM is not specific,

indicating a relatively low binding affinity that required a longer association time. They also showed that maximal binding of ^{125}I -IL-7 to FN or LN appeared to take from 2 to 4 h. Furthermore, they showed that cell pre-treatment with both soluble and FN-bound IL-7 induced T cell adhesion, but FN-bound IL-7 required lower cytokine concentrations to achieve the same effect as in soluble form. Also, they pointed out that low concentrations (5 or 50 ng/well) of IL-7 were sufficient to induce both CD4+ and CD8+ T-cell adhesion. Finally, they showed that adhesion is mediated by $\alpha 4\beta 1$ and $\alpha 5\beta 1$ integrins, since a monoclonal antibody against $\beta 1$ integrins, as well as one against the Arg-Gly-Asp (RGD) motif, inhibited IL-7 induced T cell adhesion (soluble or matrix-bound). The relevance of these findings will become evident when we discuss the results of our study of IL-7 binding to stretched manually pulled FN-fibers in Chapter 4.

Since there is growing evidence that the ECM can act as a deposit for cytokines and other signaling molecules that influence cell behavior ^{17,20-24,30}, and it has been previously shown that mechanical forces can regulate the interactions between FN and other molecules^{65-67,109}, the fact that IL-7 binds to FN, is particularly interesting in the context of inflammation.

During an inflammatory process, a rapid expansion of the lymphatic network of the inflamed area occurs, and associated lymph nodes undergo a significant change in size and tension, and extensive ECM remodeling and alterations in the ECM's mechanical properties take place to accommodate for these changes ¹⁵. These reactions are coordinated by the upregulation of chemokines, cytokines and adhesion molecules that result in functional changes in LNSCs, such as LECs and FRCs ¹¹⁰. Indeed, LECs undergo a process of proliferation, migration and tube formation that promotes lymphangiogenesis during an inflammatory response ¹¹⁰, and FRCs maintain lymph node size and tension with the onset of inflammation ¹⁵. The process is partly mediated by resident and infiltrating dendritic cells that upregulate the expression of C-type lectin domain family 1 member B (CLEC2), which inhibits podoplanin-driven actomyosin contractility of the FRCs. The resulting in FRC elongation and reduced lymph node tension enables the rapid organ expansion observed in inflamed lymph nodes ^{15 111}. The changes in ECM architecture and tensional state are important to note in the context of this work, where we explore the influence of mechanically-induced changes in FN conformation, on IL-7 binding.

Interestingly, IL-7 seems to be actively involved in the process of ECM remodeling. It has been shown that upon damage to the FRC network, FRCs upregulate IL-7 production to activate innate lymphoid cells (ILCs) that help to regenerate and rebuild the lymph node ¹⁵, and FRCs, as well as LECs have been shown to increase the production of IL-7 after LCMV infection, with consequent extensive remodeling of the lymph nodes' ECM ¹¹. It seems then, that mutual interactions between lymphatic and stromal cells, the ECM and IL-7 take place during inflammation, and the integration of multiple cues are responsible for their coordinated response.

T-cells can also alter stromal cell function, for example, by mediating fibroblast driven ECM formation through stimulation via the production of TNF- α , or Lymphotoxin- α ¹¹², as well as promoting ECM degradation ¹¹³, and IL-7 has also been shown to be involved in the regulation of stromal cell function. LECs express both IL7RA and IL2RG receptors, and it has been shown that IL-7 stimulation can increase their adhesion to FN coated plates and their migration on them ¹⁰. Also, siRNA-mediated knockdown of IL-7 in LECs resulted in reduced cell migration and lymphatic tube formation, and IL-7 stimulation induced lymphangiogenesis in an in vivo cornea micropocket assay, as well as enhanced lymphatic drainage of the skin ¹⁰. It has also been shown, in lung cancer cells, that IL-7 stimulation increase the expression of VEGF-D and lymphangiogenesis¹¹⁴.

Furthermore, IL-7's pro-adhesive effects are not restricted to stromal cells. It has also been shown that IL-7 can induce adhesion and spreading of thymocytes to immobilised fibronectin, with thymocytes at different

stages of development showing different response levels, with double negative (DN) thymocytes showing the highest response, followed by CD8+, CD4+ and double positive (DP) thymocytes¹⁹.

Given that integrins mediate the binding of cells to the ECM, and play an important role in cell adhesion, and spreading, and some are involved in mechano-sensing of the ECM mechanical properties, but also on the exertion of mechanical forces on the ECM and its remodeling, it is of interest to notice that there exists evidence of IL-7 specifically affecting integrin function of both stromal and lymphoid cells. Indeed, IL-7 stimulation results in the upregulation of fibronectin-binding integrin $\alpha 5\beta 1$ in lymphatic endothelial cells (LECs)¹⁰, the activation of $\alpha 4\beta 1$ integrins in murine thymocytes through phosphorylation of tyrosines on the β subunit¹⁹, and the IL-7 induced expression and activation of $\alpha 4\beta 7$ integrins in naive T-cells which promoted naive T-cell homing to the intestinal mucosa¹¹⁵.

To complicate matters further, IL-7 interaction with the ECM also seem to regulate the magnitude of the effects of IL-7 stimulation, since it was shown that while soluble IL-7 increased T-cell adhesion to immobilised FN, the effect was significantly increased when IL-7 was bound to surface immobilized FN, and lower doses of FN-bound IL-7 were required to induce the same effect as with soluble IL-7¹⁸. Furthermore, the effects of IL-7 stimulation on lymphocytes and stromal cells, as previously described can be potentiated by synergistic signaling through integrins. For example, CD3-dependent proliferation of fetal thymocytes was enhanced by engagement of integrins $\alpha 4$ and $\alpha 5$ with immobilized fibronectin¹¹⁶. The simultaneous activation of $\alpha 1\beta 1$ integrin and IL7R α increased the production of RANKL in effector CD4+ T cells, which increased their osteoclastogenic function and the pro-survival effect of IL-7¹¹⁷. Simultaneous integrin $\alpha 2\beta 1$ and IL7RA engagement in Th17 cells increased their IL-17 production, proliferation and cell adhesion to collagen, and was shown to drive Th17-Mediated Bone Loss¹¹⁸.

These synergistic effects might work in collaboration with additional signal potentiating mechanisms that involve ECM-cell interactions, for example, co-ligation of the TCR with ECM receptors such as $\beta 1$ integrins, which have been shown to enhance T cell proliferation¹¹⁹.

Finally, it is important to point out that IL-7 stimulation can affect the structural composition of the ECM and its mechanical properties by inducing the production of matrix metalloproteinases (MMPs) that cleave and digest the ECM, and by altering the production of ECM components. Indeed, human articular chondrocytes stimulated with IL-7 increase have been shown to increase their the production of MMP-13¹²⁰, and human subconjunctival fibroblasts reduce the production of collagen I and fibronectin, and downregulate α -smooth muscle actin (α -SMA) upon IL-7 stimulation¹²¹. Human pulmonary fibroblasts have been also shown to reduce their collagen synthesis in response to IL-7 stimulation¹²².

These observations suggest that ECM-IL-7 interactions with stromal and lymphoid cells might be tightly regulated by feedback loops between them, and the implications of these interconnected effects remain to be elucidated and integrated to better understand the physiological processes that they mediate.

2.4. IL-7 binding correlated to Fibronectin-FRET

In this chapter I will aim to provide a comprehensive guide to FRET, as well the preparation and use of FRET labelled Fibronectin, and a method to derive FRET ratios and correlate them with a third signal (in this case a ligand such as IL-7 or CD-loop peptide, but can be applied to any other signal that co-localizes with fibronectin). First, I will introduce the theoretical principle of FRET and FRET induced sensitized emission. Then I will summarize the procedures to isolate and label fibronectin with an intramolecular FRET probe that is sensitive to changes in fibronectin conformation, and I will outline the procedures to control the quality of the labelling, to validate that the changes in FRET in turn correspond to changes in fibronectin's conformation, and the mechano-sensitivity of the probe. While these are methods that have been previously developed in our lab, the objective of this section is to gather the different methods and present the procedures in detail, as a comprehensive review and guide for future work. Furthermore, detailed protocols have been produced to be used in the future in the laboratory setting. From this foundation, I will move on to describe the method used to acquire ligand correlated FRET measurements and how to correct them from unwanted bleed-through contributions, and address issues of image quality, registration and other post acquisition corrections. This method can be used both as a stand-alone FRET measurement method, with increased data accuracy, or as a ligand-correlated method, in which a third channel for a binding molecule is used.

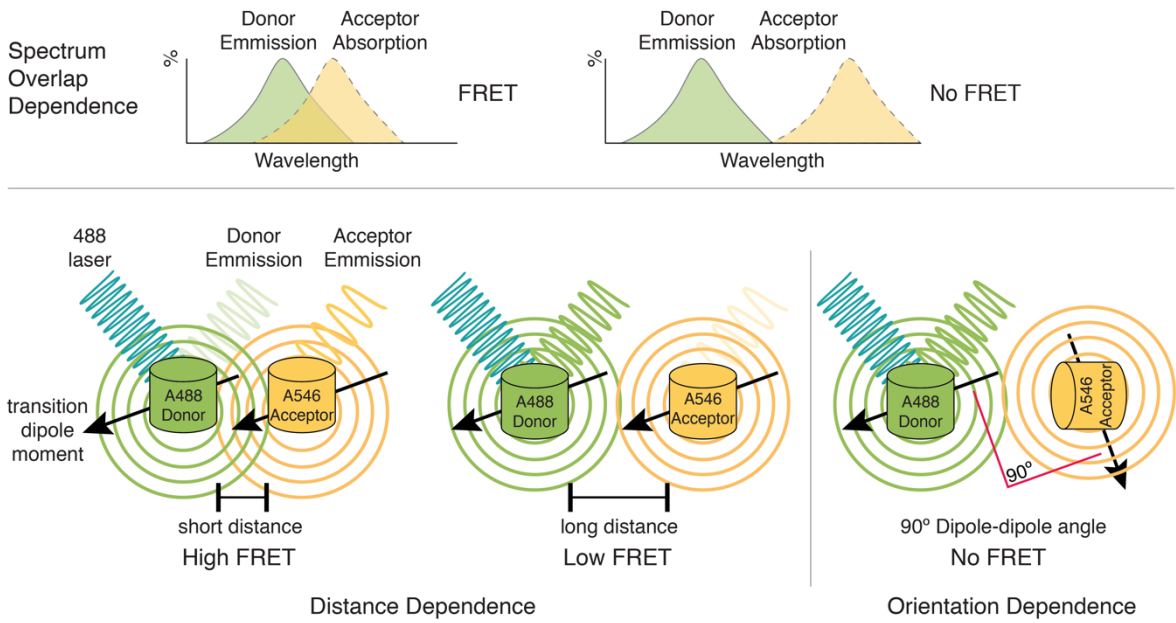
2.5. Förster Resonance Energy Transfer (FRET)

Förster Resonance Energy Transfer (FRET), sometimes referred to as Fluorescence Resonance Energy Transfer is the non-radiative energy transfer from an excited donor fluorophore to an adjacent acceptor one due to dipole interactions. It was first observed in polarization studies in the 1920s, but it was not until the 1940s that Theodor Förster developed the correct theoretical explanation for non-radiative energy transfer and published his paper "Energy migration and fluorescence" in 1946^{123,124}. In the 1950s the technique began to be applied more widely, and has found its way into the study of biological processes.
¹²⁴

Because of its unique feature of being able to detect whether the donor and acceptor fluorophores are in close proximity at a molecular scale, FRET is nowadays routinely used to study inter and intra-molecular interactions^{125,126}. FRET has been used to determine the distance between two specific locations on macromolecules and molecular complexes, to follow conformational changes of macromolecules both in static and real time conditions and to monitor the formation of multi molecular complexes, among many other applications^{126,127}. Of interest to this work, is the use of FRET as an intramolecular detector of changes in protein conformation due to protein unfolding^{128,129} specifically due to ECM remodeling and the application of mechanical force^{27,65}.

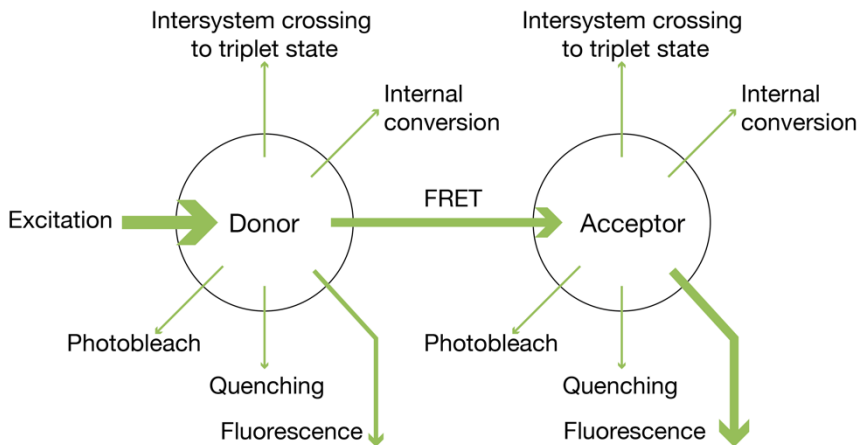
In principle, FRET is the non-radiative transfer of energy from an excited donor fluorophore, and an acceptor via long-range dipole-dipole coupling^{126,130}. This can be approximated as an electric dipole-dipole interaction and energy transfer will occur if the overlap between the emission and absorption spectra of the donor and acceptor is sufficient, if the fluorescence quantum yield of the donor, and the absorption coefficient of the acceptor are large enough, the relative-orientation of the donor and acceptor transition dipole moments, and very importantly, if the two dipoles are close enough (between 0.5 to 10 nm). Only then, a fraction of the excitation energy of the donor will be transferred non-radiatively to the acceptor (Fig. 3.1A)^{126,130}.

A Förster Resonance Energy Transmission



B Energy dissipation mechanisms that coexist with FRET

High FRET due to close interaction between donor and acceptor



Low FRET due to close interaction between donor and acceptor

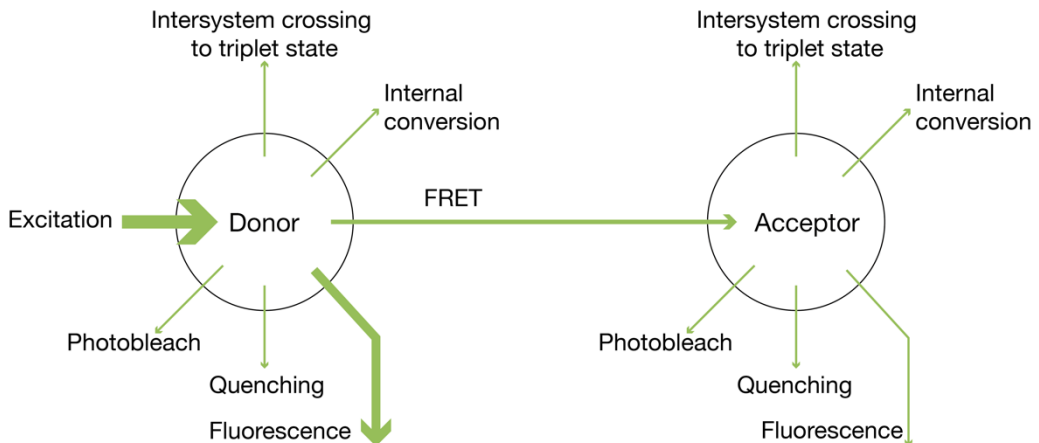


Figure 3.1. Requirements for FRET energy transfer and alternative energy dissipation mechanisms. A) FRET dependence on spectrum overlap between donor emission and acceptor absorption, distance, and orientation between donor and acceptor fluorophores. B) Energy dissipation mechanisms that coexist with FRET.

Because the efficiency of the energy transfer is a function of the distance between the donor and the acceptor, it is possible to use FRET as an indirect measure of the distance between the fluorescent pairs¹³⁰. This can be shown by Equation 3.1¹²³, where k_t is the rate constant for the transferring energy from an excited donor molecule to an acceptor molecule which are a distance r_{DA} apart, with τ_D being the fluorescence lifetime of the donor in the absence of the acceptor, and R_0 being a characteristic distance between a specific donor-acceptor pair for which the rate of energy transfer would equal the rate of decay of the excited donor from the excited state, were the acceptor not present^{123,130}.

$$k_t = \left(\frac{1}{\tau_D} \right) \left(\frac{R_0}{r_{DA}} \right)^6 \quad [3.1]$$

FRET also depends on the optical absorption coefficient of the acceptor and the quantum yield of the donor. This is because R_0 depends on the quantum yield of the donor (Q_D), the molar absorption coefficient of the acceptor $\varepsilon_A(\bar{\nu})$ and the fluorescence intensity of the measured fluorescence spectrum of the donor $F_D(\bar{\nu})$, as can be seen from Equation 3.2, with $\bar{\nu}$ being the wave number, N_A Avogadro's number and n the index of refraction pertaining the transfer¹³⁰. Finally, FRET energy transfer is also dependent on the relative orientation between the donor and acceptor, this is because κ (in Equation 3.2) is the angular function resulting from the inner product between the near unit vector of the electric field of the donor and the unit vector of the absorption dipole, and this depends on the relative position of the acceptor with respect to the donor, κ^2 is in fact known as the orientation factor of FRET¹³⁰⁻¹³³.

$$R_0^6 = \frac{9000(\ln 10)\kappa^2 Q_D}{N_A 128\pi^5 n^4} \left[\int_0^\infty \varepsilon_A(\bar{\nu}) F_D(\bar{\nu}) \bar{\nu}^{-4} d\bar{\nu} \ / \int_0^\infty F_D(\bar{\nu}) d\bar{\nu} \right] \quad [3.2]$$

For our FRET-FN labelled studies, we use Alexa 488 fluorophore (A488) as a donor, and Alexa 546 fluorophore (A546) as the acceptor. The A488 donor emission spectrum (excited by a 488nm laser) overlaps well with the absorption spectrum of the acceptor A546, and both fluorophores have a high quantum yield and photo-stability, making them an optimal FRET pair to use for this purpose.¹²⁹ Also, it is highly unlikely that the donor and acceptor fluorophores are oriented in such a way that no FRET occurs. This is a particularly sensitive issue for FRET experiments in which the fluorophores are bound to rigid proteins, with well characterised binding locations. In our case, we make the common assumption that the fluorophores are free to rotate, and that every donor and every acceptor can take up a diverse range of orientations during FRET. The orientation factor can then be replaced by an average value^{132,134}.

In terms of energy transmission, FRET competes with other possible ways in which the donor can go back from an excited state to a ground state as shown in Fig. 3.1B. When FRET takes place, it has the effect of lowering the probability of photon emission by the donor thereby lowering its intensity, and of shortening the lifetime of the donor in its excited state. In addition, an acceptor that absorbs energy due to FRET and has the capacity to fluoresce, will do with an intensity that is proportional to the amount of energy

transferred. This is called sensitized emission, and can be detected using the photomultiplier of a confocal microscope. It is also the FRET detection used in our assays ¹³⁰.

Because the signal detected from the sensitized emission of the acceptor as a direct measurement of FRET is mixed with fluorescent signals derived from the direct excitation of the donor and acceptor, and because the detected FRET signal depends on FRET efficiency but also on fluorophore concentration, level of excitation of the donor, and detector sensitivity ^{130,135}. We utilized here a method to correct signal overlap, and the issues of fluorophore concentration, level of donor excitation and detector sensitivities are overcome by normalization of the signal. These procedures will be described in detail in Section 3.3.

2.6. Intramolecular FRET probe to assess fibronectin strain

This section describes the methods used to obtain and test the FRET-labelled fibronectin used in the experiment presented in this work. Fibronectin was purified from plasma, labelled with a FRET couple (Alexa 488-Alexa 546) and the intramolecular FRET probe was tested for fibronectin conformation sensitivity by denaturing FRET-fibronectin with Guanidinium Hydrochloride (Gdn HCl), and for responsiveness to strain induced changes in FRET ratios.

2.6.1. Fibronectin purification

Fibronectin was purified from human plasma via gelatin affinity chromatography with an expected yield of 10 mg fibronectin per 100 ml. A full protocol for fibronectin purification is included in the Appendix, which is based on previous work ^{136,137}. As a summary, two columns were need to be prepared per purification: a Sepharose 4B for the first step (5ml per 100 ml of plasma) and a Gelatin-Sepharose 4B for the second step (5 ml per 100 ml of plasma). First, the Sepharose 4B and Gelatin-Sepharose 4B were re-suspended in PBS and the columns (Amersham 19-5101-01 C 16/20) packed while minimizing the introduction of air bubbles and allowed to gravity-pack overnight. The columns were then equilibrated with 5x the volume of the column with PBS/ 10 mM EDTA/ 2mM PMSF (column buffer).

The plasma was thawed in a 37 °C water bath with agitation, aliquoted in 50 ml Falcon tubes and centrifuged at 10,000x for 15 min, then 2 mM PMSF and 10 mM EDTA were added to the supernatant. The plasma supernatant was then passed through the Sepharose 4B column and the flow-through over the Gelatin-Sepharose 4B column. The Gelatin-Sepharose 4B column was washed with column buffer and the outflow checked by regularly measuring the A_{280} absorbance of the outflow until it reached background levels. The Gelatin-Sepharose 4B column was then washed with 1M NaCl in column buffer, then 0.5M urea in column buffer and subsequently 0.2M arginine in column buffer. Finally, fibronectin was eluted with 1M arginine in column buffer and 2 mL fractions collected. The fractions that contained the peak of protein concentration were identified by measuring the A_{280} absorbance. These fractions were then aliquoted and stored at -80 °C for long-term storage.

The purified fibronectin was confirmed to be dimeric and free of FN fragments by Coomassie blue staining of samples run via electrophoresis in a 4-20% Tri/glycine gels from Biorad, under reducing or non-reducing conditions as shown in Fig.3.2. Finally, FN was dialyzed for final use in PBS with pH 7.4 using a 10 kDa molecular weight cut off dialysis cassette (Thermo Scientific, Cat.No. 66380).

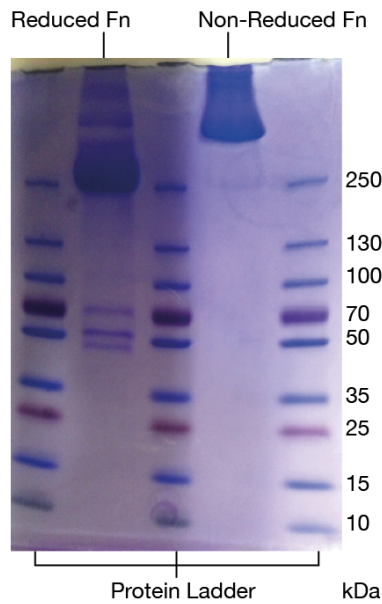


Figure 3.2. Coomassie stain gel with purified fibronectin under reducing and non-reducing conditions. The sample showing fibronectin fragments under reducing conditions that are not present in the actual non-reduced sample.

2.6.2. FRET Fibronectin labelling

In this work, we labelled fibronectin with Alexa 488 donor dyes conjugated randomly on the amines of the protein via a succinimidyl ester conjugation, and Alexa 546 acceptor dyes on the cysteines located in fibronectin type III modules FNIII₇ and FNIII₁₅ via maleimide conjugation following previously published protocols^{58,65,138} (Fig.3.3).

FRET labeled Fn (FN Monomer depicted)

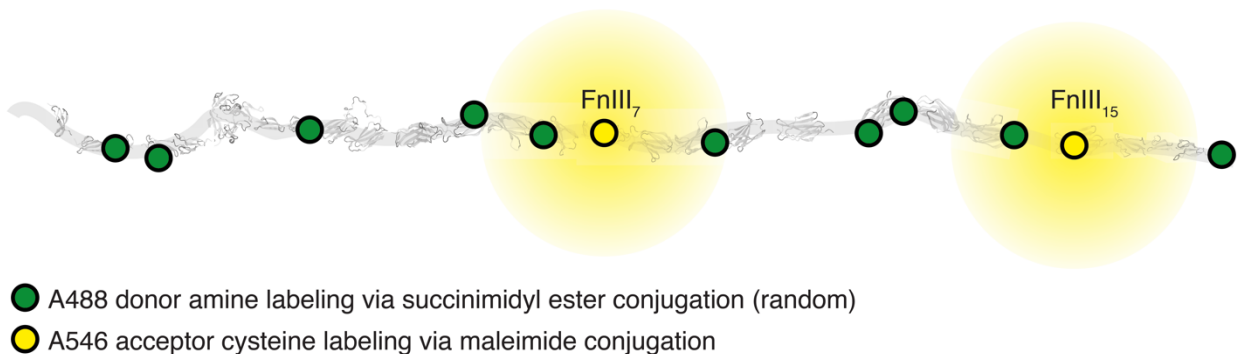


Figure 3.3. FRET Fibronectin random labeling of amines with A488 donor (typical mean labeling: ~10 per FN molecule), and site specific labeling of cysteines with A546 acceptor fluorophores (typical mean labelling 2-3 per FN molecule). FN monomer depicted, though FN is present as a dimer in solution.

Briefly, the labelling was done with about 1 mg fibronectin at high concentrations (~5 mg/ml) to reduce the loss of material during the procedure. The molar concentration of isolated FN was estimated by spectrometry using the following equation, with the extinction coefficient for unlabeled fibronectin being $563200 \text{ (M}^{-1}\text{cm}^{-1})$ ¹⁸⁶ and an optical path length of 1cm:

$$[C]_M = A_{280} / [(\text{Extinction coefficient}) (\text{Optical path})] \quad [3.3]$$

To unfold fibronectin and expose the cysteines for labelling, fibronectin was denatured by adding an equal volume of 8M GdnHCl, for a final concentration of 4M GdnHCl, and a molar excess of 30-fold of Alexa 546 maleimide was added. The solution was then mixed by inverting the eppendorf tube and incubated for 1 hour at room temperature in the dark.

The labeled protein was separated from free dye with a size-exclusion PD-10 column (Amersham), which allows for group separation of high ($M_r > 5000$) from low MW substances ($M_r < 1000$). First, the column was equilibrated with 20 ml of PBS and 0.1 M NaHCO_3 , pH 8.5 (Buffer A), and the same buffer added to the labeled FN solution to bring it to 1 ml total volume. The solution was then added to the column and allowed to enter fully, and an additional 2 ml of buffer A were added and allowed to enter the column, bringing the protein to the bottom of the column. Finally, 1 ml of buffer A was added and the eluted protein collected.

The dye and fibronectin concentration of the eluted fraction, and the cysteine labelling ratio were then estimated by measuring the absorbance at 280 and 556nm (actual peak for Alexa 546), using the following formulas:

$$[\text{Alexa 546}] = \frac{A_{556}}{\epsilon_{556}^{\text{Alexa 546}}} \quad [3.4]$$

$$[\text{Fn}] = \frac{A_{280} - [\text{Alexa 546}](\epsilon_{280}^{\text{Alexa 546}})}{\epsilon_{280}^{\text{Fn}}} \quad [3.5]$$

With A_{556} being the measured absorbance at 556nm wavelength, and $\epsilon_{556}^{\text{Alexa 546}}$ the absorption coefficient of the Alexa 546 dye at 556nm wavelength ($105000 \text{ cm}^{-1}\text{M}^{-1}$), and A_{280} being the absorbance at 280nm, $\epsilon_{280}^{\text{Alexa 546}}$ the absorption coefficient of the Alexa 546 dye at 280nm ($12500 \text{ cm}^{-1}\text{M}^{-1}$), and $\epsilon_{280}^{\text{Fn}}$ the absorption coefficient of fibronectin at 280nm ($563200 \text{ cm}^{-1}\text{M}^{-1}$). The cysteine labelling ratio being estimated by dividing the concentration of Alexa 546 over fibronectin concentration.

Next, the amines were randomly labelled with Alexa 488 succinimidyl ester. A 70-fold molar excess of Alexa 488 was added to the solution, mixed by inverting the eppendorf tube and incubated for 1 hour at room temperature in the dark. The labeled protein was then separated from free dye with a size-exclusion PD-10 column (Amersham). The column was equilibrated with 20ml PBS, and the protein solution added to the column. 2 ml of PBS were then added and allowed to fully enter the column to bring the protein to the bottom of the column. Finally, 1 ml PBS was added to the column to collect the eluted protein, and the dye and fibronectin concentration and labelling ratios were estimated by measuring the absorbance at 280, 498 (actual peak for Alexa 488), and 556 (actual peak for Alexa 546) using equation [3.4] and the additional following equations:

$$[\text{Alexa 488}] = \frac{A_{498} - [\text{Alexa 546}](\epsilon_{498}^{\text{Alexa 546}})}{\epsilon_{495}^{\text{Alexa 488}}} \quad [3.6]$$

$$[\text{Fn}] = \frac{A_{280} - [\text{Alexa 546}](\epsilon_{280}^{\text{Alexa 546}}) - [\text{Alexa 488}](\epsilon_{280}^{\text{Alexa 488}})}{\epsilon_{280}^{\text{Fn}}} \quad [3.7]$$

With A_{498} being the measured absorbance at 498nm wavelength, $\epsilon_{498}^{\text{Alexa 546}}$ the absorption coefficient of the Alexa 546 dye at 498nm wavelength ($13000 \text{ cm}^{-1}\text{M}^{-1}$), and $\epsilon_{280}^{\text{Alexa 488}}$ the absorption coefficient of the Alexa 488 dye at 280nm ($8789 \text{ cm}^{-1}\text{M}^{-1}$). The labelling ratios were estimated by dividing the concentration of Alexa 546 over fibronectin concentration for the acceptor labelling ratio, and the concentration of Alexa

488 over fibronectin concentration for the donor labelling. These normally give values of ~3.5-4 for the acceptor and ~10 for the donor (In the batch used in our experiments, we obtained a ratio of 3 acceptors to 10.5 donors). The labelled protein was stored in 5 to 10% glycerol at -20°C in small aliquots.

A full protocol for fibronectin FRET labelling, based on previous work^{138 58 65} is included in the Appendix and is available as PDF and Pages files. The Pages file contains live equations that can be used to immediately estimate the concentrations and labelling quantities needed.

2.6.3. FRET Fibronectin conformation sensitivity control

To test whether the FRET values obtained from FRET-labelled fibronectin were sensitive to changes in fibronectin concentration, a denaturation test was performed to alter the conformation of fibronectin with Guanidinium Hydrochloride and evaluate the resulting changes in FRET ratio. A full protocol for the FRET fibronectin denaturation test, based previous work developed in our lab¹²⁸ is included in the Appendix and is available as PDF and Pages files. The Pages file contains live equations that can be used to immediately estimate the concentrations and quantities needed.

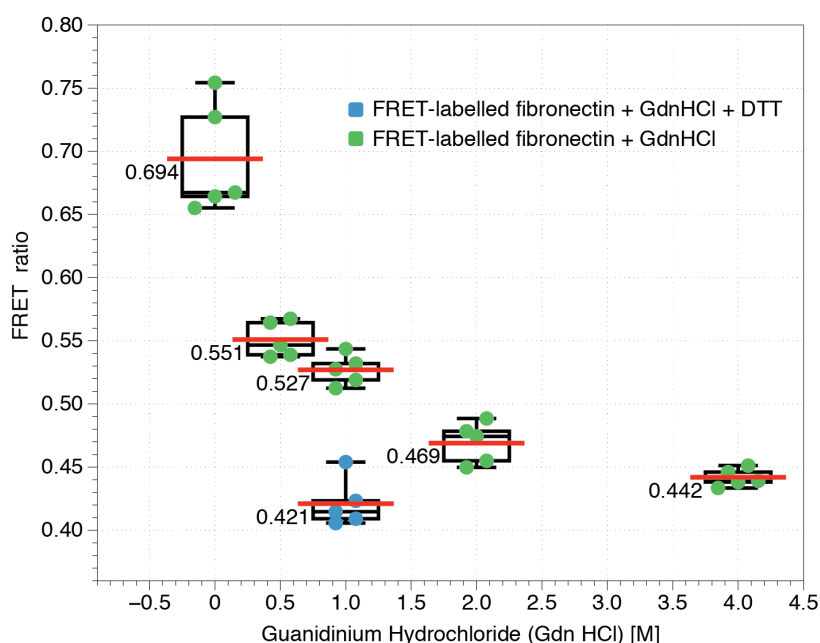


Figure 3.4. Denaturation of FRET-labeled fibronectin in solution. FRET-labeled fibronectin was chemically denatured with increasing concentrations of guanidinium hydrochloride (Gdn HCl) in solution, to assess whether the FRET signal is responsive to conformational changes in fibronectin. In agreement with previous findings^{58,128}, we observed decreasing FRET ratios upon denaturation of FN, and upon addition of DTT (Dithiothreitol), which reduces disulphide bonds and cleaves disulfide-bonded dimeric FN.

In summary, glass slides were coated with 5% BSA in PBS for 1 hr at room temperature, emptied and air dried. FRET labelled fibronectin was thawed in ice for one hour and centrifuged at 10,000rpm for 10 minutes to remove aggregates, and mixed in solution with varying concentrations of Gdn HCl (0, 0.5, 1, 2, 4M) or FRE-fibronectin which was pre-incubated in 150mM dithiothreitol DTT in PBS for one hour and then mixed with Gdn HCl to 1M Gdn HCl concentration.

After estimating the FRET values as explained in Section 3.3, it can be shown in Fig.3.4, that increasing Gdn HCl concentration leads to progressively lower FRET values as fibronectin is denatured, confirming the capability of our FRET-labeled fibronectin to be used as a FRET probe to assess fibronectin conformation, in agreement with previous findings¹²⁸. The addition of DTT to FRET labelled fibronectin, reduces disulfide bonds and separates the two fibronectin subunits causing a further reduction in FRET, as previously described¹²⁸. Five samples per condition were evaluated, and box plots for each condition are shown in Fig.3.4.

2.6.4. Mechano-sensitivity control

Once the FRET labelled fibronectin is shown to be responding to changes in fibronectin conformation, it is good practice to control that the probe is also sensitive to FRET ratio changes induced by the application of mechanical forces.

To do this, we employed an assay previously developed in our lab, where manually pulled FN fiber are deposited on silicone membranes mounted on a stretching device, and applied different levels of strain to them^{25,58,65}. Briefly, fibronectin in solution was prepared at 0.4 mg/ml in PBS with 5% FRET-labelled FN. Silicone membranes (Speciality Manufacturing) were mounted on the stretching device and a droplet of fibronectin placed on the membranes. Fibronectin fibers were then manually pulled out of this solution and deposited in parallel, on the membranes. The fibers were then washed three times with PBS and kept in PBS while the membranes were either, left as mounted (Native), stretched to twice their original length (100% tensile strain of the membrane), or relaxed to half their original length (50% compressive strain on the membrane). As the fibers are pulled out of solution, μN forces are applied to them, and they are kept under tension as the fibers are deposited on the silicone membranes, because of this, they are typically pre-strained to approximately 140%¹³⁹.

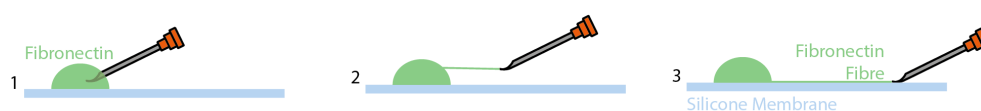
The fibers were then imaged using a confocal microscope and the FRET ratios evaluated as explained in Section 3.3. A ready to use protocol is included in the Appendix and is available as PDF and Pages files.

As reported previously^{58,65}, the results (Fig. 3.5) showed increased FRET ratios for fibronectin fibers deposited on relaxed membranes, and decreased FRET ratios for fibronectin fibers deposited on stretched membranes, with respect to fibronectin fibers deposited on native membranes. These results show that stretching of fibronectin fibers increases the distance between donor and acceptors which results in a decrease of FRET energy transfer and therefore FRET ratio values, and in contrast, relaxation of fibronectin fibers results in donor and acceptor dyes being in closer proximity and resulting in increased FRET energy transfer and increased FRET ratio values.

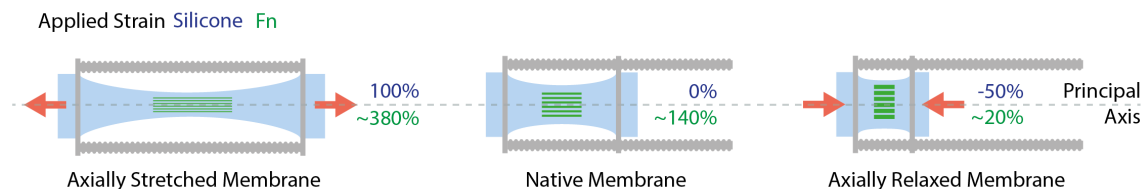
2.7. Method to correlate ligand binding with FRET ratio

Previous studies have shown how binding of a FN ligand can be affected by stretching of FN fibers as assessed by FRET⁶⁷. Since we are interested in the binding behavior of IL-7 to Fibronectin, we have further developed a method to assess the correlation between Fibronectin stretching and the associated conformational changes as assessed by changes in FRET ratios, and IL-7 binding. Since the fluorophores used for Fibronectin's intramolecular FRET probing includes Alexa 488 (A488) and Alexa 546 (A546), we chose a far red fluorophore to label the ligand, in this case, Alexa 647 (A647), to minimize possible interaction between our FRET acceptor and the ligand label A647.

a *Manually pulled Fn fiber deposition*



b *Strain application to silicone membranes*



b *Representative results for FRET values obtained at different strains in two independent samples*

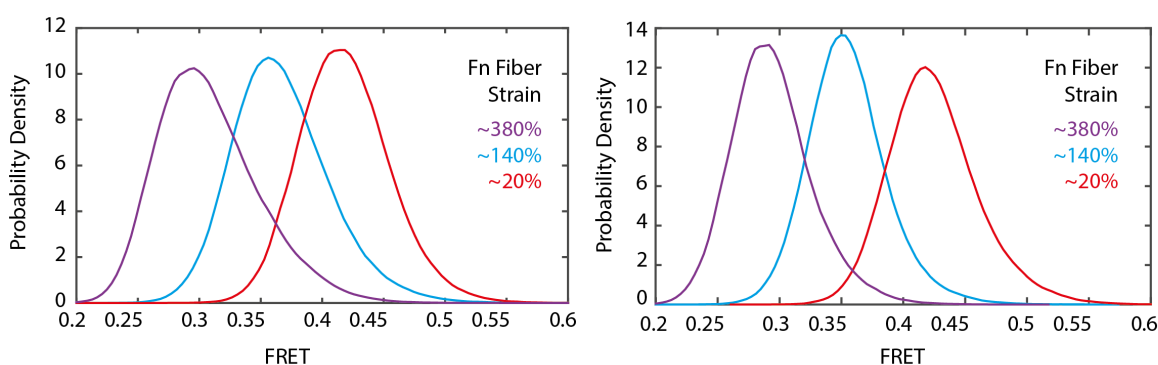


Figure 3.5. Mechanical force induced strain results in changes in FRET ratios. A) Assay to manually deposit FN-fibers on silicone membranes. B) Forces is applied on silicone membranes to modify the strain of deposited FN-fibers. C) Representative results of FN-FRET values obtained for FN-fibers exposed to different levels of strain via stretching and relaxing of silicone membranes.

2.7.1. Experimental context

We used FRET labelled fibronectin as an in-situ probe to detect conformational changes in fibronectin, either in solution (Section 3.2.3), as manually pulled fibers (Section 3.2.1 and Chapter 4), or integrated in cell-assembled ECM (Chapter 5). The ratiometric FRET signal obtained decreases upon unfolding of fibronectin either by chemical denaturing of the protein such as with Guanidine Hydrochloride (GdnHCl), as a result of mechanical stretching of manually pulled FN fibers, or as a result of cell-generated forces.

For experiments in Chapter 4, where FN fibers were manually pulled out of solution and deposited onto a silicone membrane mounted on a stretching device and stretched to different levels of FN strain, A647 labelled recombinant human/murine IL-7 or an A647 CD-loop were incubated on these fibers to assess how changes in FN conformation due to strain would affect IL-7 or CD-loop binding. To do this, we needed to simultaneously measure both the fluorescence intensity of the A647 labelled IL-7 and the signal emitted by the FRET Fibronectin probe using a confocal microscope. This posed the challenge of correcting for the issues discussed in Section 3.1 regarding spectral overlap in the recorded FRET signal, as well as FRET normalization, but also to control unwanted contributions of the ligand signal into FRET and vice-versa. Furthermore, to achieve accurate results, it was crucial to address issues of signal quality and proper image registration. These issues were resolved as explained in the following sections.

2.7.2. Data acquisition

To allow proper image co-registration, which is crucial to obtain accurate FRET ratio measurements, we implemented a method to correct for xy misalignment of the data (described in Section 3.3.3: Image registration correction), but co-registration on the z direction requires the use of complex algorithms that are beyond the scope of this work, therefore, we ensured proper alignment of the microscopes' lasers in the z direction, prior to the data acquisition, by testing proper registration of the fluorescent signals emitted by beads labelled with multiple fluorophores. A detailed description of the method to corroborate proper alignment of the laser lines is included in the Appendix.

We minimized the unwanted contribution of a fluorophore emission into the channel of another fluorophore signal of interest by optimizing the detection ranges of the detectors to capture the signals around the donor, acceptor and ligand emission peaks, while a compromise was made between choosing a large enough range to detect as many photons as possible, and small enough to remain specific enough for independent measurement of donor and acceptor signals. The following detection ranges were chosen (Fig.3.6): 500-530nm (A488 emission range), 555-610nm (A546 emission range) 650–810 nm (A647 emission range).

Furthermore, to reduce even further the chances of unwanted bleed-through contributions, the acquisition was done sequentially in three steps (Fig. 3.6): First, the samples were excited with the 488 laser and the signals in the donor, acceptor and ligand channels were recorded to capture the Donor signal (**D**), and the acceptor emission due to FRET signal (**F**), and control whether these signals are detected in the ligand channel (**Ctrl-1**). On the second step, the samples were excited with the 546 laser to directly excite the acceptor, and the signals were recorded for the directly excited acceptor (**A**), the donor as a control that no signal from the acceptor is detected in the donor channel (**Ctrl-2**), and the ligand, again as a bleed-through control (**Ctrl-3**). Finally, in the third step, the samples were excited using the 633 laser in order to directly excite the ligand's fluorophore, and the ligand signal was acquired (**L**), together with bleed through controls for the donor (**Ctrl-4**) and acceptor channels (**Ctrl-5**). An example of the acquired data for manually pulled FN fibers, with bound A647 IL-7 is shown in Fig 3.7.

Inevitably, it is possible that some amount of the recorded signal will not be contributed by the desired signal, and corrections will have to be made to correct for the unwanted contributions, but before this is done, the acquired data needs to be verified for proper registration and image quality. I will first address these issues and then develop the method to do the actual correction of the acquired signals and derivation of the corrected FRET ratio.

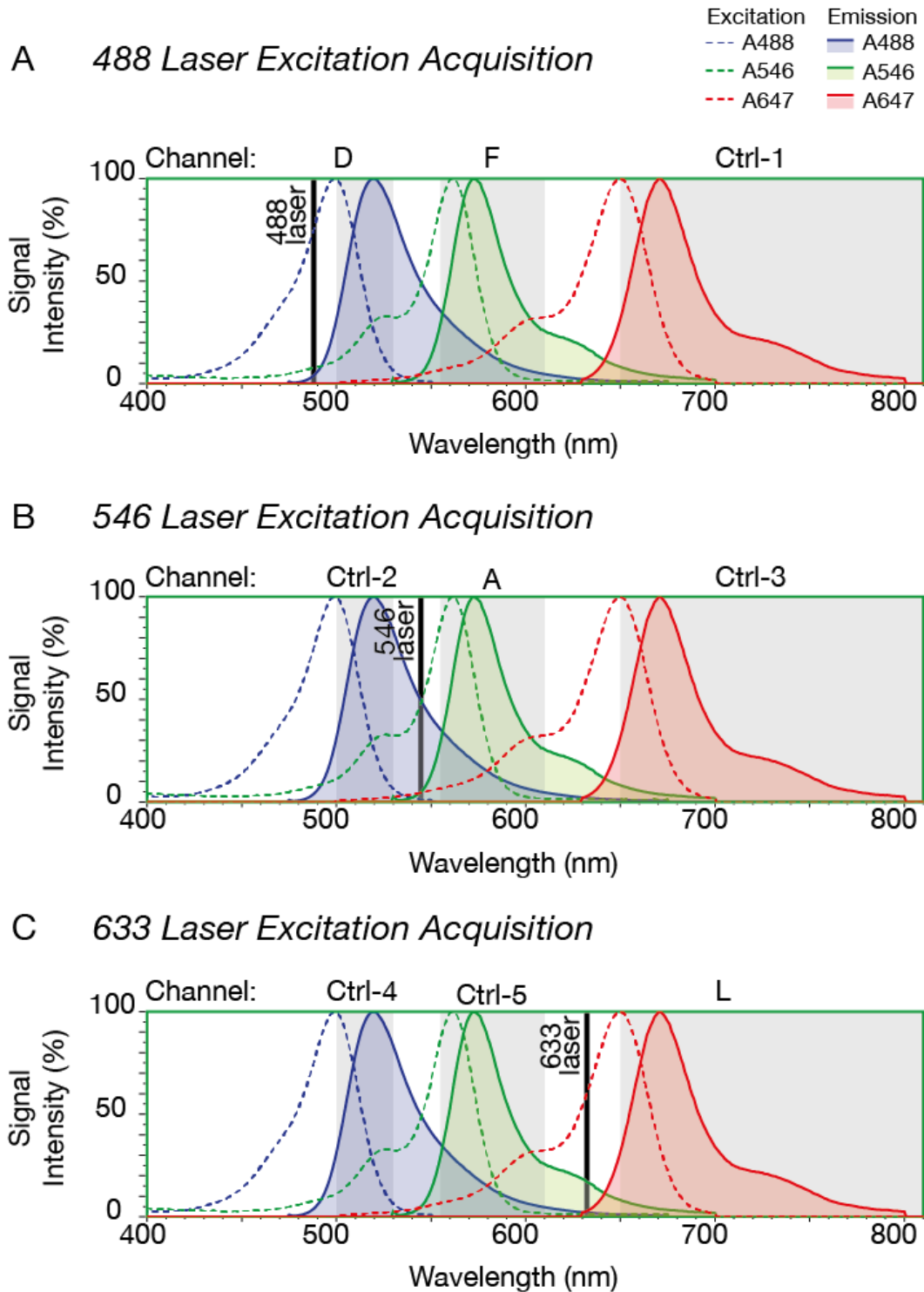


Figure 3.6. Fluorophore excitation and emission spectra of the fluorophores used in our studies as provided by the manufacturer (Life Sciences) and acquisition parameters used in our studies.

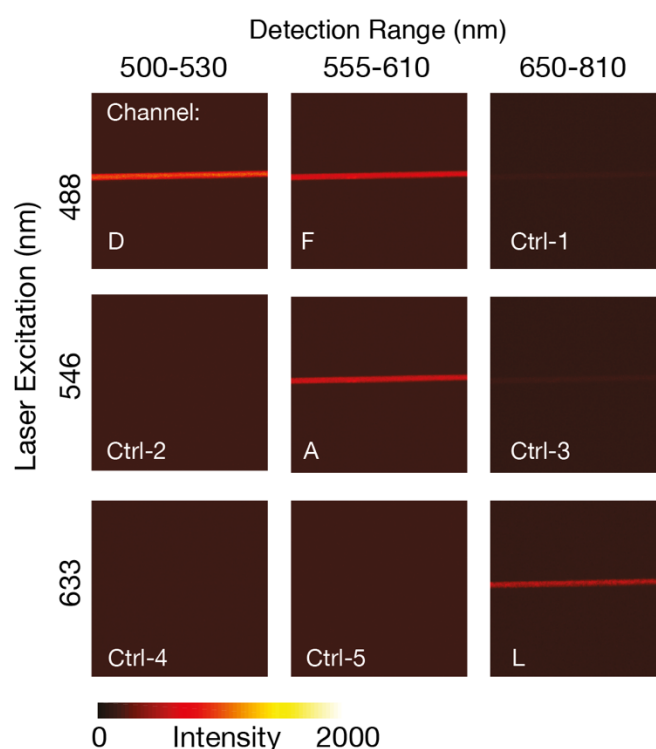


Figure 3.7. FRET and A647-IL7 binding signals and controls. A sample with FN-FRET and A647-IL7 showing bleedthrough into the Ctrl-1 and Ctrl-2 channels showing the need to sequentially acquire the ligand signal (L). Ctrl-4 and Ctrl-5 show that in such case, the ligand signal does not contain contributions from either the donor or acceptor signals respectively. Ctrl-2 shows that the signal obtained for directly exciting the acceptor with a 546 laser does not excite the donor and is therefore a reliable measure of FN content.

2.7.3. Post-acquisition processing

Image import to Matlab

Since the post-acquisition processing and ensuing calculations have been coded in Matlab, the acquired data needs to be imported. We used the open source Bioformats package from The Open Microscopy Environment, with a Creative Commons Attribution 4.0 International License ¹⁴⁰ to import the acquired Olympus '.oif' files, and converted the data to double precision value arrays to treat the images effectively as numerical matrices.

Image registration correction

We then addressed the issue of image co-registration. To obtain accurate FRET ratio values, it is important that there is proper image alignment (co-registration) between the different channels obtained, that is, that the spatial location of the pixels in one image match accurately the corresponding pixels in all the images from all other channels. An accurate registration can be assessed visually by overlaying the images from two different channels and making sure that these co-localize properly (Figure 3.8). In addition, there are Matlab built-in functions that compare two images for proper co-registration, such as 'imshowpair' which

highlights the differences between two images, and was implemented in our script. For our settings, we found that small xy-shifts could occur, probably as a result of the physical change of filters required to perform the sequential scanning. These were assessed and corrected with the Matlab built in function 'imregister', which is an intensity-based registration with monomodal image capture modality (captured on the same device), and restricted to xy translation to avoid deformation of the captured images, which would again result in false FRET values. This allowed for proper registration of the images.

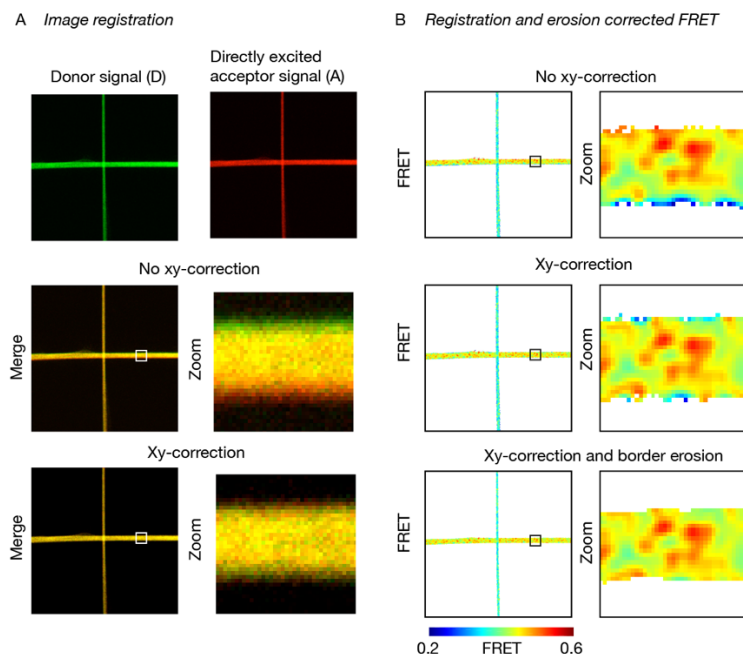


Figure 3.8. Co-registration correction and mask erosion to produce accurate FRET ratio values. Co-localization of donor signal (D) and directly excited acceptor signal (A) shows incorrect xy- registration before the application of the Matlab correction algorithm, and a correct registration after this is applied. B) Corresponding FN-FRET values show aberrant values obtained in samples that are not xy-registration corrected vs. xy corrected. Border erosion of FN-fibers further enhances the quality of the obtained data.

Thresholding and background removal.

Since we are interested in deriving FRET ratio values only for the image areas that contain FN, we set thresholds to remove pixels that did not belong to the fibers (background areas) and overexposed pixels, which would result in false FRET ratio values. These were set to zero, and then the mean background signal from the instrument was subtracted from the data. The resulting negative and zero values were then converted to Not-a-Number (NaN) values that are excluded from further analysis. Based on the non-zero data, a mask was then generated for each contributing channel, and the masks were merged to include in the analysis only data points that remained valid in all the channels of interest.

In addition, because of differences in light scattering properties of the emitted signals, and the differences in intensities between the donor, FRET excited and directly excited acceptor signals, we found that on the borders of the fibers, inaccurate FRET values could occur. A solution to this problem was to erode the obtained mask to remove pixels located on the borders of the FN fibers, which were generally of lower intensities that often showed an affect on the obtained FRET values (Fig. 3.8).

Data smoothing to reduce noise

Finally, while every effort was made to find an optimal balance between signal enhancement by increased laser power excitation and PMT gain, noise due to photon statistics will still be present in the acquired images. The effect of it can be significantly reduced by using a simple mathematical averaging with a 3x3 kernel applied to the background-subtracted, registration corrected images. This has been previously shown to be able reduce photon noise by up to 3-fold¹³⁰.

This was applied using the Matlab built-in functions ‘imfilter’ and ‘fpecial’, (used in the ‘average’ mode). Furthermore, we observed that a one-deviation Gaussian averaging filter, implemented with Matlab built-in function ‘imgaussfilt’, resulted in a significant improvement of noise contribution in our images.

2.7.4. Signal correction FRET ratio calculation

Once these image improvement measures were taken, the data is ready to be cleared of unwanted contributions included in the channels of interest (Channels **D**, **F** and **A**). These are expressed by the Equations 3.8, with the signals of interested highlighted in red, and using the notation shown in Equation 3.9^{130,135}:

$$\begin{aligned} D &= I_{D-F}^d + I_F^d + I_A^d \\ F &= I_{D-F}^f + I_F^f + I_A^f \\ A &= I_{D-F}^a + I_F^a + I_A^a \end{aligned} \quad [3.8]$$

$$Intensity_{CONTRIBUTING COMPONENT}^{detected signal} \quad [3.9]$$

In the first acquisition step, where the sample is excited with the 488 laser, the signals in the range 500-530nm (Channel D), and in the range of 555-610nm (Channel F) are recorded. The signal recorded in channel **D** is a mixture of the following contributing components (see Equations 3.8)^{130,135}:

- I_{D-F}^d is the intensity of the donor emission attenuated by the energy loss due to FRET transfer to the acceptor and detected in channel **D**. This is our signal of interest for the donor emission.
- I_F^d is the intensity of the acceptor emission due to FRET that is unwantedly recorded in the donor channel **D**.
- I_A^d is the intensity of the acceptor emission due to direct excitation via the 488 laser and that is unwantedly recorded in the donor channel **D**.

The signal recorded in channel **F** is a mixture of the following contributing components (see Equations 3.8)^{130,135}:

- I_{D-F}^f is the intensity of the donor emission attenuated by the energy loss due to FRET transfer to the acceptor and that is unwantedly detected in acceptor channel **F**.
- I_F^f is the intensity of the acceptor emission due to FRET that is recorded in the acceptor channel **F**. This is the component that we are most interested in, since it is the contribution that is altered by FRET efficiency due to changes in the distance between donor and acceptor.

- I_A^f is the intensity of the acceptor emission due to direct excitation via the 488 laser and that is unwantedly recorded in the acceptor channel **F**.

In the second acquisition step, when exciting the sample with the 546 laser, the signal in the range of 555-610nm (Channel **A**) is recorded and is composed of the following contributing components (see Equations 3.8) ^{130,135}:

- I_{D-F}^a is the intensity of the donor emission attenuated by the energy loss due to FRET transfer to the acceptor and that is unwantedly detected in acceptor channel **A**.
- I_F^a is the intensity of the acceptor emission due to FRET that is unwantedly recorded in the acceptor channel **A**.
- I_A^a is the intensity of the acceptor emission due to direct excitation via the 546 laser and that is recorded in the acceptor channel **A**. This is our signal of interest for the directly excited acceptor emission.

It can be seen in control images such as the one shown as Ctrl-2 in Fig.3.7, that signals contributed by I_{D-F}^a and therefore also by I_F^a are negligible, thus **A** can be assumed to equal I_A^a :

$$A = I_A^a \quad [3.10]$$

Correction factors

There is one concept we need to introduce in order to derive the equations that express the intensity of the acceptor's emission due to FRET (I_F^f), and that is that for a given fluorophore, a leak into one channel is proportional to another channel's loss ^{130,135}. Another way of thinking of it, is that the intensity of the leak into an unwanted channel is proportional to the signal that is detected in the wanted channel. We can therefore define a constant that determines the relationship between the signals detected for that fluorophore in different channels. The constants α, β, γ and δ are introduced as scaling factors that relate those signals, as shown in Equations 3.11 ^{130,135}.

$$\begin{aligned} I_{D-F}^f &= \beta I_{D-F}^d \\ I_A^f &= \gamma I_A^a = \gamma A \\ I_A^d &= \alpha I_A^a = \alpha A \\ I_F^d &= \delta I_F^f \\ \alpha &= \gamma \delta \end{aligned} \quad [3.11]$$

These constants will be used to obtain I_F^f . The β factor can be found by imaging a sample labelled only with donor fluorophores using exactly the same imaging parameters as the sample ^{130,135}. In such a sample, Equations 3.8 become:

$$\begin{aligned} D &= I_{D-F}^d \\ F &= I_{D-F}^f \\ A &= I_{D-F}^a \end{aligned} \quad [3.12]$$

and from Equation 3.11 for the β factor, we get:

$$\beta = \frac{I_{D-F}^f}{I_{D-F}^a} = \frac{F}{D} \quad [3.13]$$

In this case, β is then estimated from plotting the signals **F** against **D** and applying a linear fit, for which with the slope is the estimated β value as shown in Fig. 3.9^{130,135}.

In a similar way, the γ and δ factors can be found by imaging a sample labelled only with acceptor fluorophores using exactly the same imaging parameters as the sample. In a sample labelled only with acceptor fluorophores, the equations from [3.8] become^{130,135}:

$$\begin{aligned} D &= I_A^d \\ F &= I_A^f \\ A &= I_A^a \end{aligned} \quad [3.14]$$

and from Equation 3.11 for the γ and δ factors, we get:

$$\begin{aligned} \gamma &= \frac{I_A^f}{I_A^a} = \frac{F}{A} \\ \alpha &= \frac{I_A^d}{I_A^a} = \frac{D}{A} \\ \delta &= \frac{\alpha}{\gamma} = \frac{D}{F} \end{aligned} \quad [3.15]$$

In this case, γ and δ are estimated by plotting the signals **F** against **A** with a linear fit to define γ as the slope, (Fig. 3.10), and **D** against **F** for δ ^{130,135}. In our case, $D \cong 0$ and therefore $\delta \cong 0$.

Since what we are interested in is the actual value of I_F^f , which is the intensity of the acceptor due to FRET, we can now rearrange the equations from [3.8] and substitute with the equations from [3.11] as shown in Fig.3.11 to arrive to a final equation that relies on the measured signals for **D**, **F** and **A**, and the estimation of correction factors β, γ and δ , which are to be estimated for the specific microscopy parameters used in the corresponding experiment. The final equation to estimate the fret induced intensity of the acceptor in the fret acceptor channel is^{130,135}:

$$I_F^f = \frac{F - \beta D - A\gamma(1 - \beta\delta)}{(1 - \beta\delta)} \quad [3.16]$$

β -Factor estimate with donor only labeled Fn (Alexa-488)

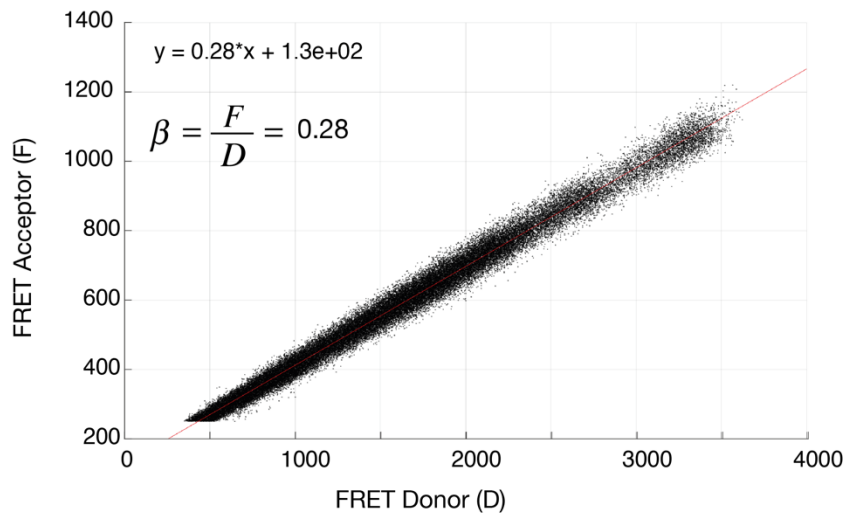
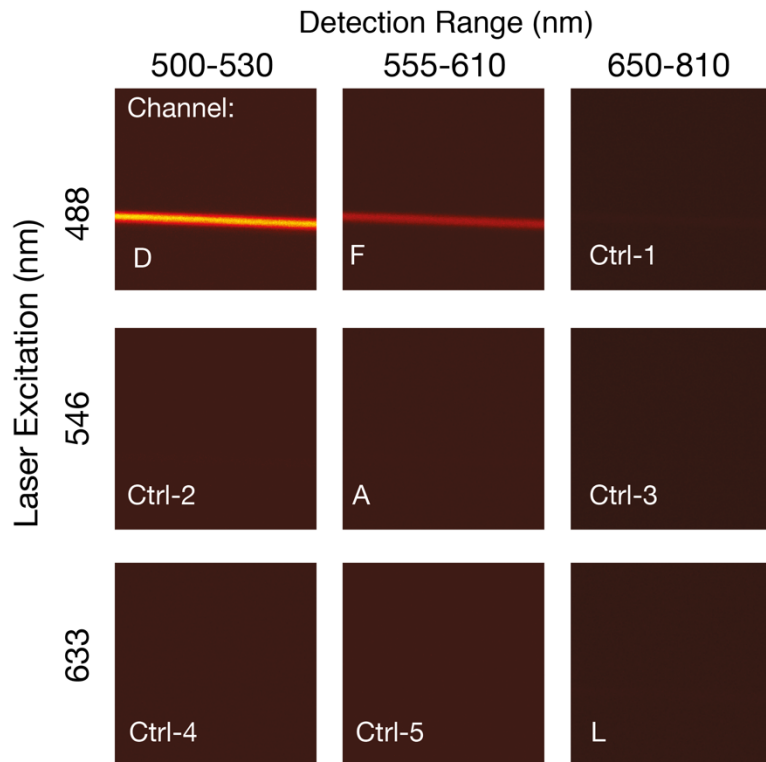


Figure 3.9. Estimation of β factor by imaging a FN fiber sample labeled with donor only (A488). Upon excitation at 488 nm, there is bleed-through into channel 2, which will affect the FRET ratio and justifies the need for FRET correction. Signals from the donor (D) were plotted against signals from acceptor due to FRET (F), and the β factor was estimated by the slope of the linear fit.

γ and δ estimate with acceptor only labeled Fn (A546)

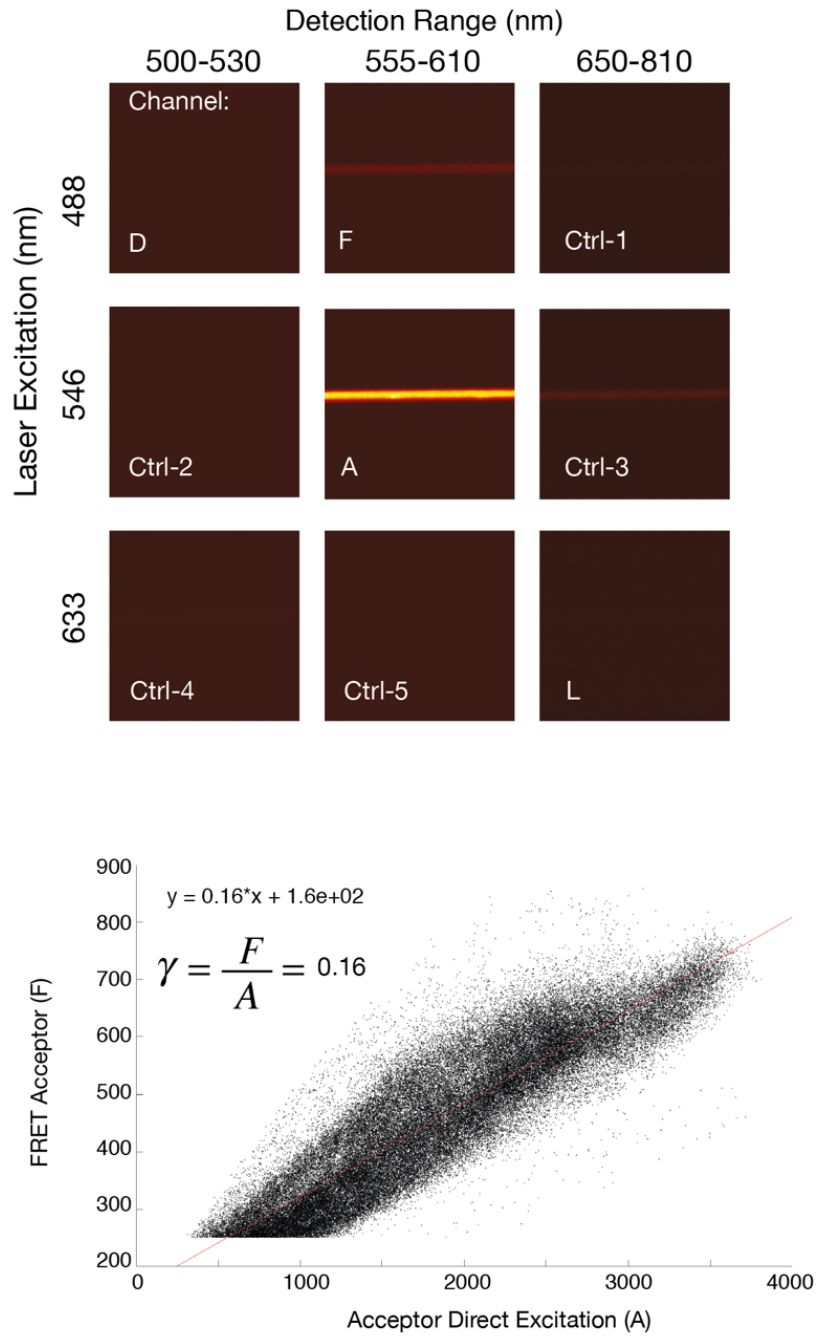


Figure 3.10. Estimation of γ and δ factors. Imaging of an FN fiber sample labeled with acceptor only (A546). Upon excitation at 546 nm, there is a signal in channel 2 as expected. However, a signal is detected in channel 2 also upon excitation at 488 nm, which will also affect the FRET ratio and further justifies the need for FRET correction. Signals from the FRET excited acceptor (F) were plotted against signals from the directly exciting the acceptor (A), and the γ factor was estimated by the slope of the linear fit.

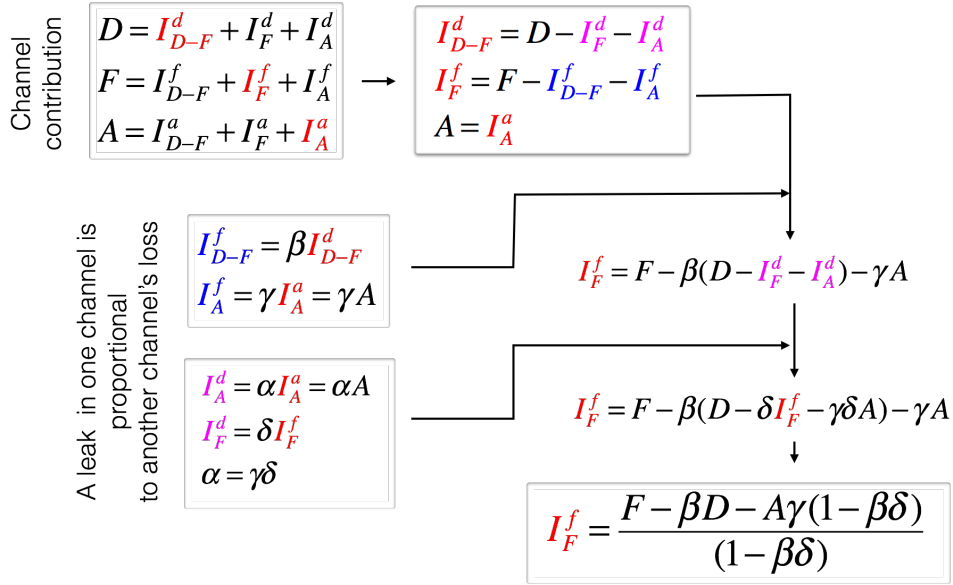


Figure 3.11. Derivation of corrected acceptor intensity due to FRET. Equation re-arrangement of Channel contribution equations and leak proportional relationship between channels to derive a final corrected FRET-induced acceptor intensity (I_F^f).

Ratiometric FRET ratio

Since I_F^f depends on FRET efficiency but also on fluorophore concentration and donor excitation^{130,135}, it is necessary to normalize the signal so that the obtained value is independent of fibronectin and fluorophore concentration, and of the level of excitation of the donor. This can be done by dividing for each pixel the value of the corrected FRET intensity I_F^f over the intensity of the signal obtained on channel **D** as shown in Equation 3.17 to obtain a ratiometric FRET value^{130,135}.

$$\text{FRET ratio} = \frac{I_F^f}{I_{D-F}^d} \cong \frac{I_F^f}{D} \quad [3.17]$$

It is important to note that the relative sensitivities of the signals obtained in the **D**, **F** and **A** channels vary non-linearly with changes in laser intensity and PMT voltage, and any change in software or hardware parameters such as filters, light paths or zoom ratios, have the potential to modify the signals obtained and the relation between them. For this reason, it is necessary to obtain the correction factors every time any parameter in the acquisition setup on the microscope is changed. The easiest way to do this is to obtain these after the parameters have been set for and the acquisition has been performed for a defined experiment. Furthermore, the FRET ratio values obtained between different experiments or samples will vary if the laser intensity, PMT voltage gain, offset, and potentially other parameters are changed.

The implications of these are many. While it is possible to compare experiments that have been obtained with the same imaging parameters, the FRET ratios obtained from experiments performed with varying settings cannot be compared.

While there would be way to correct for this limitation by scaling the nominator I_F^f to the denominator **D** in Equation 3.17, by relating the loss in donor fluorescence due to FRET to the gain in FRET signal due to

FRET, this would need the availability of a construct that can be induced to change FRET significantly, homogeneously, and with a known characterization of the labels bound to the molecule to study. In our case, since the donor labels are placed randomly throughout the fibronectin molecule, and it is not possible to know the location or characteristics of the labelling for these fluorophores, this further normalization to make the measurements independent of settings or instrument is not possible, and only a ratio metric analysis of the data can be done among samples that are acquired with the same instrument and settings.

2.7.5. Ligand Signal

To corroborate that the observed increase in IL-7 binding is due to fibronectin unfolding and not due to a higher concentration of fibronectin present in the measurement location, the A646-IL-7 intensity was normalized with the signal obtained from directly exciting the FRET acceptor fluorophore as a measure of fibronectin content:

$$\text{Normalized Ligand} = \frac{L}{A_{(ex\ 546)}} \quad [3.18]$$

2.7.6. FN-FRET/Ligand correlation

FRET-labelled manually deposited FN fiber with A643-IL-7 as a binding ligand.

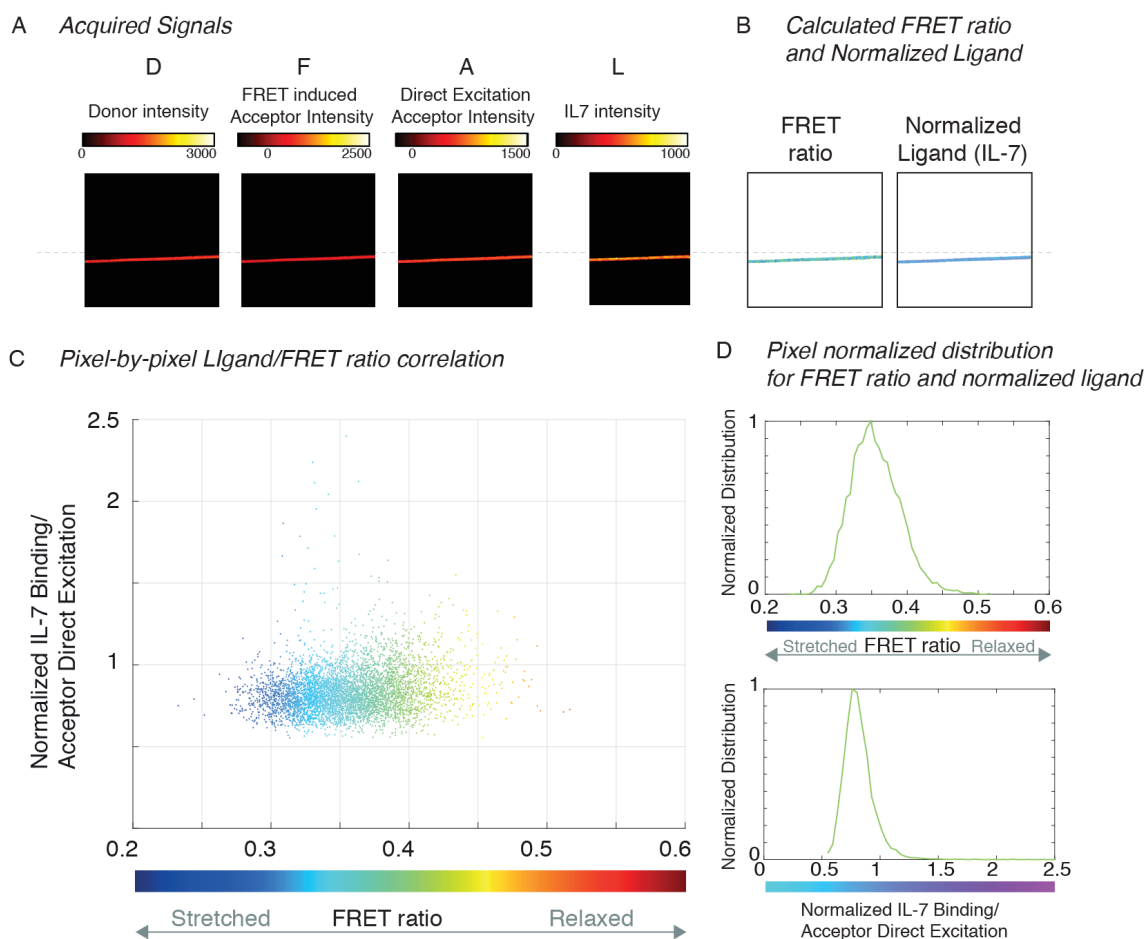


Figure 3.12. Plot showing pixel-by-pixel correlation of Normalized Ligand binding vs. FRET ratio.

Once the FRET ratio (Equation 3.17), and the normalized ligand intensity (Equation 3.18) have been estimated for each valid pixel in the images, it is possible to relate, for each pixel, its FRET value with the corresponding normalized ligand intensity. This allows to perform a pixel-by-pixel analysis of the correlation between FN conformation (via changes in FRET ratio), and Ligand Binding (changes in normalized ligand intensity). A sample of such a correlation is shown in Fig. 3.12.

2.8. Matlab based Graphic User Interface software for FRET and Ligand Correlated FRET analysis.

To simplify the processing and FRET analysis of FRET-FN samples using confocal microscopy data, we have created Graphic User Interface (GUI) that guides the user through the parameter setup and data processing.

2.8.1. Features

The features of this Matlab based GUI are the following:

- A Graphic User Interface (GUI) that allows users that are not familiar with Matlab or programming to perform FRET analysis of their confocal microscopy data without having to directly modify the Matlab code.
- Interactive definition of parameters such as thresholds and 3D stack cropping.
- Data processing, storage and built in statistical processing.
- Automatic generation of basic results.
- Data saved in various structured formats to allow easy access and further analysis using built in Matlab plotting and statistical functions
- Data is stored as raw data, processed data, pooled data by sample or stack and by grouped conditions. This allows for easy plotting and data exploration using Matlab built in functions.
- Data is processed as single sample and pooled group data, with corresponding full statistics

2.8.2. Workflow

The workflow of the software is as follows: Upon running the file 'FRETanalysis.m', the Main Panel for the analysis opens (Fig. 3.13). This offers the end-user the possibility of defining the channels in which their data was acquired, and allowing them to choose which type of analysis is to be performed:

- Definition of denaturation curves from FN in solution as explained in Section 3.2.3.
- Determination of β, γ and δ factors using donor or acceptor only labelled samples, as described in Section 3.3.4.
- FRET analysis of experimental samples that are acquired as 2D or 3D data.

This panel also offers the option of enabling/disabling the implemented xy-registration correction for 2D data, as described in Section 3.3.3, and the option of cropping a 3D stack to relevant slices.

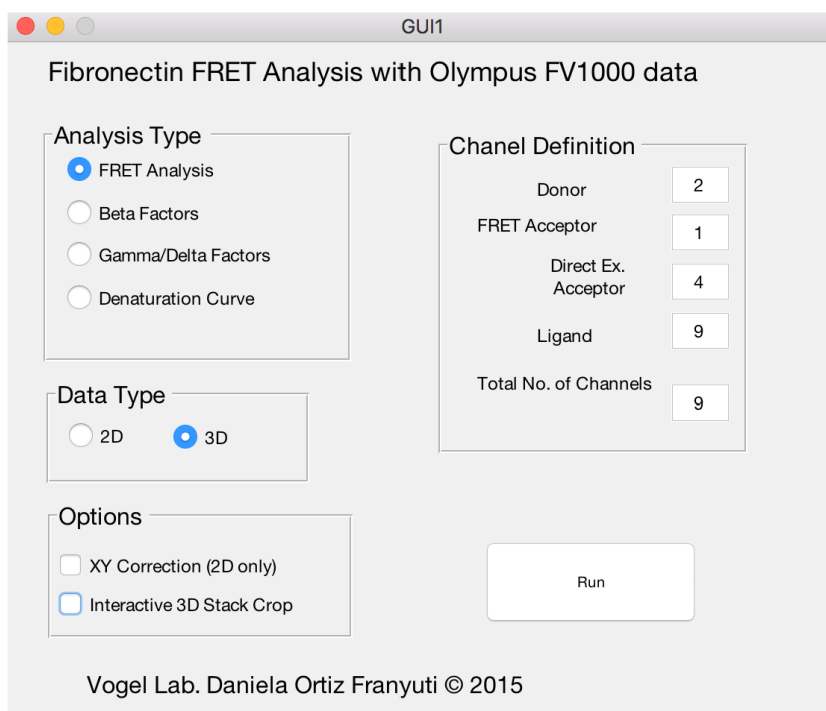


Figure 3.13. Main Panel of the Matlab based GUI software.

After pressing the 'Run' button, a window pops-up to allow the user to select the folder that contains the .oif files to be analyzed. The .oif data files belonging each experimental condition should be run separately to acquire the pooled data and statistics for that specific group, but care must be taken to ensure that the same parameters are chosen for different experimental conditions, if these are to be compared between them.

Once the folder containing the data files to be analyzed is selected, an Interactive 3D Stack Crop Panel opens if the data to be analyzed is three-dimensional (stacks), and the 3D stack cropping option was selected (Fig. 3.14). In this panel, the user can scan through the stack to be analyzed, and crop it to the relevant slices that are to be included in the analysis.

Next, the Parameters Panel opens (Fig. 3.15), where the parameters for the analysis are set, as well as further data processing is defined. For FRET analysis of experimental data, the user is required to input the correction factors that will be used in the analysis, these must be previously estimated. For the case where these factors are being estimated, these should be kept as 0. Background intensities are also to be defined by the user, as well as lower and upper thresholds for data inclusion. These can also be interactively defined by pressing the button 'Interactively Get' for the background, or 'Interactive Threshold Acquisition' for the thresholds, the user interface is shown in Fig. 3.16.

Post-acquisition refinement of the data is also defined in the Parameters panel. There is the option of applying a square shaped local averaging filter (by default defined as a 3x3 matrix, but can also be modified to other sizes), and a Gaussian filter that can be adjusted to values other than the default of 1 standard deviation. These are disabled by setting the values to zero. Furthermore, there are several mask refinement options available. It is possible here to activate/deactivate the step where the masks from FN signals (D, F and A) are combined with that of the ligand (L), this is in the case where one wants to include in the analysis

only pixels that are valid for both FN and the ligand. Also, in this panel, it is possible to define whether and what kind of erosion is applied to the resulting mask, as described in Section 3.3.3. By default, erosion is disabled, but simple erosion, close + erode, or erode + close modes are available. Furthermore, the shape and size of the eroding component can be chosen (available options are square, diamond, disk, and octagon). In addition, it is possible to limit the data range to a defined set of FRET values (FRET thresholds). As default, the FRET values are limited to a range between 0 and 1, which then eliminates invalid values. Finally, the color coding for FRET values in the produced figures can be adjusted to begin and end at values other than the default limits of FRET ratios between 0 and 1.

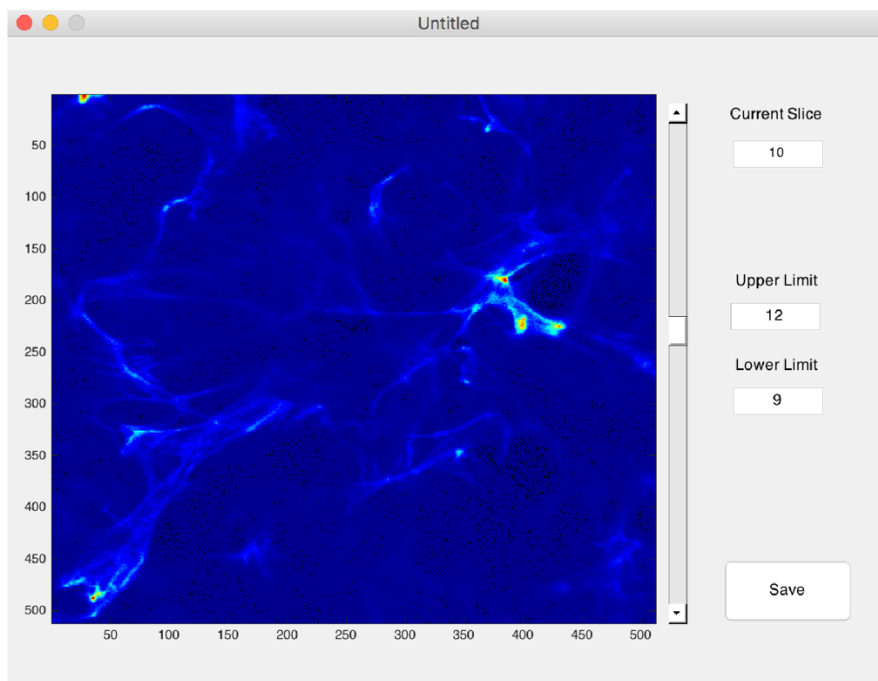


Figure 3.14. Interactive 3D Stack Crop Panel.

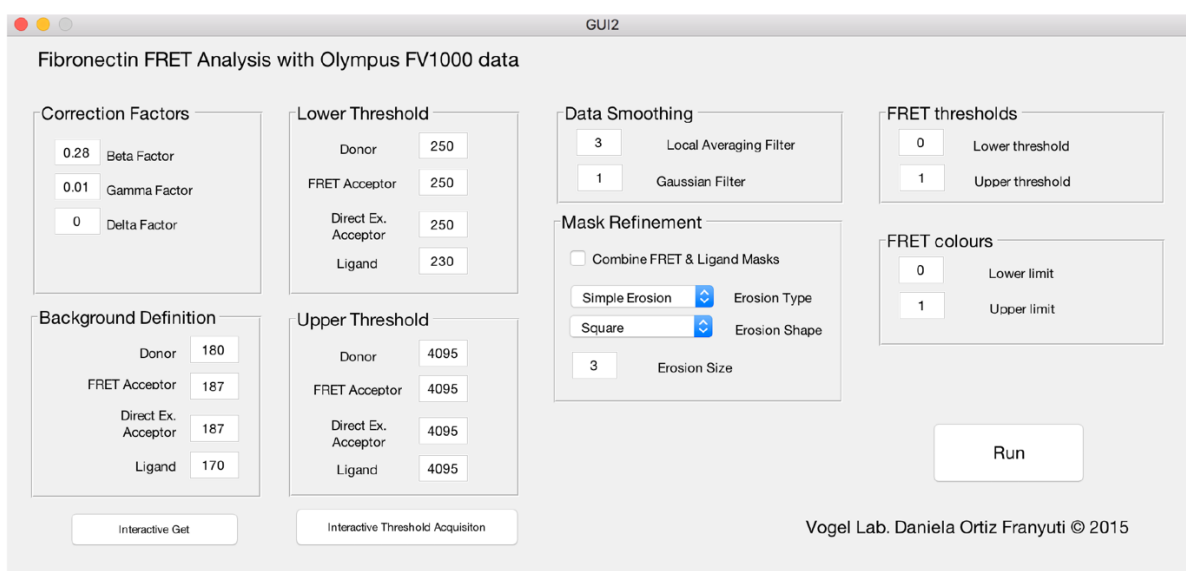


Figure 3.15. Parameters Panel – The parameters for analysis and special data handling are defined here.

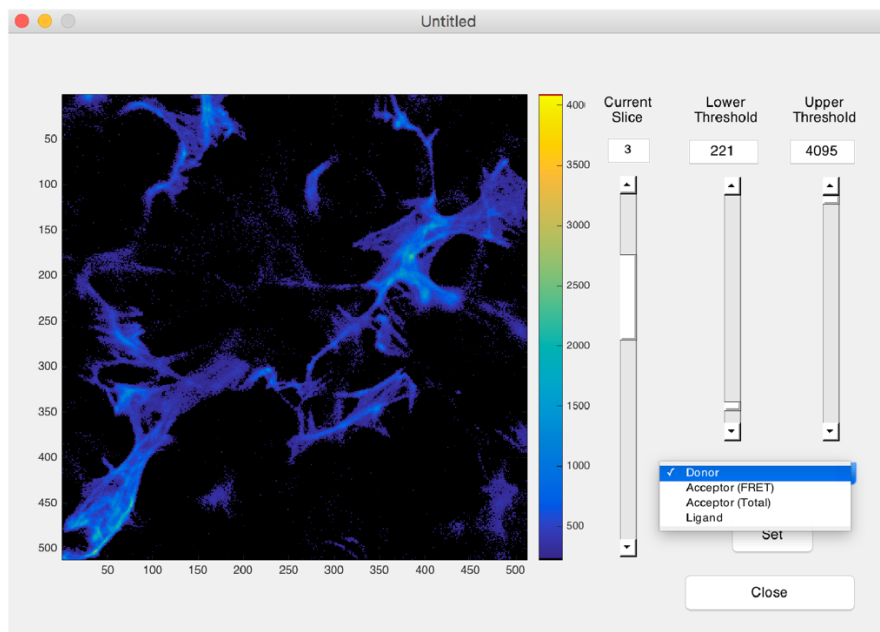


Figure 3.16. Interactive Threshold Definition

2.8.3. Generated Results

The software will calculate in the background the FRET ratio and normalized ligand values for each sample in the selected folder, and generate the following:

1. A folder with results for each image (or stack) in the folder, including the following figures and files:
 - Single '.fig' Matlab figures showing the resulting Donor (D), Acceptor Emission due to FRET (F), directly Excited Acceptor (A), and Ligand (L) signals, as well as the corrected FRET derived intensity I_F^f and the normalized ligand intensity. For 3D stacks, a sample is taken from the middle slice. An example is shown in Fig. 3.17-A for a donor intensity figure.
 - A '.fig' Matlab figure showing the FRET ratio as a color coded image. For 3D stacks, a sample is taken from the middle slice. An example is shown in Fig. 3.17-B.
 - For three-dimensional data (stacks), a file containing the FRET results as a '.tiff' stack that can be further analyzed in external software such as ImageJ. Warning: the FRET values are scaled to an 8-bit grayscale (0-255).
 - For three-dimensional data (stacks), a '.fig' Matlab figure showing a maximum intensity projection of the FRET values to provide a quick way of detecting mayor changes in FRET among different stacks. An example is shown in Fig. 3.17-C.
 - A '.fig' Matlab figure with a scatterplot of correlating the normalized ligand with the corresponding FRET value, for all the pixels included in the analysis, as explained in Section 3.3.6. The scatterplot shown in Fig. 3.12 was generated in this way.

- A .mat file containing the raw and processed data for that sample, including the resulting corrected FRET derived intensity I_F^f , and normalized ligand, as data matrices, the resulting single and combined masks used, in case they need to be inspected, as well as all the parameters and variables used. Also, a results dataset variable with columns containing the results for all the pixels for donor, acceptor, directly excited acceptor, ligand, corrected FRET intensity, and normalized ligand values. Furthermore, a dataset variable resultsstats that contains basic statistical results for that sample, such as mean, standard deviation, standard error, range, etc.

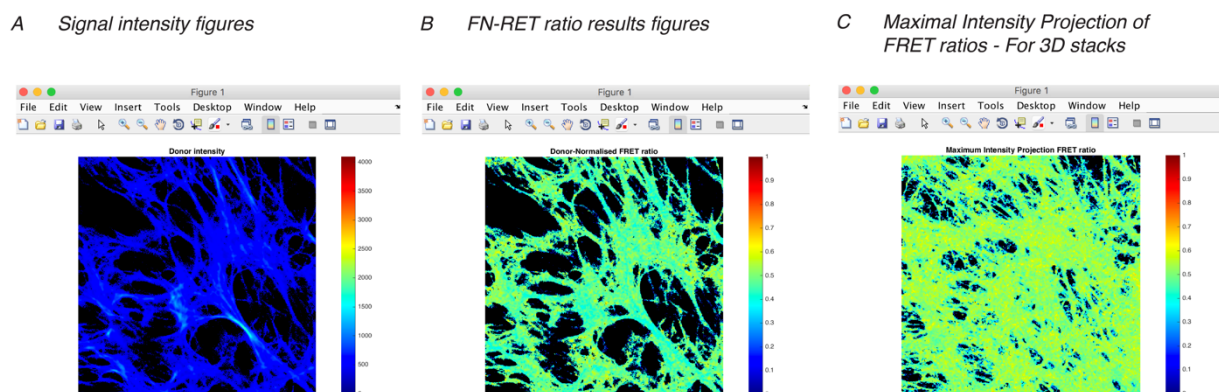


Figure 3.17. Resulting figure files produced by the FRET Matlab GUI for each sample included in a group.

- Global results for the dataset contained within the chosen folder (for that experimental condition):
 - A '.fig' Matlab figure showing the probability distribution histograms for the FRET ratio results of each sample within the folder. An example is shown in Fig. 3.18-A.
 - A '.fig' Matlab figure showing the global probability distribution histogram for the FRET ratio results of the whole dataset (pooling all the data points from all the samples contained in the folder). This is useful to grossly compare the data with that of other experimental conditions (analyzed separately). An example is shown in Fig. 3.18-B.
 - A '.fig' Matlab figure showing a scatterplot of the mean normalized ligand vs mean FRET ratio of each sample in the folder. An example is shown in Fig.3.18-C.
 - A results.mat file containing the most important global results: a pool dataset variable containing the basic statistical results for each of the samples in the folder (mean, standard deviation, standard error, range, etc.), which can be used to produce boxplots and used with other built-in Matlab functions, and the results for FRET ratios and normalized ligand as pooled pixel data of all the samples analyzed.
 - A final.mat file containing all the final results obtained, including pooled data of all the samples that can be used to plot directly histograms of both FRET ratio, and normalized ligand results.
 - For the β, γ and δ factor calculation, a '.fig' Matlab figure containing a scatterplot that can be used with Matlab's built in Basic Data Fitting Toolbox to obtain the linear fit equation, and thereby the slope of the fit, which is the β, γ or δ factor, depending on the plotted graph, as described in Section 3.3.4. An example is shown in Fig. 3.19.

- A FN-FRET Probability density histogram for each sample within a groups B Pooled results data groups (results from three conditions shown) C Ligand vs. FN-FRET - Grouped Results (results from three conditions shown)

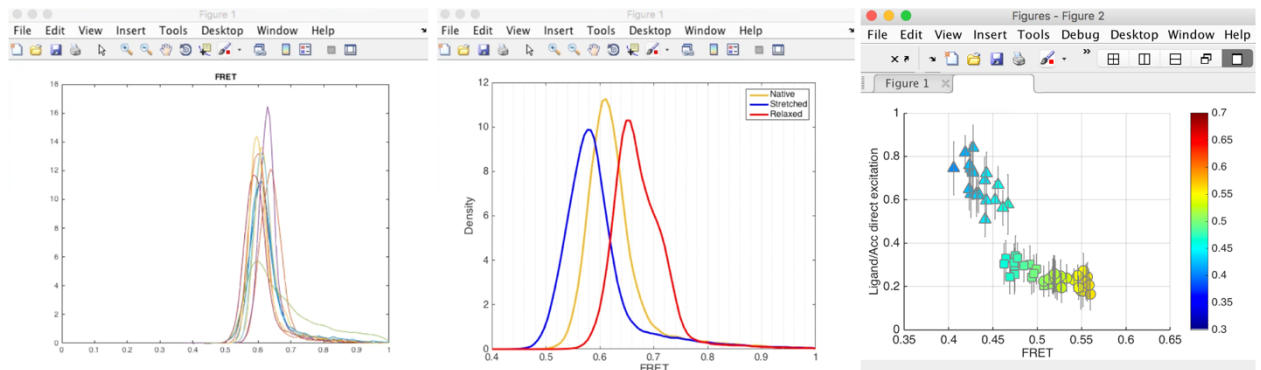


Figure 3.18. Resulting figure files produced by the FRET Matlab GUI for an analyzed group.

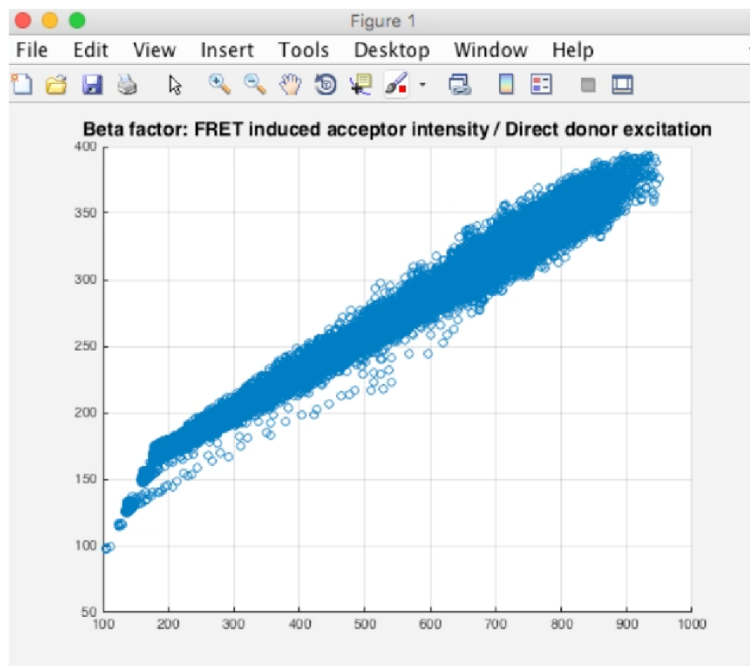


Figure 3.19. Example scatter plot generated for the determination of the β , γ and δ factors.

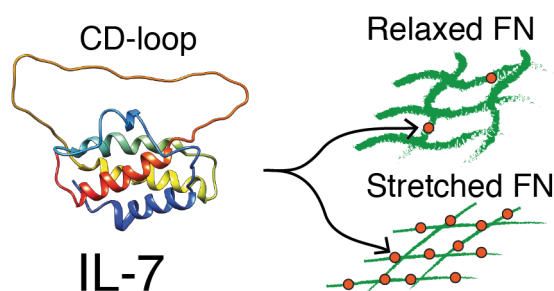
3. Mechanical stretching of fibronectin fibers upregulates binding of interleukin-7.

The work presented in this chapter has been submitted and accepted to the Journal *Nano Letters*. It is here reprinted with permission from: **Mechanical stretching of fibronectin fibers upregulates binding of interleukin-7.** Daniela Ortiz Franyuti, Maria Mitsi, and Viola Vogel. *Nano Letters* **Just Accepted Manuscript**. DOI: 10.1021/acs.nanolett.7b01617 Publication Date (Web): August 28, 2017. **Copyright © 2017 American Chemical Society**

Author Contributions

D.O.F and M.M. planned the experiments. D.O.F. performed the experiments, wrote the code to analyze the data, and produced the structural models and sequence alignments. D.O.F, M.M. and V.V analyzed the data, discussed them, and wrote the paper. All authors have given approval to the final version of the manuscript.

3.1. Abstract



Since evidence is rising that extracellular matrix (ECM) fibers might serve as reservoirs for growth factors and cytokines, we investigated the interaction between fibronectin (FN) and interleukin-7 (IL-7), a cytokine of immunological significance and a target of several immunotherapies. By employing a FN fiber stretch assay and Förster resonance energy transfer (FRET) confocal microscopy, we found that stretching of FN fibers increased IL-7 binding. We localized the FN binding site on the CD-loop of IL-7, since a synthetic CD-loop peptide also bound stronger to stretched than to relaxed FN fibers. Based on a structural model, we propose that the CD-loop can bind to FN, while IL-7 is bound to its cognate cell surface receptors. Sequence alignment with bacterial adhesins, which also bind the FN N-terminus, suggests that a conserved motif on the CD-loop ($_{110}$ TKSLEEN $_{116}$ and the truncated $_{112}$ SLEE $_{115}$ in human and mouse IL-7 respectively) might bind to the second FN type I module (FnI $_2$), and that additional epitopes enhance the stretch-upregulated binding. FN fiber stretching might thus serve as a mechano-regulated mechanism to locally concentrate IL-7 in an ECM-bound state, thereby upregulating the potency of IL-7 signaling. A feedback model mechanism is proposed that could explain the well known, but poorly understood, function of IL-7 in ECM homeostasis. Understanding how local IL-7 availability and signaling might be modulated by the tensional state of the ECM niche, and is adjusted by residing stroma cells, is highly relevant for basic science but also for advancing IL-7 based immunotherapies.

3.2. Introduction

Interleukin-7 (IL-7) is a 17.4 kDa cytokine belonging to the γ -c interleukin family, which plays a crucial role in the development of B- and T-cells in the thymus¹⁴¹, and in the survival, proliferation and differentiation of naive and memory T-cells in secondary lymphoid organs such as the lymph nodes⁴⁻⁸. IL-7 is produced by stromal cells, acts as a short-range signal for common lymphoid progenitor cell differentiation¹⁴² and enhances lymphatic endothelial cell activity *in vitro* and lymphangiogenesis *in vivo*, as well as lymphatic drainage¹⁰, and the reconstruction and remodeling of the lymph node¹¹. IL-7 has also been implicated in other cell functions, such as the development of dendritic cells, natural killer cells and lymphoid tissue inducer cells¹, and it has been shown to inhibit osteoclastogenesis from bone marrow cultures and monocytes^{143,144}.

Because of the immune-boosting properties of IL-7, there are currently several clinical trials underway which test the use of recombinant human IL-7 (rhIL-7) in immunotherapies against several diseases such as HIV, cancer, lymphocytopenia, chronic viral infections, hepatitis B and C, and congenital immunodeficiency¹, as well as to boost the immune system of older subjects who have had chemotherapy with human IL-7 vaccines¹⁴⁵.

Conversely, blocking the IL-7 signaling pathway by means of antibodies against IL-7, or its receptor IL7RA, is currently being investigated to treat diseases with an over-reactive immune response, such as multiple sclerosis, type 1 diabetes, rheumatoid arthritis, Sjögren's syndrome, inflammatory bowel disease and systemic lupus erythematosus^{1,9}. Increasing the efficacy of such treatments requires knowledge of the factors that control local IL-7 availability; this is especially important because IL-7 concentration *in vivo* is very small (10–40 pg/ml in plasma, and 15–35 pg/mL in lymph)^{10,11} and many cells, such as T-cells^{89,146,147}, B-cells, thymocytes⁸⁴, and stromal cells like lymphatic endothelial cells¹⁰ depend on and compete for it.

This tight competition suggests the existence of mechanisms that might enhance the local concentration and regulate the bioavailability of IL-7¹². Mechanically regulated sequestration and release of IL-7 could be one possibility, but this idea has never been tested. In clinical studies where rhIL-7 was administered, it was shown that although the measured half-life of IL-7 is at the range of hours (6–23 hours), the biological effects persisted for days, and in some studies, even for several weeks¹. Such long-lasting effects could result from long-term cell memory achieved through the secretion of micro-RNA¹⁴⁸; additionally, it was proposed that a combination of IL-7 binding to the extracellular matrix (ECM) (followed by slow release), and downstream changes in cell proliferation and survival that persist beyond the initial IL-7 stimulation might also contribute¹. Indeed, a few studies showed interactions between IL-7 and ECM components, such as glycosaminoglycans, collagen type IV, laminin and FN^{18,149,150}. Recombinant human IL-7 was reported to bind to ECM or surface-bound FN with IC₅₀ values of 10–100 nM¹⁸, and ECM-bound IL-7 was found to be significantly more potent than soluble IL-7 with respect to its pro-adhesive activity on T-cells¹⁸. It is therefore crucial for both basic immunological research, as well as for clinical studies, to understand how the local IL-7 availability is modulated not only by cellular production and consumption, but also by interactions with the ECM. In contrast to other cytokines such as IL-2, IL-7 is a prototypical homeostatic cytokine that provides continuous signals to resting naïve and memory T cells, but it does not activate T-cells¹. However, how it can provide for continuous signaling if available only at such low concentrations remains elusive.

FN is one of the major fibrillar components of ECM and contains many binding sites for other ECM proteins and carbohydrates (including self-association sites), cell-ECM binding proteins such as integrins^{151,152}, and other cytokines and growth factors such as tumor necrosis factor α (TNF- α)⁴³, members of the platelet-derived growth factor (PDGF) and fibroblast growth factor (FGF) families, several vascular endothelial

growth factors (VEGFs), transforming growth factor β 1 (TGF- β 1)¹⁵³ and the latent complex of TGF- β 1^{23,68,69,154,155}. Most importantly for this work, IL-7 has been shown to bind 3-4 fold stronger to substrate-adsorbed FN than to bovine serum albumin or hemoglobin¹⁸, and interacts with the FN N-terminus¹⁸. Its therein reported binding kinetics and its binding to albumin suggest that it interacts with proteins also via hydrophobic interactions. Several of the binding sites on FN have been shown already to be either cryptic or mechanosensitive, i.e., opening up or destroyed upon mechanical stretching/unfolding of FN, respectively^{17,25,47,109,139,156-158}. Unfolding and refolding of FN can be mediated by the application of cell traction forces or by proteolytic cleavage due to responses to inflammation, respectively. Alterations in the tensional state of ECM fibers are expected to result in extensive ECM and tissue remodeling, including at sites that are immunologically active, such as the lymph nodes^{13-15,58,111,113,159}. It is therefore important to understand how such changes in the tensional state of ECM fibers may affect binding, and consequently, the local availability and signaling activity of cytokines. Although binding studies of signaling molecules to fibrillar ECM have been performed, these have mostly focused on chemokines and growth factors relevant to stromal cells^{23,24,64,160}, while cytokines that have a more specific homeostatic function on immunological cells, such as IL-7, have found far less attention in the ECM community.

Previous IL-7 binding studies to FN have been performed with FN in solution or adsorbed to a rigid substrate^{18,149,150}. Since it is known that fibrillar FN has different structural and functional properties than FN in solution or substrate-adsorbed FN^{58,65,138,139,161}, we conducted our IL-7 binding studies on fibrillar FN, which constitutes a more physiologically relevant platform than surface-adsorbed or soluble FN. Indeed, previous studies have shown that FN molecules in FN fibers stretched from 0 to 400% display a range of conformations also observed in FN fibrils in native ECM produced by fibroblasts in cell culture⁶⁵. Using this platform, we investigated whether the binding affinity of IL-7 to FN fibers is altered when these get stretched. Our goal was to explore whether the tensional state of ECM fibrils can regulate the bioavailability of this immunologically relevant cytokine.

3.3. Stretching of FN fibers increases IL-7 binding.

To investigate IL-7 binding to fibrillar FN and how it is affected by the tensional state of FN fibers, we employed a stretch binding assay developed earlier in our lab^{25,58,65}, where single FN fibers were manually pulled out of a solution of FN isolated from human plasma and deposited on a stretchable silicone sheet, which was mounted on a uniaxial stretching device to control the strain of the deposited fibers (Fig. 4.1A). To avoid intermolecular FRET, the pulled FN fibers contained only 5% of FRET-labeled FN (FN-FRET) to assess the level of FN stretching at the molecular level. To exploit FN-FRET as a nanoscale strain sensor, where the FRET ratio decreases upon fiber stretching^{58,65,138}, the molecule was labeled with multiple donors and acceptors to cover a large range of conformational changes. Lysine residues on FN were randomly labeled with donor fluorophores (Alexa 488, A488), and the cysteines on FN modules Fnl₇ and FNI₁₅ were labeled with acceptor fluorophores (Alexa 546, A546). For every FN-FRET batch, we confirmed in a control experiment that changes in FN-FRET ratios occur upon chemical denaturation of FN (Supplementary Fig. S1). Since forces in the μ N-range are required to pull the fibers out of the droplet, and the fibers have to be kept under tension as they are deposited on the silicone substrate, they are typically pre-strained to approximately 140%¹³⁹ (Fig. 4.1A). This has been previously estimated by depositing manually pulled FN fibers across microfabricated trenches on a stretchable PDMS (Polydimethylsiloxane) sheet, which was pre-strained. The PDMS sheet was then slowly relaxed until the FN fibers began to sag. The PDMS strain at which 50% of the fibers were no longer straight and mechanical tension was absent, approximately correlated with a normalized FN fiber strain of 0%¹³⁹. It has also been previously shown that no slipping among FN molecules occurs upon force application, since when the applied tensile force was released,

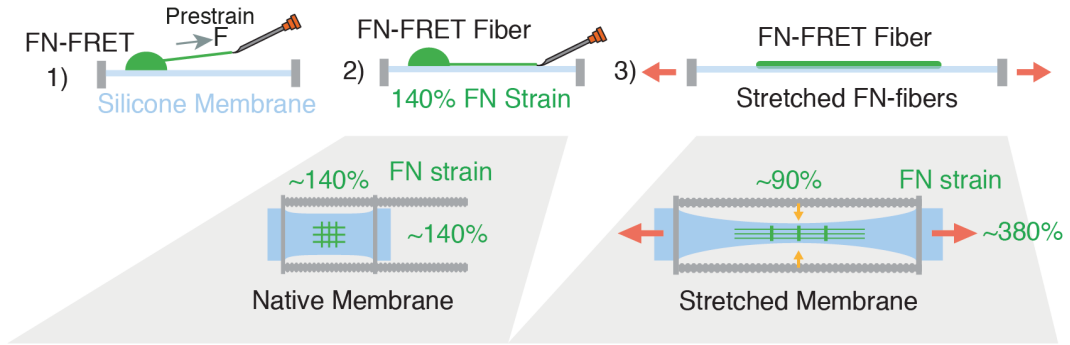
the FN fibers contracted and returned to their initial extension and recovered their mechanical properties¹³⁹. Also the initial FRET ratios were recovered⁵⁸.

To observe in one image how FN fiber straining versus relaxation affects IL-7 binding, we first deposited FN fibers in a grid configuration (native silicone membrane = 140% FN fiber strain), and then stretched the membrane along the principle axis (stretched silicone membrane = 380% FN fiber strain), which leads to a relaxation of the FN fibers deposited in the transverse direction (20% FN fiber strain) (Fig. 4.1A). Following incubation of the fiber grids with recombinant human IL-7 randomly labeled on lysines with Alexa 647 (A647-IL-7), the samples were visualized by confocal microscopy. IL-7 binding was assessed by pixel-by-pixel quantification of the A647-IL-7 fluorescence intensity over the directly excited acceptor A546-FN intensity to normalize for the FN content (Fig.4.1 and Supplementary Figs. S4.4 and S4.6). Corrections to ensure that the donor and acceptor intensities were solely due to FN-FRET were performed as previously described^{59,130,135}. A detailed description of the method, including details on image acquisition parameters, microscopy controls, and data processing for adequate image registration can be found in the Supporting Material (Materials and Methods, Supplementary Fig. S4.2 and S4.3).

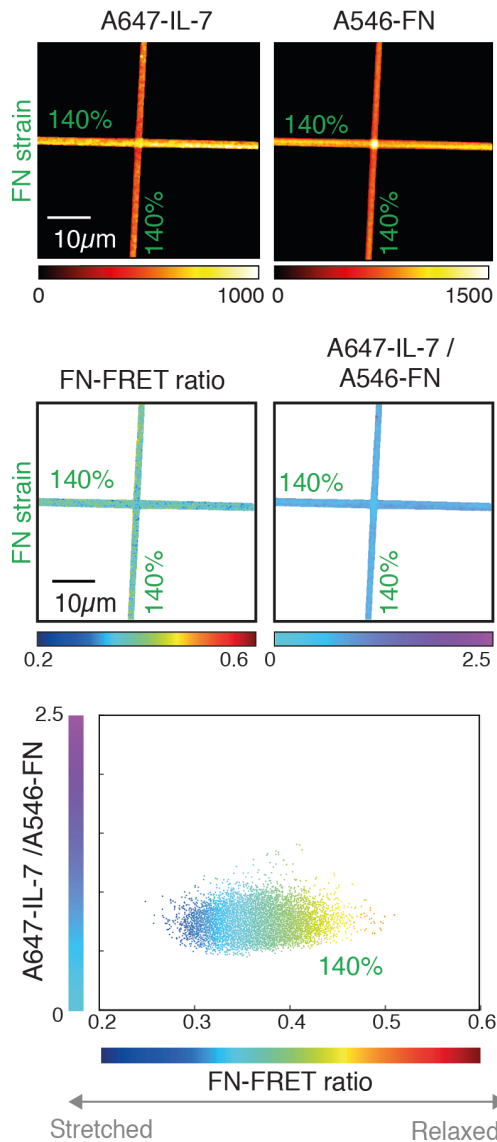
The resulting images (Fig. 4.1B) clearly show that IL-7 binding to highly stretched FN fibers (380%) is significantly higher than that to the more relaxed fibers strained to 140% and 20%. The signal enhancement was even more pronounced upon normalization of the IL-7 signal (A647-IL7/A546-FN ratios), which was performed to correct for the stretching-induced reduction in the distances between specific binding sites on FN molecules (Fig. 4.1B–C). Scatter plots of the constituent pixels for the fibers are given in Fig. 4.1C, with each strain showing a distinct pixel population, corresponding to the range of conformations that coexist in single FN fibers. Data from several fiber intersections are shown in Supplementary Fig. S4.5, confirming the consistency of the results.

To increase statistical significance, we then tested FN-FRET fibers only deposited in one direction and strained to 20%, 140%, and 380%, respectively. In contrast to the grid configuration, these FN fibers are free from shear due to physical contact at the cross-section with perpendicular fibers. We analyzed 20 fibers per strain, and confirmed that human IL-7 binding increased with increasing FN stretching (representative results are shown in Supplementary Fig. S4.6). A scatter plot of FN-FRET versus normalized IL-7 binding for each pixel is shown in Fig. 2A, along with mean values for each fiber (Fig. 4.2A; circles for 20% strain, squares for 140% strain, and triangles for 380% strain). We found statistically significant increases in IL-7 binding to fibers, from 20%, 140% to 380% strain ($p < 0.001$; Fig. 4.2A), i.e., in a range of strains typically seen in the ECM of fibroblasts in cell culture^{60,65}. Moving mean values of IL-7 binding (red curve) and their corresponding estimated standard deviation (orange curves) were thereby calculated by pooling pixels in bins of 6×10^{-3} FRET units. The values considered for the calculation of the curves were limited to the range from the 25th percentile of the lowest FRET value group (relaxed membranes) to the 75th percentile of the highest FRET value group (stretched membranes), where the data density remained sufficiently high. Box plots of fiber mean values for FRET and normalized IL-7 binding for all 20 fibers per strain are shown along with the single pixel values for the whole data set, and normalized histograms showing the underlying data distributions generated by pooling all the pixels per strain are shown next to the corresponding axes of the scatter plots. Statistical significance between groups was assessed by the non-parametric two-sided Wilcoxon rank sum test, which does not imply data distribution normality (since not all the groups showed a distinct normal distribution). Similar results were obtained in a replicate experiment and a control experiment with A488-labeled IL-7 and unlabeled FN (Supplementary Figs. S4.7-S4.8), verifying that the data reflect the intrinsic IL-7/FN interactions and are not driven by the fluorophores. In similar experiments performed with A647 labeled recombinant murine IL-7 (A647-rmIL7), we confirmed that murine IL-7 shows a rather similar binding behavior to FN fibers, although the FN fibers need to be more stretched to upregulate murine IL-7 binding (Supplementary Fig. S4.9-S4.10).

A FN-FRET fiber grids exposed to various levels of strain.



B IL-7 binding to unstretched membranes



C IL-7 binding to stretched membranes

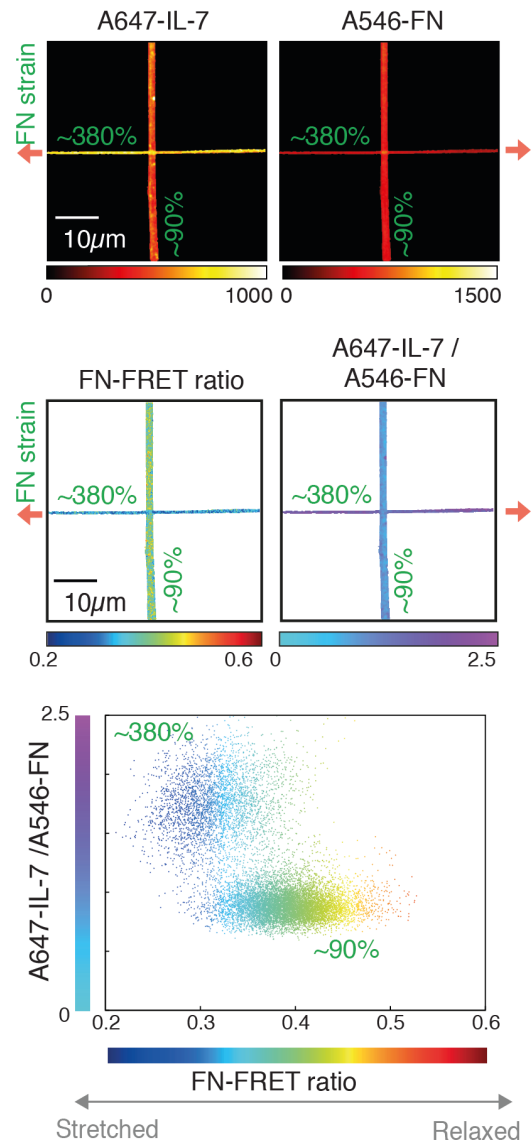
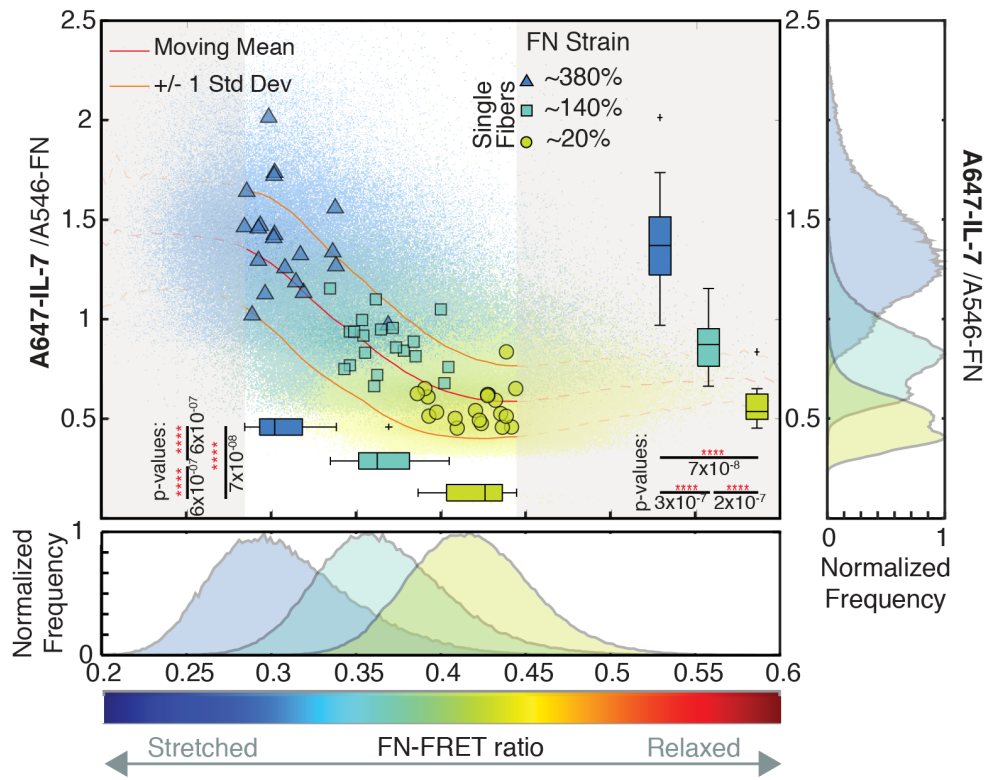


Figure 4.1. Human IL-7 binds more strongly to stretched than to relaxed FN. (A) FN fibers were manually pulled out of a droplet of FN in solution containing 5% FN-FRET, and deposited in a grid configuration on a stretchable silicone sheet, with 10 fibers deposited parallel to the stretch axis and 10 fibers perpendicular to it. The deposited FN fibers were deposited pre-stained to 140% due to the process of manually pulling them out of solution. The silicone membranes were either left as mounted with FN fibers

pre-strained to ~140% (native membrane), stretched to obtain FN strains of ~380% axially and ~90% perpendicularly, or relaxed to obtain FN strains of ~20% axially and ~219% perpendicularly (only the native and stretched membranes are depicted here). (B-C) Binding assays with FRET-labeled FN, and A647-labeled IL-7 were performed on the FN fiber grids. Representative confocal images of grid intersections between one parallel and one perpendicular fiber are shown for native membranes (B) and stretched membranes (C), showing A647-IL-7 (excitation at 647 nm) and A546-FN (directly excited acceptors to determine local FN content) intensities. The corresponding results for normalized IL-7 intensity (A647-IL-7/A546-FN) show equal levels of binding among FN fibers on grids not subjected to further stretching (140% FN-fiber strain). Conversely, grids on stretched membranes with final FN-FRET fiber strains of 90% and 380% show enhanced IL-7 binding to stretched FN-FRET fibers (380% FN-fiber strain) vs. FN-FRET fibers with reduced strain due to perpendicular compression of the membranes (90% FN-fiber strain). Decreased FN-FRET ratios correspond to increased donor and acceptor distances due to the stretching of the fibers. IL-7 binding versus FN-FRET data are shown in pixel-by-pixel scatter plots, whereby one population of binding ratios is seen on the unstretched silicone membranes; fibers on stretched grids show two distinct populations for stretched FN fibers (380% strain) versus more relaxed FN fibers (90% strain), respectively.

A Human IL-7 binding to FN fibers



B Human IL-7 CD-loop peptide binding to fibronectin fibers

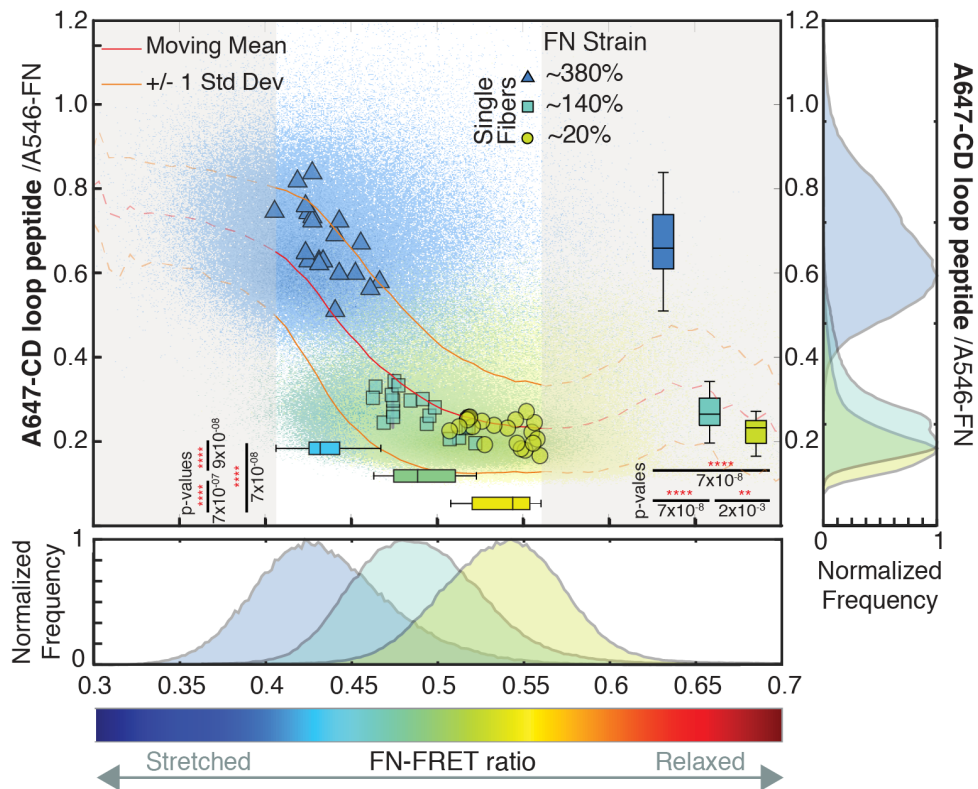


Figure 4.2. Human IL-7 and the synthesized CD-loop peptide from human IL-7 show increased binding to stretched FN-FRET fibers. Binding assays with human A647-IL-7 (A) and a synthesized CD-

loop peptide (B) were performed in a set of 20 independent FN-FRET fibers deposited on silicone membranes, which were either stretched, left in their native state, or relaxed, resulting in fiber strains of ~380%, ~140% and ~20%, respectively. Mean values for each fiber (triangles for ~380% strain, squares for ~140% strain and circles for ~20% strain) are shown along with pixel-by-pixel scatter plots of FRET ratios vs. normalized IL-7 intensities from all the pixels from all samples. From these pooled pixel-by-pixel data, moving mean curves were generated along the x-axis (FRET) with a bin of 6×10^{-3} FRET units (red curves), and their standard deviations were estimated (orange curves). To analyze the binding behavior, we limited these curves to a section between the upper and lower percentiles (25th and 75th of mean FRET values of single fibers (FRET box plots)). Box plots of the mean values for single fibers, as well as normalized histograms of all pixels are shown for both FN-FRET and normalized IL-7 binding. We found statistically significant differences between human A647-IL-7 binding to fibers at 20%, 140%, and 380% strain ($p < 0.001$). A647-CD loop peptide binding to fibers at 20%, 140%, and 380% strain also showed statistically significant differences, although the difference in binding between 20% and 140% was less marked than that observed for human A647-IL7 binding ($p < 0.005$). These results show increased binding of human IL-7 and the CD-loop peptide to FN fibers as they become stretched to strains of 20%, 140% and 380%, respectively.

3.4. The CD loop of IL-7 binds preferentially to more stretched FN fibers and is likely to mediate IL-7/FN binding.

Since the IL-7 epitope (or epitopes) recognizing FN has not yet been determined, we searched for clues on its structure, as shown in Fig. 3A. IL-7 consists of four alpha-helices (A–D) stacked in an up-up-down-down manner, bound by three major connecting loops (AB, BC, and CD) and a mini-alpha-helix located along the loop A–B⁷⁰. Since the CD loop has not been resolved in the crystallographic data⁷⁰, we used the modeling tool Modeller⁷² within the molecular imaging package UCSF Chimera⁴², to add the unstructured CD loop to the structure of IL-7 (Fig. 4.3A). Interestingly, an earlier study has shown that deletion of the CD loop (identified there as a 19 amino acid sequence) does not interfere with binding of IL-7 to its cell surface receptors and the subsequent signaling activity⁷¹. This raises the interesting possibility that while IL-7 is engaged in interactions with its receptors, the CD-loop may be free to participate in interactions with other molecules such as FN. Indeed, adding our model with the inserted CD-loop, to a model of IL-7 bound to its cognate cell surface receptors⁸, also using Modeller, supports this hypothesis. The CD loop does not seem to interfere with binding of IL-7 to its cell receptors, and appears to be relatively free for interaction with additional molecules, such as FN (Fig. 4.3B). A 3D structural model of human IL7RA/IL2RG/IL7 with the inserted CD loop and a corresponding video are provided in the Supportive Information.

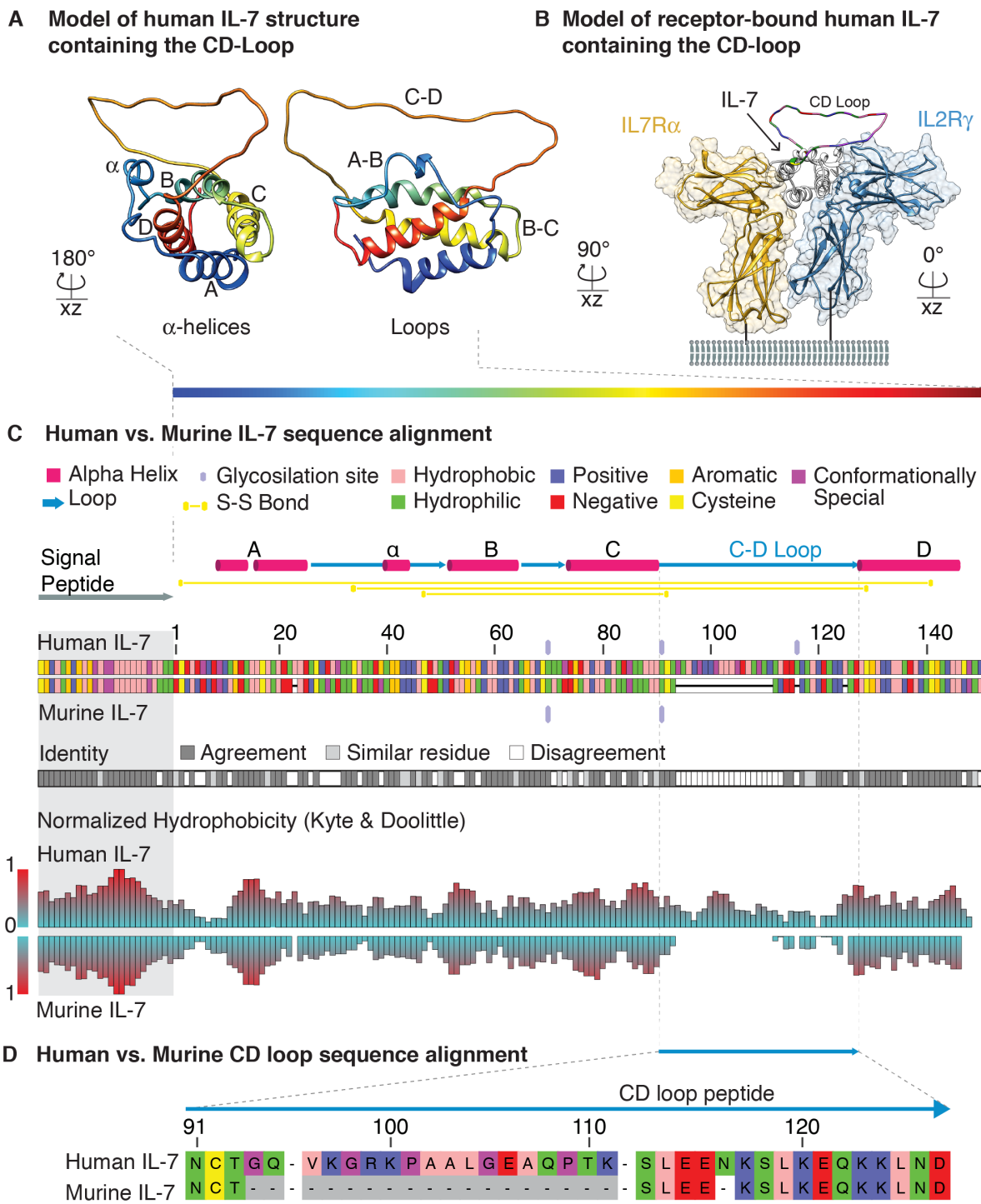


Figure 4.3. Sequence alignment and structural analysis of the IL-7 CD loop to identify potential FN binding epitopes. (A) Model of the structure of human IL-7 (PDB number: P13232) with the CD loop inserted using the molecular imaging package Chimera. The IL-7 structure is shown in two different orientations to highlight the loop running parallel to the helical bundles of IL-7. (B) Model of the receptor-bound (IL7RA and IL2RG receptors) IL-7 based on a published model^{6,70}, with the IL-7 CD loop modeled into the structure. In this orientation, the loop does not appear to be involved in the interactions between IL-7 and its receptors, and is potentially available to interact with FN. (C) Sequence alignment between human (PDB number: P13232) and murine (PDB number: P10168) IL-7 shows the CD loop to be the most

distinctive difference between the two homologs, with a similar hydrophobicity profile for the rest of the sequences. (D) Sequence alignment between the CD loop of human and murine IL-7 (as in Goodwin et al.⁷¹) highlighting the conserved as well as missing amino acid sequences between the two homologs. The sequence alignment and analysis was performed with the Matlab, Geneious, and Unipro UGENE software packages.

In our search to determine whether the CD loop could potentially mediate specific interactions between IL-7 and FN, we first evaluated the level of sequence conservation among different species. Sequence alignment between human and murine IL-7 (Fig. 4.3C), including a comparison of the hydrophobicity of the two protein homologs showed no marked differences (Fig. 4.3C), suggesting overall structural similarity, except in the CD loop region, where the CD loop of murine IL-7 is much shorter than that of human IL-7 (18 vs. 37 amino acids respectively, leading to a length of ~6.5 nm vs. ~14 nm, respectively), with the common region of the CD-loop remaining highly conserved between human and murine IL-7 (Fig. 4.3C). Among the 18 amino acids missing in the CD loop of murine IL-7, there are several positively charged residues, a row of 5 hydrophobic residues, and the N-glycosylation site at position 141 (Fig. 4.3D).

To evaluate whether the CD-loop is involved in the stretch-enhanced binding of IL-7 to FN fibers, we directly tested the binding of a synthetic CD loop peptide to differently stretched FN fibers. A 36 amino acid-long peptide with the sequence of the human CD-loop ($_{91}$ NCTGQVKGRKPAALGEAQPTKSLEENKSLKEQK $_{127}$ LND $_{127}$) was synthesized, labeled on the first cysteine (underlined) with Alexa Fluor-647, and used for binding experiments with manually pulled FN fibers at three different strains, 20%, 140%, and 380%, with 20 fibers per strain (Supporting Material: Materials and Methods). Similar to full-length IL-7, we found that the human CD loop peptide indeed bound to FN fibers in a stretch-enhanced manner (Fig. 4.2B). Although the differences between binding to fibers experiencing 20% and 140% strain were not as marked as those observed with full-length IL-7, they were statistically significant, and therefore consistent with the hypothesis that the CD-loop mediates IL-7 binding to FN.

3.5. Sequence alignment between the CD-loop peptide and bacterial adhesins that also target the FN N-terminus.

Since various bacterial adhesins also target the N-terminal Fnl modules^{25,39,44-47}, as does IL-7¹⁸, we aligned the sequence of the CD-loop with those of the bacterial peptides (Fig. 4.4). The bacterial adhesins bind to the N-terminus of FN through the formation of antiparallel β -strands with each of the Fnl₂₋₅ modules^{25,39,44-47} (Fig. 4.4). Since the IL-7 binding site on FN has not been determined, we asked whether sequence homology exists between the CD loop peptide and the bacterial adhesins⁴⁷. The sequence alignment revealed significant homology between the double negatively-charged $_{110}$ TKSLEEN $_{116}$ motif on the CD-loop peptide of human IL-7 or the truncated $_{112}$ SLEE $_{115}$ motif of mouse IL-7, and the bacterial β -strands that bind to Fnl₂ (Fig. 4.4). Less, but still remarkable homology is seen between the mostly hydrophobic $_{101}$ PAALGEA $_{107}$ motif on the human CD-loop peptide, and the bacterial β -strand that bind to the Fnl₃ module (Figs. 4.3 and 4.4). These two CD-loop peptide fragments are connected by a two amino acid-long linker ($_{108}$ QP $_{109}$). The peptide fragment containing amino acids 101–116 is flanked on both termini by highly charged residues ($_{96}$ VKGRK $_{100}$ and $_{117}$ KSLKEQK $_{127}$ LND $_{127}$), both of which have some homology with the loop regions of the respective bacterial adhesins that connect the β -strand forming sequences, but do not themselves bind to Fnl modules. The $_{101}$ PAALGEA $_{107}$, as well as the highly charged $_{96}$ VKGRK $_{100}$ motifs,

however, are missing in the CD-loop of mouse IL-7, yet binding of mouse IL-7 is also upregulated to stretched FN fibers (Supplementary Fig. S4.9 and S4.10). Taken together with the fact that the human CD-loop peptide itself can recapitulate the FN binding behavior of full-length human and mouse IL-7, we propose that the CD-loop fragment $_{110}\text{TKSLEEN}_{116}$ might be the primary epitope of IL-7 that binds to FN, and particularly, to module FnI_2 .

Sequence alignment of bacterial peptides and human/murine IL-7 CD-loop

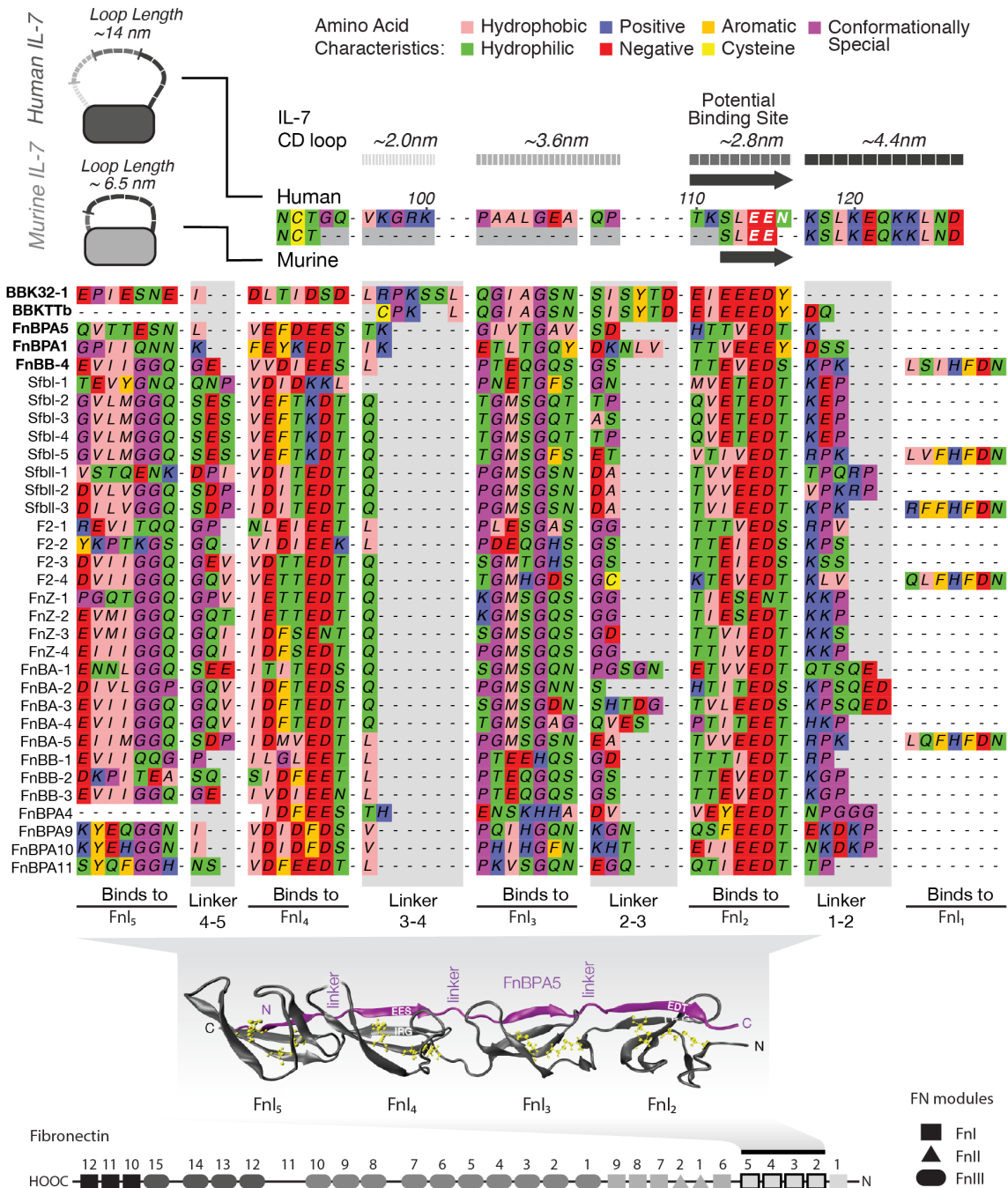


Figure 4.4. Sequence alignment reveals similarities between FN-binding bacterial adhesins and CD-loop peptide from IL-7. Human and murine IL-7 CD-loop alignment with bacterial peptides that bind to the N-terminus of FN shows significant homology between the doubly negatively-charged $_{110}\text{TKSLEEN}_{116}$

*motif on the CD-loop peptide from human IL-7, and the $_{112}$ SLEE $_{115}$ motif from mouse IL-7, with the bacterial β -strands that bind to the Fnl $_2$ module. The mostly hydrophobic $_{101}$ PAALGEA $_{107}$ motif (missing in the murine CD-loop) shows also some homology with the bacterial β -strand that binds to the Fnl $_3$ module. Other motifs with highly charged residues ($_{96}$ VKGRK $_{100}$ and $_{117}$ KSLKEQKLLND $_{127}$) show some homology with the loop regions of bacterial adhesins that connect β -strand forming sequences. These sequence homologies, together with the fact that the human CD-loop peptide itself can recapitulate the FN binding behavior of full length human and mouse IL-7, suggest that the $_{110}$ TKSLEEN $_{116}$ motif might be the primary epitope of IL-7 that binds to FN. Adapted with permission, from⁴⁷: Hertig, S.; Chabria, M.; Vogel, V. *Nano Letters* **2012**, 5162–5168. Copyright 2012 American Chemical Society.*

FN fiber strain increases IL-7 and CD-loop binding (Fig. 4.2), whereas it decreases the binding of certain bacterial peptides, as stretching of FN fibers destroys the structural match between those bacterial peptides and the stretched Fnl $_{2-5}$ segment^{25,47}. Since Fnl modules contain two disulfide bonds each, their secondary structure remains mostly intact upon stretching; however, the distance between these modules increases, mostly by stretching the linker regions between two Fnl modules^{25,47}. In contrast, the short CD-loop peptide $_{110}$ TKSLEEN $_{116}$ can only bind to one Fnl module, possibly to Fnl $_2$, as suggested by its homology to the bacterial peptides. Enhanced CD-loop peptide binding to stretched FN suggests that additional interactions stabilize IL-7 on stretched FN, for example interactions with hydrophobic residues or otherwise cryptic sites, that become exposed upon FN fiber stretching^{17,67}. Additional interactions might form with the highly charged CD-loop peptide $_{117}$ KSLKEQKLLND $_{127}$, which is highly preserved between the human and murine IL-7 CD loop (Fig. 4.3), while interactions with other parts of the protein cannot be excluded. We envision that the novel structural insights provided by our findings will motivate further studies to define the interacting epitopes between IL-7 and FN.

3.6. Model of how the tensional state of FN fibers might alter IL-7 signaling.

IL-7, which is secreted by stromal cells at very low concentrations^{10,11,103,104}, does not lead to T-cell activation but is known to provide continuous signals to resting naïve and memory T cells¹. How IL-7 can mediate a homeostasis keeper function at such low cytokine concentrations (10–40 pg/ml in plasma and 15–35 pg/mL in lymph^{10,11}) remains unknown. Bringing our findings that IL-7 is modulated by ECM tension together with existing literature, we propose the following mechanism of how the tensional state of FN fibers might alter IL-7 signaling to maintain ECM homeostasis (Fig. 4.5). Enhanced binding of IL-7 to stretched fibers (Figs. 4.1–4.2), might increase its local fiber-bound availability and potency, as suggested by studies showing ECM-bound IL-7 to be more potent than soluble IL-7 in promoting T-cell adhesion¹⁸. Consequently, IL-7 stimulation may cause changes in paracrine signaling, cell traction forces and/or ECM/cell interface, which vice versa might cause the FN fibers to relax: for example, it is known that IL-7 downregulates the expression of collagen I and FN in human subconjunctival fibroblasts¹²¹, increases the expression and activation of $\alpha 4\beta 7$ integrins in naïve T-cells¹¹⁵, increases the expression of integrin $\alpha 5\beta 1$ in lymphatic endothelial cells (LECs)¹⁰, activates $\alpha 4\beta 1$ integrins in murine thymocytes¹⁹, downregulates the expression of α -SMA^{121,162}, and increases the production of matrix metalloproteinases (MMPs) in human articular chondrocytes¹²⁰. Thus, the consequent alterations in stromal cell contractility or matrix cleavage by MMPs might lead to a partial relaxation of FN fibers, which in turn could reduce the amount of FN-bound IL-7 and its bioavailability, affect the stromal cells, and initiate a negative feed-back loop.

A similar concept can be found in bone homeostasis, which is maintained not by tightly keeping the status quo, but by constant remodeling through bone deposition and degradation, which allows bone to adapt its strength to external stimuli. Similarly, we hypothesize that IL-7 helps stromal cells to keep a responsive homeostatic environment by gradual tensing and relaxing FN fibers and thereby tuning the bioavailability of IL-7.

Additionally, IL-7 has been shown to bind to collagen IV¹⁸, and to modify the expression of collagen I¹²¹. Since it has been shown that collagen deposition increases during tumor formation, including collagen types I, II, III, V, and IX¹⁶³⁻¹⁶⁶, changes in the IL-7/ECM homeostatic balance might contribute to the altered tissue physiology observed in cancer.

To demonstrate such concepts, further studies are required to elucidate the role of stretch-enhanced IL-7 binding to FN on diverse cellular functions, ECM remodeling, and their intertwined and mechano-regulated effects.

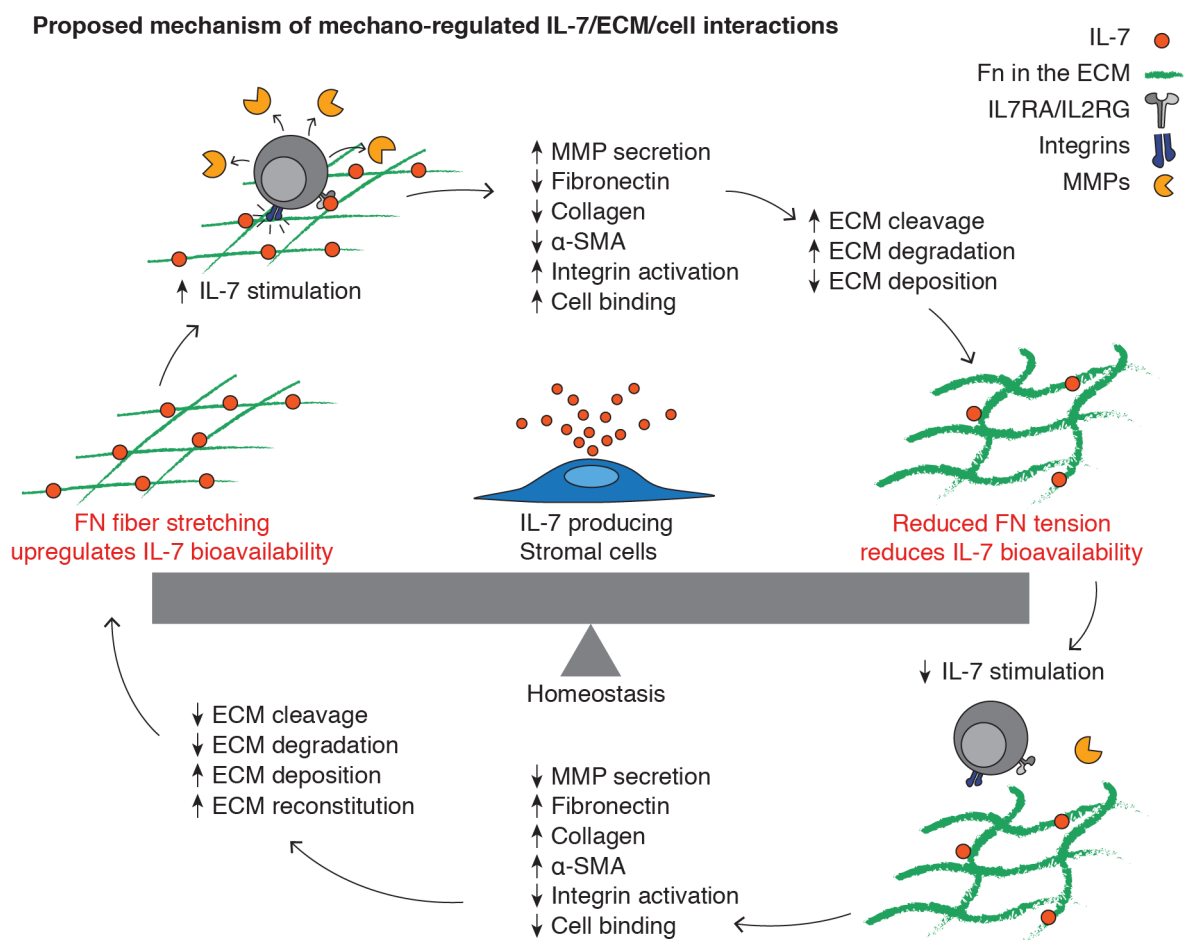


Figure 4.5. Proposed model for homeostatic regulation of ECM deposition/degradation through mechanically regulated binding of IL-7 to FN. Based on our findings and the existing literature^{10,18,19,115,120,121,162}, we propose a model whereby ECM homeostasis is balanced through a mechano-sensitive negative-feedback loop controlling the binding of IL-7 to FN in the ECM, and its effects on cellular functions, including tensional state and paracrine signaling. When FN becomes increasingly stretched by stromal cells, IL-7 binding is enhanced (as suggested by our results and highlighted in red).

ECM binding increases the local availability and bio-activity of IL-7¹⁸, and existing literature suggests that this might increase MMP production¹²⁰, reduce FN and collagen production¹²¹, increase activation of integrins^{10,19,115}, and down-regulate α -SMA expression¹²¹, which in turn regulates fibroblast contractility¹⁶². Consequently, a decrease in ECM deposition coupled with ECM cleavage and degradation might occur, thereby reducing ECM tension and relaxing the constituent FN fibers, and thus decreasing IL-7 binding (suggested by our results and highlighted in red), effectively counteracting the initial effect. Inversely, a relaxed ECM with lower binding and bio-activity of IL-7 might decrease IL-7, leading to reduced MMP secretion, integrin activation and cell binding, and increased FN, collagen, and α -SMA production, thereby reducing ECM cleavage and degradation, and increasing ECM deposition to reconstitute a matrix in a higher tensional state, which would in turn increase IL-7 binding to return to a more homeostatic state. Since it has been shown that IL-7 binds to collagen IV¹⁸, and modifies the expression of collagen I¹²¹, and several collagens, including types I, II, III, V, and IX, show increased deposition during tumor formation¹⁶³⁻¹⁶⁶, changes in the IL-7/ECM homeostatic balance might contribute to the altered tissue physiology observed in cancer.

3.7. Conclusion

We have demonstrated for the first time that the binding of a cytokine to FN fibers is regulated by fiber tension. We could show that FN fiber stretching upregulates IL-7 binding via its CD-loop (Figs. 4.1-4.2), and have suggested a structural mechanism that mediates its binding to FN (Figs. 4.3-4.4). Furthermore, we propose for the first time, a mechano-regulated feedback mechanism by which IL-7 might act as prototypical homeostatic cytokine, mediating cytokine/ECM/cell interactions via stretch enhanced IL-7 binding (Fig. 4.5). We believe that our study will motivate further investigations of nanoscale mechano-regulated mechanisms by which IL-7 and other cytokines might be stored and/or released as a result of modulating the tensional states of ECM fibers. Here we shed light into the mechano-regulation of IL-7/FN interactions and their potential effect on IL-7 bioavailability and functionality. Our proposed mechanism could be relevant for further developments on IL-7 based immunotherapies.

3.8. Supporting Information: Materials and Methods

3.8.1. FN purification.

We isolated FN from human plasma (Zürcher Blutspendedienst SRK) using gelatine-sepharose chromatography, as previously described⁵⁸. Briefly, human plasma was spun at 10,000 \times g for 15 min and the supernatant, after the addition of 2 mM phenylmethyl-sulphonyl fluoride and 10 mM EDTA, was passed through a Sepharose 4B column (Pharmacia), and subsequently through a Gelatin-Sepharose 4B column (Sigma-Aldrich). FN was eluted from the gelatin column with 1 M arginine, following three washes with 1 M NaCl, 0.5 M urea, and 0.2 M arginine respectively. FN purity was assessed by silver staining and western blotting. Isolated FN was stored at -80 °C in 1 M arginine until usage. Experiments were approved and authorized by the Swiss Federal Office for the Environment and the Swiss Federal Coordination Center for Biotechnology (Notification number A080170/2).

3.8.2. Fluorescence resonance energy transfer (FRET) labeling of FN (FN-FRET).

To label FN with FRET donor and acceptors, we followed a method previously established in our lab^{58,60,65}. Briefly, plasma FN was denatured with 4 M guanidine hydrochloride (GdnHCl) to expose otherwise buried cysteins, which were labeled with Alexa Fluor-546 (FRET acceptors) by the addition of 30 \times molar excess of Alexa Fluor-546 maleimide for 1 h at 20 °C. Labeled FN was separated from free dye using a size-

exclusion PD-10 column (Amersham) in an amine-labeling buffer (phosphate buffered saline (PBS), 0.1 M NaHCO₃, pH 8.5). Subsequently, the protein was mixed with 70× molar excess of Alexa Fluor-488 succinimidyl ester and incubated for 1 h at 20 °C to label free lysines with donors (Alexa Fluor-488). Labeled FN was separated from free dye with a PD-10 size-exclusion column in PBS. A final protein concentration of 5.4 g/l was obtained and adjusted to a working concentration of 1 g/l, and a labeling ratio of 10.5 donors and 3 acceptors per FN dimer were determined by measuring the absorbance at 280, 498, and 556 nm, using published extinction coefficients for both dyes and FN. FN-FRET was stored at –20 °C until usage. We confirmed that upon chemical denaturation with increasing GdnHCl concentrations, the ratiometric FRET signal from FN-FRET decreased, as previously described^{58,128}, confirming that FRET ratios are sensitive to changes in FN conformation (Supplementary Fig. S4.1).

3.8.3. IL-7 labeling.

Recombinant human or murine IL-7 (Peprotech) was reconstituted in 100 mM PBS, pH = 8.5, and the exposed amines were labeled with 60× molar excess Alexa Fluor-647 succinimidyl ester (Molecular Probes) dissolved in DMSO (Dimethyl sulfoxide), incubated for 2.5 h on ice, and subsequently quenched with 1.5 M hydroxylamine, pH 8.5, for 1 h on ice, which inactivated any remaining free dye. Finally, 0.1% BSA was added as a carrier protein, and labeled IL-7 was separated from free dye with a PD-10 Sephadex G-25M column. Elution of labeled IL-7 was monitored by fluorescence and the final protein concentration was determined by sandwich ELISA (enzyme-linked immunosorbent assay) using a rabbit polyclonal anti-human/mouse IL-7 primary antibody and a biotinylated rabbit polyclonal anti-human/mouse secondary antibody (Peprotech human IL-7 ELISA Development Kit, Cat. No. 900-K17, Lot No. 0405017; Peprotech rabbit anti-murine IL-7, Cat. No. 500-P57, Lot No. 099CY51RB; Peprotech biotinylated rabbit anti-murine IL-7, Cat. No. 500-P57Bt, Lot No. 099CY51RB). The reaction was developed with an avidin-HRP (Horseradish peroxidase) conjugate (Peprotech) and 2,2'-Azino-bis(3-ethylbenzthiazoline-6-sulfonic acid) (ABTS) Liquid Substrate Solution (Sigma Cat. # A3219) and measured in a TECAN INFINITE M200 plate reader.

3.8.4. Human IL-7 CD-loop peptide.

A peptide with the sequence of the CD-loop of human IL-7 (G₉₁NCTGQVKGRKPAALGEAQPTKSLEENKSLKEQKLND₁₂₇) was synthesized and labeled with Alexa Fluor 647 on the first cysteine (underlined) by Peptide Specialty Laboratories GmbH. The purity was higher than 95%, and the identity of the peptide with and without labeling was confirmed by mass spectrometry (Peptide Specialty Laboratories GmbH).

3.8.5. IL-7 binding to fibrillar FN.

Manually pulled FN-FRET fibers were produced as previously described⁶⁵. Briefly, a 2- μ l droplet from a FN solution (0.4 mg/ml in PBS, containing only 5% FN-FRET to prevent intermolecular FRET) was placed on a silicone sheet mounted on a custom-made uniaxial stretching device. FN-FRET fibers were manually pulled from this droplet using a syringe needle with a bent tip to prevent tearing, and deposited on the silicone sheet. For the independent fiber studies, 20 fibers were pulled parallel to the stretch axis (Fig. 4.2 and Supplementary Figs. S4.2, S4.6-S4.7, S4.9-S4.10). For the fiber grid studies, 10 fibers were deposited parallel to the stretch axis and 10 fibers perpendicular to it (Fig. 4.1 and Supplementary Figs. S4.4 and S4.6). FN-FRET fibers were then washed three times with PBS and the silicone sheets were either stretched, relaxed, or left as mounted, thereby subjecting them to respective membrane strains of 100%, -50%, or 0% in the direction of the stretch axis and -20%, 33%, or 0% in the direction perpendicular to it, with negative strains representing compression of the material due to relaxation of the silicone membranes

perpendicular to the strain axis. Based on previous calibration studies¹³⁹, we could convert these membrane strains to absolute FN strains of 380%, 20%, and 140% experienced by the FN-FRET fibers parallel to the stretch axis and 90%, 219%, and 140% experienced by those perpendicular to it (Fig. 4.1 and Supplementary Figs. S4.4 and S4.6).

For the binding assay, the FN-FRET fibers were blocked with 5% BSA in PBS for 30 min at 20 °C, washed three times with PBS and once with binding buffer (1% BSA in PBS), and incubated with either 100 ng/ml A647-labeled recombinant human IL-7 (A647-rhIL7), 100 ng/ml recombinant murine IL-7 (A647-rmIL7), or 1 µg/ml of A647 labeled synthetic CD-loop peptide, for 1.5 h at 37 °C in binding buffer. Following incubation, FN-FRET fibers were washed three times with binding buffer, and once with PBS to remove unbound IL-7/CD-loop peptide. They were then fixed with 2% formaldehyde in PBS for 20 min at 37 °C and washed three times with PBS. Samples were imaged immediately with an Olympus FV1000 confocal microscope, and emissions from the donor (D), acceptor excited by FRET (F), directly excited acceptor (A), and directly excited A647-labeled IL-7 (L) were recorded. To maximize signal detection while minimizing bleed-through between the channels due to overlaps in the emission spectra of the fluorophores, we acquired the images sequentially as shown in Supplementary Figure S2. The acquired data were then processed using a Matlab code to obtain the FRET ratio and the normalized IL-7 signal, described below.

3.8.6. Image processing.

Acquired images were imported to Matlab using the open source Bioformats package from The Open Microscopy Environment, with a Creative Commons Attribution 4.0 International License¹⁴⁰ and converted them to double precision value arrays. To avoid false FRET values, the images from the different channels were aligned using 'imregister', a Matlab built-in intensity-based registration with monomodal image capture modality (captured on the same device), and restricted to xy translation to avoid deformation of the captured images, which would again result in false FRET values (Supplementary Figure S3). Subsequently, appropriate thresholds were set to remove pixels that did not belong to the fibers (background areas) and overexposed pixels, and the mean background signal from the instrument was subtracted from the data. The values set to zero as a result of these processing steps were excluded from the next calculations. Based on the non-zero data, a mask was generated, and was eroded to remove pixels from the borders of the fibers, which are generally of low intensities due to light scattering, and may affect FRET values (Supplementary Fig. S4.3). A local, 3 × 3 pixel, square averaging filter (Matlab functions: 'imfilter', 'fspecial', 'average') and a one-deviation Gaussian averaging filter (Matlab function 'imgaussfilt') were applied to smooth the data, and the mask was applied again. The values set to zero as a result of these processing steps were excluded from the following calculations.

3.8.7. FRET intensity signal correction.

We calculated the FRET ratios between donors and acceptors upon donor excitation from the following generalized consideration, and following the notation $Intensity_{CONTRIBUTING SIGNAL}^{detection channel}$. Upon excitation at 488 nm, the measured signal intensity detected in the donor channel D is composed of the donor emission attenuated by the energy loss due to FRET to the acceptor (I_{D-F}^d) (Equation 4.1). Depending on the choice of the donor and acceptor fluorophores as well as on the bandpass filters, the signal intensity in the donor channel D might also contain unwanted contributions from the acceptor emission due to direct acceptor excitation at 488 nm (I_A^d), and the acceptor emission due to FRET (I_F^d) leaking back into the donor channel. I_A^d and I_F^d are thereby fractions of the corresponding signals detected in the acceptor channel, respectively: $I_A^d = \alpha_A^a$ and $I_F^d = \delta_F^f$.

$$\text{donor channel} \quad D_{(ex\ 488)} = I_{D-F}^d + I_A^d + I_F^d = I_{D-F}^d + \alpha I_A^d + \delta I_F^d \quad (4.1)$$

$$\text{acceptor channel} \quad F_{(ex\ 488)} = I_F^f + I_{D-F}^f + I_A^f = I_F^f + \beta I_{D-F}^d + \gamma I_A^d \quad (4.2)$$

$$\text{acceptor channel} \quad A_{(ex\ 546)} = I_A^a + I_{D-F}^a + I_F^a \cong I_A^a \quad (4.3)$$

Similarly, upon excitation at 488 nm, the measured signal in the acceptor channel F is due to FRET (I_{FRET}^f), which is the term we are interested in, and again might include two additional unwanted crosstalk contributions, namely from the donor emission, attenuated by the energy loss due to FRET, leaking into the acceptor channel (I_{D-F}^f), and the acceptor emission due to direct acceptor excitation at 488 nm (I_A^f) (Equation 4.2). I_{D-F}^f and I_A^f are again fractions of the corresponding signals detected in the donor (D) and acceptor (A) channels, respectively: $I_{D-F}^f = \beta I_{D-F}^d$ and $I_A^f = \gamma I_A^a$, whereby I_A^a can be easily measured by direct excitation at 546 nm. In principle, direct excitation at the acceptor wavelength at 546 nm, might directly excite the donors if the fluorophores are not chosen properly and would then have to be considered. Because these unwanted contributions are normally negligible^{130,135}, as corroborated by our control experiments (Ctrl-2 in Supplementary Figure S4.2-C and D), A is equal to I_A^a (Equation 4.3). For completeness, though, we still write here the full equations for D , F and A .

A look at the spectral characteristics of the fluorophores chosen here and of the respective bandpass filters (Supplementary Figure S4.2-A), reveals that a small part of the donor emission spectrum overlaps with the FRET acceptor channel F , suggesting that upon excitation at 488 nm (Imaging Step 1) a non-negligible signal from the donor emission can be detected in the FRET acceptor channel F (I_{D-F}^f). As shown in Supplementary Figure S2-B, acquiring images from fiber samples containing only donor-labeled FN revealed a non-negligible signal that was detected in the FRET acceptor channel (F) (marked with *). We then estimated the β factor as previously described^{130,135}, by plotting F against D from these samples. The slope of the linear fit (Equation 4.4) yields the β factor, with $\beta = 0.28$ (Supplementary Figure S4.2-E).

$$\beta = \frac{F}{D} \quad (4.4)$$

Similarly, a small contribution (I_{D-F}^f) from directly excited acceptor fluorophores at 488 nm is expected (Supplementary Figure S4.2-A). To determine the magnitude of the γ factor, we acquired images from fiber samples containing only acceptor-labeled FN (Supplementary Figure S4.2-C). We estimated the γ factor as previously described^{130,135}, by plotting F against A from these samples. The slope of the linear fit (Equation 4.5) yields the γ factor with $\gamma = 0.16$ (Supplementary Figure S4.2-F).

$$\gamma = \frac{F}{A} \quad (4.5)$$

From Equations 4.1-4.3, and as previously published^{130,135}, we calculate the acceptor emission due to FRET (I_F^f) in terms of the measured signal contributions D , F , and A , and the estimated correction factors β , γ , and δ :

$$I_F^f = \frac{F - \beta D - \gamma A (1 - \beta \delta)}{(1 - \beta \delta)} \quad (4.6)$$

We implemented this standard generic equation in our Matlab code to obtain the corrected intensity of the acceptor emission due to FRET (I_F^f), independently of factors that are specific to the choice of fluorophores, detection windows, and most importantly, microscope setup, including the laser power, photomultiplier

gain values, and filters used. Thus, it is possible to use our code for experiments with different experimental or microscopy settings. However, the correction factors β , γ , and δ need to be estimated for each specific case.

3.8.8. Ratiometric FRET calculation.

We obtained the FRET ratios shown in our data sets, by dividing the corrected intensity of the acceptor emission due to FRET I_F^f (from Equation 4.6) by the signal obtained on the D channel, which is the intensity of the donor, since no leakage of the acceptor back into the donor channel occurs, as we shown in Supplementary Figure S4.2-C (Ctrl-2) and corroborated by the fact that correction factors α and δ are indeed negligible:

$$\text{FRET ratio} = \frac{I_F^f}{I_{D-F}^d} \cong \frac{I_F^f}{D} \quad (4.7)$$

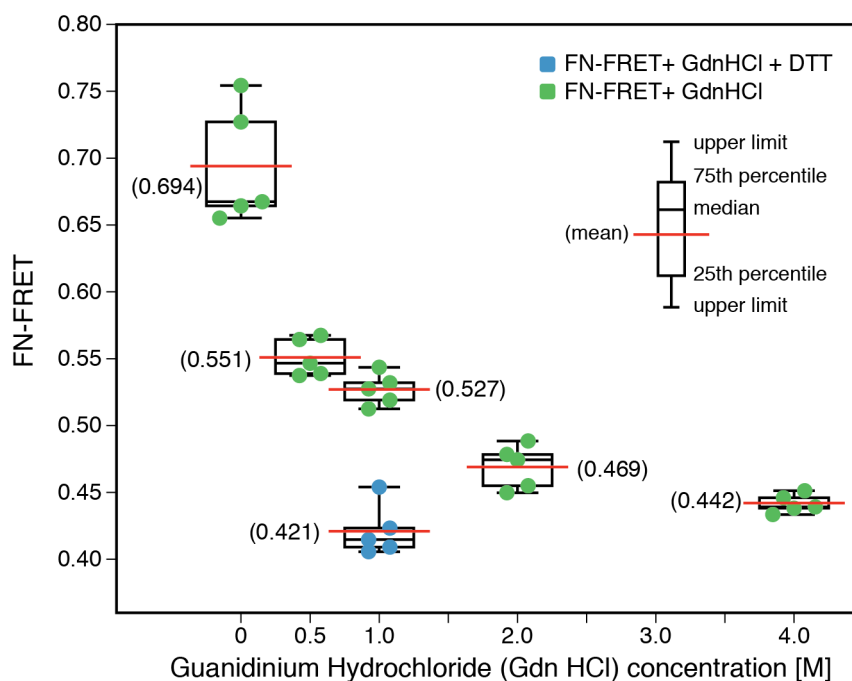
3.8.9. Ligand signal normalization.

Since binding of the ligand (IL-7 or CD-loop labeled with Alexa Fluor 647) is also dependent on the FN density, we normalized the signal obtained on the ligand channel with the directly excited acceptor signal.

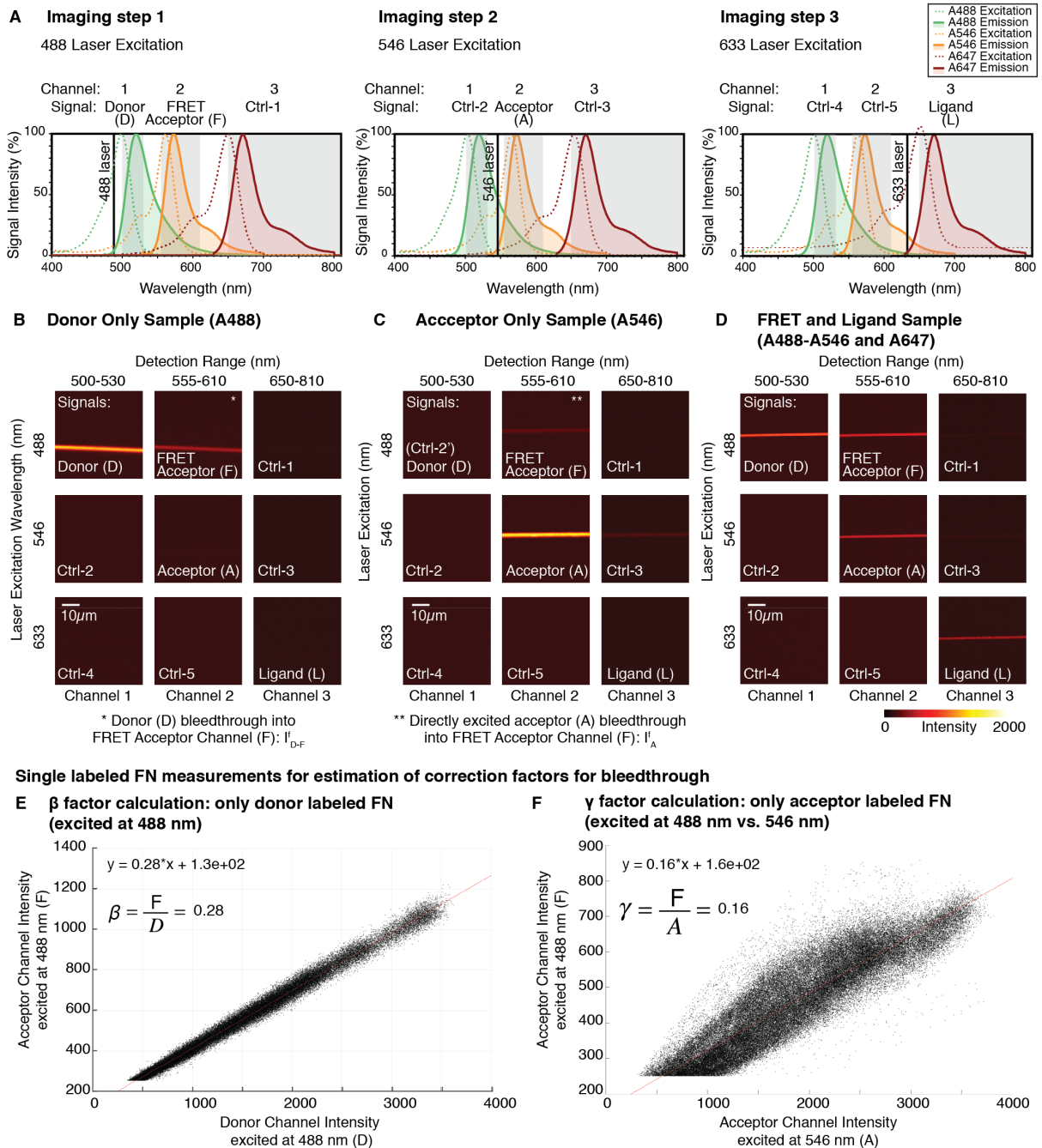
$$\text{Normalized Ligand} = \frac{L}{A_{(ex\ 546)}} \quad (4.8)$$

The Matlab codes used to perform the analysis are included as Supplementary files “parameters.txt”, “FRETanalysis.txt” and “registration.txt”. The file extensions need to be changed to .m file for usage in Matlab. Once this is done, the parameters for the analysis need to be defined beforehand in the “parameters.m” file, and the “registration.m”, and the bioformats libraries (www.openmicroscopy.org)¹⁴⁰ need to be added to the Matlab path. Then, the “FRETanalysis.m” script can be run to perform the analysis.

3.9. Supporting Information: Supplementary Figures

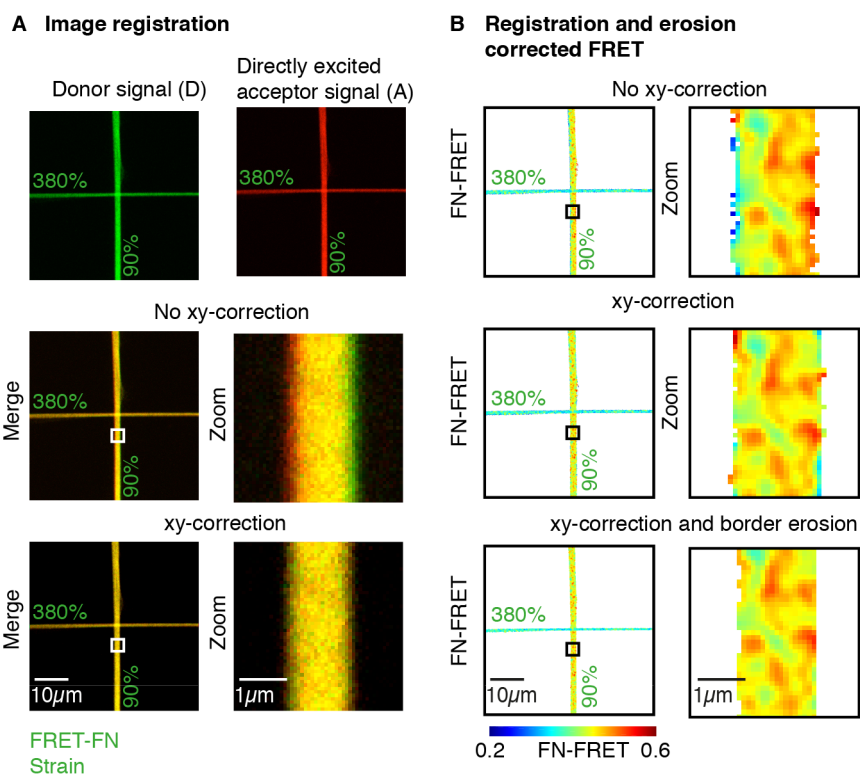


Supplementary Figure S4.1. Responsiveness of FN-FRET probe to conformational changes induced by chemical denaturation in solution. FN-FRET was chemically denatured with increasing concentrations of guanidinium hydrochloride (GdnHCl) in solution, in order to assess whether the FRET signal is responsive to the loss of secondary structure as previously described¹³⁸. Briefly, FRET-FN was mixed in solution with varying concentrations of GdnHCl in contact with a glass substrate blocked with 5% BSA in PBS for 1 h at 20 °C. Five samples per condition were imaged with a confocal microscope and their FRET ratios calculated (circles). Box plots for each condition are shown with corresponding means (red brackets). Increasing GdnHCl concentrations lead to progressively lower FRET values as FN loses its tertiary and then secondary structure upon denaturation, confirming the capability of our FRET-FN to be used as a FRET probe to assess a large range of FN conformations. Incubation of FRET-FN with 50 mM dithiothreitol (DTT) for 1 h before mixing with GdnHCl (1M final GdnHCl concentration), which reduces disulfide bonds and separates the two FN subunits, caused a further reduction in FRET, as previously described¹²⁸.



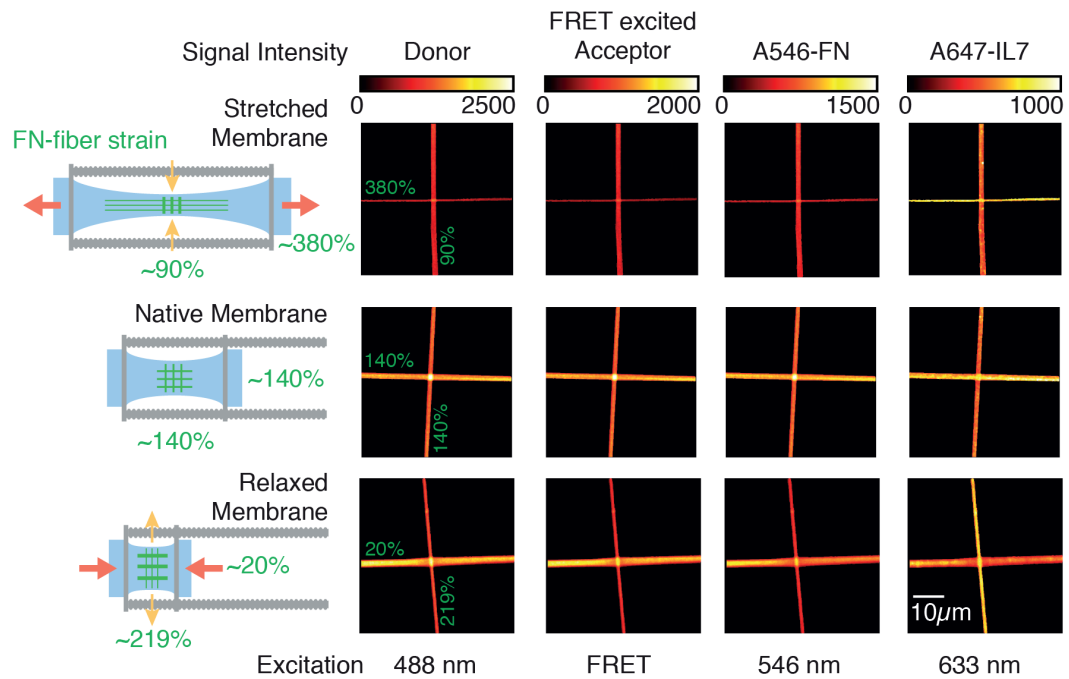
Supplementary Figure S4.2. Image acquisition parameters and microscopic controls. (A) Complete data sets (for measurements and correction factors) were acquired in three sequential imaging steps (1–3). In each step, a different laser excitation line (488, 546, or 633 nm) was used, and data were collected in three wavelength windows: 500–530 nm (channel 1), 555–610 nm (channel 2), and 650–810 nm (channel 3). For each step, the excitation laser lines and the collection wavelength windows are shown along with the excitation and emission spectra of the three fluorophores used in the measurements (A488, A546, and A633). The following signals were acquired: FRET donor (imaging step 1, channel 1), FRET acceptor (imaging step 1, channel 2), directly excited acceptor (imaging step 2, channel 2), and ligand (imaging step 3, channel 3). Additional signals to control for bleed-through were acquired, as described in B–C. (B–C) Control experiments with single-labeled FN fibers imaged at all channels for image acquisition controls and calculation of FRET correction factors. (B) Imaging of a FN fiber sample labeled with donor only (A488). Upon excitation at 488 nm, there is bleed-through into channel 2, which will affect the FRET

ratios and requires the need for FRET corrections, as explained in the 'FRET signal correction' section in the Materials and Methods, included in the Supplementary Information file. (C) Imaging of a FN fiber sample labeled with acceptor only (A546). Upon excitation at 546 nm, there is a signal in channel 2 as expected. However, a signal is detected in channel 2 also upon excitation at 488 nm, which will also affect the FRET ratio and further justifies the need for a FRET correction. Upon excitation at 546 nm, there is no signal detected in channel 1, verifying the assumed simplification of Equation 4.3 described in the 'FRET intensity signal correction' section in the Materials and Methods, included in the Supplementary Information file. (D) Imaging of a FN fiber sample labeled with both donor and acceptor fluorophores (A488 and A546) (complete sample). Upon excitation at 488 and 546 nm, there is bleed-through to channel 3. To avoid such unwanted contributions from the donor and acceptor signals, excitation at 633 nm was always performed separately in all data shown in Figs.4.1-4.2 and Supplementary Figs. S4.2-S4.7 and S4.9-S4.10. (E) Estimation of β correction factor (Eq.4.4). Following excitation of a donor-only labeled sample at 488 nm, signals from channel 2 were plotted against signals from channel 1, and the β factor was estimated by the slope of the linear fit. (F) Estimation of γ correction factor (Eq.4.5). An acceptor-only labeled sample was imaged, and signals from channel 2 upon 488 nm excitation were plotted against signals from the same channel upon 546 nm excitation and the γ factor was estimated by the slope of the linear fit.

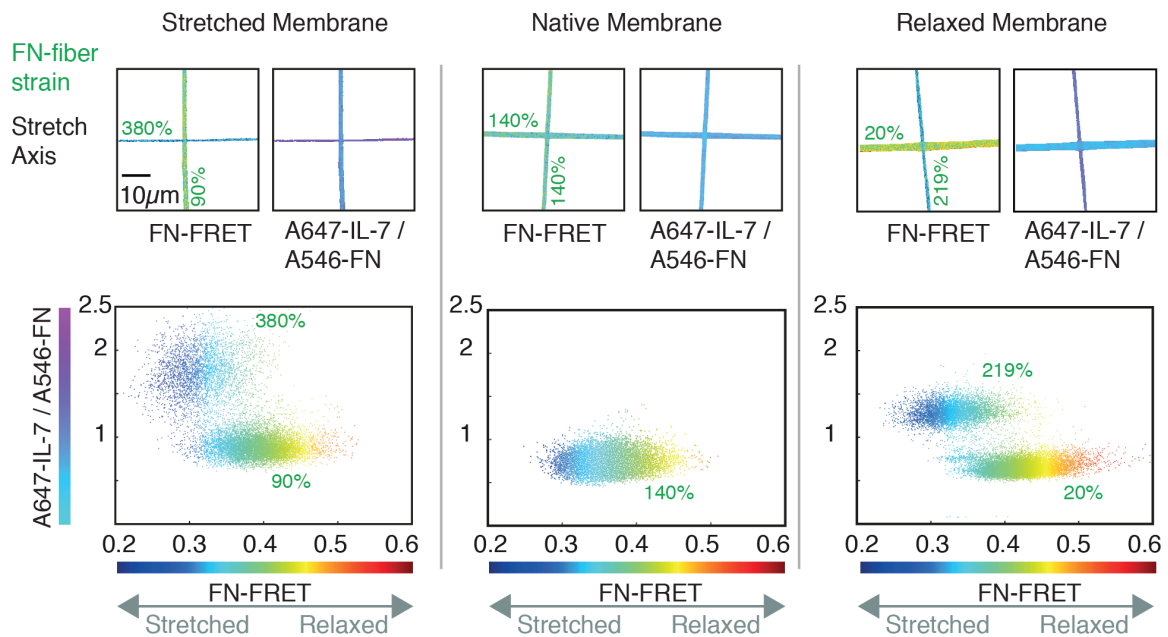


Supplementary Figure S4.3. Image registration and refinement. To avoid false FRET values due to improper alignment of the acquired images, the images from the different channels were aligned using the intensity-based registration Matlab built-in function 'imregister', a monomodal image capture modality restricted to xy translation. To illustrate the need for this, as well as the obtained results, we show: (A) signals acquired for the FRET donor (D; green) and the directly excited acceptor (A; red) overlaid (merge), before and after registration correction, showing that without registration (no xy-correction), there is a degree of misalignment between the channels, and (B) FRET ratios obtained with or without xy registration, to show how misalignment between channels can lead to false FRET values. The FRET images were further subjected to border erosion using the Matlab built-in function 'imerode' with a square structuring element of 3×3 pixels; we show (B) that this removes pixels at the border of the fibers, where low intensity and light scattering can also lead to false FRET values.

A Human IL-7 binding to FN-FRET fiber grids at various levels of strain.

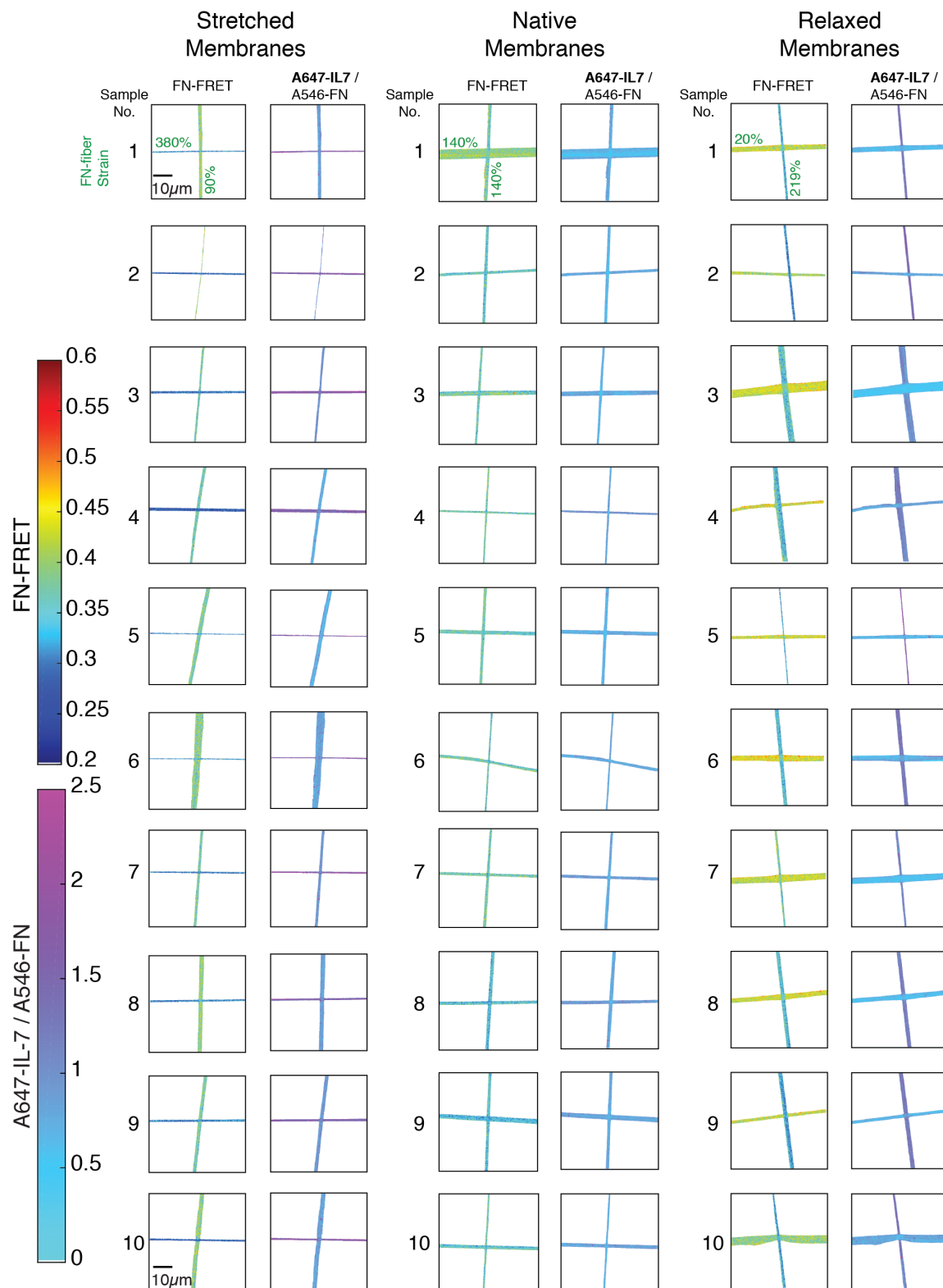


B FRET and normalized IL-7 binding

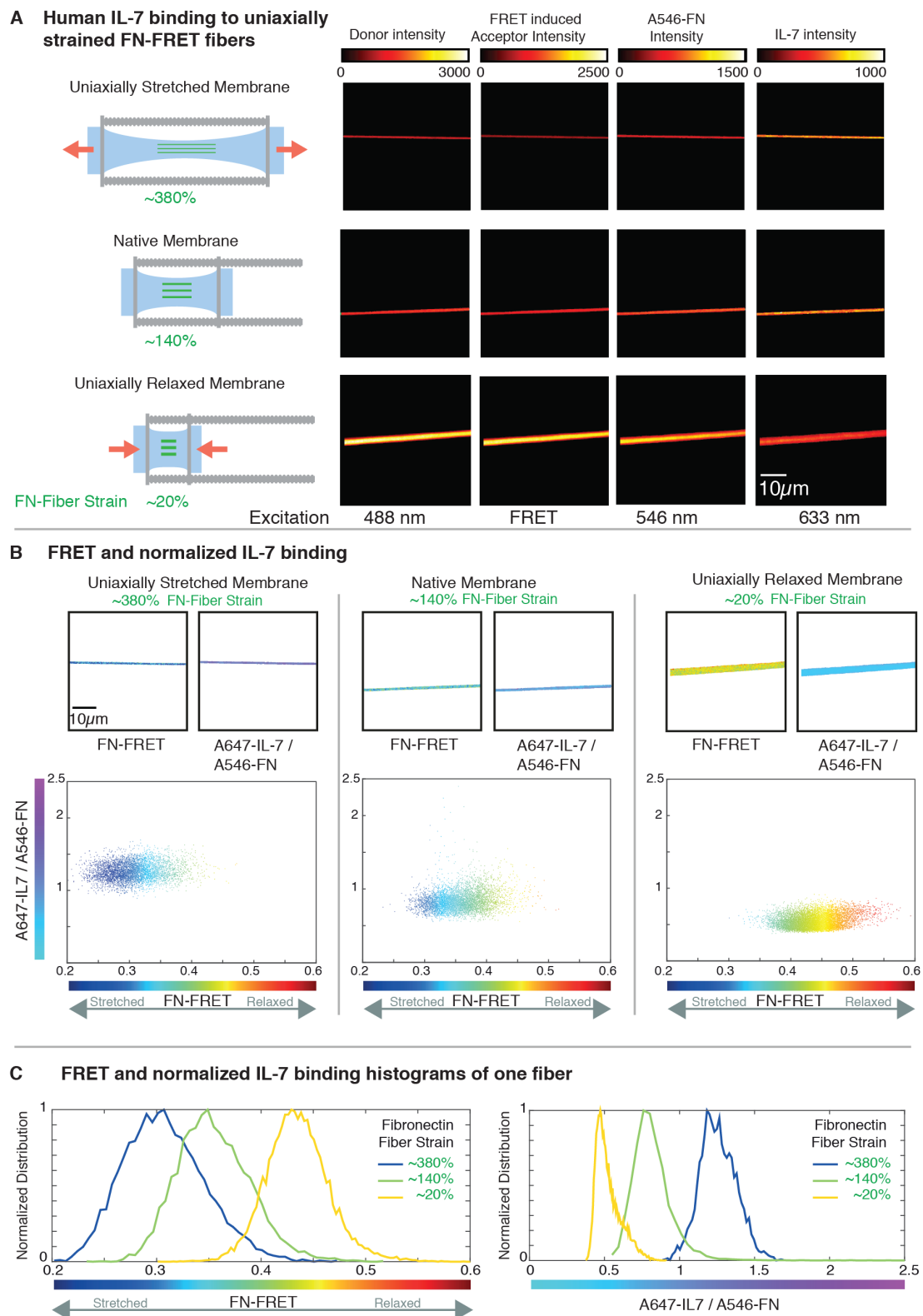


Supplementary Figure S4.4. Human IL-7 binding to FN fiber grids at different strains. (A) FN-FRET fibers were deposited as a grid on silicone membranes mounted on a uniaxial stretching device, with 10 fibers parallel, and 10 fibers perpendicular to the membrane stretch axis. The silicone membranes were either left as mounted (native), with FN-FRET fibers pre-stretched to ~140% due to the manual pulling and deposition on the silicone membranes¹³⁹, uniaxially stretched to obtain FN fiber strains of ~380% axially

and ~90% perpendicularly, or uniaxially relaxed to obtain FN fiber strains of ~20% axially and ~219% perpendicularly. Binding assays with FN-FRET, and A647-labeled IL-7 were performed on such grids, and representative confocal images of grid intersections between one parallel and one perpendicular fiber are shown: donor and FRET-induced acceptor intensities (excitation at 488 nm), direct excitation acceptor intensity (excitation at 546 nm) (A546-FN), and IL-7 intensity (excitation at 647 nm). (B) The resulting FRET ratios (I_F^f/D), and normalized IL-7 intensity (A647-IL-7 intensity/A546-FN) of grid intersections, with their corresponding pixel-by-pixel scatter plots, show increased IL-7 binding to more stretched FN-FRET fibers.



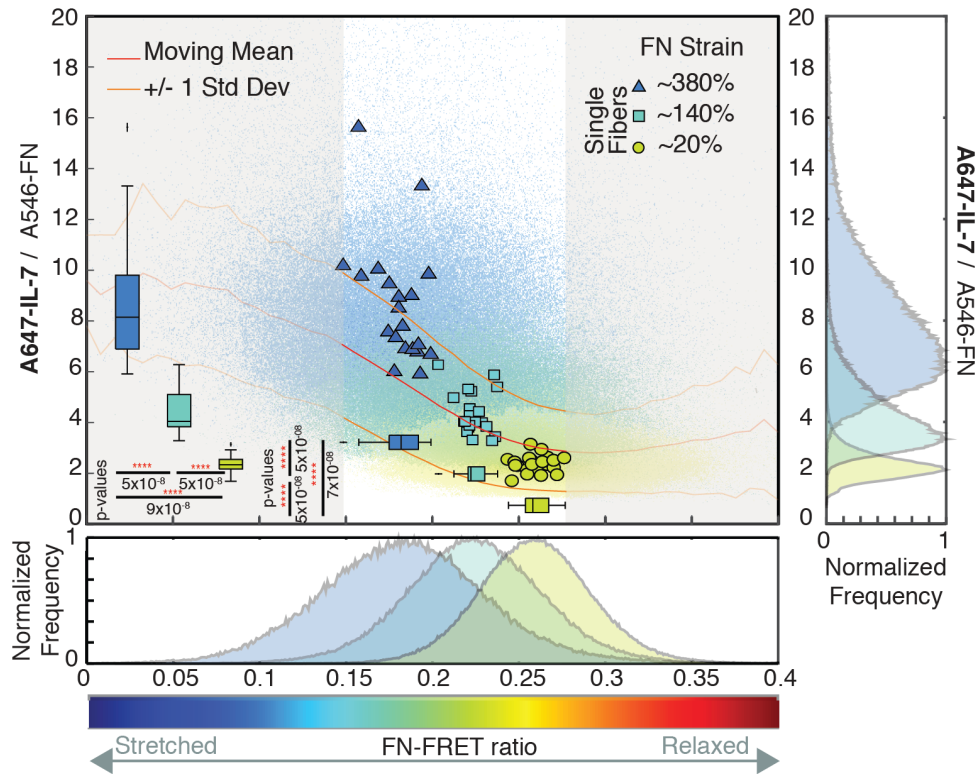
Supplementary Figure S4.5. Comparison of several samples to show the consistency of our data among fibers within a single experiment. FN-FRET ratios and normalized IL-7 intensity (A647-IL-7/A546-FN) images from 10 different FN fiber grids from native, stretched, and relaxed silicone membranes are shown, illustrating the reproducibility of our findings that IL-7 shows higher binding to stretched compared to relaxed FN fibers.



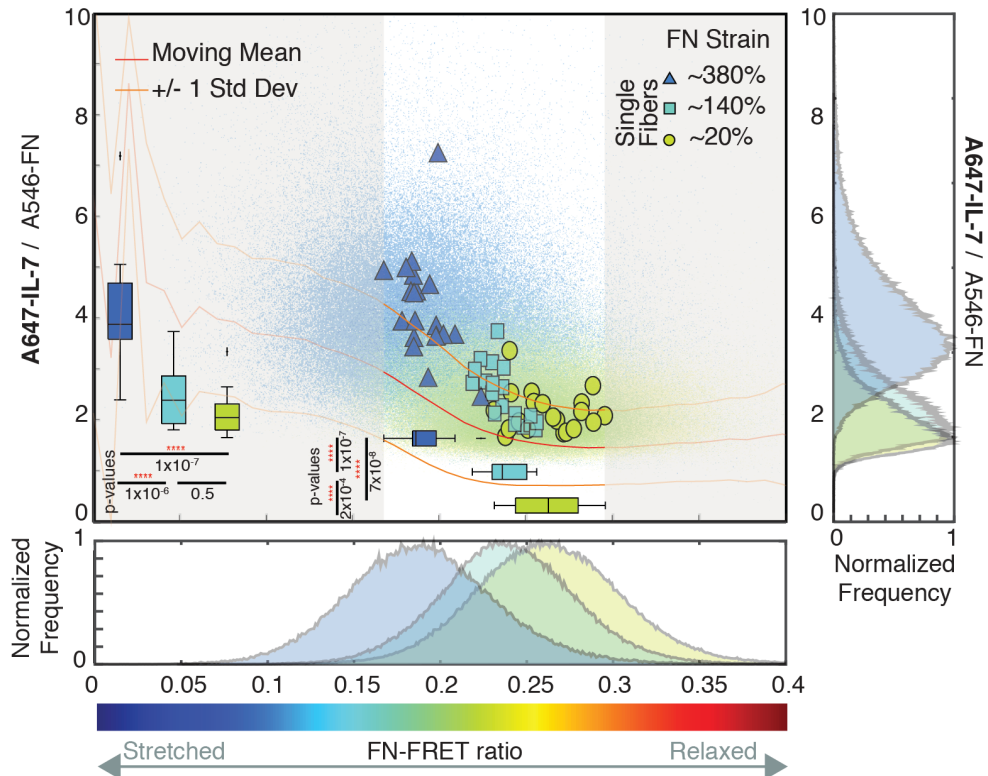
Supplementary Figure S4.6. Human IL-7 binding to stretched single fibers. (A) Twenty FN-FRET fibers were deposited on silicone membranes mounted on a uniaxial stretching device. The membranes were either left as mounted (native), were stretched, or pre-strained membranes were relaxed in order to

obtain FN fibers of different strains: ~140%, ~380%, or ~20%, respectively (the fibers on the native sheets are already pre-strained owing to the manual pulling). Binding assays with A647-labeled human IL-7 were performed, and representative confocal images are shown: donor and FRET-induced acceptor intensities (488 nm excitation), direct excitation acceptor intensity (546 nm excitation) (A546-FN), and A647 intensity (633 nm excitation). (B) Representative FRET ratios (I_p^f/D) and normalized IL-7 intensity (A647-IL-7 intensity/directly excited A546-FN intensity) images, and their corresponding pixel-by-pixel scatter plots are shown. Stretched fibers show increased IL-7 binding compared to the relaxed fibers. (C) Normalized histograms of FRET ratios and normalized IL-7 intensities for a single fiber of each strain are shown.

A Human IL-7 binding to FN fibers



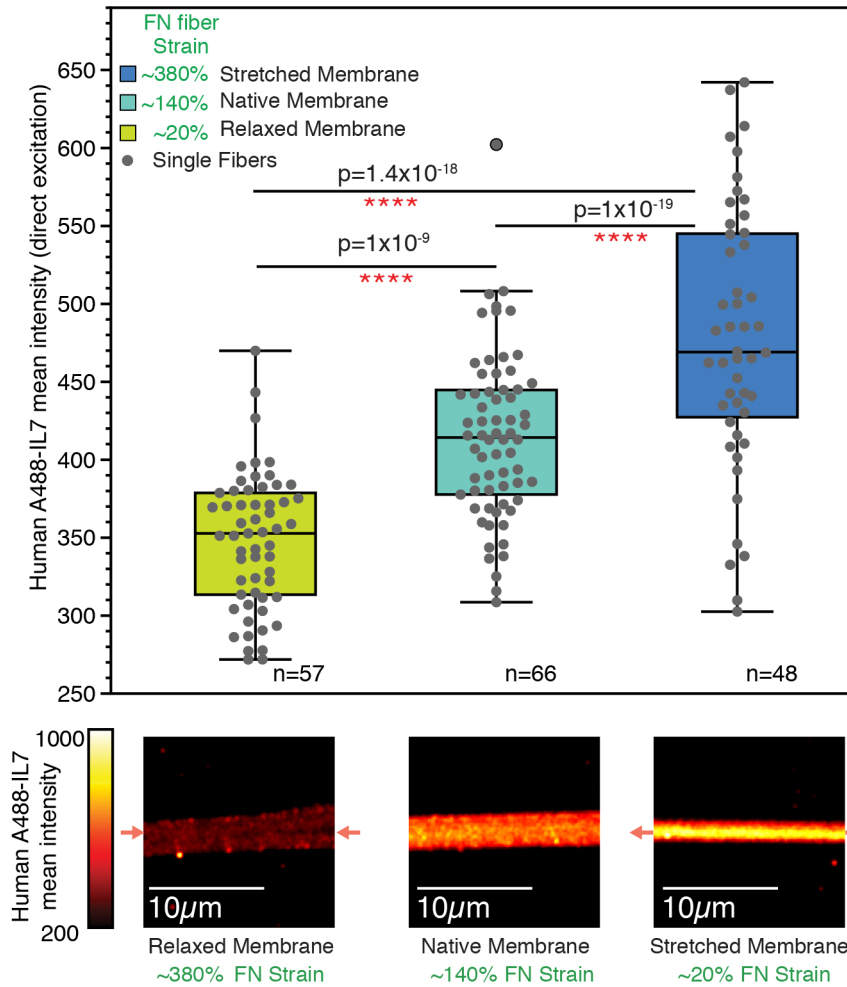
B Murine IL-7 binding to FN fibers



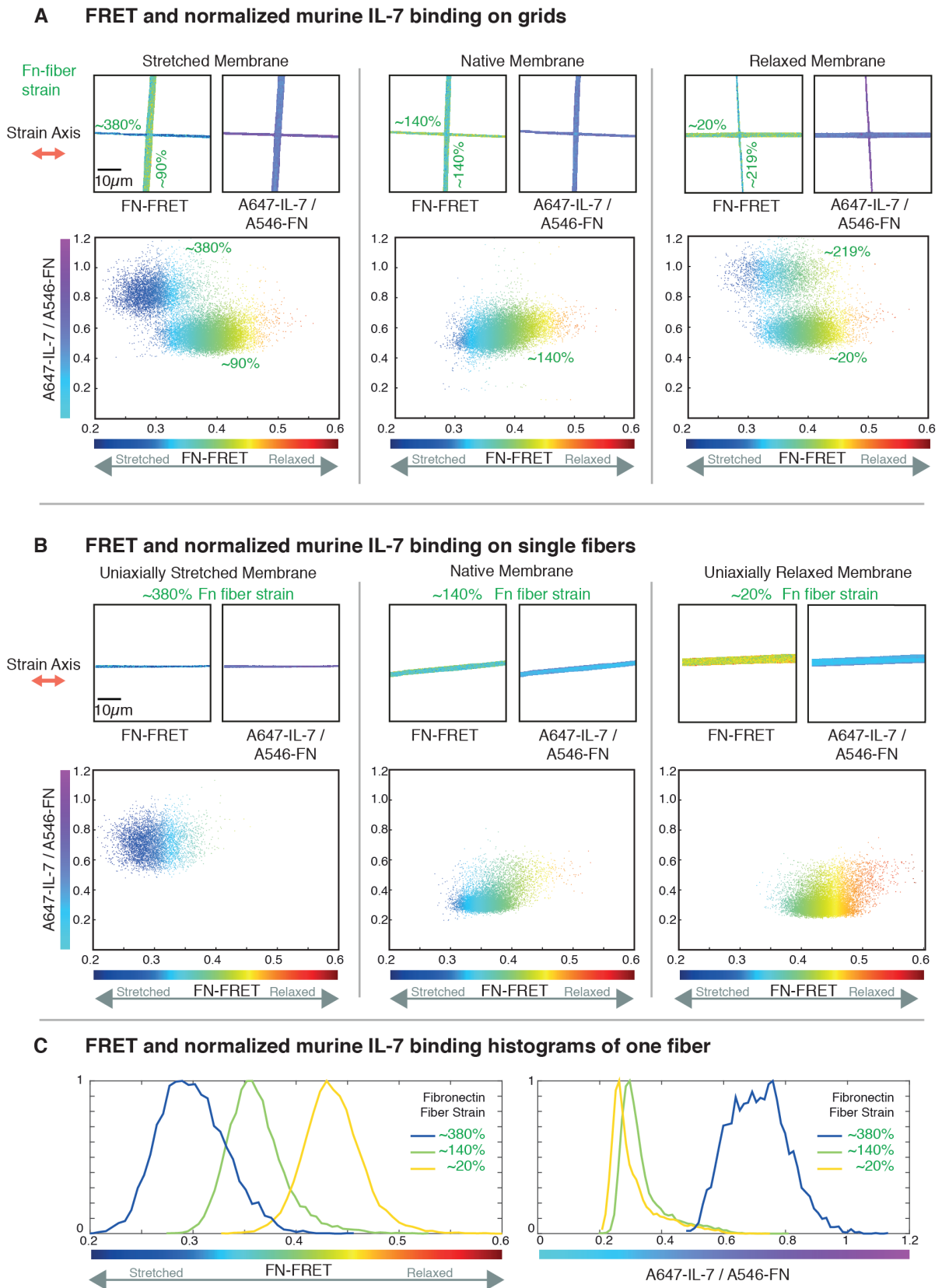
Supplementary Figure S4.7. FRET scatter plots of replicate experiment confirming increased binding of human and murine IL-7 to stretched FN fibers. Consistent with the results shown in Fig.

2 and Supplementary Fig. S10, we show here that human and murine IL-7 show distinct mechanosensitive binding patterns to FN fibers. Binding assays with human (A) or murine (B) A647-IL-7 were performed in a set of 20 independent fibers deposited on silicone sheets at three different strains: ~380%, ~140% and ~20%. Mean values for each fiber (triangles for ~380% strain, squares for ~140% strain, and circles for ~20% strain) are shown along with pixel-by-pixel scatter plots of FRET ratios vs. normalized IL-7 intensities from all the pixels from all samples. From this pooled pixel-by-pixel data, moving mean curves were generated along the x-axis (FRET) with a bin of 6×10^{-3} FRET units (red curves), and their standard deviations were estimated (orange curves). To analyze the binding behavior, we limited these curves to a section between the upper and lower mean FRET percentiles (25th and 75th of mean FRET values of single fibers (FRET box plots)). Box plots of the mean values for single fibers, as well as the normalized histograms of all pixels are shown for both FRET and normalized IL-7 binding (A647-IL-7 intensity/A546-FN intensity). While human IL-7 shows a gradual increase in IL-7 binding, murine IL-7 binding increases only at higher strains.

Human A488 labeled IL-7 binding to FN fibers

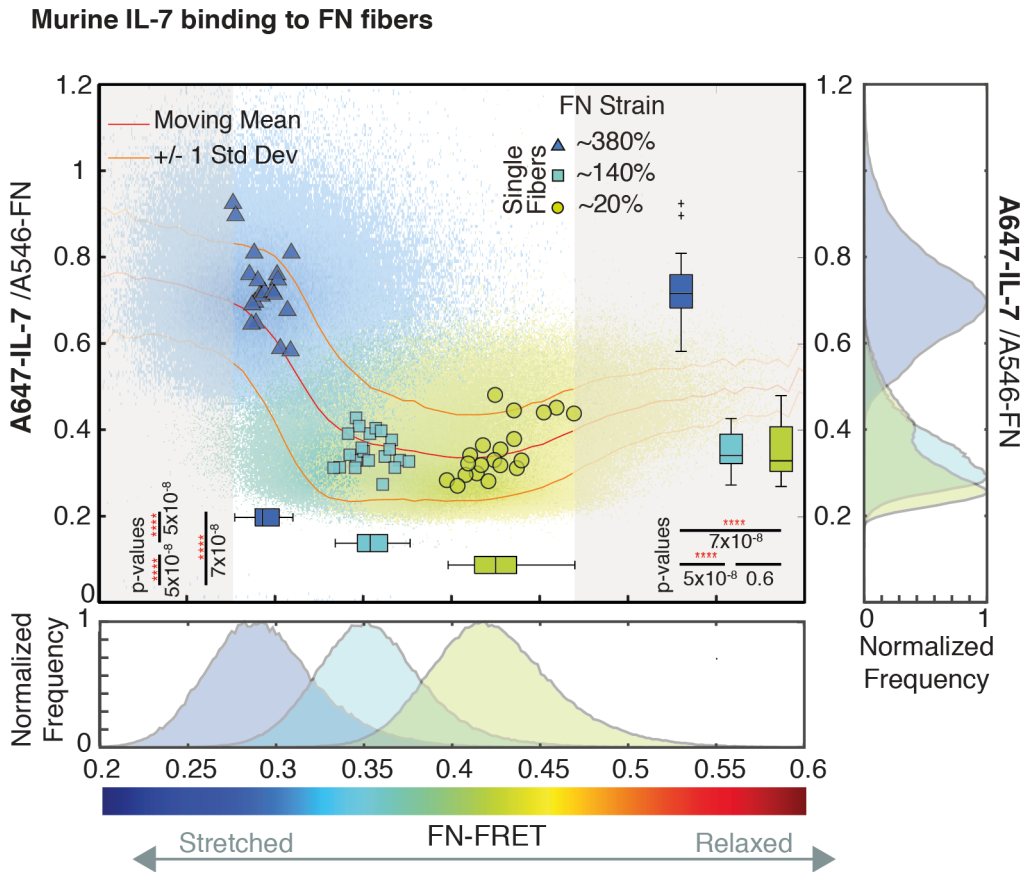


Supplementary Figure S4.8. Increased IL-7 binding to stretched FN is not affected by the presence of the FN-fluorophores. Binding of A488-labeled human IL-7 to unlabeled FN fibers also shows enhanced binding to stretched fibers. Binding assays were performed with fibers deposited on silicone sheets at three different strains: ~380%, ~140% and ~20%, as in the experiments shown in Fig. 2 and Supplementary Fig. S4.6, except that no FRET-FN probes were present and human IL-7 was labeled with Alexa Fluor 488. Mean values for the A488-IL7 of each fiber, with the corresponding box plots for each of the three strain conditions, and a representative image of the detected signals are shown (circles). This control experiment shows that our results are independent of the presence of FN-FRET probes and do not depend on the fluorophore used to label IL-7. These results are not normalized for FN content, and are therefore less accurate than the results presented with A647-IL7, but they nevertheless show the same trend of increasing binding of IL-7 with increasing FN fiber strain.



Supplementary Figure S4.9. Murine IL-7 binding to FN fiber grids or single fibers is also enhanced by fiber stretching. (A) Twenty FN fiber grids were deposited on silicone membranes mounted on a uniaxial stretching device with half of the fibers parallel to the stretch axis and the other half perpendicular

to it. The membranes were either left as mounted (native) or were uniaxially stretched or relaxed, to obtain FN fibers of different strains: ~140%, ~380%, or ~20% for the fibers parallel to the stretch axis, and ~140%, ~90%, or ~219% for the fibers perpendicular to it, respectively. Binding assays with murine A647-labeled IL-7 were performed. Representative FRET ratios and normalized IL-7 intensity (A647-IL-7 intensity/A546-FN intensity) images, and their corresponding pixel-by-pixel scatter plots are shown. Fibers of higher strain show higher IL-7 binding. (B) Twenty FN-FRET fibers were deposited on silicone membranes mounted on a uniaxial stretching device. The membranes were either left as mounted (native) or were uniaxially stretched or relaxed, to obtain FN fibers of different strains: ~140%, ~380%, or ~20%, respectively (the fibers on the native sheets are already pre-strained owing to the manual pulling). Binding assays with A647-labeled murine IL-7 were performed on these fibers, and representative FRET ratios and normalized IL-7 intensity (A647-IL-7 intensity/A546-FN intensity) images, and their corresponding pixel-by-pixel scatter plots are shown. Stretched fibers show the highest IL-7 binding, whereas native and relaxed fibers, the lowest. (C) Normalized histograms of FRET values and normalized IL-7 intensities for a single fiber of each strain are shown.



Supplementary Figure S4.10. Scatter plots of FN-FRET ratios versus murine IL-7 binding. Statistical analysis of murine IL-7 binding shows that enhanced binding to stretched FN fibers requires higher levels of strain than human-IL7. Murine IL-7 binding to FN-FRET fibers is also enhanced by fiber stretching, but in contrast to human IL-7 binding to FN-FRET fibers, murine IL-7 binding is enhanced only at higher strains. Binding assays with murine A647-IL-7 were performed in a set of 20 independent fibers deposited and experiencing three different strains: ~380%, ~140%, and ~20%. Mean values for each fiber (triangles for ~380% strain, squares for ~140% strain, and circles for ~20% strain), along with pixel-by-pixel scatter plots of FRET ratios vs. normalized IL-7 intensities from all the pixels from all samples, are shown. From this pooled pixel-by-pixel data, moving mean curves were generated along the x-axis (FRET) with a bin of 6×10^{-3} FRET units (red curves), and their standard deviations were estimated (orange curves). To analyze the binding behavior, we limited these curves to a section between the upper and lower mean FRET percentiles (25th and 75th of mean FRET values of single fibers (FRET box plots)). Box plots of the mean values for single fibers, as well as normalized histograms of all pixels are shown for both FRET and normalized IL-7 binding (A647-IL-7 intensity/A546-FN intensity). Whereas human IL-7 shows a gradual increase in IL-7 binding, murine IL-7 binding increases only at higher strains. The difference in binding of mouse A647-IL-7 to FN-FRET fibers to 20% or 140% is not statistically significant (p values > 0.5).

3.10. Supportive Information: Additional files

Source codes for data analysis (MATLAB Scripts) are included as .m files: 'parameters.m', "FRETanalysis.m" and "registration.m". These are included in the Appendix.

The 3D structural model of human IL7RA/IL2RG/IL7 with the inserted CD loop (IL7RA-IL2RG-IL7-CDloopModel.vml), and a corresponding video (IL7RA-IL2RG-IL7-CDloopModel.mpg) were also submitted and are available in the published version.

4. Preliminary studies contextualizing IL-7/FN binding and stromal cell behavior.

Since we found that binding of IL-7 increases with mechanical stretching of fibronectin fibers, we aimed to understand the biological significance of our findings. Since IL-7 is produced by lymph node stromal cell's (LNSCs), and stromal cells from the thymus, and these cells in turn respond to IL-7, we aimed to characterize mechano-biological behavior of these cells, their ECM, and make the first steps towards elucidating whether these cells can bring about changes in the ECM that could result in differential binding of IL-7 to fibronectin in the ECM, and in turn, whether changes in IL-7 binding levels can have an effect on their function. In this chapter I will present preliminary studies that were performed to lay a foundation on these issues, and motivate further experiments to address them.

4.1. Lymph Node Stromal Cell contractility characterization

This preliminary study was performed by Daniela Ortiz Franyuti (DOF) in collaboration with Dr. Jau-Ye Shiu (JYS). DOF and JYS prepared the method, JYS fabricated the nano-pillars, DOF and JYS performed the experiments and analyzed the data.

Since lymph nodes undergo large structural modifications and extensive ECM remodeling upon the onset of inflammation (See Section 2.3), and the remodeling of the ECM is done by stromal cells, we performed a preliminary study to characterize the contractility of LNSCs and compare it with that of Normal Human Dermal Fibroblasts (NHDFs) (Promocell C-12302), which reside in locations that do not experience such drastic structural modifications. We hypothesized that LNSCs would be able to exert higher forces to be able to accommodate for the extensive ECM remodeling they need to perform in vivo. We used a nanopillar assay to assess the magnitude of the forces applied by both cell types on FN coated nanopillar substrates. The LNSCs were a kind gift from Dr. Shannon Turley, at the time of the experiments from the Dana Farber Cancer Institute and Harvard Medical School.

4.1.1. Method

Nano-pillar substrates were prepared from a silicon template of nanopillars fabricated through nanosphere lithography and plasma etching. This template was filled with polydimethylsiloxane (PDMS) to create a negative mold, which was then filled with SU-8 solution and merged with a glass coverslip to hold the final nano-pillar structures and allow for confocal imaging of the substrates. The solution was degassed under vacuum and cured by exposing it to UV light. Once cured, the PDMS mold was removed, exposing the SU8 nanopillar array. The nanopillars were then coated with 25 $\mu\text{g}/\text{ml}$ FN in PBS for 1 hour and washed twice with PBS before culturing cells on them¹⁶⁷.

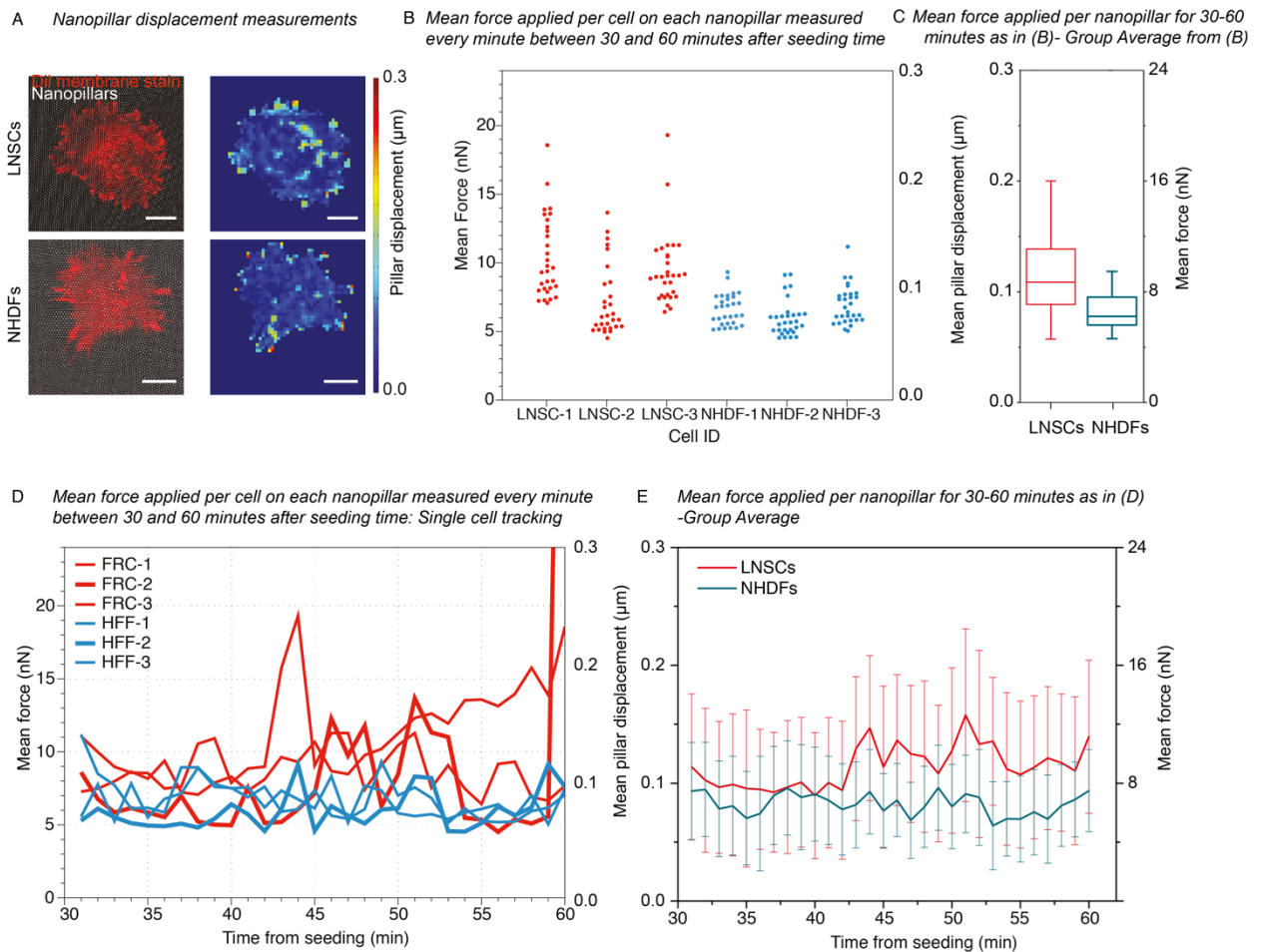


Figure 5.1. Force exertion of Lymph Node Stromal Cells (LNSCs) and Normal Human Dermal Fibroblasts (NHDFs). LNSCs exert higher forces on nanopillar than NHDFs, and forces increase with adhesion time. LNSCs and NHDFs adhered for 30 min on FN-coated nanopillars and then monitored for 30 min. A) confocal image of indicated cell labelling membrane dye (DiI, red) adhering to a nanopillar array (grey, DIC) (left), respectively whole cell colorimetric map of horizontal nanopillar displacements(right). Scale bars, 10 μ m. B) Average pillar displacements and forces for each one minute time point between 30 and 60 minutes of seeding time, of LNSCs (red) and NHDFs (cyan) grouped by single cell. C) Mean force applied per group for 30 minutes measured between 30 and 60 minutes of seeding time. D) Single cell tracking of mean pillar displacements and traction forces of LNSCs (red) and NHDFs (cyan) over time between 30 and 60 minutes of seeding time (total time= 30 min, frame interval 1 min per each cell). E) Time tracking of mean pillar displacements of grouped LNSCs (red) and NHDFs (cyan) (n=3 cells per each condition).

Cells were cultured to about 80% confluency, washed with PBS and detached using 0.25% Trypsin with EDTA for 2-3 minutes. Complete medium (DMEM + 10% FBS + 1% Penicillin/Streptomycin) was added to stop the reaction, and the suspended cells were transferred to a 15ml centrifuge tube and spun for 5 min at 1,000 rpm. Cells were then reconstituted in 1ml serum-free culture medium making sure that the concentration was not higher than 1×10^6 cells/mL. To stain the cell membranes, 5 μ L DiI Vybrant were added per mL of cell suspension, mixed well by gentle pipetting and incubated for 10 minutes at 37°C. The cells were then centrifuged at 1100 rpm for 5 minutes at 37°C, the supernatant removed, and the cells washed by gently re-suspending them in complete medium at 37°C. The washing procedure was repeated two more times. The cells were then seeded at 1×10^5 cells per nano-pillar substrate sample and

incubated for 30 minutes to allow the cells to deposit and adhere to the substrates. Three samples with Lymph Node Stromal Cells (LNSCs) and three samples with Normal Human Dermal Fibroblasts (NHDFs) were prepared, and the cells were imaged live with a Leica confocal microscope for 30 minutes. Both the cell membrane and the pillar locations were recorded.

Using the measured cell-induced displacement of the pillars, and using the previously estimated mechanical properties of the nanopillars' constituent material, it was possible to estimate the force that cells applied on each of the pillars. The analysis of pillar displacements was limited to nanopillars that were in contact with the cell membrane, as identified by co-localization with the membrane dye signal (Figure 5.1 A-B).

To obtain the applied forces, each nanopillar was assumed to behave as an elastic spring with a defined spring constant. This was previously measured using atomic force microscopy by applying incremental force with an AFM tip of known spring constant of 63nN/ μ m and deriving the new spring constant from the slope of the force after compensating for AFM tip indentation. The spring constant was found to be $k=78.8\text{nN}/\mu\text{m}$. Then, the displacements were measured for each nanopillar within a range 0.01 to 0.8 μ m, and the force applied on each nanopillar by the bound cell was calculated with the formula ¹⁶⁷:

$$\text{Force} = \text{displacement} * k \quad [5.1]$$

The forces were estimated for the duration of the imaging (30 minutes) for each of the 6 measured samples and their magnitude compared (Fig. 5.1). The displacements in xy direction of the nanopillar tips were quantified by calculating the respective comparison of two images, that is the pillar tops versus bottom planes processing with particle tracking software (Diatrack 3.03), respectively, using confocal microscopy.

4.1.2. Results

We observed that LNSCs exert an overall higher magnitude of forces than NHDFs on the nanopillars, with higher magnitudes being more evident after about 10 minutes after the beginning of imaging (40 minutes from seeding time) (Figure 5.1 C). The forces exerted by each of the LNSCs cells being higher than the ones observed for NHDFs (Figure 5.1 D), as well as the overall mean forces (Figure 5.1 E). In future experiments, it would be recommended to use DIC to identify the cell borders, to avoid any photo-toxicity induced reduction of cell contractility due to the use of a DiL dye. Raw displacement data is included in the Appendix

4.1.3. Conclusion

We have observed a first trend in preliminary experiments, that LNSC seem to exert higher forces on nanopillars than NHDFs and the applied forces increase with adhesion time. While the statistical significance of these observations remains to be determined in experiments with higher numbers of cells, the significance of confirming these findings would be that LNSCs could be capable of exerting higher levels of force on their ECM, thereby unfolding constituent FN fibers to higher degrees. It has been shown that FRCs' contractility is regulated by podoplanin mediated actomyosin contractility ¹⁵⁹, but FRC contractility was assessed by their ability to contract a collagen gel, and the magnitude and characteristics of the forces applied by these cells has not been measured or further characterized. The nano-pillar assay would be an optimal alternative to perform a more precise characterization of the forces exerted by these, and other LNSCs. These preliminary results motivated us to assess and compare the FN conformation found in cell- assembled ECM produced by both cell types.

4.2. FN conformation in Lymph Node Stromal Cell-assembled ECM in cell culture.

Having obtained preliminary results showing that LNSC exert higher forces than NHDFs on our preliminary study using the nanopillar assay, and knowing that LNSCs are capable of extensive remodeling of their ECM, because of the drastic changes in size and tension of the lymph node during inflammation,¹⁵ we aimed to study whether these cells produce ECM with different levels of ECM stretching, as assed by differences in fibronectin conformation within ECM produced by them. We also aimed to determine whether any differences observed are dependent on the time. To do this, we cultured LNSCs and NHDFs in FRET-FN enriched medium that allowed cells to incorporate it into their newly synthesized ECM. We then evaluated the FRET ratio of the FN in the produced ECM after 2 and 4 days of culture, and the actin cytoskeleton network of the cells, by staining for F-actin with Alexa 633 (A633) Phalloidin.

4.2.1. Method

We covalently bound FN to glass substrates and cultured cells to produce ECM enriched with FN-FRET to probe FN conformation, based on previous work⁶⁰. We used glass substrates and covalently bound FN to them by first plasma-cleaning the substrates for 30 s (approx. 0.36 mbar at 200 W load coil power; air plasma), immediately coating them with a 2% solution of 3-aminopropyltrimethoxysilane in water solution, and incubated them at room temperature for 15 min. We rinsed the substrates twice with deionized water and immediately covered the surface with 0.125% glutaraldehyde in water and incubated them at room temperature for 30 min. Finally, the substrates were rinsed twice with deionized water, and 50 µg/ml fibronectin in PBS was added and incubated for 1 h at room temperature. The substrates were sterilized before culturing cell on them for 15 min by UV irradiation. After this, the substrates were rinsed with PBS and cells (LNSCs or NHDFs) were seeded at 8×10^4 cells/cm² and incubated for 30 min to allow the cells to adhere. After this, the medium was replaced with medium enriched with 50 µg/ml fibronectin (10% of this being FRET labelled FN) and the cells were cultured for 2 days (48 hours) or 4 days (96 hours), after which the samples were fixed. The samples that were kept incubating for 4 days had their medium replaced with medium containing 50 µg/ml fibronectin (10% FRET labelled FN) after two days, in order to replenish the availability of FRET labelled FN. To fix the samples, the medium was removed 2% formaldehyde in PBS was added and incubated at 37°C for 20min, after which the samples were washed twice with PBS before starting the procedure to stain for F-actin with A633-Phalloidin. For the strain, the cells were permeabilized with Triton X-100 (0.1% vol/vol) in PBS for 2 minutes and rinsed 3x with PBS. Then the samples were blocked for 1 hr with 5% BSA in PBS (vol/vol), washed 3x with PBS, and incubated with A633-Phalloidin (1:100) in 5% BSA in PBS (vol/vol) for 60 min, washed 3x with PBS, the PBS removed, and the samples mounted with Prolong-Gold (with DAPI) anti-fade agent from Invitrogen.

Finally, the samples were imaged using an Olympus Fluoview confocal microscope. The data acquisition and FRET analysis were performed as explained in Chapter 3, with the exception that the Ligand signal was not included in the analysis, as the F-actin signal does not co-localize with that of FRET-FN. We acquired data for 10 samples of each condition (LNSC/NHDFs after 2/4 days of culture). The LNSCs were a kind gift from Dr. Shannon Turley, at the time of the experiments from the Dana Farber Cancer Institute and Harvard Medical School. NHDFs were obtained from Promocell (C-12302).

4.2.1. Results

As shown in Fig. 5.2, after 2 days of ECM deposition and remodeling, the ECM produced by LNSC contained FN in a more stretched state, as reflected by lower FRET values, than that produced by NHDFs, suggesting that LNSCs produce ECM with FN in a more stretched conformation. After 4 days of culture,

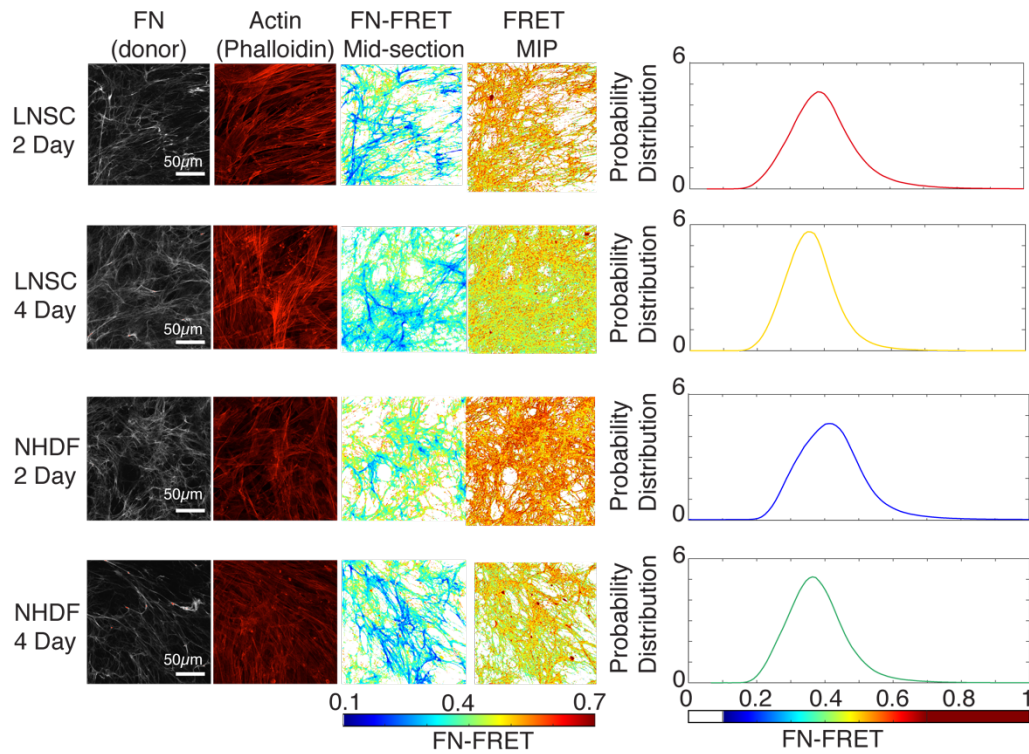
NHDFs showed FRET values similar to the ones observed for LNSC after 2 days of culture, but LNSC after 4 days of culture showed even lower FRET values than those observed after 2 days, suggesting that NHDFs take longer to achieve similar levels of FN stretching as those observed by LNSC at an earlier time point (2days of culture), but LNSCs continue to remodel and stretch the underlying ECM to achieve even higher levels of FN unfolding. The aforementioned differences can be visually observed by looking at the FRET ratios in the mid-section of single stacks, and become even more obvious when looking at the maximum intensity projection of whole stacks and when comparing their probability distribution histograms (Fig. 5.2-A). The resulting probability distributions for each of the 10 samples per condition are shown in Fig. 5.2B, and Fig. 5.2-C shows the pooled data from each experimental condition, making it easier to identify differences and compare them.

In addition, we also observed that distribution of FRET values of the ECMs of both NHDFs and LNSCs after 4 days of culture were narrower than after 2 days, suggesting that initial ECM deposition contains a broader range of FN conformations, but as ECM deposition and remodeling progresses, a more homogeneous population of increasingly stretched FN fibers are present in the ECM. This applies to both cell types. Finally, it seems that LNSCs feature a more defined actin-network than NHDFs, which might explain the increased tensional state of the ECM produced by these cells.

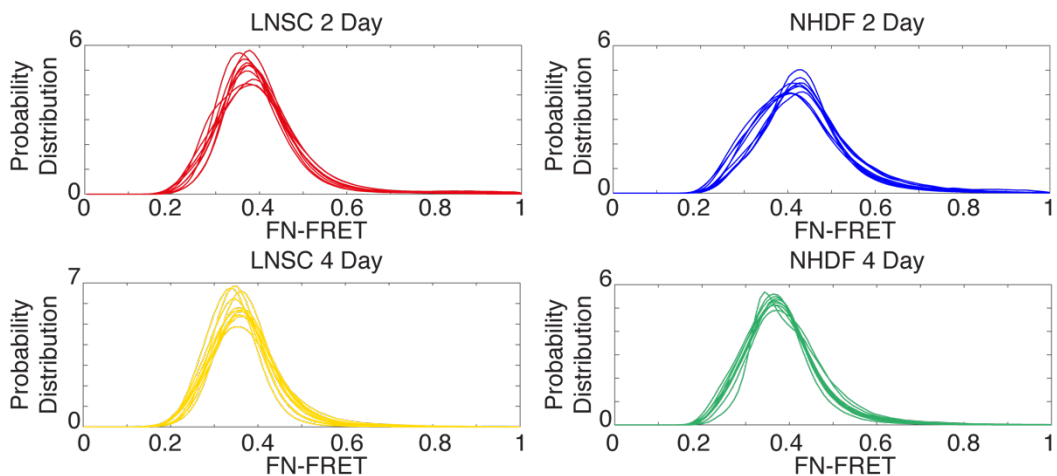
4.2.1. Conclusion

In agreement with the findings in our contractility characterization preliminary study, where LNSCs exerted higher magnitude of forces on FN-coated nano-pillars than NHDFs (Section 5.1), this preliminary study showed that LNSCs seem to produce ECM with more unfolded FN, and supports the notion that LNSCs can exert higher levels of force on their ECM, thereby unfolding constituent FN fibers to higher degrees. This would be in agreement with the notion that LNSCs are capable of achieving more radical remodeling of their ECM, since rapid expansion of the lymphatic network occurs upon inflammation, and associated lymph nodes undergo a significant change in size and tension, and extensive ECM remodeling and alterations in the ECM's mechanical properties take place to accommodate for these changes¹⁵. In effect, LECs undergo a process of proliferation, migration and tube formation that promotes lymphangiogenesis during an inflammatory response¹¹⁰, and FRCs maintain lymph node size and tension with the onset of inflammation¹⁵.

A FRET differences between LNSC and NHDFs - Single sample data



B FRET differences between LNSC and NHDFs



C LNSC/NHDFs FRET differences - Pooled Data

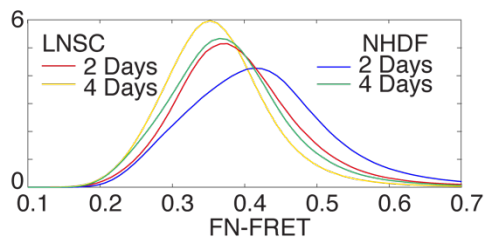


Figure 5.2. Characterization of differences in the tensional state of FN fibers within the ECM produced by LNSCs vs. NHDFs assessed by FN conformation differences probed by FRET after 2 and 4 days of culture. LNSCs/NHDFs were cultured with medium enriched with 50 µg/ml fibronectin (10% of this being FRET labelled FN) for 2 days (48 hours) or 4 days (96 hours), after which the samples were fixed. A) ECM produced by LNSC contained FN in a more stretched state, as reflected by lower FRET values, than that

produced by NHDFs after 2 days. After 4 days, NHDFs showed FRET values similar to those of LNSC after 2 days of culture, but LNSC after 4 days of culture showed even lower FRET values than those observed after 2 days. A mid-section image of FN and F-actin, as well as FN-FRET values are shown, as well as a maximum intensity projection of FN-FRET for a representative sample of each condition, with the corresponding distribution of FN-FRET values. B) FN-FRET distribution of 10 samples per condition corroborate the results illustrated in (A). C) pooled data from the 10 samples per condition further corroborates the above described trend.

Further experiments would be required to corroborate that these findings are replicable, and to understand whether the qualitative differences observed in the actin cytoskeleton are quantitatively and statistically significant, and what role do they play.

That aside, these preliminary results motivated us to determine whether the differences in FN conformation found in LNSCs vs NHDFs would translate into differences in IL-7 binding to FN within these ECMs, as we have found in our manually-pulled FN fiber assays.

4.3. IL-7 internalization and FN conformation in LNSC cultures.

Since we observed differences in the FRET ratio, and therefore in FN conformation between LNSCs and NHDFs, we aimed to determine whether IL-7 binds to FN in these ECMs, and if the differences in FN conformation observed would translate into differences in IL-7 binding. We produced LNSC and NHDF cultures which incorporated FRET labelled fibronectin into their ECM and incubated them with A647 labelled human and murine IL-7 to identify binding on the ECM in conjunction with an evaluation of changes in fibronectin conformation as assessed by FRET. While the assay seems to require further work in terms of determining these binding characteristics, we found that human IL-7 is internalized by stromal cells.

4.3.1. Method

Glass substrates were functionalized with covalently-bound FN, sterilized, and fibroblasts (LNSC or NHDFs) were seeded and allowed to adhere as described in Section 5.2.1. Unbound cells were washed and the medium replaced with one supplemented with 50 µg/ml fibronectin (10% FRET labelled FN) also as previously described. The cells were cultured and the medium replenished after 2 days of culture. After 4 days of culture, the cultures with their synthesized ECM were washed and incubated with medium supplemented with 5% sterile filtered BSA for 30min @ 37°C and 5%CO₂ to further minimize non-specific binding. The samples were rinsed once more and incubated with recombinant human or murine A647-IL7 at 100ng/ml in cell culture medium supplemented with 5%BSA for 1.5 hours @ 37°C 5%CO₂. The samples were then quickly wash once with PBS and fixed with 2%PFA for 20min at 37°C, washed 3x with PBS and imaged with Olympus confocal microscope. The data acquisition and FRET analysis were performed as explained in Chapter 3, with the Ligand signal included in the analysis. We acquired data for 4 samples of each condition (LNSC/NHDFs with human/murine IL-7 after 4 days of culture). The LNSCs were a kind gift from Prof. Shannon Turley, at the time of the experiments from the Dana Farber Cancer Institute and Harvard Medical School. NHDFs were obtained from Promocell (C-12302).

4.3.2. Results

While we wanted to assess the binding of human and murine IL-7 to the LNSC and NHDF cell derived ECM, we were not able to detect a signal co-localizing with FN. What we did observe, was internalization of A647-labelled human IL-7 to the nucleus of some cells from the LNSC population, but not of murine IL-7, as shown in Fig. 5.3. Analysis of the FRET ratios from FN in the ECM also showed an increase in the

FRET values of FN in LNSC's ECM that showed human IL-7 internalization, indicating the presence of FN in a more relaxed state. This can be visually observed by looking at the FRET ratios in the mid-section of single stacks as depicted in Fig. 5.3-A, and by the resulting probability distributions for each of the 4 samples per condition as shown in Fig. 5.3-B, and Fig. 5.3-C shows the pooled data from each experimental condition, making it easier to identify and compare them. Fig. 5.3-D shows a box plot including the mean values for each of the four samples per condition, showing that mean FRET values are higher for IL-7 stimulated LNSCs.

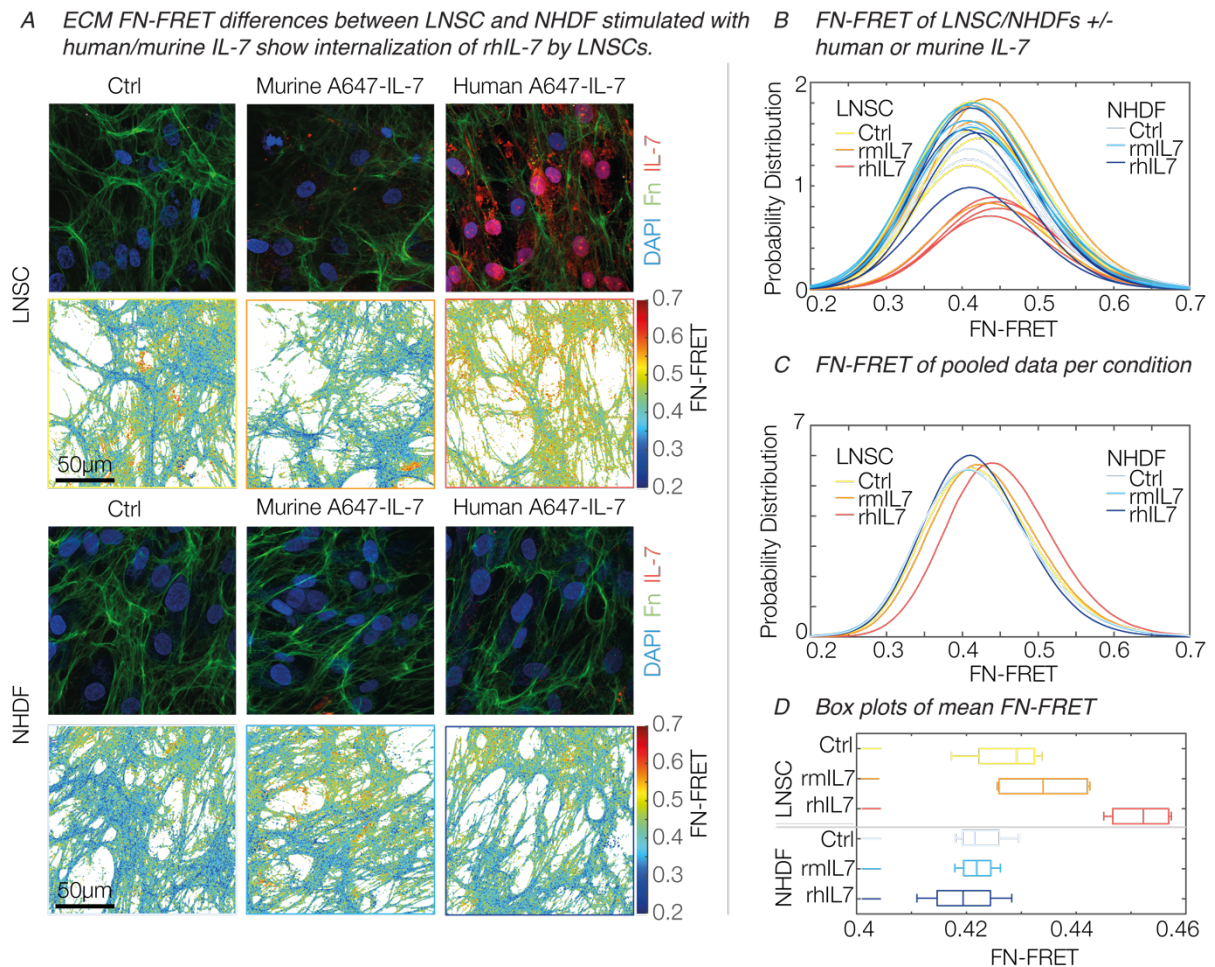


Figure 5.3. Human IL-7 stimulated lymph node stromal cells (LNSCs), but not in dermal fibroblasts (NHDFs), show IL-7 internalization that correlates with an increase in Fibronectin FRET ratio. LNSCs/NHDFs were cultured for 4 days in the presence of FN-FRET that because incorporated in the produced ECM. They were then incubated with recombinant human or murine A647-IL7 at 100ng/ml in cell culture medium supplemented with 5%BSA for 1.5 hours @ 37°C 5%CO₂. The samples were then washed with PBS and fixed with 2%PFA for 20min. A) ECM produced by LNSCs and NHDFs show that LNSCs incubated with human A647-IL-7 internalize it, and show an increase in FN-FRET ratio with respect to LNSCs incubated with murine A647-IL-7 or a control without IL-7 stimulation, and NHDFs. B) Histograms showing the distribution of FN-FRET in single samples (one sample/plotted distribution) showing increased FN-FRET ratio in LNSCs + A647-IL-7. C) FRET-FN distribution of pooled pixels for each condition showing the same trend as in B. C) Box plots showing the mean results for samples of each condition (minimum, first quartile, median, third quartile, and maximum)

4.3.3. Discussion and conclusions

We were not able, as hoped, to detect IL-7 binding to the ECM under the experimental conditions described above, but we did observe internalization of IL-7 by LNSCs, and an associated increase in FRET ratios, indicating the presence of more relaxed FN in their ECM. I will now address these two concluding observations separately:

Failure to detect IL-7 binding to FN in cell-assembled ECMs.

We are uncertain of the reason(s) why we could not detect a signal of IL-7 binding co-localizing with FN fibers in the cell derived ECMs, but there are several possible explanations for this. One reason could be, that the manually pulled FN fibers in the assay where we observed IL-7 binding, contains a much larger amount of FN than cell-assembled ECM, the fibers they are thicker, better defined and more homogeneous than native ECM assembled by LNSCs in 2D cell culture, after 4 days of cell culture.

This could mean that the higher concentration of FN results in more bound IL-7 that we can detect within the detection range of our confocal system. Using the same concentrations of added A647-IL7 used for the manually pulled fibillar FN system might not be enough to be able to detect binding on the cell-assembled ECM using the detection range of our system. If the amount of IL-7 binding to the ECM is sparse, the fluorescent signal detected via confocal microscopy might simply not be sensitive enough to detect it. Indeed, *in vivo* and histological studies where it has been tried to visualize IL-7 binding, have found it challenging or impossible to achieve detection^{12,103}, and tools like bacterial artificial chromosome transgenic mice with Cre-recombinase expression under the control of the IL-7 promoter¹⁶⁸ have been used instead to assess *in situ* localization of IL-7-expressing cells *in vivo*, to show IL7 activity during embryonic LN development, virus-induced LN remodeling and LN reconstruction after avascular transplantation, showing that FRCs and LECs strongly up-regulated IL-7 expression during these processes¹¹.

Table 5.1. *IL-7 Concentrations found in the literature*

IL-7 Concentration (pg/ml)	Finding	Reference
100,000	Activates pSTAT5 in LECs after 15min IL-7 stimulation	10
50,000	Induced closure of scratch closure test on LECs	10
20	Detected concentration produced by LECs	10
~30	Peak of IL-7 concentration for max T-cell adhesion to FN	18
~10-40	Detected concentration in plasma	10
~15-35	Detected concentration in lymph	10
2nM (~35ng/ml)	Concentration needed to activate pSTAT5 in human CD4+ T-cells	73
100,000	Reduces production of Collagen I and FN in human subconjunctival fibroblasts	121
50,000	Induced thymocyte binding to FN and Integrin β 1 phosphorylation	19
100,000	Concentration used in IL-7/Fn fiber binding experiments	Chapter 4

It would be worth, to experiment with different concentrations to determine if it is possible to achieve an optimal IL-7 concentration where binding to the ECM can be detected. As a guideline, Table 5.1 shows examples of concentrations detected and used in various experiments found in the literature. In doing so, caution must be exercised, since it has been shown, as described in Section 2.3, that IL-7 can also have

an effect on stromal cell function, and different concentrations might also have an effect on how these cells interact with the ECM.

It is also unclear whether the labelled IL-7 we are supplying is primarily binding to cells, or internalized in the case of human IL-7, and depriving the medium of IL-7 that would also bind to the ECM, exacerbating the effect of having low concentrations of FN-bound IL-7 that remain beyond the detection limits of confocal microscopy. Perhaps it is possible to minimize this effect by blocking binding of IL-7 to the IL7RA with the use of a polyclonal anti-IL7RA antibody, though it is possible that engaging the IL7RA receptor in this way may trigger changes in cell function, as observed in studies where the use of anti-IL7RA antibodies affected cell function. ¹⁶⁹⁻¹⁷¹.

Alternatively, it would be worth trying the experiments in cell cultures that have been fixed with paraformaldehyde, to stop cells from actively processing IL-7 or IL-7 having an effect on the cells during the incubation process. There is also the possibility of performing the experiments on de-cellularized ECM as described in ^{60 172 173 174 175}, or more recently ¹⁷⁶. It is possible that these cell-free ECMs can allow for controlling for the presence of cells that can potentially bind and internalize IL-7, and removing cellular membranes would also include a control for IL-7 bound to membrane receptors, even if the cells are fixed.

Another possibility to try is to assess whether a different range of stretching of the ECM is required to detect binding of IL-7. This could be done by assessing binding of IL-7 to ECM matrices that have been deposited and remodeled for a larger range of time-scalars (perhaps a range of 2 days to up to 2 weeks could be a good start). Another way that could be tried is to grow ECM under fluid flow conditions and see whether cells produce ECM with FN in even more extended conformations than those found in static culture. An assay to produce such cell-assembled ECM matrices was developed for that purpose, though time limitations did not enable the full characterization of the ECMs produced. This method is presented in Section 5.6.

LNSCs internalize human IL-7

We have detected internalization of human IL-7 by several cells in the LNSC population, with an associated increase in FRET ratios of FN in the ECM of LNSCs. While previous studies have shown internalization of the IL7RA receptor upon IL-7 stimulation in T-cells ⁷⁴, and cytoskeleton mediated translocation of STAT5 to the nucleus, upon IL-7 stimulation in CD4+ T-cells ⁷³, so far it has not been shown, to our knowledge, that IL-7 is translocated to the nucleus, and in particular, not in stromal cells. This finding, therefore, might open a new line of research into understanding the function of such translocation. It is important to point out, though, that these are preliminary experiments, and thorough experiments would have to be performed to confirm these findings. As a starting point, it would be interesting to assess whether the results observed by ⁷⁴ of IL7RA internalization in T-cells are reproducible in LNSCs, and whether IL-7 internalization as observed here occurs in combination with its receptors, and in effect occurring as a protein complex internalization, perhaps even including other intracellular components such as JAK1/JAK3 and/or STAT5. Since LNSCs are a heterogeneous population of four subtypes of stromal cells (See Section 2.2.4), and we observed heterogeneous internalization by the LNSCs in culture, we became interested in assessing which cells subsets from the LNSC population internalize IL-7, and what is the time-frame of the internalization.

4.4. Time-frame of uptake and internalization of IL-7

We performed a basic time based study using LNSCs to investigate the time needed for A647-hIL7 internalization. We cultured LNSCs and incubated them with IL-7 in parallel, and fixed them at different time points. We found cells with internalized IL-7 after 60 minutes of incubation, but once again, not all cells internalize it.

4.4.1. Method

To simplify the experiment, we used glass substrates with adsorbed, instead of covalently-bound FN, by adding 20 µg/ml un-labelled fibronectin in PBS to the substrates and incubating them for 1 hour at room temperature, then washed the wells 2x with PBS, and sterilized the substrates for 15 min by UV irradiation. The substrates were then washed 1x with sterile PBS prior to cell seeding. The cell membranes of LNSCs were first stained with a DiL dye (Life Sciences) as follows: Cells were cultured to about 80% confluency, after which the culture medium was removed, and the cells washed with PBS, and detached by adding incubating them with 0.25% Trypsin for 5 minutes, after which complete medium was added to the reaction and the cells were collected and centrifuged at 1100rpm for 5 minutes. The cells were then reconstituted in 1ml PBS and 5 µL DiL Vybrant (5µl per mL for a max of 1×10^6 cells/ml) were added. The cells in suspension were well mixed with the dye by gentle pipetting, and incubated for 15 minutes @ 37°C with 5%CO₂, then they were centrifuged at 1100 rpm for 5 minutes, at 37°C, the supernatant was removed, and the cells re-suspended in warm (37°C) complete medium. This washing procedure was repeated twice, then the cells were once more reconstituted in complete medium, counted, and the concentration adjusted to seed at 8×10^4 cells/cm².

After staining their membranes, the cells were then seeded and incubated on the substrates for 30 minutes to allow them to adhere. Once the cells had adhered, the non-adherent cells were washed off with serum-free medium, and the adherent cells incubated in serum-free medium for 1 hour, this was done to clear their surface receptors. Then, the cells were once more washed with serum free medium, and recombinant human A647-IL7 at 100ng/ml was added to each well. The cells were then incubated independently at 37°C 5%CO₂, in separate wells for 0 min (no added IL-7 and immediate fixation), 1, 5, 15, 30, 45, 60 and 90 minutes. After the corresponding time, the medium with IL-7 was removed, the cells washed once with PBS to avoid unspecific fixing of molecules from the medium, and fixed with 2%PFA in PBS for 20min @ 37°C. The cells were then washed 3x with PBS prior to mounting with Prolong-DAPI (Life Sciences), which was allowed to polymerise at room temperature overnight. Samples were then imaged with an Olympus confocal microscope. The LNSCs were a kind gift from Dr. Shannon Turley, at the time of the experiments from the Dana Farber Cancer Institute and Harvard Medical School.

4.4.2. Results

We observed in independent cultures fixed at different time points, internalization of IL-7 after 60 minutes of incubation (Fig. 5.4). Interestingly, the nuclei of the cells that had internalized IL-7 seemed more compact, with a higher intensity of DAPI, than the cells observed in cultures at earlier time points.

4.4.3. Conclusions

Further experiments are required to properly assess the internalization dynamics of these cells, preferentially live-imaging studies where single cells are assessed throughout time. This will allow for a more precise measurement of internalization, since independent cultures, as was done in these experiments, do not guarantee that the observed internalization has begun at the same time as in

concurrent experiments, and the rate of internalization might vary among the different cells imaged. Of interest is to understand the relationship between IL-7 presence in the nucleus and changes in nuclear size and shape, and the time frames on which these events occur.

Experiments to confirm and characterize IL-7 internalization and translocation to the nucleus will be required, as well as to identify the LNSC subsets that undergo such process. While translocation of IL-7 itself has not been shown, there are studies showing that the IL7RA can be internalized by thymocytes and T cells^{177, 74}, and CD8 T cells¹⁷⁸. These studies might provide a starting point to plan and perform relevant experiments to show internalization and translocation of IL-7 to the nucleus. Nuclear translocation reviews showing known mechanisms of membrane to nuclear trafficking^{179, 180} might also be helpful, as well as the knowledge that STAT molecules can also be translocated to the nucleus¹⁸¹.

Because we were not sure whether the same subset of cells is being tracked, as the LNSC population consists of FRCs, LECs, BECs and DN cells, we proceeded to attempt to identify the subset of LNSCs that internalize iL-7.

Time assessment of IL-7 internalization

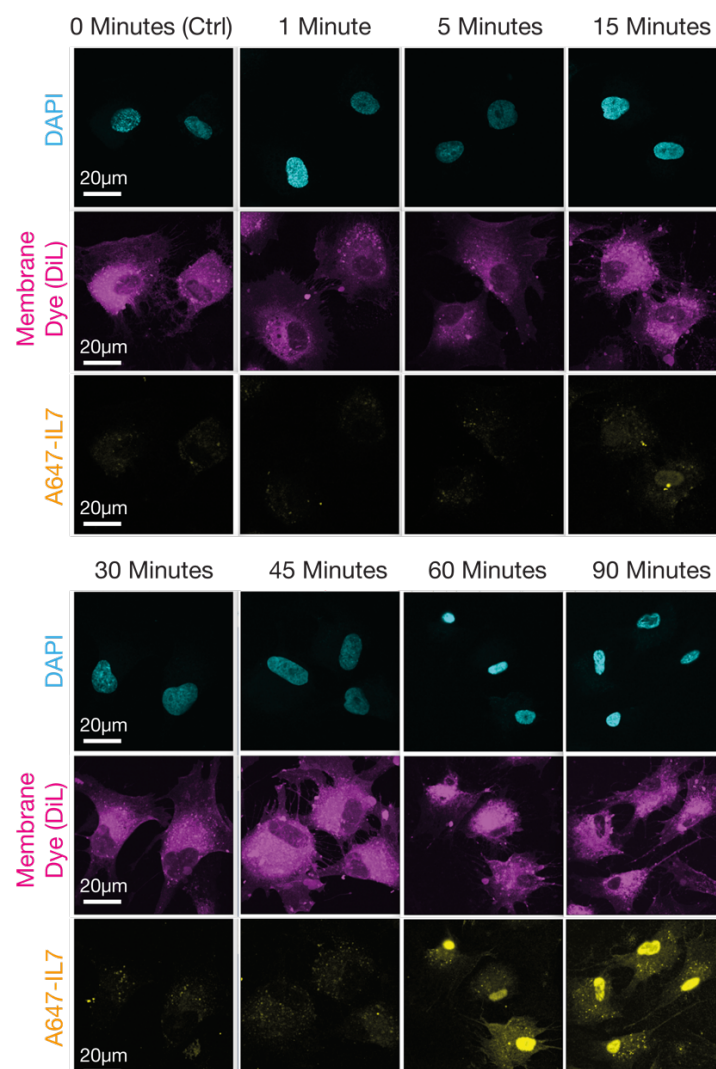


Figure 5.4. Time assessment of IL-7 internalization by LNSCs in cell cultures with A647-IL7 and fixed at different time points. A647-IL7 internalization and translocation into the nucleus can be seen in cells cultured for 60 and 90 minutes. Interestingly, these cells show a different nuclear morphology and size.

4.5. Identification of LNSC subsets that internalize IL-7

In this preliminary study, we aimed at identifying which specific cell population from the LNSCs is responsible for the internalization of IL-7 (See Section 5.3). Recalling Section 2.2.4, that the expression of Popoplanin and PECAM-1 have been used to identify the different subsets that comprise the more generic LNSC population, with FRCs - podoplanin (+)/PECAM-1 (-) - forming the lymph node conduits, and involved in the development of tolerance; Lymphatic Endothelial Cells (LECs) - podoplanin (+)/PECAM-1 (+) , which facilitate the entry of antigen-bearing dendritic cells (DCs) and soluble antigens into lymph nodes and control lymphocyte egress, and are involved in the development of tolerance; Blood Endothelial Cells, - podoplanin (-)/PECAM-1 (+) - forming vessels that allow naive lymphocytes to enter lymph nodes through high endothelial venules; Finally, the double negative subset (DN) podoplanin (-)/PECAM-1 (-) – which have not yet been characterized^{94,105-107}. We thus attempted to identify the cells that internalize IL-7, by assessing the expression of these markers on the LNSC population.

4.5.1. Method

In these experiments, we functionalized glass slide chambers with 0.1g/l Poly-L-Lysine for 5 minutes, washed three times with sterile water and UV sterilized the substrates for 15 minutes. We then washed them twice with PBS and once with complete fibroblast cell culture medium from ScienCell (Basal medium + 2% FBS + 1% Fibroblast Growth Supplement + 1% P/S). LNSCs were cultured to about 80% confluence, rinsed with PBS (-Ca/-Mg), and detached with 0.25% Trypsin solution at 37°C for 5 minutes. After cell detachment, the reaction was stopped by adding neutralizing solution (-Ca/-Mg PBS with 10%FBS) to the flask. The cells were then transferred and centrifuged at 1000 rpm for 5 min and re-suspended in 1ml culture medium. They were then counted, and the volume adjusted to seed cells at a density of 5×10^3 cells /cm². We then incubated the cells for 1 hour at 37°C with 5%CO₂, to allow them to adhere, after which, the substrates were washed once with medium to remove any non-adhering cells.

We then proceeded to incubate the LNSCs with IL-7. In a first set, we incubated them with recombinant human A647-rhIL7 at 100 ng/ml. In a second set, we added A647-rhIL7 and a goat polyclonal anti-IL7RA antibody (R&D AF-306-PB) at 2.5µg/ml, to assess if we could block the internalization. After 20 or 60 minutes, the cells were fixed with 4% paraformaldehyde in PBS for 10 minutes at 37°C, and washed three times with PBS, 5 min each time.

To stain the first set of LNSCs, the samples were first blocked and permeabilized for 1 hour in 5% Goat Serum (secondary antibody species) and 0.3% Triton X-100 and then incubated with a Mouse monoclonal IgG anti-Podoplanin Clone 18H5 (Acris Antibodies) and a Rabbit polyclonal anti PECAM-1a (Novus Bio) primary antibodies overnight at 4°C in 1%BSA, 0.3%Triton X-100. Washed three times with PBS for 5 min each time, and incubated with and Alexa 488 Goat anti-mouse and Alexa 546 Goat anti-rabbit secondary antibodies in 5% Goat Serum (secondary antibody species) and 0.3% Triton X-100 for one hour at room temperature. Finally, the samples were rinsed three times with PBS for 5 min each time, mounted with DAPI ProlongGold, cured at room temperature overnight and imaged with a confocal microscope.

The second set was stained only for Popoplanin, since the antibody against PECAM-1a was raised in goat, as the anti-IL7RA antibody we used for blocking the receptors, and we used 5% BSA + 0.3% Triton X-100 in PBS instead of Goat serum for blocking.

4.5.2. Results

For the first set, where LNSCs were incubated with A647-rhIL-7, we found that in contrast to the preliminary experiment described in Section 5.4, some cells had already internalized IL-7 at an earlier time point of 20min after adding A647-IL-7 (Fig. 5.5). Interesting observations are that IL-7 inversely localizes with the DAPI signal, that Podoplanin is present above the nucleus, but not under it (Figs. 5.5 and 5.6), and the differences in size, morphology and spreading of these cells in comparison with cells within the same well that did not internalize IL-7 (Fig. 5.7). While the goal was to find differences in the expression of Podoplanin and PECAM-1 that would allow us to identify LNSC subsets (Section 2.2.4), we were not able to find a robust way of quantifying the signals obtained with confocal microscopy of three-dimensional data and derive relative values to determine the cells' subset identity. As for the second set, where cells were simultaneously incubated with A647-rhIL-7 and a goat polyclonal anti-IL7RA antibody, we found that cells were able to internalize IL-7, even in the presence of the antibody (Fig. 5.8).

4.5.3. Conclusions

Because we observed IL-7 internalization at earlier time points than those observed in Section 5.4, it is all the more important to characterize the dynamics of internalization in a more controlled assay, preferentially live-imaging studies where single cells are assessed throughout time, and where the cell subtype is specified, to reduce the variability in the experiment.

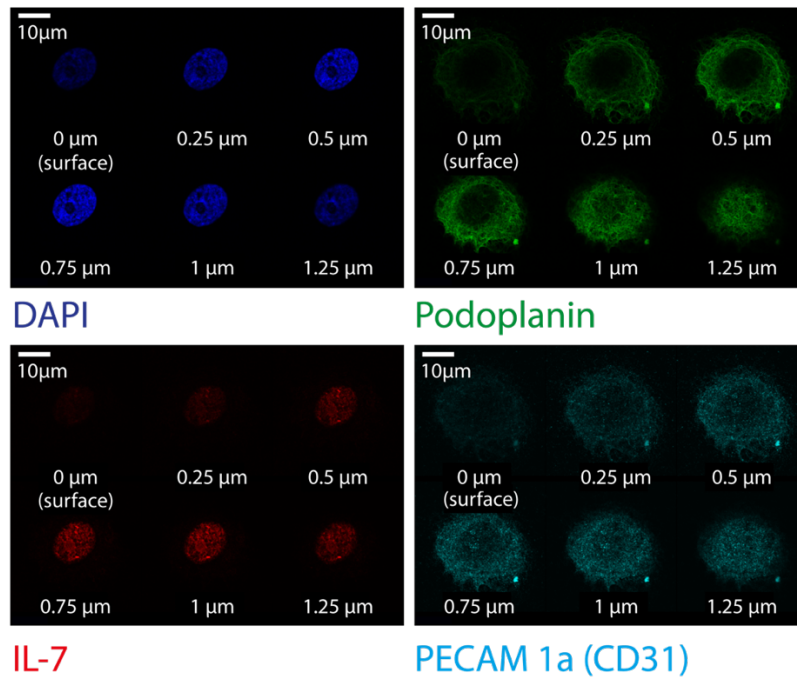
As for Podoplanin being present above the nucleus, but not under it (Figs. 5.5 and 5.6), this might be due to involvement in the formation of a nuclear cap, though a thorough discussion about this observation and topic is beyond the scope of this thesis, but could be an observation to follow up in the future, since it is known that under homeostatic conditions, Podoplanin regulates actomyosin contractility of FRCs, which provides physical tension throughout the FRC network¹⁵, it could be an interesting protein to include in further studies of mechanical regulation of ECM homeostasis by LNSCs.

Also, we observed that IL-7 localizes inside the nucleus, but in the areas where the DAPI signal is missing. We are unsure about the causes and consequences of this observation, but it is worth noting that the Nucleolus is not normally stained by DAPI, and it has been shown to be involved in the sequestration of specific proteins to regulate specific activities during the cell cycle¹⁸². A thorough discussion of this topic is also beyond the scope of this thesis, but these observations could be followed up in the future.

We were not able to derive any conclusions based on the analysis of PECAM-1a distribution. Since it is a membrane bound receptor, the sparse location of the stain throughout the cell may be due to absence of the receptor on the membrane, or a problem with the staining itself. Also, we were not able to block the internalization with the antibody tested. We are not sure whether this is because the concentration of the antibody was too low, in combination with the fact that a polyclonal antibody (in fact a population of different antibodies that bind to different parts of the receptor), decreases the probability of actually blocking the binding site for IL-7 on the receptor. It would be worth testing higher concentrations of this antibody to see if blockade of IL-7 binding and processing can be achieved, and alternatively, using a different antibody source. In addition, it would be worth trying to block the receptors before cell exposure to IL-7, since in this setup, it is possible that both IL-7 and the antibody are binding to the receptors at the same time, and competing for the binding instead. Another suggestion for a follow up experiment, would be to investigate whether the IL7RA receptor is internalized in conjunction with IL-7. This should point toward the involvement of the clathrin-mediated internalization previously mentioned in Section 5.3.3⁷⁴.

LNSC with internalised IL-7 after 20 min incubation.

A Z-Stack



B Merge

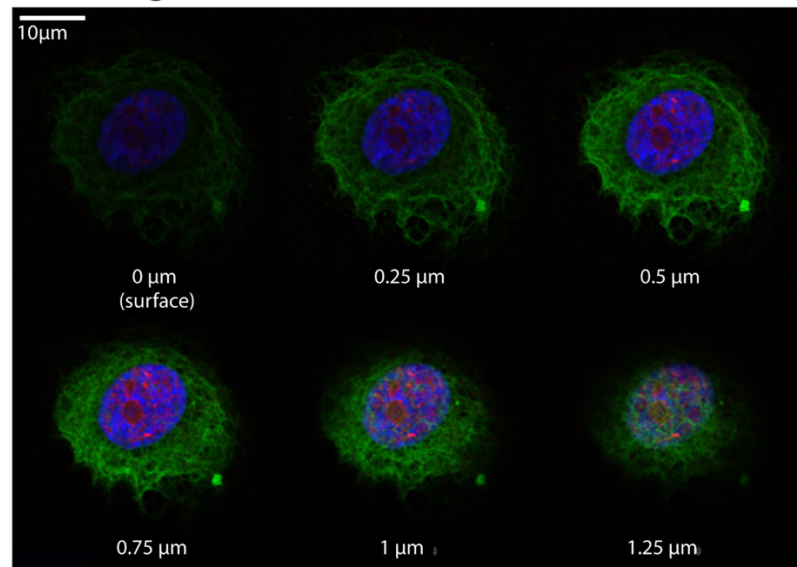
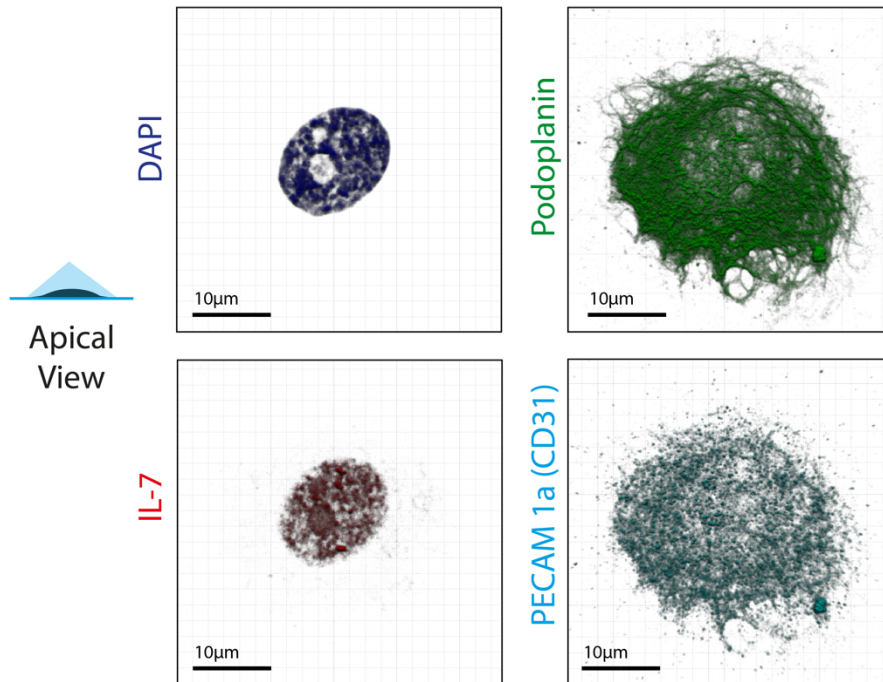


Figure 5.5. Attempt to identify LNSC subsets that undergo A647-hIL7 internalisation. Here, an A647-hIL7 internalization by a LNSC after 20min of A647-hIL7 incubation, stained for Podoplanin (A488-green), PECAM-1 (A546-cyan), DAPI (blue). Cells were seed at a density of 5×10^3 cells /cm² on Poly-L-Lysine coated glass slides, incubated for 1 hour at 37°C with 5%CO₂, the substrates washed once with medium to remove non-adhering cells, and with recombinant human A647-rhIL7 at 100 ng/ml. After 20 or 60 minutes, the cells were fixed with 4% paraformaldehyde in PBS for 10 minutes at 37°C, washed and prepares for immunocytochemistry. A) Stack showing the distribution of DAPI, Podoplanin, A647-IL-7 and PECAM-1a at different heights from the glass culture surface. B) Merge of same signals.

Detail of Internalised IL-7 into LNSC after 20 min incubation.

A 3D volume reconstruction



B 3D surface reconstruction

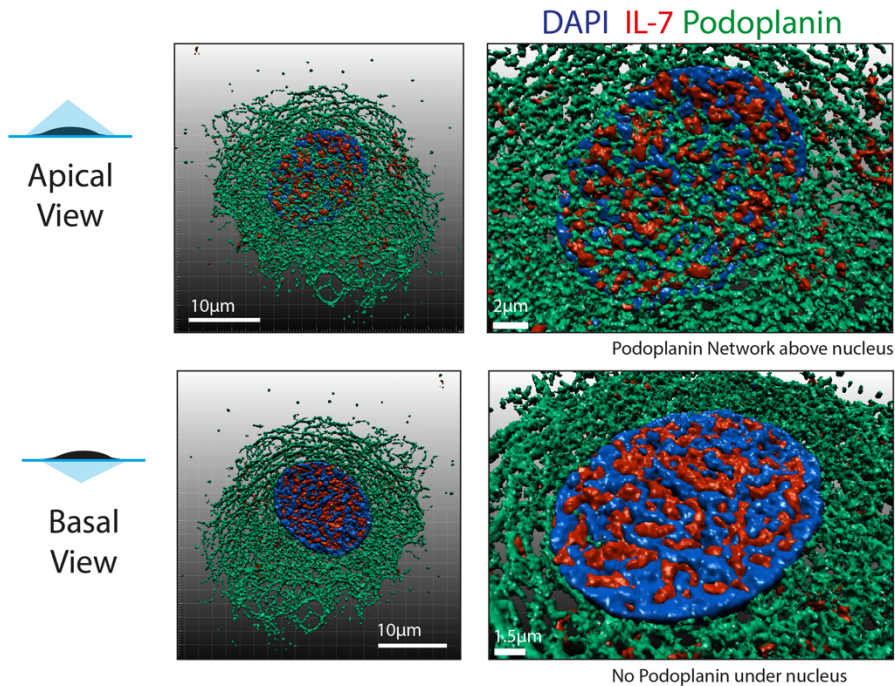
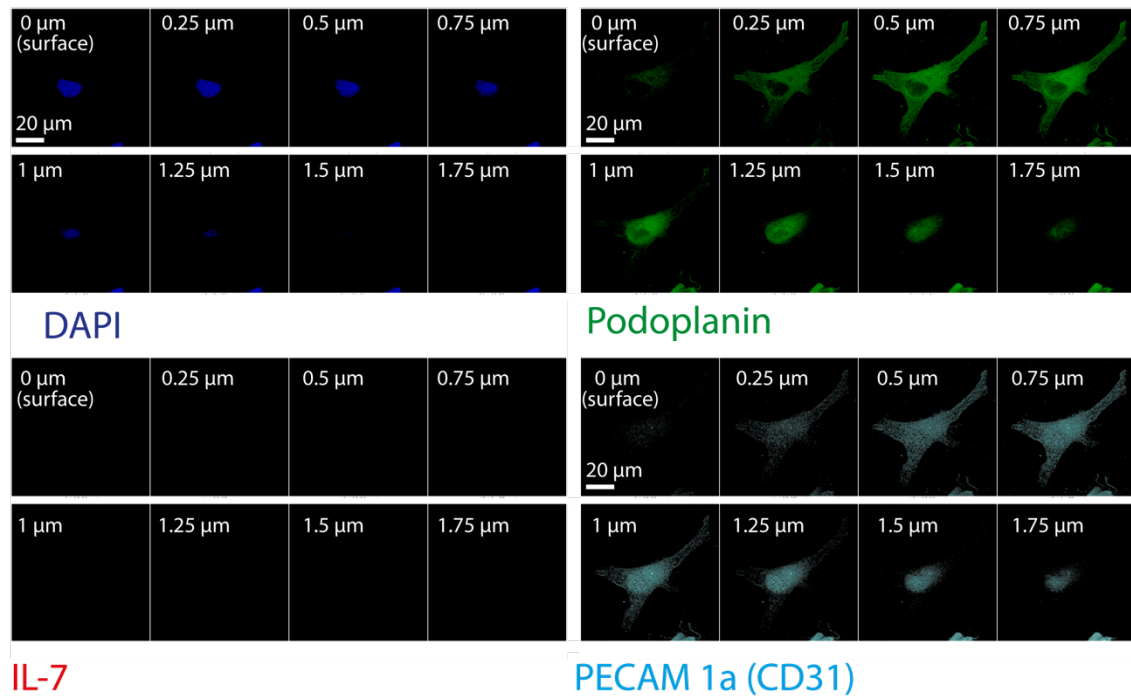


Figure 5.6. A647-hIL-7 internalization by LNSCs after 20min of A647-hIL7 incubation. Structural analysis by 3D reconstruction of components: A647-rhIL-7 (red), Podoplanin (A488-green), PECAM-1 (A546-cyan), and DAPI (blue). A) 3D volume reconstruction showing the fibrillar nature of Podoplanin, a sparse signal for PECAM-1a, and inversely localized signals for DAPI and IL-7. B) 3D surface reconstruction showing a clear z-axial polarization of Podoplanin fibers, where Podoplanin localizes above the nucleus of the cell (Upper View), but not under (Under view).

LNSC without internalised IL-7 after 20 min incubation.

A Z-Stack



B Merge

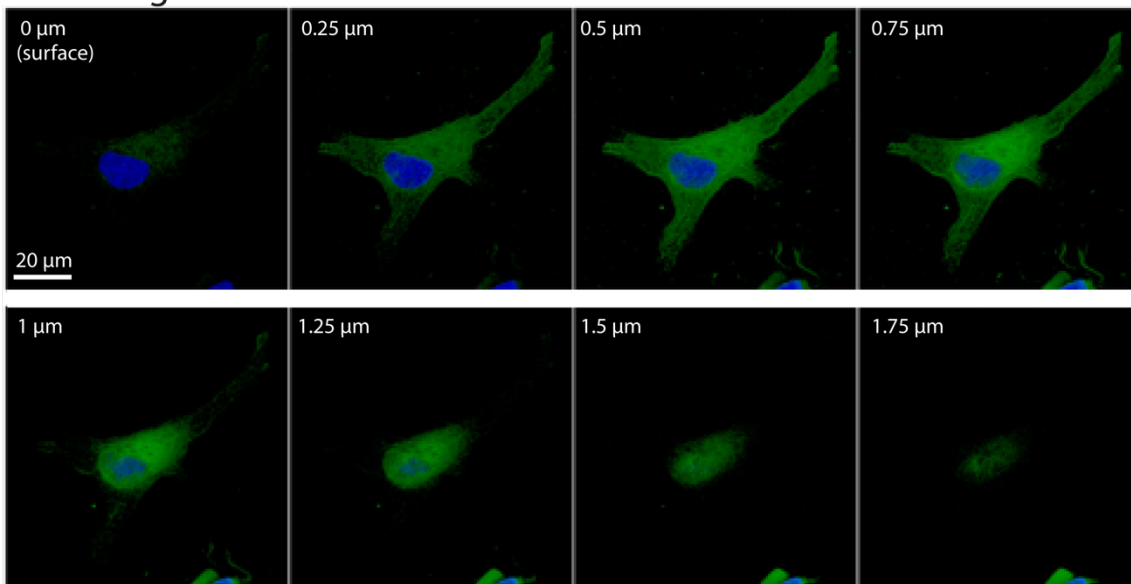


Figure 5.7. Attempt to identify LNSC subsets that undergo A647-hIL7 internalization. Cells were seeded at a density of 5×10^3 cells /cm² on Poly-L-Lysine coated glass slides, incubated for 1 hour at 37°C with 5%CO₂, the substrates washed once with medium to remove non-adhering cells, and with recombinant human A647-rhIL7 at 100 ng/ml. After 20 or 60 minutes, the cells were fixed with 4% paraformaldehyde in PBS for 10 minutes at 37°C, washed and prepares for immunocytochemistry. Here, a cell exposed to A647-hIL-7 that did not internalize it after 20min of A647-hIL7 incubation. Staining was performed for Podoplanin (A488-green), PECAM-1 (A546-cyan), DAPI (blue). A) Stack showing the distribution of DAPI, Podoplanin, A647-IL-7 and PECAM-1a at different heights from the glass culture surface. B) Merge of same signals.

LNSC + A647-rhIL-7 + anti-IL7RA after 60 minute incubation.

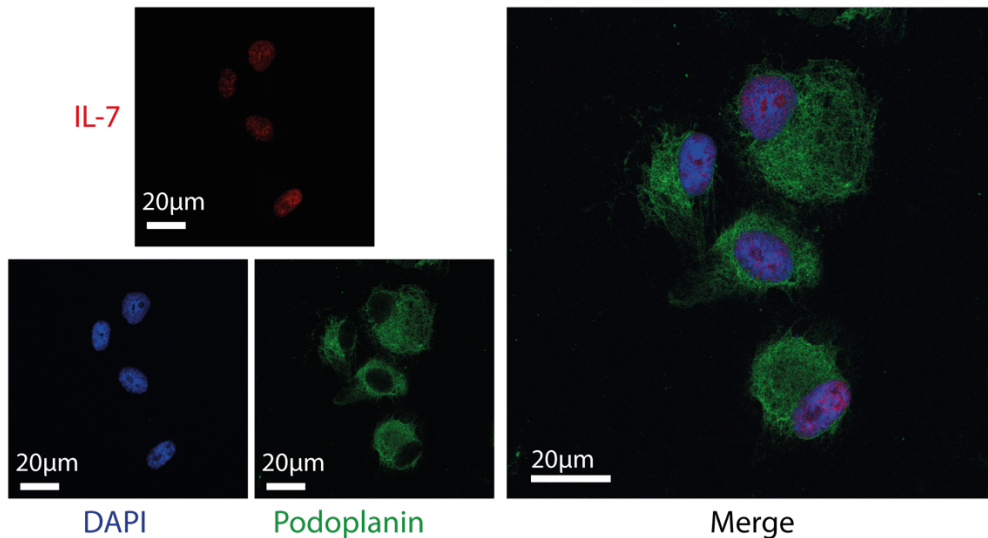


Figure 5.8. Attempt to block human A647-IL-7 internalization by LNSC, by the addition of a goat polyclonal anti-IL7RA antibody (R&D AF-306-PB). Cells were seed at a density of 5×10^3 cells /cm² on Poly-L-Lysine coated glass slides, incubated for 1 hour at 37 °C with 5%CO₂, the substrates washed once with medium to remove non-adhering cells, after which A647-rhIL7 at 100 ng/ml and a goat polyclonal anti-IL7RA antibody (R&D AF-306-PB) at 2.5µg/ml were added to assess whether we could block the internalization. After 20 or 60 minutes, the cells were fixed with 4% paraformaldehyde in PBS for 10 minutes at 37 °C, washed and prepares for immunocytochemistry. IL-7 internalization was still observed after 20 minutes of culture.

Finally, we wanted to find a way to detect this in situ, which cells are responsible for IL-7 internalization, so we could further use the method in our FN-FRET assays, such as cell-assembled ECM, and manually pulled FN fibers. Using the method presented, we were not able to find a robust way of quantifying the signals needed to identify LNSCs subsets responsible for IL-7 internalization, but more suitable methods exist to address this issue, such as flow cytometry. The presented findings hopefully motivate new work in this area.

4.6. Assay to assess cell function on de-cellularized ECM substrates subjected to perpendicular flow.

Since we were interested in obtaining cell-assembled ECMs with different FN conformations that would allow us to test binding of IL-7 to different conformations of FN, we resorted to the idea of producing ECM under fluid flow conditions that could potentially alter the deposited ECM. Indeed, in experimental 3D culture models, it was found that interstitial flow of 3–10 µm per second can cause fibroblasts to align collagen fibers within 12–24 hours¹⁸³, and shear stress has also been shown to drive the formation of ECM by FRCs¹⁸⁴. Furthermore, increased lymph flow is an immediate and essential response to tissue injury or inflammation, and a suitable platform to investigate the influence of fluid flow on ECM structure, cell migration, and to add the possibility of using FN-FRET to assess FN conformation, would be very useful for further studies.

To address this issue, we developed an assay to subject fibroblast/ECM cultures to perpendicular flow. The idea behind this assay is that while most fluid flow cells apply flow perpendicular to the surface of a

cell culture or cell-assembled ECM. This assay, in contrast, allows for the application of fluid flow perpendicular to the ECM surface. Furthermore, it is also possible to study migration of lymphocytes through cell- assembled ECM. As a first step, we tested the assay by producing de-cellularized ECM and investigated whether Jurkat T-cells (used as a model lymphocyte cell-line) could migrate through the produced de-cellularized ECM, under the influence of fluid flow. In previous experiments, we were confronted with the situation that these cells do not infiltrate cell- assembled ECM if they are simply seeded on them, but we found that in our perpendicular fluid-flow assay, they do.

4.6.1. Method

First, an initial ECM was produced inside a sterile and empty Falcon 8.0 μm pore size PET track-etched membrane cell culture insert in 24 well format (Cat. No. 35-3097) as follows: The membranes were coated with 20 $\mu\text{g}/\text{ml}$ fibronectin in PBS and incubated for 30 minutes at room temperature and then rinsed with PBS. We then seeded NIH 3T3 fibroblasts at 8×10^4 cells/ cm^2 and incubated them for 30 min to allow them to adhere. Non-adhering cells were then removed by washing once with medium, and then the medium was replaced with one containing 50 $\mu\text{g}/\text{ml}$ fibronectin (10% of this was labelled only with the donor dye Alexa 488). 48 hours later, the medium was replenished again with medium enriched with 50 $\mu\text{g}/\text{ml}$ fibronectin (with 10% A488-FN), and after 48 more hours, the produced ECMs were de-cellularized using a previously used method⁶⁰, which is further based on the methods described in¹⁷²⁻¹⁷⁵. An updated paper describing related protocols can be found in¹⁷⁶.

First, the medium was removed and the cells washed twice with PBS, and subsequently, rinsed three times with Wash Buffer I (0.1 M Na_2HPO_4 , 2 mM MgCl_2 , 2nM EGTA in distilled water, adjusted to pH 9.6 with NaOH). Then, the samples were incubated with Lysis Buffer (8 mM Na_2HPO_4 in distilled water, adjusted to pH 9.6 with 0.1 M NaOH + 1% Triton X-100) for 15 minutes at 37°C. The Lysis Buffer was then removed, leaving about 50 μl in the well to preserve the remaining de-cellularized ECM, and the next steps performed leaving 50 μl of liquid, for the same purpose. The cultures were then subjected to a second incubation with fresh Lysis Buffer, for one hour at 37°C, and then rinsed with Wash Buffer II (10 mM Na_2HPO_4 , 0.3M KCl in distilled water, adjusted to pH 7.5 with HCl), and washed three times with deionized water, and one final time with PBS. These de-cellularized ECM were stored at 4°C if needed and for no longer than a week.

Prior to the addition of Jurkat T-cells to the system, these were membrane stained to localize them by suspending them at a density of 1×10^6 /mL in serum-free culture medium, and adding 5 μL Vybrant per mL of cell suspension and mixing well by gentle pipetting. The cells were then incubated for 2 minutes at 37°C and then centrifuged at 1100 rpm for 5 minutes. The supernatant was then gently removed and the cells re-suspend the cells in warm (37°C) serum-free medium. This washing was repeated two more times.

To prepare the system, the fluid flow chamber was first assembled as shown in Fig. 5.9-A using 1mm diameter tubing, Amersham chromatography holders (red), various connectors and washer from an Amersham GE Healthcare Peristaltic Pump P-1, (Product No. 18-1110-91), and an inverted syringe with inserted tubing as depicted, and a sterile and empty Falcon 8.0 μm pore size PET track-etched membrane cell culture insert in 24 well format (Cat. No. 35-3097). With the system assembled, 50ml of 70% Ethanol were drained through, and the system was then disconnected with ethanol still inside the tubes. All the materials were then immersed in 70% ethanol and left for disinfection overnight. Work after disinfection of the material was done with sterile gloves and in the cell culture hood to avoid contamination. The device was once more assembled and drained with 50 ml sterile PBS to clear the ethanol. This procedure was repeated twice and the system drained completely. Very carefully, the empty cell membrane insert was replaced with the one holding the de-cellularized ECM. The system was then drained with 50 ml of medium with the pump at speed 1×10 (Fig. 5.9-B-C), while check that no air bubbles were present in the

system. We did not encounter mayor issues with bubble formation, but if this becomes an issue, bubble trap can be inserted between tubing connections. Once the medium was drained (but not fully, the speed was adjusted to 1x1 (Fig. 5.9-C) to get the adequate flow rate. A 1x1 setting with 1mm tube diameter provided a flow rate of 1ml/hr.

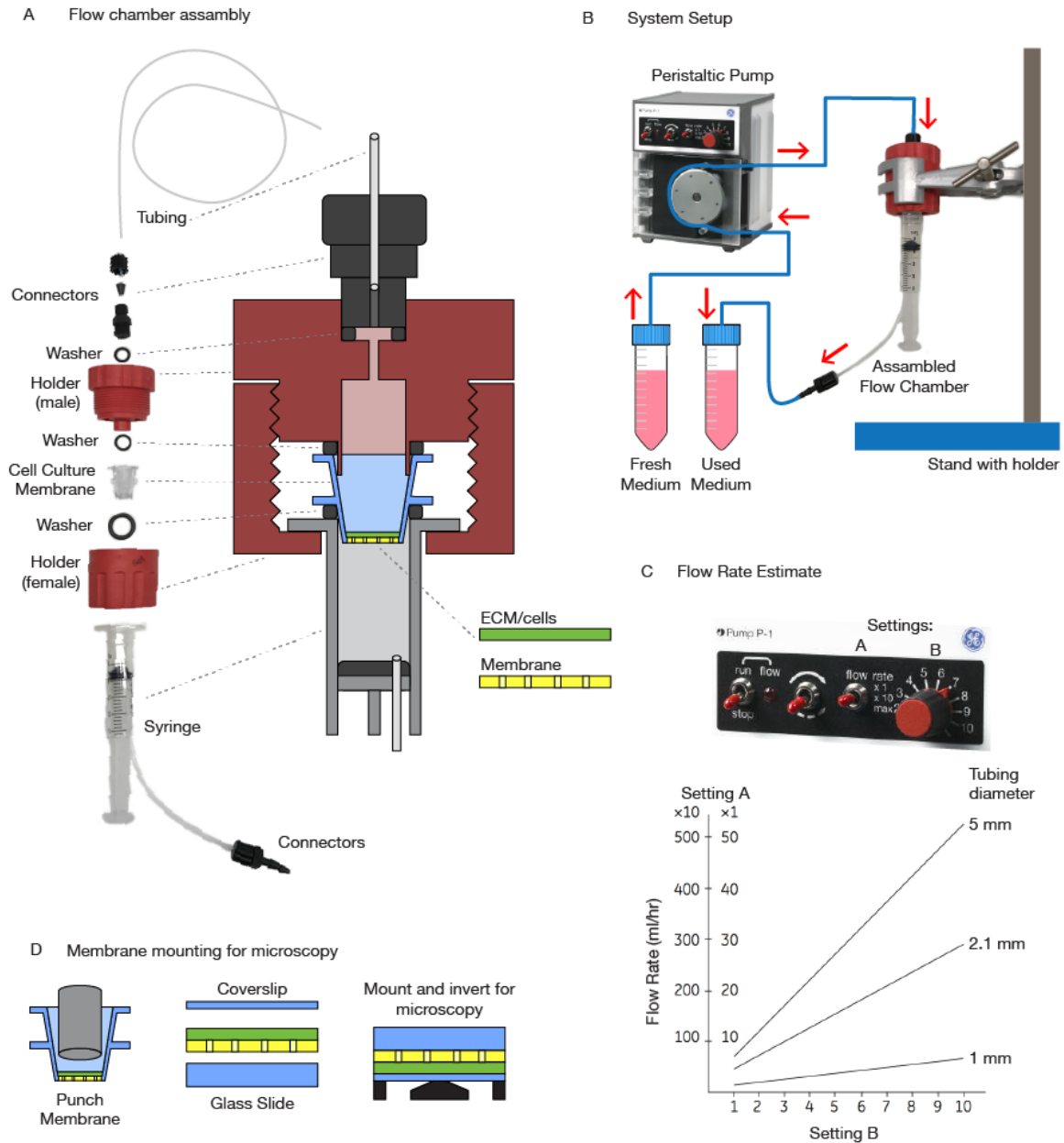


Figure 5.9. Fluid flow chamber with perpendicular fluid flow. A) Flow chamber assembly. B) System setup with peristaltic pump C) Physiologically relevant flow rate estimate. D) Membrane mounting for confocal microscopy.

As shown in the following derivation, where R_v is the volumetric flow rate, A is the surface area of the cross section on which the flow occurs (i.e. the membrane's area = 30 mm^2), and v being the velocity of the flow, this provides a fluid velocity of $10 \mu\text{m/s}$ in our system, which closely resembles that found in fluid flow

flowing through the lymph nodes (0.1–1 $\mu\text{m}/\text{second}$), and that has been previously used in experimental 3D culture models (interstitial flow of 3–10 $\mu\text{m}/\text{second}$ caused fibroblasts to align collagen fibres within 12–24 hours), as reviewed by ¹⁸³:

$$R_v = Av \quad [5.2]$$

$$R_v = 1\text{ml/hr} = 3 \times 10^{-4}\text{ml/s} = 0.3\text{mm}^3/\text{s} \quad [5.3]$$

Solving for v in Equation 5.2, we obtain a fluid velocity in our system of:

$$v = \frac{R_v}{A} = \frac{0.3\text{mm}^3/\text{s}}{30\text{mm}^2} = 0.01\text{mm/s} = 10\mu\text{m/s} \quad [5.4]$$

To seed the cells, the previously stained Jurkat cells were re-suspended in 10ml medium and drained through the system. Once the volume of medium/cells has passed through the system, fresh medium was continuously supplied for the duration of the experiment (30 min).

After 30 minutes, the membranes were collected and mounted for microscopy. Carefully, on a bowl to hold any spilling liquid, the fluid flow was stopped, and the assembled flow chamber unplugged from the tubing. Very carefully, the syringe plug was pulled to retract the remaining liquid from the chamber with the cell membrane insert, and the system was disassembled to remove the cell membrane insert. This was then placed on a petri dish and the cells fixed with 5% formaldehyde in PBS and incubated at 37°C for 20min. The membranes were then washed 3x with PBS, and punched out of the insert with a tissue punch. They were then mounted between a glass slide and a coverslip with mounting medium, with the ECM side looking towards the coverslip. The mounting medium was then allowed to cure before imaging with a confocal microscope (Fig. 5.9D).

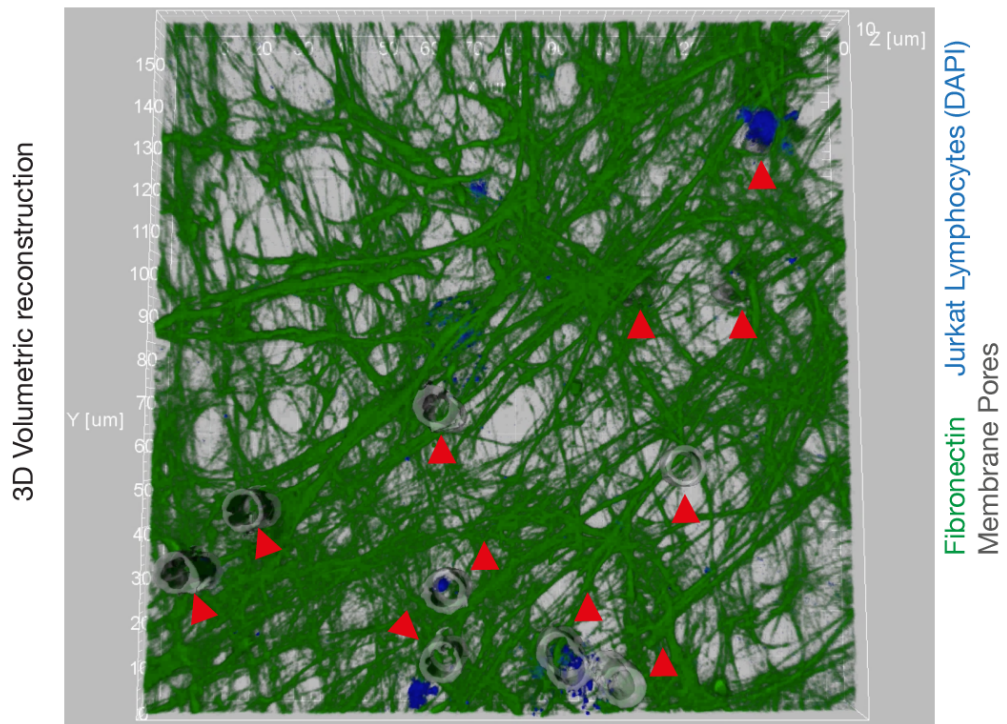
4.6.2. Results

We show here, as proof of concept, that this assay can be used to culture cells on de-celularized ECM under fluid flow. Jurkat cells were shown to actively infiltrate the produced ECMs, and cross the pores that sustain the ECM (Fig. 5.10). It is important to note that the pore size is large enough for lymphocytes to be able to cross them, yet small enough to make it difficult for fibroblasts to do so, thus enabling them to use the membrane as a substrate to grow ECM.

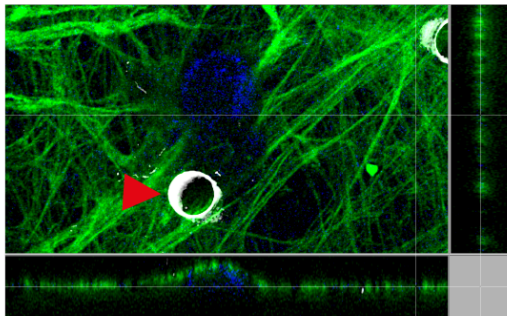
4.6.3. Discussion and Conclusion

While these results show only a proof of concept, it would also be possible to initially culture cells on the constructs, and transfer them to the flow chamber to perform experiments where fibroblasts, or of interest in the context of this thesis, LNSCs, can proceed with the production and/or remodeling of their ECM under the influence of fluid flow. Furthermore, the medium can be enriched with FN-FRET, instead of single labelled A488-FN, and in such way, allow for the assessment of FN conformation using the techniques previously described (Chapter 3). The limitation of this assay is that it is not possible to perform live-studies. Membranes need to be resected and mounted to be able to image them. Further studies would need to be performed to assess whether this manipulation affects the conformation of FN or the properties of the ECM in a significant way. As an alternative for analysis of lymphocytes cells that have gone through the process of migration through these membranes, it would be possible to collect the medium that has passed through the system, including these cells, centrifuge them, and fix these cells with 5% formaldehyde in PBS, incubated at 37°C for 20min and washed three times with PBS for further analysis. The possibilities of use of this assay can be extended to other cell types, and since the membranes are available commercially, this assay provides an easy and affordable method to perform this kind of studies.

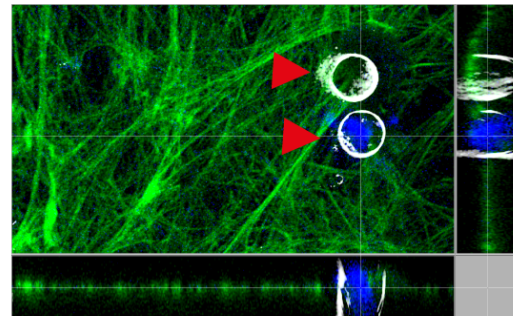
Confocal Microscopy of Jurkat Lymphocytes penetrating cell-derived ECM membranes.



Cell digging into ECM to reach the pores



Cell crossing through a membrane pore



Jurkat Lymphocytes (DAPI) Fibronectin Membrane Pores ▶

Figure 5.10. Jurkat Lymphocytes migrating through a de-cellularized ECM while subjected to a perpendicular fluid flow in a flow chamber.

5. Outlook

Since we have found that stretching of FN fibers increases IL-7 binding, it would be of interest to determine what impact do these findings have on cell function. The preliminary experiments presented in Chapter 5 provide a starting point to motivate the refinement and/or development of adequate assays to test the physiological implications of our findings. In addition to the experiments presented in Chapter 5, we performed very preliminary experiments to attempt to detect changes in STAT5, NFAT-c1 and Bcl-2 signaling due to the increased concentration of IL-7 on stretched FN fibers. These very first attempts were inconclusive, and an adequate read-out system needs still to be developed to be able to identify such changes in downstream signaling. A mayor limitation is the fact that is not possible to harvest cells that have specifically interacted with FN-bound IL7, and therefore, an on-site readout system needs to be developed. As a possible alternative, novel methods have recently been developed that allow, using a nanosyringe, the extraction of the contents of single cells bound to a substrate to further analyze their content at the molecular level ¹⁸⁵.

Since we localized the FN binding site on the CD-loop region of IL-7, which seems to remain available for simultaneous interaction with FN while IL-7 is bound to its cognate cell receptors, a suggested experiment to corroborate this finding could be to assess whether recombinant human IL7R α and/or IL7RG are able to binding to FN-fiber-bound IL-7, though the design of such experiments should consider the possibility that both receptors need to be forming a heterodimer to bind IL-7. A good review to consider these aspects can be found in ⁸.

Since we have proposed a negative-feedback mechanism reciprocally regulating the tensional state of FN fibers and IL-7 signaling, it would be interesting to test the different cell-ECM-IL-7 interactions in a controlled way. The assays developed and presented in Chapter 5 provide a good starting point towards the understanding of LNSC-IL-7-ECM interactions, even though the initial findings need to be further investigated and corroborated for reproducibility and accuracy, and some assays still require further refinement and development.

The fluid flow assay developed (Section 5.6) could also be considered as a candidate for the development of ECM with varied conformations of FN on which to test binding of IL7. FRET-FN enriched medium can be used in the production of ECM within these assay in order to assess FN conformation. Furthermore, ECM produced by different subsets of LNSC could reveal different FN conformation ranges, and the assay could be used simply to characterize the ECM produced by these cells with and without the influence of shear stresses derived from the application of fluid flow.

6. Conclusion

With this work, we demonstrate how force-induced conformational changes in FN can have an impact on cytokine binding. Though often postulated, our findings that stretching of FN fibers increased IL-7 binding, show for the first time evidence of a mechano-regulated binding of a cytokine to the ECM. We have demonstrated for the first time that the binding of a cytokine to FN fibers is regulated by fiber tension. We could show that FN fiber stretching upregulates IL-7 binding via its CD-loop and suggested a structural mechanism that mediates its binding to FN. We also proposed a mechano-regulated feedback mechanism by which IL-7 might act as prototypical homeostatic cytokine by mediating cytokine/ECM/cell interactions via stretch enhanced IL-7 binding. This work therefore contributes to the understanding of how mechanically induced changes of the ECM affect chemokine and cytokine binding. Furthermore, the FRET based method presented here, which correlates ligand-binding to changes in FN, could be applied to the study of other FN-binding cytokines with the potential of exhibiting mechano-regulated binding. Finally, we have also presented initial attempts at determining the impact of our findings on cellular function.

These studies will hopefully motivate further investigations of mechano-regulated mechanisms by which IL-7 and other cytokines might be stored and/or released as a result of modulating the tensional states of ECM fibers, and the effects that this may have on cellular function. This work therefore raises awareness on the influence of the mechanical properties of the ECM on cytokine binding, and more broadly, on lymphocyte and stromal cell behaviour.

7. References

- (1) Mackall, C. L.; Fry, T. J.; Gress, R. E. Harnessing the Biology of IL-7 for Therapeutic Application. *Nat. Rev. Immunol.* **2011**, *11*, 330–342.
- (2) Restifo, N. P.; Dudley, M. E.; Rosenberg, S. A. Adoptive Immunotherapy for Cancer: Harnessing the T Cell Response. *Nat. Rev. Immunol.* **2012**, *12* (4), 269–281.
- (3) Milone, M. C.; June, C. H. Adoptive Immunotherapy: New Ways to Skin the Cat? *Clin Immunol* **2005**, *117* (2), 101–103.
- (4) Bradley, L. M.; Haynes, L.; Swain, S. L. IL-7: Maintaining T-Cell Memory and Achieving Homeostasis. *Trends Immunol.* **2005**, *26*, 172–176.
- (5) Jiang, Q.; Li, W. Q.; Aiello, F. B.; Mazzucchelli, R.; Asefa, B.; Khaled, A. R.; Durum, S. K. Cell Biology of IL-7, a Key Lymphotrophin. *Cytokine Growth Factor Rev.* **2005**, *16*, 513–533.
- (6) Shitara, S.; Hara, T.; Liang, B.; Wagatsuma, K.; Zuklys, S.; Holländer, G. A.; Nakase, H.; Chiba, T.; Tani-ichi, S.; Ikuta, K. IL-7 Produced by Thymic Epithelial Cells Plays a Major Role in the Development of Thymocytes and TCR $\gamma\delta$ + Intraepithelial Lymphocytes. *J. Immunol.* **2013**, *190*, 6173–6179.
- (7) Surh, C. D.; Sprent, J. Homeostasis of Naive and Memory T Cells. *Immunity* **2008**, *29*, 848–862.
- (8) Walsh, S. T. R. Structural Insights Into the Common Γ -Chain Family of Cytokines and Receptors From the Interleukin-7 Pathway. *Immunol. Rev.* **2012**, *250*, 303–316.
- (9) Dooms, H. Interleukin-7: Fuel for the Autoimmune Attack. *J. Autoimmun.* **2013**, *45*, 40–48.
- (10) Iolyeva, M.; Aebischer, D.; Proulx, S. T.; Willrodt, A.-H.; Ecoiffier, T.; Häner, S.; Bouchaud, G.; Krieg, C.; Onder, L.; Ludewig, B.; Santambrogio, L.; Boyman, O.; Chen, L.; Finke, D.; Halin, C. Interleukin-7 Is Produced by Afferent Lymphatic Vessels and Supports Lymphatic Drainage. *Blood* **2013**, *122*, 2271–2281.
- (11) Onder, L.; Narang, P.; Scandella, E.; Chai, Q.; Iolyeva, M.; Hoorweg, K.; Halin, C.; Richie, E.; Kaye, P.; Westermann, J.; Cupedo, T.; Coles, M.; Ludewig, B. IL-7-Producing Stromal Cells Are Critical for Lymph Node Remodeling. *Blood* **2012**, *120*, 4675–4683.
- (12) Mazzucchelli, R.; Durum, S. K. Interleukin-7 Receptor Expression: Intelligent Design. *Nat. Rev. Immunol.* **2007**, *7*, 144–154.
- (13) Bonnans, C.; Chou, J.; Werb, Z. Remodelling the Extracellular Matrix in Development and Disease. *Nat. Rev. Mol. Cell Bio.* **2014**, *15*, 786–801.
- (14) Sorokin, L. The Impact of the Extracellular Matrix on Inflammation. *Nat. Rev. Immunol.* **2010**, *10*, 712–723.
- (15) Fletcher, A. L.; Acton, S. E.; Knoblich, K. Lymph Node Fibroblastic Reticular Cells in Health and Disease. *Nat. Rev. Immunol.* **2015**, *15*, 350–361.
- (16) Hynes, R. O. The Extracellular Matrix: Not Just Pretty Fibrils. *Science* **2009**, *326* (5957), 1216–1219.
- (17) Vogel, V. Mechanotransduction Involving Multimodular Proteins: Converting Force Into Biochemical Signals. *Annu. Rev. Biophys. Biomol. Struct.* **2006**, *35*, 459–488.
- (18) Ariel, A.; HersHKoviz, R.; Cahalon, L.; Williams, D. E.; Akiyama, S. K.; Yamada, K. M.; Chen, C.; Alon, R.; Lapidot, T.; Lider, O. Induction of T Cell Adhesion to Extracellular Matrix or Endothelial Cell Ligands by Soluble or Matrix-Bound Interleukin-7. *Eur. J. Immunol.* **1997**, *27*, 2562–2570.

- (19) Kitazawa, H.; Muegge, K.; Badolato, R.; Wang, J. M.; Fogler, W. E.; Ferris, D. K.; Lee, C. K.; Candéias, S.; Smith, M. R.; Oppenheim, J. J.; Durum, S. K. IL-7 Activates Alpha4beta1 Integrin in Murine Thymocytes. *J. Immunol.* **1997**, *159*, 2259–2264.
- (20) Zollinger, A. J.; Smith, M. L. Fibronectin, the Extracellular Glue. *Matrix Biol.* **2016**, *60-61*, 27–37.
- (21) Pankov, R.; Yamada, K. M. Fibronectin at a Glance. *J Cell Sci* **2002**.
- (22) Leiss, M.; Beckmann, K.; Girós, A.; Costell, M.; Fässler, R. The Role of Integrin Binding Sites in Fibronectin Matrix Assembly in Vivo. *Curr Opin Cell Biol* **2008**, *20* (5), 502–507.
- (23) Martino, M. M.; Hubbell, J. A. The 12th-14th Type III Repeats of Fibronectin Function as a Highly Promiscuous Growth Factor-Binding Domain. *FASEB J.* **2010**, *24*, 4711–4721.
- (24) Zhu, J.; Clark, R. A. F. Fibronectin at Select Sites Binds Multiple Growth Factors and Enhances Their Activity: Expansion of the Collaborative ECM-GF Paradigm. *J. Invest. Dermatol.* **2014**, *134*, 895–901.
- (25) Chabria, M.; Hertig, S.; Smith, M. L.; Vogel, V. Stretching Fibronectin Fibres Disrupts Binding of Bacterial Adhesins by Physically Destroying an Epitope. *Nat. Commun.* **2010**, *1*, 135.
- (26) Humphrey, J. D.; Dufresne, E. R.; Schwartz, M. A. Mechanotransduction and Extracellular Matrix Homeostasis. *Nat. Rev. Mol. Cell Bio.* **2014**, *15* (12), 802–812.
- (27) Antia, M.; Baneyx, G.; Kubow, K. E.; Vogel, V. Fibronectin in Aging Extracellular Matrix Fibrils Is Progressively Unfolded by Cells and Elicits an Enhanced Rigidity Response. *Faraday Discuss* **2008**, *139*, 229–249; discussion309–discussion325, 419–420.
- (28) Schwarzbauer, J. E.; Desimone, D. W. Fibronectins, Their Fibrillogenesis, and in Vivo Functions. *Cold Spring Harbor Perspectives in Biology* **2011**, *3* (7), a005041–a005041.
- (29) Singh, P.; Carraher, C.; Schwarzbauer, J. E. Assembly of Fibronectin Extracellular Matrix. *Annu Rev Cell Dev Bi* **2010**, *26* (1), 397–419.
- (30) Mosher, D. F.; Furcht, L. T. Fibronectin: Review of Its Structure and Possible Functions. *Journal of Investigative Dermatology* **1981**, *77* (2), 175–180.
- (31) Potts, J. R.; Campbell, I. D. Fibronectin Structure and Assembly. *Curr Opin Cell Biol* **1994**, *6* (5), 648–655.
- (32) Hynes, R. O. *Fibronectins*; Springer-Verlag: New York, NY, 1990.
- (33) Baron, M.; Norman, D.; Willis, A.; Campbell, I. D. Structure of the Fibronectin Type 1 Module. *Nature* **1990**, *345* (6276), 642–646.
- (34) Ozhogina, O. A.; Trexler, M.; Bányai, L.; Llinás, M.; Patthy, L. Origin of Fibronectin Type II (FN2) Modules: Structural Analyses of Distantly-Related Members of the Kringle Family Idey the Kringle Domain of Neurotrypsin as a Potential Link Between FN2 Domains and Kringles. *Protein Sci* **2001**, *10* (10), 2114–2122.
- (35) Dickinson, C. D.; Gay, D. A.; Parello, J.; Ruoslahti, E.; Ely, K. R. Crystals of the Cell-Binding Module of Fibronectin Obtained From a Series of Recombinant Fragments Differing in Length. *J. Mol. Biol.* **1994**, *238* (1), 123–127.
- (36) Dickinson, C. D.; Veerapandian, B.; Dai, X. P.; Hamlin, R. C.; Xuong, N. H.; Ruoslahti, E.; Ely, K. R. Crystal Structure of the Tenth Type III Cell Adhesion Module of Human Fibronectin. *J. Mol. Biol.* **1994**, *236* (4), 1079–1092.
- (37) White, E. S.; Muro, A. F. Fibronectin Splice Variants: Understanding Their Multiple Roles in Health and Disease Using Engineered Mouse Models. *IUBMB Life* **2011**, *63* (7), 538–546.

- (38) White, E. S.; Baralle, F. E.; Muro, A. F. New Insights Into Form and Function of Fibronectin Splice Variants. *J. Pathol.* **2008**, *216* (1), 1–14.
- (39) Bingham, R. J.; Rudiño-Piñera, E.; Meenan, N. A. G.; Schwarz-Linek, U.; Turkenburg, J. P.; Höök, M.; Garman, E. F.; Potts, J. R. Crystal Structures of Fibronectin-Binding Sites From *Staphylococcus Aureus* FnBPA in Complex with Fibronectin Domains. *Proc. Natl. Acad. Sci. U. S. A.* **2008**, *105*, 12254–12258.
- (40) Erat, M. C.; Schwarz-Linek, U.; Pickford, A. R.; Farndale, R. W.; Campbell, I. D.; Vakonakis, I. Implications for Collagen Binding From the Crystallographic Structure of Fibronectin 6FnI1-2FnII7FnI. *J. Biol. Chem.* **2010**, *285* (44), 33764–33770.
- (41) Main, A. L.; Harvey, T. S.; Baron, M.; Boyd, J.; Campbell, I. D. The Three-Dimensional Structure of the Tenth Type III Module of Fibronectin: an Insight Into RGD-Mediated Interactions. *Cell (Cambridge, MA, U. S.)* **1992**, *71* (4), 671–678.
- (42) Pettersen, E. F.; Goddard, T. D.; Huang, C. C.; Couch, G. S.; Greenblatt, D. M.; Meng, E. C.; Ferrin, T. E. UCSF Chimera--a Visualization System for Exploratory Research and Analysis. *J. Comput. Chem.* **2004**, *25*, 1605–1612.
- (43) Alon, R.; Cahalon, L.; Hershkovich, R.; Elbaz, D.; Reizis, B.; Wallach, D.; Akiyama, S. K.; Yamada, K. M.; Lider, O. TNF-Alpha Binds to the N-Terminal Domain of Fibronectin and Augments the Beta 1-Integrin-Mediated Adhesion of CD4+ T Lymphocytes to the Glycoprotein. *J. Immunol.* **1994**, *152*, 1304–1313.
- (44) Schwarz-Linek, U.; Werner, J. M.; Pickford, A. R.; Gurusiddappa, S.; Kim, J. H.; Pilka, E. S.; Briggs, J. A. G.; Gough, T. S.; Höök, M.; Campbell, I. D.; Potts, J. R. Pathogenic Bacteria Attach to Human Fibronectin Through a Tandem Beta-Zipper. *Nature* **2003**, *423*, 177–181.
- (45) Schwarz-Linek, U.; Höök, M.; Potts, J. R. Fibronectin-Binding Proteins of Gram-Positive Cocci. *Microbes Infect.* **2006**, *8* (8), 2291–2298.
- (46) Norris, N. C.; Bingham, R. J.; Harris, G.; Speakman, A.; Jones, R. P. O.; Leech, A.; Turkenburg, J. P.; Potts, J. R. Structural and Functional Analysis of the Tandem B-Zipper Interaction of a Streptococcal Protein with Human Fibronectin. *J. Biol. Chem.* **2011**, *286*, 38311–38320.
- (47) Hertig, S.; Chabria, M.; Vogel, V. Engineering Mechanosensitive Multivalent Receptor-Ligand Interactions: Why the Nanolinker Regions of Bacterial Adhesins Matter. *Nano Lett.* **2012**, *12*, 5162–5168.
- (48) Bellis, S. L. Advantages of RGD Peptides for Directing Cell Association with Biomaterials. *Biomaterials* **2011**, *32* (18), 4205–4210.
- (49) Yamada, K. M. Fibronectins: Structure, Functions and Receptors. *Curr Opin Cell Biol* **1989**, *1* (5), 956–963.
- (50) George, E. L.; Georges-Labouesse, E. N.; Patel-King, R. S.; Rayburn, H.; Hynes, R. O. Defects in Mesoderm, Neural Tube and Vascular Development in Mouse Embryos Lacking Fibronectin. *Development* **1993**, *119* (4), 1079–1091.
- (51) Vega, M. E.; Schwarzbauer, J. E. Collaboration of Fibronectin Matrix with Other Extracellular Signals in Morphogenesis and Differentiation. *Curr Opin Cell Biol* **2016**, *42*, 1–6.
- (52) Lenselink, E. A. Role of Fibronectin in Normal Wound Healing. *Int Wound J* **2015**, *12* (3), 313–316.
- (53) Wang, Y.; Ni, H. Fibronectin Maintains the Balance Between Hemostasis and Thrombosis. *Cell Mol Life Sci* **2016**, *73* (17), 1–13.
- (54) Cukierman, E.; Bassi, D. E. Physico-Mechanical Aspects of Extracellular Matrix Influences on Tumorigenic Behaviors. *Seminars in Cancer Biology* **2010**, *20* (3), 139–145.
- (55) Wang, K.; Seo, B. R.; Fischbach, C.; Gourdon, D. Fibronectin Mechanobiology Regulates Tumorigenesis. *Cel. Mol. Bioeng.* **2016**, *9* (1), 1–11.

- (56) Iijima, J.; Konno, K.; Itano, N. Inflammatory Alterations of the Extracellular Matrix in the Tumor Microenvironment. *Cancers (Basel)* **2011**, *3* (3), 3189–3205.
- (57) Zhang, X.; Chen, C. T.; Bhargava, M.; Torzilli, P. A. A Comparative Study of Fibronectin Cleavage by MMP-1, -3, -13, and -14. *Cartilage* **2012**, *3* (3), 267–277.
- (58) Smith, M. L.; Gourdon, D.; Little, W. C.; Kubow, K. E.; Eguiluz, R. A.; Luna-Morris, S.; Vogel, V. Force-Induced Unfolding of Fibronectin in the Extracellular Matrix of Living Cells. *PLoS Biol.* **2007**, *5*, e268.
- (59) Legant, W. R.; Chen, C. S.; Vogel, V. Force-Induced Fibronectin Assembly and Matrix Remodeling in a 3D Microtissue Model of Tissue Morphogenesis. *Integr. Biol.* **2012**, *4*, 1164–1174.
- (60) Kubow, K. E.; Klotzsch, E.; Smith, M. L.; Gourdon, D.; Little, W. C.; Vogel, V. Crosslinking of Cell-Derived 3D Scaffolds Up-Regulates the Stretching and Unfolding of New Extracellular Matrix Assembled by Reseeded Cells. *Integr. Biol.* **2009**, *1*, 635–648.
- (61) García, A. J.; Vega, M. D.; Boettiger, D. Modulation of Cell Proliferation and Differentiation Through Substrate-Dependent Changes in Fibronectin Conformation. *Mol. Biol. Cell* **1999**, *10* (3), 785–798.
- (62) Sun, Z.; Guo, S. S.; Fässler, R. Integrin-Mediated Mechanotransduction. *J. Cell Biol.* **2016**, *215* (4), 445–456.
- (63) Bradshaw, M. J.; Smith, M. L. Multiscale Relationships Between Fibronectin Structure and Functional Properties. *Acta Biomaterialia* **2013**, *10* (4), 1524–1531.
- (64) Klingberg, F.; Chow, M. L.; Koehler, A.; Boo, S.; Buscemi, L.; Quinn, T. M.; Costell, M.; Alman, B. A.; Genot, E.; Hinz, B. Prestress in the Extracellular Matrix Sensitizes Latent TGF- β 1 for Activation. *J. Cell Biol.* **2014**, *207*, 283–297.
- (65) Little, W. C.; Smith, M. L.; Ebnetter, U.; Vogel, V. Assay to Mechanically Tune and Optically Probe Fibrillar Fibronectin Conformations From Fully Relaxed to Breakage. *Matrix Biol.* **2008**, *27*, 451–461.
- (66) Zhong, C.; Chrzanowska-Wodnicka, M.; Brown, J.; Shaub, A.; Belkin, A. M.; Burrige, K. Rho-Mediated Contractility Exposes a Cryptic Site in Fibronectin and Induces Fibronectin Matrix Assembly. *J. Cell Biol.* **1998**, *141* (2), 539–551.
- (67) Little, W. C.; Schwartlander, R.; Smith, M. L.; Gourdon, D.; Vogel, V. Stretched Extracellular Matrix Proteins Turn Fouling and Are Functionally Rescued by the Chaperones Albumin and Casein. *Nano Lett.* **2009**, *9*, 4158–4167.
- (68) Wan, A. M. D.; Chandler, E. M.; Madhavan, M.; Infanger, D. W.; Ober, C. K.; Gourdon, D.; Malliaras, G. G.; Fischbach, C. Fibronectin Conformation Regulates the Proangiogenic Capability of Tumor-Associated Adipogenic Stromal Cells. *Biochim. Biophys. Acta* **2013**, *1830*, 4314–4320.
- (69) Sack, K. D.; Teran, M.; Nugent, M. A. Extracellular Matrix Stiffness Controls VEGF Signaling and Processing in Endothelial Cells. *J. Cell. Physiol.* **2016**, *231*, 2026–2039.
- (70) McElroy, C. A.; Dohm, J. A.; Walsh, S. T. R. Structural and Biophysical Studies of the Human IL-7/IL-7R α Complex. *Structure (Oxford, U. K.)* **2009**, *17*, 54–65.
- (71) Goodwin, R. G.; Lupton, S.; Schmierer, A.; Hjerrild, K. J.; Jerzy, R.; Clevenger, W.; Gillis, S.; Cosman, D.; Namen, A. E. Human Interleukin 7: Molecular Cloning and Growth Factor Activity on Human and Murine B-Lineage Cells. *Proc. Natl. Acad. Sci. U. S. A.* **1989**, *86*, 302–306.
- (72) Sali, A.; Blundell, T. L. Comparative Protein Modelling by Satisfaction of Spatial Restraints. *J. Mol. Biol.* **1993**, *234*, 779–815.
- (73) Tamarit, B.; Bugault, F.; Pillet, A.-H.; Lavergne, V.; Bochet, P.; Garin, N.; Schwarz, U.; Thèze, J.; Rose, T. Membrane Microdomains and Cytoskeleton Organization Shape and Regulate the IL-7 Receptor Signalosome in Human CD4 T-Cells. *J. Biol. Chem.* **2013**, *288* (12), 8691–8701.

- (74) Henriques, C. M.; Rino, J.; Nibbs, R. J.; Graham, G. J.; Barata, J. T. IL-7 Induces Rapid Clathrin-Mediated Internalization and JAK3-Dependent Degradation of IL-7 α in T Cells. *Blood* **2010**, *115* (16), 3269–3277.
- (75) Zeng, Y. X.; Takahashi, H.; Shibata, M.; Hirokawa, K. JAK3 Janus Kinase Is Involved in Interleukin 7 Signal Pathway. *Febs Lett* **1994**, *353* (3), 289–293.
- (76) McElroy, C. A.; Holland, P. J.; Zhao, P.; Lim, J.-M.; Wells, L.; Eisenstein, E.; Walsh, S. T. R. Structural Reorganization of the Interleukin-7 Signaling Complex. *Proc. Natl. Acad. Sci. U. S. A.* **2012**, *109* (7), 2503–2508.
- (77) Rose, T.; Pillet, A.-H.; Lavergne, V.; Tamarit, B.; Lenormand, P.; Rousselle, J.-C.; Namane, A.; Thèze, J. Interleukin-7 Compartmentalizes Its Receptor Signaling Complex to Initiate CD4 T Lymphocyte Response. *J. Biol. Chem.* **2010**, *285* (20), 14898–14908.
- (78) Heltemes-Harris, L. M.; Willette, M. J. L.; Vang, K. B.; Farrar, M. A. The Role of STAT5 in the Development, Function, and Transformation of B and T Lymphocytes. *Ann N Y Acad Sci* **2011**, *1217*, 18–31.
- (79) Palmer, M. J.; Mahajan, V. S.; Trajman, L. C.; Irvine, D. J.; Lauffenburger, D. A.; Chen, J. Interleukin-7 Receptor Signaling Network: an Integrated Systems Perspective. *Cell. Mol. Immunol.* **2008**, *5* (2), 79–89.
- (80) Patra, A. K.; Avots, A.; Zahedi, R. P.; Schüler, T.; Sickmann, A.; Bommhardt, U.; Serfling, E. An Alternative NFAT-Activation Pathway Mediated by IL-7 Is Critical for Early Thymocyte Development. *Nat. Immunol.* **2013**, *14* (2), 127–135.
- (81) Venkitaraman, A. R.; Cowling, R. J. Interleukin-7 Induces the Association of Phosphatidylinositol 3-Kinase with the Alpha Chain of the Interleukin-7 Receptor. *Eur. J. Immunol.* **1994**, *24* (9), 2168–2174.
- (82) Klein, L.; Kyewski, B.; Allen, P. M. Positive and Negative Selection of the T Cell Repertoire: What Thymocytes See (and Don't See). *Nat. Rev. Immunol.* **2014**, *14* (6), 377–391.
- (83) Rothenberg, E. V.; Moore, J. E.; Yui, M. A. Launching the T-Cell-Lineage Developmental Programme. *Nat. Rev. Immunol.* **2008**, *8* (1), 9–21.
- (84) Boudil, A.; Matei, I. R.; Shih, H.-Y.; Bogdanoski, G.; Yuan, J. S.; Chang, S. G.; Montpellier, B.; Kowalski, P. E.; Voisin, V.; Bashir, S.; Bader, G. D.; Krangel, M. S.; Guidos, C. J. IL-7 Coordinates Proliferation, Differentiation and Tcra Recombination During Thymocyte B-Selection. *Nat. Immunol.* **2015**, *16*, 397–405.
- (85) Corfe, S. A.; Paige, C. J. The Many Roles of IL-7 in B Cell Development; Mediator of Survival, Proliferation and Differentiation. *Semin Immunol* **2012**, *24* (3), 198–208.
- (86) Clark, M. R.; Mandal, M.; Ochiai, K.; Singh, H. Orchestrating B Cell Lymphopoiesis Through Interplay of IL-7 Receptor and Pre-B Cell Receptor Signalling. *Nat. Rev. Immunol.* **2013**, *14* (2), 69–80.
- (87) Rathmell, J. C.; Farkash, E. A.; Gao, W.; Thompson, C. B. IL-7 Enhances the Survival and Maintains the Size of Naive T Cells. *J. Immunol.* **2001**, *167* (12), 6869–6876.
- (88) Sprent, J.; Surh, C. D. Normal T Cell Homeostasis: the Conversion of Naive Cells Into Memory-Phenotype Cells. *Nat. Immunol.* **2011**, *131* (6), 478–484.
- (89) Kimura, M. Y.; Pobeziński, L. A.; Guinter, T. I.; Thomas, J.; Adams, A.; Park, J.-H.; Tai, X.; Singer, A. IL-7 Signaling Must Be Intermittent, Not Continuous, During CD8⁺ T Cell Homeostasis to Promote Cell Survival Instead of Cell Death. *Nat. Immunol.* **2013**, *14*, 143–151.
- (90) Hennion-Tscheltzoff, O.; Leboeuf, D.; Gauthier, S.-D.; Dupuis, M.; Assouline, B.; Grégoire, A.; Thiant, S.; Guimond, M. TCR Triggering Modulates the Responsiveness and Homeostatic Proliferation of CD4⁺ Thymic Emigrants to IL-7 Therapy. *Blood* **2013**, *121* (23), 4684–4693.

- (91) Huppa, J.; Davis, M. T-Cell-Antigen Recognition and the Immunological Synapse. *Nat. Rev. Immunol.* **2003**, *3* (12), 973–983.
- (92) Sixt, M.; Kanazawa, N.; Selg, M.; Samson, T.; Roos, G.; Reinhardt, D. P.; Pabst, R.; Lutz, M. B.; Sorokin, L. The Conduit System Transports Soluble Antigens From the Afferent Lymph to Resident Dendritic Cells in the T Cell Area of the Lymph Node. *Immunity* **2005**, *22* (1), 19–29.
- (93) Mueller, S. N.; Germain, R. N. Stromal Cell Contributions to the Homeostasis and Functionality of the Immune System. *Nat. Rev. Immunol.* **2009**, *9* (9), 618–629.
- (94) Bajénoff, M.; Egen, J. G.; Koo, L. Y.; Laugier, J. P.; Brau, F.; Glaichenhaus, N.; Germain, R. N. Stromal Cell Networks Regulate Lymphocyte Entry, Migration, and Territoriality in Lymph Nodes. *Immunity* **2006**, *25* (6), 989–1001.
- (95) Turley, S. J.; Fletcher, A. L.; Elpek, K. G. The Stromal and Haematopoietic Antigen-Presenting Cells That Reside in Secondary Lymphoid Organs. *Nat. Rev. Immunol.* **2010**, *10* (12), 813–825.
- (96) Ghazawi, F. M.; Faller, E. M.; Sugden, S. M.; Kakal, J. A.; MacPherson, P. A. IL-7 Downregulates IL-7R α Expression in Human CD8 T Cells by Two Independent Mechanisms. *Immunol Cell Biol* **2013**, *91* (2), 149–158.
- (97) Farber, D. L.; Yudanin, N. A.; Restifo, N. P. Human Memory T Cells: Generation, Compartmentalization and Homeostasis. *Nat. Rev. Immunol.* **2014**, *14* (1), 24–35.
- (98) Kaech, S. M.; Tan, J. T.; Wherry, E. J.; Konieczny, B. T. Selective Expression of the Interleukin 7 Receptor Identifies Effector CD8 T Cells That Give Rise to Long-Lived Memory Cells. *Nature* **2003**, *4* (12), 1191–1198.
- (99) Kondrack, R. M.; Harbertson, J.; Tan, J. T.; McBreen, M. E.; Surh, C. D.; Bradley, L. M. Interleukin 7 Regulates the Survival and Generation of Memory CD4 Cells. *J Exp Med* **2003**, *198* (12), 1797–1806.
- (100) Deshpande, P.; Cavanagh, M. M.; Le Saux, S.; Singh, K.; Weyand, C. M.; Goronzy, J. J. IL-7- and IL-15-Mediated TCR Sensitization Enables T Cell Responses to Self-Antigens. *J. Immunol.* **2013**, *190* (4), 1416–1423.
- (101) Cha, E.; Graham, L.; Manjili, M. H.; Bear, H. D. IL-7 + IL-15 Are Superior to IL-2 for the Ex Vivo Expansion of 4T1 Mammary Carcinoma-Specific T Cells with Greater Efficacy Against Tumors in Vivo. *Breast Cancer Res. Treat.* **2010**, *122* (2), 359–369.
- (102) Guo, Z.; Wang, G.; Miyahara, Y.; Khatat, M.; Linkes, S. P.; Wang, C.; Xia, J.; Pan, Y.; Chen, W.; He, X.; Stepkowski, S. M. IL-7, but Not Thymic Stromal Lymphopoietin (TSLP), During Priming Enhances the Generation of Memory CD4⁺ T Cells. *Immunol Lett* **2010**, *128* (2), 116–123.
- (103) Link, A.; Vogt, T. K.; Favre, S.; Britschgi, M. R.; Acha-Orbea, H.; Hinz, B.; Cyster, J. G.; Luther, S. A. Fibroblastic Reticular Cells in Lymph Nodes Regulate the Homeostasis of Naive T Cells. *Nat. Immunol.* **2007**, *8*, 1255–1265.
- (104) Miller, C. N.; Hartigan-O'Connor, D. J.; Lee, M. S.; Laidlaw, G.; Cornelissen, I. P.; Matloubian, M.; Coughlin, S. R.; McDonald, D. M.; McCune, J. M. IL-7 Production in Murine Lymphatic Endothelial Cells and Induction in the Setting of Peripheral Lymphopenia. *Int. Immunol.* **2013**, *25*, 471–483.
- (105) Fletcher, A. L.; Lukacs-Kornek, V.; Reynoso, E. D.; Pinner, S. E.; Bellemare-Pelletier, A.; Curry, M. S.; Collier, A.-R.; Boyd, R. L.; Turley, S. J. Lymph Node Fibroblastic Reticular Cells Directly Present Peripheral Tissue Antigen Under Steady-State and Inflammatory Conditions. *J Exp Med* **2010**, *207* (4), 689–697.
- (106) Malhotra, D.; Astarita, J.; Lukacs-Kornek, V.; Tayalia, P.; Gonzalez, S. F.; Elpek, K. G.; Chang, S. K.; Knoblich, K.; Hemler, M. E.; Carroll, M. C.; Mooney, D. J.; Turley, S. J.; Immunological Genome Project Consortium; Fletcher, A. L.; Brenner, M. B. Transcriptional Profiling of Stroma From Inflamed and Resting Lymph Nodes Defines Immunological Hallmarks. *Nat. Immunol.* **2012**, *13* (5), 499–510.

- (107) Mempel, T. R.; Junt, T.; Andrian, von, U. H. Rulers Over Randomness: Stroma Cells Guide Lymphocyte Migration in Lymph Nodes. *Immunity* **2006**, *25* (6), 867–869.
- (108) Kimura, K.; Matsubara, H.; Sogoh, S.; Kita, Y.; Sakata, T.; Nishitani, Y.; Watanabe, S.; Hamaoka, T.; Fujiwara, H. Role of Glycosaminoglycans in the Regulation of T Cell Proliferation Induced by Thymic Stroma-Derived T Cell Growth Factor. *J. Immunol.* **1991**, *146* (8), 2618–2624.
- (109) Kubow, K. E.; Vukmirovic, R.; Zhe, L.; Klotzsch, E.; Smith, M. L.; Gourdon, D.; Luna, S.; Vogel, V. Mechanical Forces Regulate the Interactions of Fibronectin and Collagen I in Extracellular Matrix. *Nat. Commun.* **2015**, *6*, 1–11.
- (110) Aebischer, D.; Iolyeva, M.; Halin, C. The Inflammatory Response of Lymphatic Endothelium. *Angiogenesis* **2014**, *17* (2), 383–393.
- (111) Acton, S. E.; Farrugia, A. J.; Astarita, J. L.; Mourão-Sá, D.; Jenkins, R. P.; Nye, E.; Hooper, S.; van Blijswijk, J.; Rogers, N. C.; Snelgrove, K. J.; Rosewell, I.; Moita, L. F.; Stamp, G.; Turley, S. J.; Sahai, E.; Reis e Sousa, C. Dendritic Cells Control Fibroblastic Reticular Network Tension and Lymph Node Expansion. *Nature* **2014**, *514*, 498–502.
- (112) Katakai, T.; Hara, T.; Sugai, M.; Gonda, H.; Shimizu, A. Lymph Node Fibroblastic Reticular Cells Construct the Stromal Reticulum via Contact with Lymphocytes. *J Exp Med* **2004**, *200* (6), 783–795.
- (113) Mikko, M.; Fredriksson, K.; Wahlström, J.; Eriksson, P.; Grunewald, J.; Sköld, C. M. Human T Cells Stimulate Fibroblast-Mediated Degradation of Extracellular Matrix in Vitro. *Clin. Exp. Immunol.* **2008**, *151*, 317–325.
- (114) Jian, M.; Qingfu, Z.; Yanduo, J.; Guocheng, J.; Xueshan, Q. Anti-Lymphangiogenesis Effects of a Specific Anti-Interleukin 7 Receptor Antibody in Lung Cancer Model in Vivo. *Mol. Carcinog.* **2015**, *54* (2), 148–155.
- (115) Cimbri, R.; Vassena, L.; Arthos, J.; Cicala, C.; Kehrl, J. H.; Park, C.; Sereti, I.; Lederman, M. M.; Fauci, A. S.; Lusso, P. IL-7 Induces Expression and Activation of Integrin A4β7 Promoting Naive T-Cell Homing to the Intestinal Mucosa. *Blood* **2012**, *120*, 2610–2619.
- (116) Halvorson, M. J.; Magner, W.; Coligan, J. E. Alpha4 and Alpha5 Integrins Costimulate the CD3-Dependent Proliferation of Fetal Thymocytes. *Cellular Immunology* **1998**, *189* (1), 1–9.
- (117) Gendron, S.; Boisvert, M.; Chetoui, N.; Aoudjit, F. Alpha1beta1 Integrin and Interleukin-7 Receptor Up-Regulate the Expression of RANKL in Human T Cells and Enhance Their Osteoclastogenic Function. *Immunology* **2008**, *125* (3), 359–369.
- (118) Azreq, El, M.-A.; Arseneault, C.; Boisvert, M.; Pagé, N.; Allaëys, I.; Poubelle, P. E.; Tessier, P. A.; Aoudjit, F. Cooperation Between IL-7 Receptor and Integrin A2β1 (CD49b) Drives Th17-Mediated Bone Loss. *J. Immunol.* **2015**, *195* (9), 4198–4209.
- (119) Dustin, M. L.; de Fougères, A. R. Reprogramming T Cells: the Role of Extracellular Matrix in Coordination of T Cell Activation and Migration. *Curr Opin Immunol* **2001**, *13* (3), 286–290.
- (120) Long, D.; Blake, S.; Song, X.-Y.; Lark, M.; Loeser, R. F. Human Articular Chondrocytes Produce IL-7 and Respond to IL-7 with Increased Production of Matrix Metalloproteinase-13. *Arthritis Res. Ther.* **2008**, *10*, R23.
- (121) Yamanaka, O.; Saika, S.; Ikeda, K.; Miyazaki, K.-I.; Ohnishi, Y.; Ooshima, A. Interleukin-7 Modulates Extracellular Matrix Production and TGF-Beta Signaling in Cultured Human Subconjunctival Fibroblasts. *Curr. Eye Res.* **2006**, *31*, 491–499.
- (122) Zhang, L.; Keane, M. P.; Zhu, L. X.; Sharma, S.; Rozengurt, E.; Strieter, R. M.; Dubinett, S. M.; Huang, M. Interleukin-7 and Transforming Growth Factor-Beta Play Counter-Regulatory Roles in Protein Kinase C-Delta-Dependent Control of Fibroblast Collagen Synthesis in Pulmonary Fibrosis. *J. Biol. Chem.* **2004**, *279* (27), 28315–28319.

- (123) Forster, T. Energiewanderung Und Fluoreszenz. *Naturwissenschaften* **1946**, 33 (6), 166–175.
- (124) Clegg, R. M. The History of FRET. In *Reviews in Fluorescence 2006*; Reviews in Fluorescence; Springer US: Boston, MA, 2006; Vol. 2006, pp 1–45.
- (125) Vogel, S. S.; Thaler, C.; Koushik, S. V. Fanciful FRET. *Sci. STKE* **2006**, 2006 (331), re2–re2.
- (126) Jares-Erijman, E. A.; Jovin, T. M. FRET Imaging. *Nat Biotechnol* **2003**, 21 (11), 1387–1395.
- (127) Okamoto, K.; Sako, Y. Recent Advances in FRET for the Study of Protein Interactions and Dynamics. *Curr Opin Struct Biol* **2017**, 46, 16–23.
- (128) Baugh, L.; Vogel, V. Structural Changes of Fibronectin Adsorbed to Model Surfaces Probed by Fluorescence Resonance Energy Transfer. *Journal of biomedical materials research Part A* **2004**, 69 (3), 525–534.
- (129) Antia, M.; Islas, L. D.; Boness, D. A.; Baneyx, G.; Vogel, V. Single Molecule Fluorescence Studies of Surface-Adsorbed Fibronectin. *Biomaterials* **2006**, 27 (5), 679–690.
- (130) Jalink, K.; van Rheenen, J. FilterFRET: Quantitative imaging of sensitized emission. In FRET and FLIM techniques; Gadella, T. W. J., Ed.; Laboratory Techniques in Biochemistry and Molecular Biology; Elsevier: Amsterdam, The Netherlands; Oxford, UK, 2009; Vol. 33, pp 289–349.
- (131) Haas, E.; Katchalski-Katzir, E.; Steinberg, I. Z. Effect of the Orientation of Donor and Acceptor on the Probability of Energy Transfer Involving Electronic Transitions of Mixed Polarization. *Biochemistry* **1978**, 17 (23), 5064–5070.
- (132) Dale, R. E.; Eisinger, J.; Blumberg, W. E. The Orientational Freedom of Molecular Probes. the Orientation Factor in Intramolecular Energy Transfer. *Biophys J* **1979**, 26 (2), 161–193.
- (133) Wu, P.; Brand, L. Orientation Factor in Steady-State and Time-Resolved Resonance Energy Transfer Measurements. *Biochemistry* **1992**, 31 (34), 7939–7947.
- (134) van der Meer, B. W. Kappa-Squared: From Nuisance to New Sense. *Journal of Biotechnology* **2002**, 82 (3), 181–196.
- (135) van Rheenen, J.; Langeslag, M.; Jalink, K. Correcting Confocal Acquisition to Optimize Imaging of Fluorescence Resonance Energy Transfer by Sensitized Emission. *Biophys. J.* **2004**, 86, 2517–2529.
- (136) Pal, S.; Chen, Z.; Xu, X.; Mikhailova, M. Co-Purified Gelatinases Alter the Stability and Biological Activities of Human Plasma Fibronectin Preparations. *Journal of periodontal ...* **2010**.
- (137) Speziale, P.; Visai, L.; Rindi, S.; Di Poto, A. Purification of Human Plasma Fibronectin Using Immobilized Gelatin and Arg Affinity Chromatography. *Nat Protoc* **2008**, 3 (3), 525–533.
- (138) Baneyx, G.; Baugh, L.; Vogel, V. Coexisting Conformations of Fibronectin in Cell Culture Imaged Using Fluorescence Resonance Energy Transfer. *Proc. Natl. Acad. Sci. U. S. A.* **2001**, 98, 14464–14468.
- (139) Klotzsch, E.; Smith, M. L.; Kubow, K. E.; Muntwyler, S.; Little, W. C.; Beyeler, F.; Gourdon, D.; Nelson, B. J.; Vogel, V. Fibronectin Forms the Most Extensible Biological Fibers Displaying Switchable Force-Exposed Cryptic Binding Sites. *Proc. Natl. Acad. Sci. U. S. A.* **2009**, 106, 18267–18272.
- (140) Linkert, M.; Rueden, C. T.; Allan, C.; Burel, J.-M.; Moore, W.; Patterson, A.; Loranger, B.; Moore, J.; Neves, C.; Macdonald, D.; Tarkowska, A.; Sticco, C.; Hill, E.; Rossner, M.; Eliceiri, K. W.; Swedlow, J. R. Metadata Matters: Access to Image Data in the Real World. *J. Cell Biol.* **2010**, 189 (5), 777–782.

- (141) Anderson, G.; Jenkinson, E. J. Lymphostromal Interactions in Thymic Development and Function. *Nat. Rev. Immunol.* **2001**, *1*, 31–40.
- (142) Gomes, A. C.; Hara, T.; Lim, V. Y.; Herndler-Brandstetter, D. Hematopoietic Stem Cell Niches Produce Lineage-Instructive Signals to Control Multipotent Progenitor Differentiation. *Immunity* **2016**, *45*, 1219–1231.
- (143) Lee, S. K.; Kalinowski, J. F.; Jastrzebski, S. L.; Puddington, L.; Lorenzo, J. A. Interleukin-7 Is a Direct Inhibitor of in Vitro Osteoclastogenesis. *Endocrinology* **2003**, *144*, 3524–3531.
- (144) Colucci, S.; Brunetti, G.; Cantatore, F. P.; Oranger, A.; Mori, G.; Quarta, L.; Cirulli, N.; Mancini, L.; Corrado, A.; Grassi, F. R.; Grano, M. Lymphocytes and Synovial Fluid Fibroblasts Support Osteoclastogenesis Through RANKL, TNF α , and IL-7 in an in Vitro Model Derived From Human Psoriatic Arthritis. *J. Pathol.* **2007**, *212*, 47–55.
- (145) Gress, R. Improving the Immune System with Human IL-7 Vaccine in Older Subjects Who Have Had Chemotherapy, 2011, ClinicalTrials.gov Identifier: NCT01339000. Website: <https://clinicaltrials.gov/ct2/show/NCT01339000> (accessed 17 Aug, 2017)
- (146) Gratz, I. K.; Truong, H.-A.; Yang, S. H.-Y.; Maurano, M. M.; Lee, K.; Abbas, A. K.; Rosenblum, M. D. Cutting Edge: Memory Regulatory T Cells Require IL-7 and Not IL-2 for Their Maintenance in Peripheral Tissues. *J. Immunol.* **2013**, *190*, 4483–4487.
- (147) Niu, N.; Qin, X. New Insights Into IL-7 Signaling Pathways During Early and Late T Cell Development. *Cell. Mol. Immunol.* **2013**, *10*, 187–189.
- (148) Li, C. X.; Talele, N. P.; Boo, S.; Koehler, A.; Knee-Walden, E.; Balestrini, J. L.; Speight, P.; Kapus, A.; Hinz, B. MicroRNA-21 Preserves the Fibrotic Mechanical Memory of Mesenchymal Stem Cells. *Nat. Mater.* **2017**, *16*, 379–389.
- (149) Borghesi, L. A.; Yamashita, Y.; Kincade, P. W. Heparan Sulfate Proteoglycans Mediate Interleukin-7-Dependent B Lymphopoiesis. *Blood* **1999**, *93*, 140–148.
- (150) Zhang, F.; Liang, X.; Pu, D.; George, K. I.; Holland, P. J.; Walsh, S. T. R.; Linhardt, R. J. Biophysical Characterization of Glycosaminoglycan-IL-7 Interactions Using SPR. *Biochimie* **2012**, *94*, 242–249.
- (151) Hynes, R. O. Integrins: Bidirectional, Allosteric Signaling Machines. *Cell (Cambridge, MA, U. S.)* **2002**, *110*, 673–687.
- (152) Schiller, H. B.; Hermann, M.-R.; Polleux, J.; Vignaud, T.; Zanivan, S.; Friedel, C. C.; Sun, Z.; Raducanu, A.; Gottschalk, K.-E.; Théry, M.; Mann, M.; Fässler, R. B1- and Av-Class Integrins Cooperate to Regulate Myosin II During Rigidity Sensing of Fibronectin-Based Microenvironments. *Nat. Cell Biol.* **2013**, *15*, 625–636.
- (153) Mooradian, D. L.; Lucas, R. C.; Weatherbee, J. A.; Furcht, L. T. Transforming Growth Factor-Beta 1 Binds to Immobilized Fibronectin. *J. Cell. Biochem.* **1989**, *41*, 189–200.
- (154) Mitsi, M.; Hong, Z.; Costello, C. E.; Nugent, M. A. Heparin-Mediated Conformational Changes in Fibronectin Expose Vascular Endothelial Growth Factor Binding Sites. *Biochemistry* **2006**, *45* (34), 10319–10328.
- (155) Wipff, P.-J.; Rifkin, D. B.; Meister, J.-J.; Hinz, B. Myofibroblast Contraction Activates Latent TGF-Beta1 From the Extracellular Matrix. *J. Cell Biol.* **2007**, *179*, 1311–1323.
- (156) Schoen, I.; Pruitt, B.; Vogel, V. The Yin-Yang of Rigidity Sensing: How Forces and Mechanical Properties Regulate the Cellular Response to Materials. *Annu. Rev. Mater. Res.* **2013**, *43*, 589–618.
- (157) Gao, M.; Craig, D.; Vogel, V.; Schulten, K. Identifying Unfolding Intermediates of FN-III(10) by Steered Molecular Dynamics. *J. Mol. Biol.* **2002**, *323*, 939–950.

- (158) Ohashi, T.; Erickson, H. P. Domain Unfolding Plays a Role in Superfibronectin Formation. *J. Biol. Chem.* **2005**, *280*, 39143–39151.
- (159) Astarita, J. L.; Cremasco, V.; Fu, J.; Darnell, M. C.; Peck, J. R.; Nieves-Bonilla, J. M.; Song, K.; Kondo, Y.; Woodruff, M. C.; Gogineni, A.; Onder, L.; Ludewig, B.; Weimer, R. M.; Carroll, M. C.; Mooney, D. J.; Xia, L.; Turley, S. J. The CLEC-2–Podoplanin Axis Controls the Contractility of Fibroblastic Reticular Cells and Lymph Node Microarchitecture. *Nat. Immunol.* **2014**, *16*, 75–84.
- (160) Buscemi, L.; Ramonet, D.; Klingberg, F.; Formey, A.; Smith-Clerc, J.; Meister, J.-J.; Hinz, B. The Single-Molecule Mechanics of the Latent TGF-B1 Complex. *Curr. Biol.* **2011**, *21*, 2046–2054.
- (161) Mitsi, M.; Handschin, S.; Gerber, I.; Schwartlander, R.; Klotzsch, E.; Wepf, R.; Vogel, V. The Ultrastructure of Fibronectin Fibers Pulled From a Protein Monolayer at the Air-Liquid Interface and the Mechanism of the Sheet-to-Fiber Transition. *Biomaterials* **2015**, *36*, 66–79.
- (162) Hinz, B.; Celetta, G.; Tomasek, J. J.; Gabbiani, G.; Chaponnier, C. Alpha-Smooth Muscle Actin Expression Upregulates Fibroblast Contractile Activity. *Mol. Biol. Cell* **2001**, *12*, 2730–2741.
- (163) Lu, P.; Weaver, V. M.; Werb, Z. The Extracellular Matrix: a Dynamic Niche in Cancer Progression. *J. Cell Biol.* **2012**, *196*, 395–406.
- (164) Huijbers, I. J.; Irvani, M.; Popov, S.; Robertson, D.; Al-Sarraj, S.; Jones, C.; Isacke, C. M. A Role for Fibrillar Collagen Deposition and the Collagen Internalization Receptor Endo180 in Glioma Invasion. *PLoS ONE* **2010**, *5*, e9808.
- (165) Kauppila, S.; Stenbäck, F.; Risteli, J.; Jukkola, A.; Risteli, L. Aberrant Type I and Type III Collagen Gene Expression in Human Breast Cancer in Vivo. *J. Pathol.* **1998**, *186*, 262–268.
- (166) Zhu, G. G.; Risteli, L.; Mäkinen, M.; Risteli, J.; Kauppila, A.; Stenbäck, F. Immunohistochemical Study of Type I Collagen and Type I pN-Collagen in Benign and Malignant Ovarian Neoplasms. *Cancer (Hoboken, NJ, U. S.)* **1995**, *75*, 1010–1017.
- (167) Kuo, C.-W.; Shiu, J.-Y.; Chien, F.-C.; Tsai, S.-M.; Chueh, D.-Y.; Chen, P. Polymeric Nanopillar Arrays for Cell Traction Force Measurements. *Electrophoresis* **2010**, *31* (18), 3152–3158.
- (168) Repass, J. F.; Laurent, M. N.; Carter, C.; Reizis, B.; Bedford, M. T.; Cardenas, K.; Narang, P.; Coles, M.; Richie, E. R. IL7-hCD25 and IL7-Cre BAC Transgenic Mouse Lines: New Tools for Analysis of IL-7 Expressing Cells. *Genesis* **2009**, *47* (4), 281–287.
- (169) Racapé, M.; Vanhove, B.; Soullilou, J.-P.; Brouard, S. Interleukin 7 Receptor Alpha as a Potential Therapeutic Target in Transplantation. *Arch. Immunol. Ther. Exp. (Warsz.)* **2009**, *57* (4), 253–261.
- (170) Jin, J.; Goldschneider, I.; Lai, L. In Vivo Administration of the Recombinant IL-7/Hepatocyte Growth Factor B Hybrid Cytokine Efficiently Restores Thymopoiesis and Naive T Cell Generation in Lethally Irradiated Mice After Syngeneic Bone Marrow Transplantation. *J. Immunol.* **2011**, *186* (4), 1915–1922.
- (171) Lee, L.-F.; Logronio, K.; Tu, G. H.; Zhai, W.; Ni, I.; Mei, L.; Dilley, J.; Yu, J.; Rajpal, A.; Brown, C.; Appah, C.; Chin, S. M.; Han, B.; Affolter, T.; Lin, J. C. Anti-IL-7 Receptor-A Reverses Established Type 1 Diabetes in Nonobese Diabetic Mice by Modulating Effector T-Cell Function. *Proc. Natl. Acad. Sci. U. S. A.* **2012**, *109* (31), 12674–12679.
- (172) Cukierman, E.; Pankov, R.; Stevens, D. R.; Yamada, K. M. Taking Cell-Matrix Adhesions to the Third Dimension. *Science* **2001**, *294* (5547), 1708–1712.
- (173) Mao, Y.; Schwarzbauer, J. E. Stimulatory Effects of a Three-Dimensional Microenvironment on Cell-Mediated Fibronectin Fibrillogenesis. *J Cell Sci* **2005**, *118* (Pt 19), 4427–4436.
- (174) Amatangelo, M. D.; Bassi, D. E.; Klein-Szanto, A. J. P.; Cukierman, E. Stroma-Derived Three-Dimensional Matrices Are Necessary and Sufficient to Promote Desmoplastic Differentiation of Normal Fibroblasts. *Am J Pathol* **2005**, *167* (2), 475–488.

- (175) Chen, L. B.; Murray, A.; Segal, R. A.; Bushnell, A.; Walsh, M. L. Studies on Intercellular LETS Glycoprotein Matrices. *Cell (Cambridge, MA, U. S.)* **1978**, *14* (2), 377–391.
- (176) Franco-Barraza, J.; Beacham, D. A.; Amatangelo, M. D.; Cukierman, E. Preparation of Extracellular Matrices Produced by Cultured and Primary Fibroblasts. *Curr Protoc Cell Biol* **2016**, *71* (3), 10.9.1–10.9.34.
- (177) Luo, H.; Wu, Z.; Qi, S.; Jin, W.; Han, B.; Wu, J. Ephrinb1 and Ephrinb2 Are Associated with Interleukin-7 Receptor A and Retard Its Internalization From the Cell Surface. *J. Biol. Chem.* **2011**, *286* (52), 44976–44987.
- (178) Faller, E. M.; Ghazawi, F. M.; Cavar, M.; MacPherson, P. A. IL-7 Induces Clathrin-Mediated Endocytosis of CD127 and Subsequent Degradation by the Proteasome in Primary Human CD8 T Cells. *Immunol Cell Biol* **2016**, *94* (2), 196–207.
- (179) Wells, A.; Marti, U. Signalling Shortcuts: Cell-Surface Receptors in the Nucleus? *Nat. Rev. Mol. Cell Bio.* **2002**, *3* (9), 697–702.
- (180) Bryant, D. M.; Stow, J. L. Nuclear Translocation of Cell-Surface Receptors: Lessons From Fibroblast Growth Factor. *Traffic* **2005**, *6* (10), 947–954.
- (181) Reich, N. C.; Liu, L. Tracking STAT Nuclear Traffic. *Nat. Rev. Immunol.* **2006**, *6* (8), 602–612.
- (182) Boisvert, F.-M.; van Koningsbruggen, S.; Navascués, J.; Lamond, A. I. The Multifunctional Nucleolus. *Nat. Rev. Mol. Cell Bio.* **2007**, *8* (7), 574–585.
- (183) Swartz, M. A.; Lund, A. W. Lymphatic and Interstitial Flow in the Tumour Microenvironment: Linking Mechanobiology with Immunity. *Nature Publishing Group* **2012**, *12* (3), 210–219.
- (184) Tomei, A. A.; Siegert, S.; Britschgi, M. R.; Luther, S. A.; Swartz, M. A. Fluid Flow Regulates Stromal Cell Organization and CCL21 Expression in a Tissue-Engineered Lymph Node Microenvironment. *J. Immunol.* **2009**, *183* (7), 4273–4283.
- (185) Guillaume-Gentil, O.; Grindberg, R. V.; Kooger, R.; Dorwling-Carter, L.; Martinez, V.; Ossola, D.; Pilhofer, M.; Zambelli, T.; Vorholt, J. A. Tunable Single-Cell Extraction for Molecular Analyses. *Cell (Cambridge, MA, U. S.)* **2016**, *166* (2), 506–516.
- (186) Gee, E. P. S.; Yüksel, D.; Stultz, C. M.; Ingber, D. E. SLLISWD sequence in the 10FNIII domain initiates fibronectin fibrillogenesis. *J. Biol. Chem.* **2013**, *288*, 21329–21340.

8. Acknowledgements

I would like to thank the following people, without whom this work would simply not have been possible:

My supervisor Professor Viola Vogel for her continuous support, motivation, and creativity. Dr. Maria Mitsi for supervising my work and being a constant guide, and sharing her knowledge with me. Dr. Florian Herzog for and advice regarding the use of protein sequencing and structure software, Dr. Ingmar Schön for help revising the Matlab analysis code. Dr. Ingmar Schön, Dr. Lina Aires and Dr. Philip Kollmannsberger for helpful and engaging discussions regarding methodology and analysis. Chantel Spencer-Hänsch for purifying FN from human plasma. Dr. Jau-Ye Shiu for his contribution towards the preliminary study using nano pillars. Prof. Michael Dustin and members of the National Institute of Health Nanomedicine Center for Mechanobiology Directing the Immune Response for insightful discussions, for sharing their knowledge, and helping with experimental issues. Prof. Cornelia Halin for insightful discussions. Dr. Shannon Turley and members of her laboratory, at the time of the experiments from the Dana Farber Cancer Institute and Harvard Medical School for kind provision of LNSCs and advice in their handling. Chantel Spencer and Isabel Gerber for help with laboratory administration, safety and advice in general issues. Norma De Giuseppe for her continuous kind support and encouragement.

I also would like to thank members of the lab that have made of my PhD a fun and enriching experience, and that have given me support throughout, and have developed into a hopefully long-lasting friendship: Lina Aires, Florian Herzog, Norma de Giuseppe, Melanie Burkhardt, Jasper Foolen, Lukas Braun, Samuel Hertig, Isabel Gerber, Chantel Spencer, Ima Avalos, Susanna Frueh, Jau-Ye Shiu, Garif Yalak, Nikhil Jain, Mario Benn, Jenna Graham, Sebastian Lickert.

Finally, I would like to thank my Swiss family, Doris, Ruedi, Bendicht and Lisa Lüthi, Melanie Rogger, and Roman Suter for the continuous support and encouragement, and for helping me in times when I needed more than two hands to be able to achieve this, I'm deeply thankful. My Mexican family Ortiz and Franyuti, who provided me with motivation and perspective to enjoy this experience. My husband Hannes Lüthi for being an unconditional source of strength and love, and for standing by my side so I would have the courage and strength to go through this experience. My son Lorenzo Agustín for motivating me with his beautiful smile. My mother Rosy Franyuti for being my most avid fan and encourager and always believing unconditionally in me.

8.1. Funding Sources

This research was supported by the Swiss National Science Foundation (Grant SNF- 310030B_133122 (Viola Vogel)), the National Institute of Health (Nanomedicine Center for Mechanobiology Directing the Immune Response, NIH Common Fund) and the European Research Council (ERC Advanced Grant 233157 (Viola Vogel)).

9. Curriculum Vitae



Daniela Ortiz Franyuti

MSc, BEng (Hons)

Dr.sc ETH Zurich
Preliminary Confirmation:
13th October 2017

Bahnhofstrasse 2
6210 Sursee
Switzerland

+41 (0) 79 617 1504
daniela.ortiz@hest.ethz.ch

Nationality: Swiss / Mexican

Languages

	English
	Español
	Deutsch
	Schweizerdeutsch

Personal Statement

I am a passionate scientist and a creative engineer who loves to bring ideas together from different fields to tackle challenging questions and formulate creative solutions. My multidisciplinary background has allowed me to combine traditional biological methods with custom engineered assays to investigate biological processes with a new perspective.

My work has focused on mechanobiology at the interface between cell and ECM biology, including mechanosensing at the cellular and protein levels, and mechanical regulation of binding of signalling molecules, with a focus on immunology. I am currently looking for a position where I can use my skills to address novel research questions.

Research

Mechanical stretching of fibronectin fibers upregulates binding of interleukin-7.
Daniela Ortiz Franyuti, Maria Mitsi, Viola Vogel.

Nano Letters, American Chemical Society. Just Accepted Manuscript.
Publication Date (Web): August 28, 2017. DOI:10.1021/acs.nanolett.7b01617

How the stretching of extracellular matrix fibers modules interleukin-7 binding.
Daniela Ortiz Franyuti, Maria Mitsi, Viola Vogel.

Laboratory of Applied Mechanobiology, ETH Zurich. 4th Lymphoid Tissue Meeting within the Swiss Society for Allergology and Immunology, and Swiss Society of Paediatrics Joint Annual Meeting. St.Gallen, Switzerland, 2017.

T-Cells and Substrate Rigidity: Possible roles of integrins $\beta 1$, $\beta 2$ and $\beta 3$ in T-Cell adhesion and Distal Pole Complex formation.

Nanomaterial Laboratory. Department of Materials, ETH Zurich. 2010

The Effect of Electrical Fields on the Production of Extracellular Matrix by Chondrocytes Seeded in Collagen Membranes for Cartilage Tissue Engineering. Institute of Pathology Universität Bern and Geistlich AG. 2009

Developing a Methodology for the Analysis of Infant Spine Kinematics for the Investigation of the Shaken Baby Syndrome. Michael Jones, Catherine Holt, Daniela Ortiz Franyuti. *Journal of Biomechanics*, Volume 41, S355.
[http://dx.doi.org/10.1016/S0021-9290\(08\)70354-3](http://dx.doi.org/10.1016/S0021-9290(08)70354-3).
16th Congress of the European Society of Biomechanics. Lucerne, 2008.

Collaborations

Nanomedicine Development Center for Mechanobiology: Directing the Immune Response, funded by the National Institutes of Health (NIH) Common Fund Nanomedicine program (PN2 EY016586).

Education

Doctor of Sciences of ETH Zurich at the Laboratory of Applied Mechanobiology. Department of Health Sciences and Technology, ETH Zurich. Doctoral thesis and examination approved on the 12th of May 2017. Title to be officially granted after the Departmental Conference in October 2017.

Master of Science in Biomedical Engineering (MSc). University of Bern. 2007-2010. Insigni cum laude

Bachelor of Engineering in Medical Engineering (BEng Hons). Cardiff University. 2004-2007. First Class Honours Degree

Daniela Ortiz Franyuti

daniela.ortiz@hest.ethz.ch

MSc, BEng (Hons) Dr.sc ETH Zurich Preliminary Confirmation: 13th October 2017

Awards

- **Frederic Barnes Waldron Best Student Prize.** Institute of Mechanical Engineering (IMechE), UK. 2007
- **Best Project Certificate.** Institute of Mechanical Engineering (IMechE), UK.2007
- **Best admission exam scholarship.** Universidad Iberoamericana, Mexico
- **Academic Excellence Award.** Instituto Asunción de México

Meetings and Additional Courses

- **ETH Project Management for Research Course,** 2013. Zurich, Switzerland
- **CIMST Bioimaging Summer School,** 2012. Zurich, Switzerland.
- **4th Lymphoid Tissue Meeting** within the Swiss Society for **Allergology and Immunology**, and Swiss Society of Paediatrics Joint Annual Meeting. June 2017. St. Gallen, Switzerland
- **ScienceComm Swiss Science Communication Conference** 2014. Beromünster/Sursee, Switzerland
- **European Microscopy Congress,** 2012. Manchester, United Kingdom.
- **ETH Health Sciences and Technology Research Day,** 2012. Zurich, Switzerland
- **NIH Nanomedicine Development Center Internal Conferences:** 2012, 2011 (Spring/Autum), 2010. NY, U.S.
- **5th Annual Awardee Meeting NIH Nanomedicine Development Centers** 2011. Maryland,U.S.
- **ETH Biological and Bioinspired Materials Day** 2011. Zurich, Switzerland.
- **FASEB Immunoreceptors** 2010. Snowmass Colorado, U.S.
- **First Annual Conference of the American Society for Nanomedicine.** 2009. Maryland, U.S.
- **16th Congress of the European Society of Biomechanics,** 2008. Luzern, Switzerland

IT Competences

<u>Apple/ Windows/Office</u> Computer Platforms	<u>Omni Platform</u> Project Management	<u>Quartz/ Labguru</u> Lab Management	<u>Manuscripts/Papers/Endnote</u> Scientific Literature/Writing
<u>Matlab / Fiji / ImageJ / Imaris / Osirix</u> Image analysis and processing	<u>Matlab / Mathematica</u> Programming Languages	<u>Genious / UGENE / VMD / Chimera</u> Sequencing & molecular structure	
<u>Arduino / Fritzing</u> Hardware	<u>Adobe CC (incl.Photoshop/Illustrator/etc.) / Sketchup / Maya</u> Graphics, Design and Animation		

Other Activities

- Chief of civilian security and evacuation brigade. Instituto Asunción de México.
- Emergency Medical Technician Basic. Iberomed Voluntarios. Mexico City.
- Neurophysiology Internship. Dr. Lilia de la Maza Krzeptowsky. Hospital Angeles del Pedregal, Mexico City.
- Latinamerica Softball Team First Catcher. Senior/Little League Softball World Series 1997 and 1996.
- Mexican National Softball Team First Catcher (1995-2000). National Olympics Champion 1999.
- Camp Leader/ Volunteer/ Department of Economic Resources. Colonias de Vacaciones I.A.P. (Institution promoting and providing camps for children of low-income families in Mexico City).
- Community Development Volunteer. ARISE Texas. Community program for communities of migratory background. Texas, U.S.

2/2

Appendix:

The following ready to print protocols for use in the laboratory setting are included:

- 1) FN Purification from Human Plasma protocol.
- 2) FN-FRET Labeling protocol.
- 3) FN-FRET denaturation curve protocol.
- 4) FN-FRET labelled FN fibre stretching protocol.

The following documents are also included:

- 5) Procedure to test performance of confocal microscope.
- 6) Nanopillar displacement data for LNSCs and NHDFS.
- 7) Matlab codes for FN-FRET analysis: 'parameters.m'; 'FRETanalysis.m'; 'registration.m'

Fn Purification from Human Plasma

Materials

- Column buffer: PBS/ 10 mM EDTA/ 2mM PMSF
- 1M NaCl in column buffer
- 0.5M Urea in column buffer
- 0.2M Arginine in column buffer
- 1M Arginine in column buffer
- 20% Ethanol

- Amersham columns: 2x 19-5101-01 C 16/20
- Ringstands
- Clamps (for two columns)
- Column tubing and small tubing clamp

1. Preparing the column medium - Resuspend the slurries (Sepharose 4B and Gelatin-Sepharose 4B) in PBS

- Mix well the slurry by gently inverting the bottle several times - DO NOT VORTEX!
- Pour the needed volume into 50 ml Falcon tubes and spin at 500 rpm for 10 min.
- Carefully pipet off the supernatant and add an equal amount of ddH₂O.
- Mix gently by inversion, spin down again, and resuspend in an equal volume of PBS.

2. Packing the columns

- 2 columns need to be prepared per purification:
 - 1) Sepharose 4B for the first step (5ml per 100 ml of plasma)
 - 2): Gelatin-Sepharose 4B for the second step (5 ml per 100 ml of plasma)
 - Equilibrate all materials/buffers at room temperature (temperature at which the chromatography will be performed).

The buffers used should not contain agents, which significantly increase the viscosity. The column may be equilibrated with viscous buffers at reduced flow rates after packing is completed.

- Eliminate air form the column dead spaces by flushing the end pieces with buffer.

- Fill the bottom end piece with PBS, then close the column outlet by clamp or stopcock; allow no air into the system. (At this point the bottom tube will be full of buffer coming up out of the small hole on the lower end-piece. There should be a drop of buffer on the platform where you place the filter and net.)
- Dip the filter in 20% EtOH then place it on the platform of the bottom end piece.
- Without trapping air, snap the net on top of the filter then place a drop of buffer on top.
- With a kimwipe, remove excess fluid around the rubber gasket, but don't disturb the bubble on the net.
- With the glass column attached by clamp to the ring-stand, gently attach the lower plug and tighten.
- Using a pipette, gently add buffer to the column by placing the pipette against the side of the column. Again, limit generation of air bubbles.
- Open the column outlet slowly and allow the buffer to flow for a bit. Check for leaks and be sure there is an un-impeded flow of buffer through the system. If it drips very slowly then air may have been trapped in the system and it will have to be disassembled, dried, and reassembled. Close the valve, leaving a few cms of buffer in the column.

- Pour the slurry into the column in one smooth, continuous motion. Pouring the slurry down a glass rod held against the wall of the column, or through a glass funnel, will minimize the introduction of air bubbles.
- Allow it to sit for a few hours (or overnight, after sealing with parafilm) to gravity-pack the sepharose bed until it reaches a constant height.

- Equilibrate columns with 5 column volumes of column buffer.
- The columns can be stored at 4 degrees upright, protected from air.

3. Preparation of plasma

- Thaw plasma in a 37 °C water bath with agitation. Remove immediately upon thawing.
- Aliquot in 50 ml Falcon tubes and spin at 10,000x for 15 min.
- Add 2 mM PMSF and 10 mM EDTA to the supernatant.

4. Affinity purification

- Pass the plasma supernatant of the Sepharose 4B column and the flow-through over the Gelatin-Sepharose 4B column. A good flow rate is 1 drop/2 seconds. It seems possible to get a higher yield by loading the gelatin column overnight, using a slower flow rate.
- Wash the Gelatin-Sepharose 4B column with column buffer. Check regularly the A280 of the outflow. When it reaches background levels, the washing is complete.
- Wash the Gelatin-Sepharose 4B column with 1M NaCl in column buffer (30 ml per 5 ml of slurry).

- Wash the Gelatin-Sepharose 4B column with 0.5M urea in column buffer (30 ml per 5 ml of slurry).
- Wash the Gelatin-Sepharose 4B column with 0.2M arginine in column buffer (30 ml per 5 ml of slurry).
- Elute fibronectin with 1M arginine in column buffer. Collect 2 mL fractions (about 20 in total).
- Check the A280 of the fractions and pool fractions that correspond to the peak of protein concentration.
- Aliquot and store at -80 oC for long-term storage.

FRET-Fn Labeling

1. Cysteine Labelling with Alexa 546 (maleimide)

- Use about 1 mg Fn (200 µl of 5 mg/ml stock). The isolated Fn was kept at -80°C in 6 M urea.
- Measure the concentration of isolated Fn by spectrometer to estimate the amount of Fn.

	A280	MW (µg/µmol)	Extinction Coef (M ⁻¹ cm ⁻¹)	Optical Path (cm)	Concentration A280 / [(Extinction coef.) (Optical path)](M)	Concentration (µg/µl)
Fn	4.958	440000	563200.0	1.0E+00	8.80E-06	3.9

$$[C]_M = A_{280} / [(\text{Extinction coef.}) (\text{Optical path})]$$

- Denature protein by adding an equal volume of 8M GdnHCl. Final concentration is now 4M GdnHCl (and 3 M urea; all total, the Fn is experiencing the equivalent of about 5.5 M GdnHCl).
- Add 30-fold molar excess of Alexa 546. The exact amount of molar excess required can vary between 20 and 30-fold depending on the batch of Fn.

	Mass (µg)	MW (µg/µmol)	mol , ie. mass/ MW (µmol)	30xµmol	Concentration (µg/µl)	Volume (µl)
Fn	1162.03	440000	2.6E-03	7.9E-02	3.9	300.0
Alexa 546-Maleimide	81.92	1034	7.9E-02	-	5.0	16.4

- Mix by inverting the eppendorf tube.
- Incubate 1 h at room temperature in the dark.
- Prepare amine-labeling buffer ("**buffer A**" - PBS, 0.1 M NaHCO₃, pH 8.5).
- Separate labeled protein from free dye with a size-exclusion PD-10 column (Amersham). This column allows for group separation of high (M_r>5000) from low MW substances (M_r<1000). The bed volume is 8.3 ml with recommended sample volume of 2.5 ml. However, the volumes listed below were determined empirically using drop preservation and subsequent Western blot analysis to determine the point at which full length FN has exited the column and fragments begin to appear.
- Equilibrate column with 20 ml Buffer A.

- Add buffer A to labeled Fn solution to bring to 1 ml total volume.
- Add protein solution directly to the column, and wait until it fully enters the column.
- Add 2 ml buffer A to the column. Allow Buffer A to fully enter the column.
- You have thus discarded the first 3 ml of elutant which came out as a result of the 1ml protein solution plus the 2 ml PBS. This will bring the protein (which appears yellow) to the bottom of the column.
- Add 1 ml Buffer A to the column and collect the eluted protein. Discard the column.
- Remove protein and determine protein concentration and cysteine labelling ratio by measuring absorbances at 280 and 556 (actual peak for Alexa 546).

Wavelength	Absorbance				Molecule	λ	ϵ (cm ⁻¹ M ⁻¹)	MW
280	1.123				Fn	280	563200	440000
556	0.639					556	0	
Concentration	Molar		g/l					
[Alexa 546]	6.09E-06	M			Alexa 546	280	12500	1034
[Fn]	1.86E-06	M	8.18E-01	g/L		556	105000	

$$[\text{Alexa 546}] = \frac{A_{556}}{\epsilon_{556}^{\text{Alexa546}}}$$

$$[\text{Fn}] = \frac{A_{280} - [\text{Alexa 546}](\epsilon_{280}^{\text{Alexa546}})}{\epsilon_{280}^{\text{Fn}}}$$

2. Amine Labelling with Alexa 488 (succinimidyl ester)

- Add 70-fold molar excess of Alexa 488 (exact excess can vary between 60 and 70). Mix by inverting the eppendorf tube.

	Mass (μg)	MW ($\mu\text{g}/\mu\text{mol}$)	mol, ie. mass/MW (μmol)	70x μmol	Concentration ($\mu\text{g}/\mu\text{l}$)	Volume (μl)
Fn	817.91	440000	1.9E-03	1.3E-01	0.8	1000.0
Alexa 488SE	93.69	720	1.3E-01	-	5.0	18.7

- Incubate 1 hr.
- Separate labeled protein from free dye with a size-exclusion PD-10 column (Amersham).
 - Equilibrate column with 20ml PBS.
 - Add protein solution directly to the column, and wait until it fully enters the column.
 - Add 2 ml PBS to the column. Allow PBS to fully enter the column.

- You have thus discarded the first 3 ml of elutant which came out as a result of the 1ml protein solution plus the 2 ml PBS. This will bring the protein (which appears pink) to the bottom of the column.
- Add 1 ml PBS to the column and collect the eluted protein. Discard the column.
- Determine protein concentration and labelling ratios by measuring absorbances at 280, 498 (actual peak for Alexa 488), and 556.

Wavelength	Absorbance				Molecule	λ	ϵ (cm ⁻¹ M ⁻¹)	MW
280	0.853				Fn	280	563200	440000
495	1.046					498	0	
556	0.387					556	0	
Concentration	Molar		g/l		Alexa 488	280	8789	720
[Alexa 546]	3.69E-06	M				498	78000	
[Alexa 488]	1.28E-05	M				556	0	
[Fn]	1.23E-06	M	5.43E-01	g/L				
					Alexa 546	280	12500	1034
Labeling Ratio						498	13000	
Alexa 488 : Fn	10.4					556	105000	
Alexa 546 : Fn	3.0							
(Calculations assuming that Fn was labeled with Alexa 546 FIRST)								

$$[\text{Alexa 488}] = \frac{A_{498} - [\text{Alexa 546}](\epsilon_{498}^{\text{Alexa 546}})}{\epsilon_{498}^{\text{Alexa 488}}}$$

$$[\text{Alexa 546}] = \frac{A_{556}}{\epsilon_{556}^{\text{Alexa 546}}}$$

$$[\text{Fn}] = \frac{A_{280} - [\text{Alexa 546}](\epsilon_{280}^{\text{Alexa 546}}) - [\text{Alexa 488}](\epsilon_{280}^{\text{Alexa 488}})}{\epsilon_{280}^{\text{Fn}}}$$

- Add glycerol to the labeled protein to a final concentration of 5 or 10% glycerol.
- Store the protein in small aliquots at -20C.

Notes from Amine Reactive Dyes, a Molecular Probes publication:

- Succinimidyl esters are susceptible to hydrolysis, suggesting a loss of donor molecules from Fn stored for long periods of time.
- Protein concentration should be at least 2 g/l for optimal results (likely a reference to repeatability).
- Succinimidyl esters do form a very stable amide bond relative to other amine-reactive groups.
- Amine-reactive reagents react with non-protonated aliphatic amine groups, including the amine terminus of proteins and the ϵ -amino group of lysines. The ϵ -amino group has a pKa of around 10.5; in order to maintain this amine group in the non-protonated form, the conjugation must take place in a buffer with slightly basic pH. It is important to avoid buffers that contain primary amines, such as Tris, as these will compete for conjugation with the amine-reactive compound. We

recommend the following buffers for conjugation with amine-reactive compounds with proteins: 0.1-0.2 M sodium bicarbonate buffer, pH 8.3 for succinimidyl esters. More specific labeling of the amine terminus may be achieved using a buffer closer to neutral pH, as the pKa of the terminal amine is lower than that of the lysine amino group.

5. The stop reaction may be used to remove "weakly bound probes". Not sure if they mean non-specifically bound probes or not.
6. Antibodies that have been previously dissolved in buffers containing amines can be dialyzed against 10-20 mM phosphate-buffered saline (PBS), and the desired pH for the reaction can be obtained by adding 0.1 mL of 1 M sodium bicarbonate buffer (pH 8.3-9.0) for each mL of protein solution. The presence of low concentrations of sodium azide (<3 mM) or thimerosal (<1 mM) will not interfere with the conjugation reaction.
7. Point (6) above suggest FN which is already in PBS can be made suitable for donor conjugation by simply adding 0.1ml of 0.1M sodium bicarbonate to each 1.0 ml of protein solution in PBS.

Notes from Michael Smith:

8. Any **air bubbles left in the dialysis cassette** could cause major problems in the form of FN aggregate formation. This comes from Erickson et al. 1983. JBC, "Dialysis with an air bubble in the bag often resulted in formation of a stringy precipitate, especially when dialyzing into a low ionic strength buffer." We also see this occurring regularly, and it is advisable to lose some solution at the expense of complete removal of the air bubble.
9. Concerning **glycerol in the storage solution**, "Even after several weeks of storage, FN frozen in glycerol showed no loss of gelatin-binding activity and no change in solubility, sedimentation properties, or appearance under the electron microscope." This also comes from reference listed in 8. It is not explicitly stated, but one must assume these properties did change after storage in the absence of glycerol.
10. Concerning the **starting concentration of FN**, Molecular Probes did not write their user info in consideration of a protein such as 440 kDa FN. We have experienced frequent loss of protein into aggregates when using FN at concentrations of 2 g/l or above. My best results have come from starting concentrations around 1 g/l. Although the final concentration is low with an ~60% loss of protein, it is advisable in my opinion to use 1 g/l.
11. Concerning addition of glycerol and **mixing in general**, a simple back of the envelope calculation shows that the mean shear rate at the tip of a pipette well exceeds 1000 s⁻¹, while the mean shear rate during inversion of an eppendorf tube is 100 s⁻¹. Although from a mixing standpoint higher shear and higher Re are better, I also generally see string formation in the tips. Hence, it is advisable to mix by pipette inversion when adding glycerol, adding free dye, etc. This should result in higher final yields.
12. Although a **stop solution** was used in the past in the Vogel group, I don't see the need for 2 reasons. First the protein is almost instantly removed from free dye by the PD10 column, and second the dye will hydrolyze in water during the 1 hr incubation period anyway.
13. Concerning **hydrodynamic chromatography for removal of free dye**, the column works on the principle that the largest proteins remain nearer to the middle of the flow stream due to exclusion from the smaller cracks and holes found in the packed bed. Hence, the dimeric FN reaches the bottom of the column first. The larger fragments arrive second, smaller fragments third, and finally come the free dye. The free dye is more strongly apparent due to its color (labeled protein also has color since it is labeled, but less apparent), and marks the end of the moving protein fragments. The best way to set up the column specifications is to save each drop and run them separately on a silver stain or better yet Western blot. William Little found each drop to be about 40 ul.
14. Also **concerning the column**, hydrodynamic chromatography works best when it is most closely approximated by a pulse entry of the mixed solution of protein, fragments, and free dye. We only raise the starting volume to 1 ml since we've found that volumes less than 1 ml do not enter the column evenly. Columns with different diameters, etc, should be reevaluated for optimal use.

FRET fibronectin denaturation curve

Part 1 - Prepare materials

- Coat imaging surface with 5% BSA in PBS for 1 hr at room temperature OR at 4°C overnight.
- Empty the wells and air dry wells.
- Thaw FRET labelled fibronectin - Keep in ice.
- Spin down at 10,000rpm for 10 minutes
- Prepare 150mM DTT in PBS:

MW DTT : 154.25 g/mol

$(150 \times 10^3 \text{ mol/L}) (154.25 \text{ g/mol}) = 23.14 \text{ mg/ml}$

for **0.5ml PBS**: add **11.5mg DTT**

- Prepare Guanidin Hydrochloride (GdnHCl) at different concentrations as follows:

Gdn HCl (M)	8	6	4	2	1
Start (μl)	225	25	100	100	100
Add	0	75	100	100	100
Vol (μl)	225	100	200	200	200
Pass (μl)	125	0	100	100	0
End (μl)	100	100	100	100	200

* Stock GdnHCl:

MW GdnHCl: 95.53 Da (g/mol)

For 8M solution (8mol/L) in a volume of 10ml:

$$C = n/V ; MW = m/n ; C = m/(V \cdot MW) \text{ therefore: } m = C \cdot V \cdot MW$$

$$m = (8 \text{ mol/L}) (0.010 \text{ L}) (95.53 \text{ g/mol}) = 7.64 \text{ g} + 10 \text{ ml ddH}_2\text{O}.$$

Part 2 - Prepare DTT-FRET Fn

- Add 2.5 μl DTT in PBS + 5 μl FRET fibronectin and incubate for 1 hr in an eppendorf tube.

Part 3 - Experiment

Prepared: Daniela Ortiz Franyuti Oct 2013

Page 1 of 2

Date: _____

- In eppendorf tubes, prepare solvent as follows:

Gdn HCl (M)		0	0.5	1	1 + DTT
FRET Fn	5 μ l	5 μ l	5 μ l	5 μ l	
Solvents	5 μ l PBS	5 μ l 1M GdnHCl	5 μ l 2M GdnHCl	2.5 μ l 4M GdnHCl	
				2.5 μ l DTT in PBS	
Gdn HCl (M)		2	3	4	PBS
FRET Fn	5 μ l	5 μ l	5 μ l	-	
Solvents	5 μ l 4M GdnHCl	5 μ l 6M GdnHCl	5 μ l 8M GdnHCl	10 μ l PBS	

- Do one by one: add FRET Fn in eppendorf tube, mix and put a drop on imaging substrate.
- Find the surface, go 50 μ m higher and image.

Note: Avoid borders of the droplet.

FRET-labelled FN fibres. Native/3x Stretched/2x Relaxed

1) Prepare manually pulled fibronectin fibres

- Prepare FN solution: 0.4 mg/ml in PBS with 5% FRET-labelled Fn.
- Prepare silicone membrane on stretching device and pull for each sample 20 fibres parallel to the stress axis.
- Wash 3x with PBS and keep in PBS.
- Apply or release strain, while the fibres are on PBS.
- Image with Confocal

	Native	Stretched	Relaxed	
Initial length (L_1)	4 cm	4 cm	8 cm	
Final length (L_2)	4 cm	8 cm	4 cm	
Strain $((L_2-L_1)/L_1)(100\%)$		0%	100%	-50%

Procedure to test performance of confocal microscope.

Prepared by: Daniela Ortiz Franyuti

Tuesday, 9 October 2012

Objective:

To evaluate the performance of a confocal microscope regarding: dichroic reflectivity, lens performance, PMT reliability, and system noise.

laser power, laser stability, field illumination, spectral registration, lateral resolution, axial Z-resolution, lens cleanliness, lens functionality, and Z-drive reproducibility

Based on Reference:

Cell Imaging Techniques (Methods in Molecular Biology). Douglas J. Taatjes (Editor), Brooke T. Mossman (Editor). Humana Press; 2006 edition (November 1, 2005)

Materials:

- ➔ *Chroma Slides*
- ➔ *Test slide with micro beads: The beads are from Molecular Probes and a slide can be prepared by following the procedure in Appendix A.*
- ➔ *Single Reflective Mirror*

Confocal Microscope setup

- 1) Turn power on 15 to 60 min prior to use.
- 2) Set the confocal microscope at sufficient laser power to eliminate laser noise, generally this is at 1/2 the maximum power.
- 3) Clean objective carefully with methanol, or an equivalent optical cleaning solvent.
- 4) Adjust the system for Köhler illumination.
- 5) Make sure the lenses are adjusted for parfocality.

Procedures with Chroma Slides:

A. Field Illumination Test

Each laser line must be tested to insure they are aligned properly and that each one of them has an adequate field illumination. Furthermore, the tests should be carried out for all objective lenses since alignment with one objective does not always translate into good field illumination with other objectives.

- 1) Seal a #1.5 coverslip on the plastic slide (Chroma or API) with oil or anti-fade to eliminate potential scratching.
- 2) Place fluorescent slide on the stage and find the maximum intensity on the surface of the slide. Chroma red slides yield good excitation and spectra for both visible or UV excitation. Blue slides are used for UV excitation.
- 3) Measure the field illumination at a specific depth in the plastic slide, as the intensity distribution may change from the surface to the interior of the slide. The depth should be adjusted between 30–100 μm , dependent on the objective that is used: 5x (100 μm); 10x (75 μm); 20x (50 μm); 40x (40 μm); 63x (30 μm); 100x (30 μm). Be careful not to observe deep within the plastic slide, as it will usually yield a better field illumination than with the regions closer to the surface due to light scattering, light absorption, and light refraction.

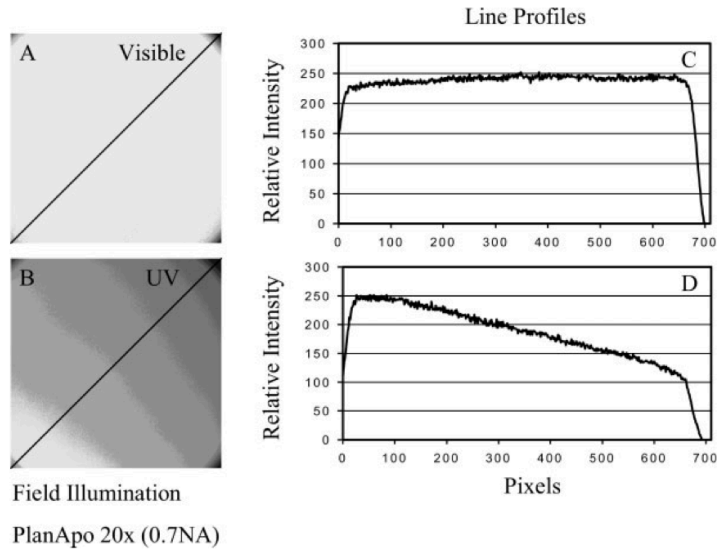
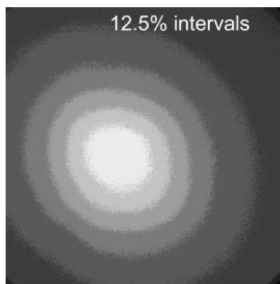


FIG. 1. Field illumination pattern of visible (A) and UV (B) excitation using a 20x (Plan Apo, NA 0.7) lens. The visible field illumination shows uniform illumination with the brightest intensity being in the center of the objective. The line running diagonally in panels A and B measures the histogram intensity of the field illumination graphically represented in Figures C and D. The variation in intensity from the left to right side of the field is less than 10% for visible excitation and over 150% for UV excitation. The intensity regions were prepared by using Image Pro Plus to divide the GSV into 10 equal regions and a median filter was used for additional processing. Acceptable field illumination has brightest intensity in the center of the objective decreasing less than 25% across the field.



The maximum intensity should be in the centre of the objective, and it should decrease by less than 25% across the field in all directions. The range of intensity decrease is partially dependent on the characteristics of the objective and its magnification. If the maximum light intensity is not located in the centre of the field, there is an alignment problem that needs to be addressed.

Note: The 647 line cannot be used with Chroma slides, as they were not excited by this wave-length.

Note: Not all problems with the field illumination test are the result of bad alignment, lens design/quality, or incompatibility of a lens with specific wavelengths of light. If a lens is dirty or covered with dried oil, then it would yield a nonuniform pattern.

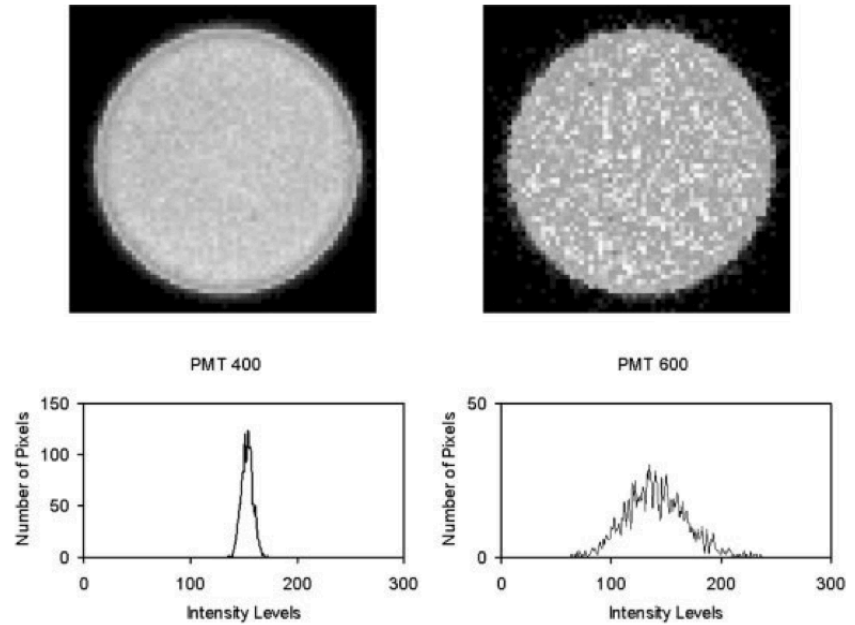
B. Noise presence using the Coefficient of Variation principle

The noise present in the system can be evaluated using a large 10 μm bead or a Chroma slide. The 10- μm bead consists of nearly uniform size and intensity (CV 5.5% by flow cytometry) is zoomed 4x to increase the number of pixels contained in the ROI with either a 100x objective (Plan Apo NA 1.4) or a 63x (Plan Apo 1.32 NA) lens.

1. Determine the mean, standard deviation (SD), and CV of the pixel intensities obtained from a ROI of the bead or fluorescence slide
2. It is important to maintain the machine variables (pin-hole, size-Airy Disk, PMT voltage, averaging, etc.) at reproducible values. Set the laser power at a constant value that allows the mean intensity level of the bead to be ~ 150 (out of 255) for each PMT setting.
3. Higher PMT voltage yields a broader histogram, which translates into more pixel intensity variations. One can compare the quality of images using this technique. As the

quality (less bead noise) of the images increases, the CV of the population of pixel intensities within the bead decreases.

Fig. 6. Bead pixel variations. TIFF images of a 10- μm Spherotech bead were obtained with two different PMT settings (PMT = 400, PMT = 600) with a zoom of four and no frame averaging using a 100 \times Plan Apo lens (1.4 NA). A ROI was drawn in the interior of the bead and the histogram of the population of pixel intensities is displayed in the bottom panels. The mean pixel intensity in both images was approximately 150 intensity levels and was obtained by keeping the PMT at 400 or 600 and adjusting the laser power with the AOTE. The coefficient of variation (CV = σ/μ) is defined as the standard deviation (σ) divided by the mean (μ) intensity. The noise at a specific setting can be reduced if frame averaging is increased. The averaging decreases the pixel variation, which lowers the SD and decreases the CV. Theoretically by averaging the image “ n ” times the CV and SD are decreased by the square root of “ n .”



Reducing the PMT and increasing the averaging both have the net result of decreasing the CV value. More averaging and lower PMT settings result in better image quality. Figure 7 illustrates the histogram relationship of averaging. The more averaging the more narrow the histogram and the lower the CV.

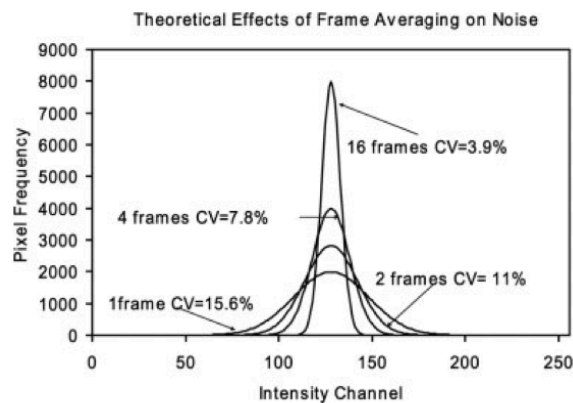


Fig. 7. Histogram relationships. The histogram of pixels located in a bead or any object narrows as averaging is increased. The averaging reduces the standard deviation and CV of the bead pixels by the square root of N , where N is the number of times the image is averaged.

In addition, many acquisition parameters, such as scan speed, pinhole setting, and objectives, will affect the PMT setting and thus the CV value.

Since PMTs will deteriorate with time, it is important to measure the initial CV (bead) and then to periodically measure how the CV (image quality) changes over time as a reference point for possible replacement of the PMT or realignment of the system.

One of the major elements responsible for a bad image results from operating the PMT at relatively high voltage values. High PMT voltages can be the result of insufficient sample staining, a misaligned system, a failing hardware component or attenuation of light through a fiber optic.

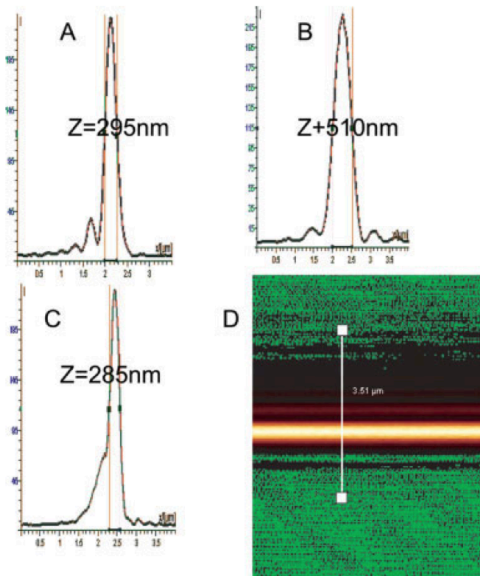
Procedures with reflective mirror:

C. Axial (z) Resolution

- 1) Place the mirror on the stage and use a high N.A. 60x or 100x oil lens.
- 2) Set the microscope up in reflecting (RT 30/70) dichroic mode.
- 3) Fully open up the lens condenser so that the lens is operating at the highest N.A.
- 4) Using *xy* scanning find the reflected surface of the mirror with an open pinhole aperture. This will be the brightest intensity. Zoom should be 1x.
- 5) Switch to *xz* scanning mode.
- 6) Find the line and adjust it so that it is located in the middle of the field.
- 7) Adjust the offset so that there is a little background. This will reduce the axial value by about 7 nm, but it will allow the diffraction pattern to be better observed.
- 8) Adjust the zoom to approximately 10x and reduce the pinhole to minimum size values (20 μm on a Leica SP and 10 μm on a Zeiss LSM 510).
- 9) The reflected image is then obtained and the intensity profile across the reflected surface is determined as shown in Figure 3.
- 10) The maximum of the peak is determined and then the half-maximum intensity value of the profile is obtained to determine the full-width half-maximum (FWHM) distance to determine the axial resolution.
- 11) The data can be observed graphically or it can be transferred into MS Excel or equivalent to measure the peak and the half-maximum values.
- 12) The specification for axial registration in a Leica TCS- SP system using 1003 NA 1.4 is below 350 nm.

It is important that the pattern show a symmetrical large peak followed by smaller peaks and valleys to left of it indicating diffraction patterns of an acceptable lens (Fig. 3A). This pattern relates to the airy disk pattern of the confocal system. The axial resolution of the system should be maximised to yield a minimal axial Z-resolution value with a symmetrical histogram and smaller diffraction peaks. If the lens is dirty (dried oil), the axial pattern will yield a very narrow peak with a broad shoulder.

Wavelengths of light that are longer will produce axial resolution values with higher numbers. Using a 633 (1.32 NA), we obtained the following axial values of the different wavelengths: 488 (299 nm), 568 (343 nm), and 657 (380 nm). The type of oil and cover-glass thickness will also affect the FWHM values obtained.



Plan APO 633 lenses (NA 1.32). One lens gave an excellent full-width half maximum (FWHM) of 295 nm (A) while the other lens yielded a bad value of 524 nm (B). The system was aligned properly in both cases. A symmetrical major peak and a diffraction pattern consisting of smaller peaks and valleys were shown in A, which is suggestive of an excellent quality lens. The pattern when the collar is not entirely open resulting in a lens that has less of a NA. (B) By accident, a dirty lens with dried oil was measured and it also was found to have a smaller FWHM (C). However, the pattern of this dirty lens showed a peak with a large shoulder, which is not desirable.

The axial Z resolutions of three different lenses on an aligned Leica TCS-SP1 system were the following: a 403 (Fluor, NA 1.0) was 610 nm; a 633 oil immersion Plan Apo (1.32 NA) was 315 nm, and a 1003 Plan Apo (1.4 NA) was 285 nm. These are considered good values for high-resolution work and can be used as reference values for other investigators.

D. Spectral Registration

1. In the Leica SP system, approximately a 10 nm reflection bandwidth is put over each excitation wavelength and the reflection is measured sequentially. This is similar to axial resolution mirror test using reflection mode and xz scanning, which can be acquired sequentially or simultaneously for the three laser lines.

2. By tweaking the AOTF and PMT voltage adjustments, the intensity of each reflected line was adjusted, so that the maximum intensity of the image was approximately 250 gray-scale value (GSV). The reflected light is adjusted so the maximum peak is close to 255, but does not exceed it.

The images representing three laser lines (i.e., 488, 568, and 647) are displayed as an overlay and a line is drawn through the composite image. The overlapping histograms will represent three laser lines and will have a distribution representing the spectral registration of optical system with an argon–krypton laser to distribution represents the lens quality.

With the multi-laser system, the distribution represents the composite of lens spectral properties and the laser alignment. Studying multiple magnification lenses should allow one to determine if lens quality or system alignment is correct.

The emission from either specimens or beads are normally recorded at least 10–40 nm above the excitation wavelengths, and not at the excitation wavelength. Many lenses have difficulty in co-localising far-red fluorescence with the blue and green fluorescence, so measuring the emission at 647 \pm 10 nm will yield a better resolution value than measuring the emission at 660–700 nm.

Procedures with Beads:

E. Axial (z) registration

Scan the TetraSpek beads in the xy direction and then in the xz direction. Adjust the power for near saturation values. They are then zoomed to approximately 8x and averaged 4x.

The size of the bead in the horizontal is compared with that in the vertical size. The difference between the two numbers will yield the axial resolution of the lens. This method is slightly more subjective than the axial resolution mirror test, but it does yield similar values. For unknown reasons, the bead derived axial values may be better or worse than the mirror tests.

Note: The immersion oil can play a role: Zeiss oil, Leica oil, and Cargill DF oil all yielded superior axial resolution, compared to other brands and types of immersion oil.

F. Spectral Registration

1. Obtain an xz scan at a proper zoom magnification (eg. 4x–8x) to observe the bead. Adjust the laser power level and zoom level to reduce possible bleaching effects. Adjust the gain and offset for optimum image quality levels.

Make sure that there is no fluorescence emission cross-talk between the detection channels by turning off each laser line sequentially and identifying if any signal is detected

in the corresponding channels. If necessary, decrease the laser power and increase the PMT voltage, to help eliminate cross talk.

The following is an example of data from an un-acceptable and an acceptable system. An acceptable difference was 210 nm in an aligned system. This test is critical for co-localisation studies.

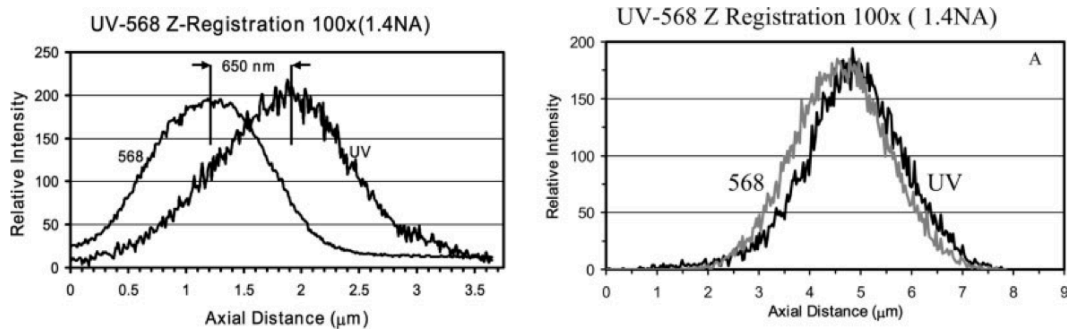


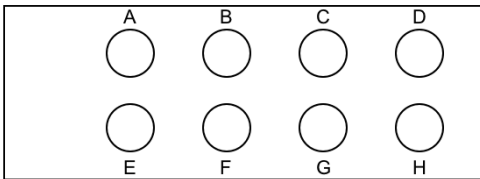
FIG. 4. Spectral registration (UV and visible). The axz spectral colocalization of this UV (365 nm) and visible wavelength (568 nm) was evaluated with a 100 \times Plan Apo NA 1.4 lens using a 1 μ m multiple wavelength fluorescent bead (Tetra Spec T7284 Molecular Probes). An aligned system has a full-width half-maximum (FWHM) of less than 210 nm (A) while a misaligned system has a FWHM difference of 650 nm (B). The bead was imaged using axz scans with a 8 \times zoom and xy with a zoom of approximately 16 \times . A slow scanning rate was used and the bead was averaged eight times. The 568 line was chosen instead of the 488 line to minimize the crossover between the visible and UV wavelengths.

The spectral registration test is measuring both the lens spectral registration and the laser spectral registration in newer confocal systems that contain three visible lasers and a merge module. It would be useful to measure a few different objectives to determine if there is correct laser spectral registration or misalignment in the system. The spectral pattern observed with multiple lenses should indicate if there are potential problems with either the lasers or the objectives.

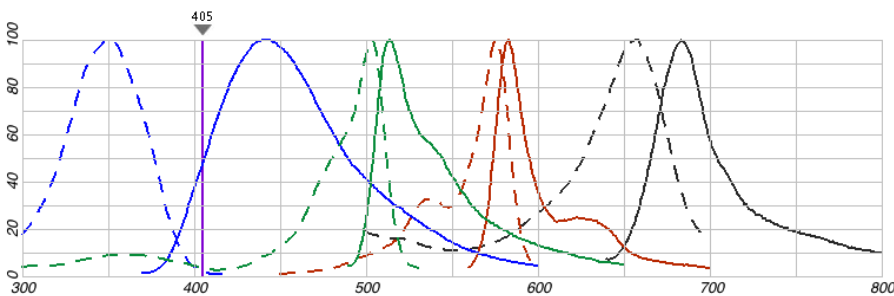
Appendix A: How to prepare a micro bead test slide.

Procedure:

- 1) Use clean glass microscope slides, i.e. oil and dust-free. Special cleaning is usually not required.
- 2) Mark the location where the beads will be placed for easy identification.



- A- PS-Speck Component A: Blue (360/440) 0.17 μ m
 B- PS-Speck Component B: Yellow/green (505/515) 0.17 μ m
 C- PS-Speck Component C: Orange (540/560) 0.17 μ m
 D- PS-Speck Component D: Deep Red (633/660) 0.17 μ m
 E- TetraSpeck- Blue,green,Orange, Dark Red 0.1 μ m
 F- TetraSpeck- Blue,green,Orange, Dark Red 0.5 μ m
 G- TetraSpeck- Blue,green,Orange, Dark Red 0.2 μ m



- 3) If desired, the beads in suspension can be diluted with distilled water before use. Before sampling, be sure that the beads are uniformly suspended by mixing on a vortex mixer or by sonicating.
- 4) Apply 2 to 5 μ L of the bead suspension to the surface of a slide and spread with the pipette tip. Wait for the droplet to dry completely.
- 5) Warm the bottle of ProLong® Gold anti-fade reagent to room temperature before use.
- 6) Apply 1 drop (or suitable quantity) of the anti-fade reagent to the specimen.
- 7) Cover slide-mounted specimens with a coverslip; carefully lower the coverslip onto the anti-fade reagent to avoid trapping any air bubbles.
- 8) Allow the preparation to cure on a flat surface in the dark for 24 hours.
- 9) After curing is complete, fully seal the edges with nail polish for optimum sample longevity. This will prevent excessive shrinkage of the mounting medium, which can result in sample distortion.
- 10) After sealing, store the slide upright in a covered slide box at 4°C.

Nanopillar displacements for LNSCs and NHDFS

Pillar displacement (um)

Time(min)	LNSC 1	STDEV	LNSC 2	STDEV	LNSC 3	STDEV	NHDF 1	STDEV	NHDF 2	STDEV	NHDF 3	STDEV
1	0.0923	0.03987	0.10908	0.05979	0.1405	0.08547	0.0707	0.04495	0.06715	0.03	0.1419	0.04917
2	0.09489	0.04074	0.08593	0.04899	0.12678	0.09343	0.09872	0.03757	0.0775	0.04041	0.10789	0.04204
3	0.10136	0.04367	0.07427	0.04996	0.11396	0.07421	0.06667	0.04001	0.07006	0.03782	0.09802	0.04391
4	0.10974	0.04004	0.0781	0.05201	0.10882	0.08789	0.09934	0.0456	0.06494	0.03426	0.07767	0.04688
5	0.10365	0.05138	0.07417	0.06134	0.10852	0.08679	0.06988	0.04469	0.06285	0.02847	0.07832	0.04593
6	0.11918	0.03943	0.07022	0.03849	0.095	0.07515	0.08607	0.06137	0.06231	0.04263	0.07428	0.04184
7	0.09184	0.04694	0.08848	0.03192	0.09674	0.07335	0.09078	0.04518	0.06449	0.04162	0.11344	0.0377
8	0.08976	0.0459	0.06635	0.03949	0.13394	0.08384	0.11311	0.06174	0.06117	0.02955	0.1135	0.02874
9	0.10008	0.04292	0.06359	0.02781	0.1387	0.09454	0.09651	0.05543	0.06877	0.03844	0.09892	0.03986
10	0.10537	0.04189	0.06315	0.03836	0.10002	0.08015	0.09557	0.0463	0.08133	0.03916	0.0952	0.03425
11	0.09311	0.04553	0.09573	0.0364	0.1125	0.08374	0.08747	0.04919	0.07275	0.02421	0.09623	0.03887
12	0.10301	0.04718	0.06511	0.03041	0.11402	0.09799	0.09667	0.04593	0.05804	0.02573	0.07864	0.0444
13	0.12234	0.05169	0.06593	0.03494	0.1995	0.09646	0.07493	0.036	0.07677	0.04052	0.09322	0.03325
14	0.1182	0.0487	0.07693	0.04978	0.2452	0.08589	0.07691	0.04465	0.11582	0.03176	0.08572	0.03099
15	0.13555	0.05207	0.09082	0.06037	0.1151	0.09302	0.09345	0.02498	0.05832	0.02894	0.07783	0.04104
16	0.11024	0.05378	0.15577	0.04672	0.14336	0.06602	0.07144	0.03177	0.07975	0.02786	0.10575	0.03327
17	0.1076	0.0579	0.12363	0.0503	0.14329	0.06612	0.06868	0.02909	0.07152	0.03641	0.06531	0.03154
18	0.12409	0.06627	0.14954	0.04612	0.09406	0.08023	0.07713	0.03777	0.06465	0.03732	0.09775	0.02834
19	0.12946	0.06555	0.07982	0.0408	0.11516	0.06764	0.11842	0.03068	0.07677	0.04513	0.09328	0.03233
20	0.14293	0.07217	0.10731	0.04445	0.1327	0.09393	0.089	0.03103	0.07791	0.04188	0.07355	0.03474
21	0.15641	0.08087	0.17343	0.06603	0.14334	0.07276	0.09605	0.03722	0.10551	0.02698	0.07106	0.03453
22	0.1602	0.07623	0.14375	0.08868	0.09572	0.07321	0.08681	0.05098	0.10421	0.02927	0.07274	0.04199
23	0.15162	0.06866	0.13984	0.03053	0.11524	0.0634	0.06517	0.04341	0.05794	0.03283	0.06862	0.03593
24	0.17182	0.07165	0.06954	0.04199	0.09492	0.08044	0.07786	0.02987	0.05756	0.02885	0.07409	0.03623
25	0.1724	0.07078	0.068	0.04979	0.08158	0.06654	0.06669	0.0363	0.06491	0.03178	0.07729	0.04165
26	0.16671	0.07841	0.05733	0.03739	0.11646	0.06608	0.06585	0.03651	0.07924	0.03678	0.08133	0.03566
27	0.17727	0.06993	0.0682	0.03451	0.1183	0.07787	0.06631	0.0385	0.07184	0.03826	0.07046	0.03554
28	0.20006	0.06715	0.06463	0.03158	0.08754	0.07593	0.07539	0.03459	0.07861	0.04282	0.08919	0.02658
29	0.17633	0.07632	0.07064	0.0383	0.08458	0.0738	0.07832	0.02995	0.11623	0.03667	0.06404	0.02874
30	0.23583	0.07943	0.85	0.03	0.09748	0.08578	0.08964	0.03776	0.09655	0.03417	0.09493	0.03272
	0.23583	0.08087	0.85	0.08868	0.2452	0.09799	0.11842	0.06174	0.11623	0.04513	0.1419	0.04917

Pillar spring constant=78.8nN/um

Force=displacement*78.6

```

%% Matlab codes for FN-FRET analysis

%% -----
%%parameters.m
%% TO RUN SCRIPT IN MATLAB, SAVE AS .m FILE BEFORE USE.
%% Enable xy shift correction? - Set to 1 to activate

p.shift = 1;

%% Define channel source

p.donCH = 2;
p.accCH = 1;
p.acctotCH = 4;
p.ligCH = 9;
p.otherCH = 0;

p.chtot = 9; %total number of channels

% if you are not measuring one channel, set to 0

%% Background

% This needs to be measured for the microscope used .

p.don_bkg = 156; % 156 estimated for microscope setting in our experiments
p.acc_bkg = 169; % 169 estimated for microscope setting in our experiments
p.ligand_bkg = 169; % 169 estimated for microscope setting in our experiments
p.acctot_bkg = 169; % 169 estimated for microscope setting in our experiments

%% Local averaging filter

p.filt = 3; %3 filter size to remove noise

%% Lower Thresholding. No thresholding or min = 0

p.acc_thr_L = 250; % 250 estimated for microscope setting in our experiments
p.don_thr_L = 250; % 250 estimated for microscope setting in our experiments
p.ligand_thr_L = 120; % 120 estimated for microscope setting in our
experiments
p.acctot_thr_L = 250; %250 estimated for microscope setting in our experiments
p.fret_int_L = 0;

%% Upper Thresholding. No thresholding or max = 4095
p.acc_thr_U = 4095;
p.don_thr_U = 4095;
p.ligand_thr_U = 4095;
p.acctot_thr_U = 4095;
p.fret_int_U = 4095;

%% Erosion level for mask - To reduce measurement error at the borders of the
fibres.
p.erosiontype = 1 ;
% Set 1 to activate erosion

p.erosionshape = 'square';
% Other possible types:'diamond', 'disk', 'octagon', 'square'

```

```

p.erodesize = 4; % size or erosion (for 'square' it's the length of the square)

%% Spectral overlap correction factors:

% These need to be estimated separately with samples containing only donors
% (beta factor), or only acceptors (delta and gamma factors)

beta = 0.28;      % 0.28 estimated for microscope setting in our experiments
delta = 0;        % 0 estimated for microscope setting in our experiments
gamma = 0.01;     % 0.01 estimated for microscope setting in our experiments

% See supplementary method

%% To remove invalid FRET ratios

p.maxfret = 1;
p.minfret = 0;

%% -----

%% FRETanalysis.m
%% TO RUN SCRIPT IN MATLAB, SAVE AS .m FILE BEFORE USE.

%% Parameter Setup

    parameters;

%% Image import

    rawdata = b fopen;
    data1 = rawdata{1,1};

%% Image preparation

    raw_don = data1{p.donCH,1};
    raw_acc = data1{p.accCH,1};
    raw_ligand = data1{p.ligCH,1};
    raw_acctot = data1{p.acctotCH,1};

    W=size(raw_acc,1);
    L=size(raw_acc,2);
    H=1;

    % Convert data to double precision values

    don = double(raw_don);
    acc = double(raw_acc);
    ligand = double(raw_ligand);
    acctot = double(raw_acctot);

%% Correct xy shift:

    if (p.shift == 1)

```



```

        [ acctot ] = registration( don, acctot ); %[ ImageRegistered ] =
registration( fixedimage, movingimage )
        [ ligand ] = registration( acctot, ligand );

        % Re-apply threshold

        acctot(acctot<=p.acctot_thr_L)=0;
        acctot(acctot>=p.acctot_thr_U)=0;

    end

%% Remove overexposed pixels

    don(don>=4095)=0;
    acc(acc>=4095)=0;
    ligand(ligand>=4095)=0;
    acctot(acctot>=4095)=0;

%% Apply thesholds

    % Thresholding - Lower

    don(don<=p.don_thr_L)=0;
    acc(acc<=p.acc_thr_L)=0;
    ligand(ligand<=p.ligand_thr_L)=0;
    acctot(acctot<=p.acctot_thr_L)=0;

    % Thresholding - Upper

    don(don>=p.don_thr_U)=0;
    acc(acc>=p.acc_thr_U)=0;
    ligand(ligand>=p.ligand_thr_U)=0;
    acctot(acctot>=p.acctot_thr_U)=0;

%% Subtract background

    don = don - p.don_bkg;
    acc = acc - p.acc_bkg;
    ligand = ligand - p.ligand_bkg;
    acctot = acctot - p.acctot_bkg;

%% Remove zeros and negative values

    acc(acc<=0)= NaN;
    don(don<=0)= NaN;
    ligand(ligand<=0)= NaN;
    acctot(acctot<=0)= NaN;

%% Create mask
    acc(isnan(acc))=0;
    don(isnan(don))=0;
    ligand(isnan(ligand))=0;
    acctot(isnan(acctot))=0;

    don_mask = logical(don);
    acc_mask = logical(acc);
    ligand_mask = logical(ligand);

```

```

        acctot_mask = logical(acctot);

%% Apply local averaging filter

        if(p.filt>0)
            f=p.filt;
            h=fspecial('average',f);
            acc = imfilter(acc,h);
            don = imfilter(don,h);
            ligand = imfilter(ligand,h);
            acctot = imfilter(acctot,h);
        end;

%% Combine Masks

        mask = don_mask .* acc_mask .* acctot_mask; %.*ligand_mask;

%% Erode mask to get rid of non-registered borders

        if (p.erosiontype == 1)
            seerode = strel(p.erosionshape,p.erodesize);
            mask = imerode(mask,seerode);
        end

%% Apply mask

        acc = double(acc) .* mask;
        don = double(don) .* mask;
        acctot = double(acctot) .* mask;

        ligand = double(ligand);
        ligand = ligand .* mask;

%% Remove zeros and negative values

        acc(acc<=0)=NaN;
        don(don<=0)=NaN;
        ligand(ligand<=0)=NaN;
        acctot(acctot<=0)=NaN;

%% FRET calculation

        factor1 = 1 - (beta * delta);

        fret_int = (acc - (beta .* don) - (acctot .* gamma .* factor1))
./ factor1 ;

%% Calculate appFRET:

        appFRETb = fret_int ./ don;

%% Ligand normalisation

        lignorm_a = ligand ./ acctot;

%% Filter out invalid pixels

```

```

    appFRETb(appFRETb>p.maxfret)=NaN;
    appFRETb(appFRETb<p.minfret)= NaN;

%% -----

%% registration.m
%% TO RUN FUNCTION IN MATLAB, DELETE THIS LINE AND SAVE AS .m FILE BEFORE USE.
function [ ImageRegistered ] = registration( fixedimage, movingimage )
%REGISTRATION Register two images
%   Registration of two images

fixed = fixedimage;
moving = movingimage;

% Uncomment the following line to see the differences between the two images
% to register:

% imshowpair(fixed, moving,'diff');

% Create a configuration suitable for registering images from the different
sensors.

[optimizer, metric] = imregconfig('monomodal');

% Perform the registration.
ImageRegistered = imregister(moving, fixed, 'translation', optimizer, metric);

% Uncomment the following two lines to see the differences between the two
% images after the registration process:

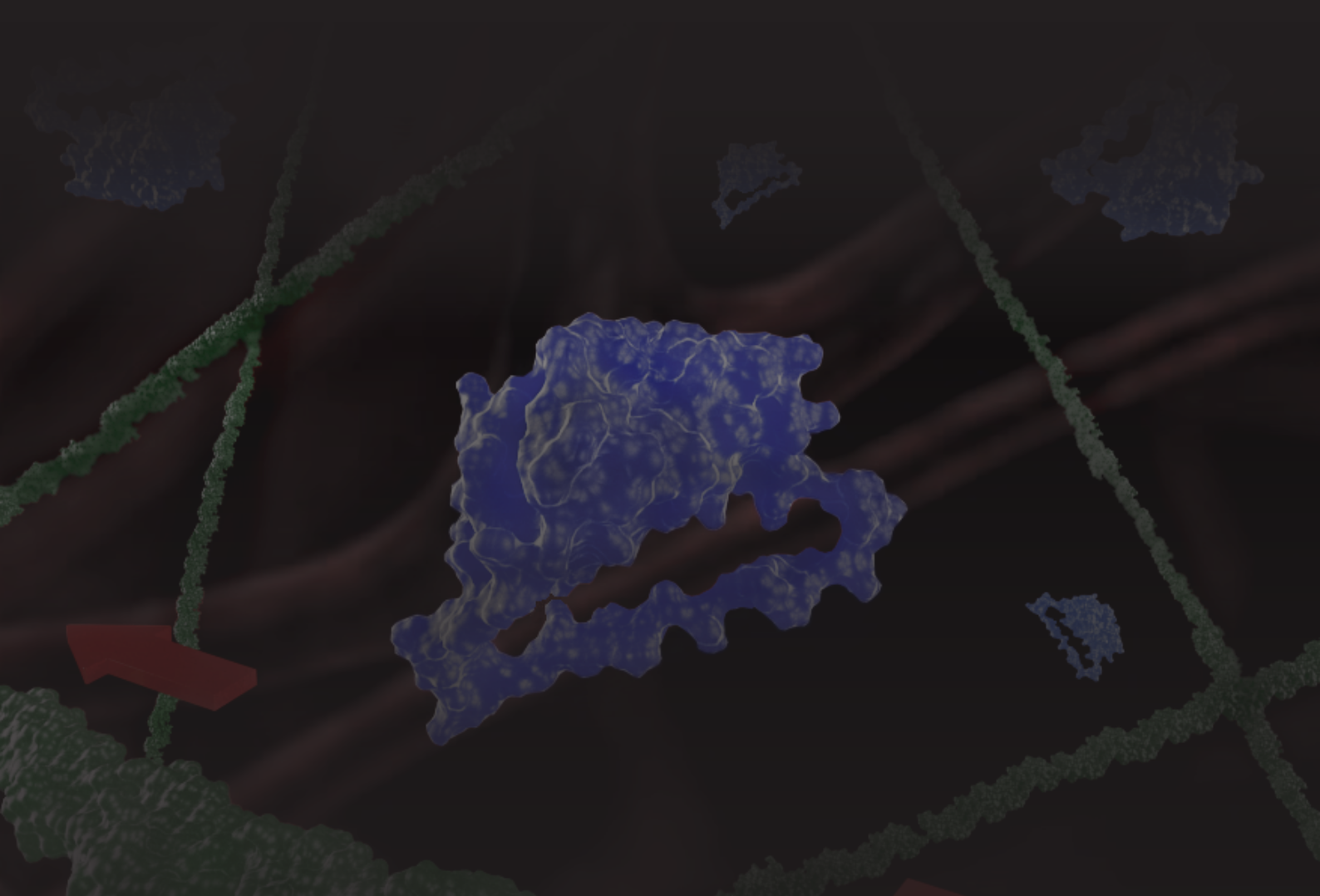
% figure
% imshowpair(fixed, ImageRegistered,'diff');

close all

end

%% -----

```



During inflammation and other physiological processes, swelling of tissue and extracellular matrix (ECM) remodeling can induce mechanical stretching or relaxing of the ECM, which can in turn induce a change in the conformation of fibronectin (FN). Since ECM fibers might serve as reservoirs for growth factors and cytokines, we investigated the interaction between FN and interleukin-7 (IL-7), a cytokine of immunological significance and a target of several immunotherapies. By employing a FN fiber stretch assay and Förster resonance energy transfer (FRET) confocal microscopy, we found that stretching of FN fibers increased IL-7 binding. We localized the FN binding site on the CD-loop of IL-7, and propose that the CD-loop can bind to FN, while IL-7 is bound to its cognate cell surface receptors. Sequence alignment with bacterial adhesins suggests that a conserved motif on the CD-loop might bind to the second FN type I module (FnI2), and that additional epitopes enhance the stretch-upregulated binding. FN fiber stretching might thus serve as a mechano-regulated mechanism to locally concentrate IL-7 in an ECM-bound state, thereby upregulating the potency of IL-7 signaling. Understanding how local IL-7 availability and signaling might be modulated by the tensional state of the ECM niche, and is adjusted by residing stroma cells, is highly relevant for basic science but also for advancing IL-7 based immunotherapies. First steps towards determining what impact these findings may have on lymph node and thymic stromal cell function are also presented.